Universidad de Alcalá

Departamento de Electrónica

Programa de Doctorado en Electrónica: Sistemas Electrónicos Avanzados. Sistemas Inteligentes

Limits of Performance of Chirped-Pulse Phase-sensitive OTDR

TESIS DOCTORAL

Autor

Luís Duarte Pereira da Costa

Directores

Dr. Miguel González Herráez

Dra. María del Rosario Fernández Ruiz

Alcalá de Henares

2020

Abstract

Distributed acoustic sensing is an emerging field of research which aims to develop methods capable of using a single optical fiber as a long, dense, and high-sensitivity sensor array. Currently, the most promising implementations measure the interference of Rayleigh backscattered light, obtained by probing the fiber with light from a source of high coherence.

These methods are known as Phase-sensitive Optical Time-Domain Reflectometers (φOTDR), and are currently undergoing a period of active research and development, both academically and industrially. One of its variants, known as the Chirped-Pulse φOTDR (CP-φOTDR), was developed in 2016. This technique has proven to be remarkably sensitive to strain and temperature, with an attractively simple implementation.

In this thesis, we delve into the intricacies of this technique, probing its fundamental limits and addressing current limitations. We discuss the implications of estimation on the performance statistics, the impact of different noise sources and the origin of cross-talk between independent measured positions. In doing so, we also propose methods to reach the current fundamental limitations, and overcome the upper bound of measurable perturbations.

We then demonstrate new potential applications of the technique: in seismology, by exploiting the high spatial density of measurements for array signal processing; in the fast characterization of linear birefringence in standard single-mode fibers; and on the measurement of sound pressure waves, by using a special flat cable structure to embed the fiber under test.

Finally, we summarize and comment on the aforementioned achievements, proposing some open lines of research that may originate from these results.

Acknowledgements

First and foremost, I wish to offer my heartfelt thanks to my thesis directors, Prof. Miguel González Herráez and Dra. María del Rosario Fernández Ruiz, for allowing me to integrate this research group, and for exposing me to interesting and challenging research projects during the course of my doctoral work. They have, time and time again, inspired me to persevere when research was challenging or results were slow to come. Their dedication, and constant availability to provide clear and clever advice was invaluable. To both of them I am extremely grateful.

On a similar note, I must extend my appreciation to Dr. Hugo Martins and Prof. Sonia Martín López, who provided crucial support on the development of the PhD, both in the form of technical advice and suggestions, as well as in support in the duties imposed by the university. A huge thank you to both of them.

I am also thankful to Prof. Luc Thévenaz and Prof. Zhongwen Zhan for hosting me in their institutions. I grew immensely (both as a person, and as a researcher) from the opportunity to work in such different environments, and from coming into contact with new ideas and approaches to research.

I would also like to thank all the professors and colleagues with whom I have shared the lab during my time as a student in the University of Alcalá: Prof. Fernando Naranjo and Prof. Óscar Esteban, as well as Andrés, Juan, Alejandro, Alexia, Piedad, Miguel, Pablo, Paco, Marco, Arantxa, Javier and Sirona. Thank you for the collaboration and friendly talks. These thanks extend also to those that worked with me outside of Alcalá: Li, Simon, Zhisheng and Pabitro, at EPFL. Thanks for immediately integrating me as part of your team, and for taking the time to aid me at each step of the way. Similarly, to everyone I collaborated with during their visits to our lab in Alcalá: Leonardo, Hari, Gil, Hagai, and Marcelo. Your expertise was extremely important, and I have learned a lot from interacting with all of you. These thanks extend to other collaborators: Prof. Avi Zadok, Prof. Luca Palmieri and Prof. Moshe Tur.

Evidently, I would like to thank the members of the FINESSE project. To all those that were part of the organization and the PIs, a huge thank you for the outstanding quality of the FINESSE training events. And to my fellow ESRs, for the discussions, the collaboration, and the companionship.

I also must acknowledge the role of my family. To my parents, João and Deolinda, thank you for all the support and encouragement. To my twin brother João, thank you for all the patience you showed when answering my incessant questions about optimization of CUDA code. Hopefully I will be able to repay it someday.

Last but not least, to Regina, for sharing this journey with me. It has been wonderful having you so close during this time. Thank you for everything.

Contents

List of Figures

List of Abbreviations

φOTDR	Phase-sensitive Optical Time-domain Reflectometer
AC	Alternate Current
AOM	Acousto-optic Modulator
ASE	Amplified Spontaneous Emission
AWG	Arbitrary Waveform Generator
AWGN	Additive White Gaussian Noise
BOCDA	Brillouin Optical Correlation-domain Analysis
BOTDA	Brillouin Optical Time-domain Analyzer
BOTDR	Brillouin Optical Time-domain Reflectometer
CP-φOTDR	Chirped-pulse Phase-sensitive Optical Time-domain Reflectometer
CRLB	Cramér-Rao Lower Bound
CW	Continuous-wave
DAS	Distributed Acoustic Sensing / Distributed Acoustic Sensor
DC	Direct Current
DG	Delay Generator
DOP	Degree of Polarization
DWDM	Dense Wavelength Division Multiplexer
ECL	External Cavity Laser
EOM	Electrooptical Modulator
EOM	Electro-optic Modulator
ER	Extinction Ratio
FBG	Fiber Bragg Grating
FDR	Frequency-domain Reflectometry
FFT	Fast Fourier Transform
FPU	Fermi-Pasta-Ulam
FUT	Fiber under test
FWHM	Full width at half maximum
GCC	Generalized Cross-Correlation
IQ	In-phase/Quadrature
LD	Laser Diode
LO	Local oscillator
LP	Linearly Polarized
MI	Modulation Instability
OCC-BOTDA	Optical Chain Chirp Brillouin Optical Time-domain Analyzer
OFDR	Optical Frequency-domain Reflectometry

OP	Optical Path
OTDR	Optical Time-domain Reflectometry
P-OTDR	Polarization Optical Time-domain Reflectometer
PD	Photodetector
PMD	Polarization Mode Dispersion
PSD	Power Spectral Density
PZT	Piezoelectric Transducer
RF	Radio Frequency
RIN	Relative Intensity Noise
SA-BOTDA	Slope-assisted Brillouin Optical Time-domain Analyzer
SMF	Single Mode Fiber
SNR	Signal-to-Noise Ratio
SOA	Semiconductor Optical Amplifier
SOP	State of Polarization
SPL	Sound Pressure Level
SR	Spatial Resolution
TDE	Time Delay Estimation
TDM	Time Division Multiplexing
TDR	Time-domain Reflectometry
VOA	Variable Optical Attenuator
WDM	Wavelength Division Multiplexing

Chapter 1

Introduction

1.1 Motivation

The modern world is increasingly aware of the value and competitive advantage provided from accessing large amounts of reliable data. By continuously observing changes in the environment, one can build systems that intelligently respond to a plethora of potential situations. This proves to be invaluable when aiming for greater sustainability, optimized yields and improved quality of life. In our way towards building truly smart cities, buildings and infrastructures, we cannot neglect the foundations: high quality and ubiquitous sensing.

In many real-world scenarios, however, there are clear implementation challenges for traditional electrical sensing alternatives. Scaling the number of sensed positions poses logistical problems with cabling and power supply, the devices may be unsuitable for installation in hazardous environments, and the costs of achieving high sensor density over very long distances is often prohibitively high. Fortunately, fiber optic sensing technology has stepped up to these challenges in the past decades, granting the possibility of fully distributed measurements over several kilometers, at low cost-per-sensor and using only passive glass fibers as a whole sensing array.

The value provided by distributed sensors is already well-recognized by several industries and fields, and is becoming increasingly commonplace. A particular branch of distributed sensing that is quickly rising in attention is Distributed Acoustic Sensing (DAS), in the interest of measuring fast dynamic deformations. The applications are vast, with examples ranging from traffic control or intrusion detection, to damage assessment in large structures, improvement of current geophysical models, or improved safety and yields in the energy sector.

The most common DAS implementations rely on a time-domain probing of the elastic scattering of light within the fiber to produce interferometric measurements at each position, a technique known as Phase-sensitive Optical Time-Domain Reflectometer (φOTDR). These already comprise a vast body of research, but there is still plenty of room for improvement in order to completely fulfill the requirements of several industries and applications. For a solution to have wide applicability and commercial interest, the technique must provide accurate measurements, robust performances, avoid unnecessary complexity and have an affordable entry price.

In 2016, one interrogation method for these techniques was developed, which adds a linear modulation to the probe pulse of traditional φOTDR implementations. This simple alteration fundamentally changes the estimation process of the technique, and ensures improved linearity and robustness, with comparatively low costs. Being a recent technique, however, there is ample room to study potential new improvements and applications. The fundamental limitations of the technique must be understood, as well as potential methods do address any perceived limitations.

This is the aim of this thesis: to improve the current understanding of chirped-pulse φOTDR (CP-φOTDR), optimize its performance, and attest the applicability of the method to new applications.

1.2 Objectives

The motivation stated above prompted the consideration of the following objectives for research over the course of the thesis work:

- Identification and theoretical description of the current limits of the CP-φOTDR technique.
- Development of algorithms and methods to reach fundamental limits and address current limitations.
- Assess the viability of these methods in a laboratory environment.
- Identify and develop new applications that may benefit from application-specific algorithms or variants of the technique.

1.3 Structure of the work

This thesis is structured as follows:

Chapter 2: Fundamentals of Fiber Optics

In the following chapter, we shall briefly cover some fundamentals of fiber optics technology which are required to understand the exposition of the chapters that follow. We introduce the propagation of light in fiber waveguides, the mechanisms governing attenuation, and describe the different scattering processes. We also introduce the formalism to describe the polarization of light, and the discuss birefringence in optical fibers.

Chapter 3: Distributed Acoustic Sensing

In the third chapter, we introduce the reader to sensing using optical fibers. We then describe briefly the notion of distributed sensing and review the applicability of the main methods for the sensing of dynamic perturbations. Afterwards, we introduce the reader to the fundamentals of Optical Time-Domain

Reflectometry in its coherent and incoherent variants, and present a state-of-the-art of sensing implementations of the technology. Finally, we present an in-depth description of the CP-φOTDR technique, in which the research work was focused.

Chapter 4: Limits of Performance of CP-φOTDR

The fourth chapter of this work is dedicated to the description of several limits and fundamental properties of CP-φOTDR. Specifically, we present a statistical analysis of performance, and compare it to other common interrogation techniques, we describe an analysis of the fundamental limits imposed on the system from estimation, and on the implications of cross-talk among sensing channels due to the measurand estimation algorithm. We also propose specific algorithms and methods to reach the fundamental limit of performance given by the additive noise on the recovered intensity trace, as well as alternative methods to overcome the technique's limit of measurable strain.

Chapter 5: New applications of CP-φOTDR

In this chapter, we explore new potential applications of CP-φOTDR that were demonstrated during our research work, requiring either application-specific processing, alterations to the standard optical setup or tailored sensing elements. Specifically, we demonstrate the technique for the fast characterization of linear birefringence in single-mode fiber links; the measurement of seismic activity using pre-installed dark fibers in metropolitan areas; and measurements of sound pressure by using a sensitivity-enhancing flat cable structure.

Chapter 6: Conclusions

In the final chapter, we summarize the important conclusions from the research work developed during the doctoral program, and comment on potential future research paths.

Chapter 2

Fundamentals of Fiber Optics

The first reported observations of light propagation in cylindrical waveguides can be attributed to Jean-Daniel Colladon and Jacques Babinet, circa 1842 [1–3], as they noticed the ability of a stream of water to guide light even as it propagated in a curved path. While somewhat unnoticed at the time, these findings were later popularized by John Tyndall [4, 5]. It was not until 1966, however, that Nobel prize winner Charles Kao [6] proposed the waveguides which, through this approach, would transform the landscape of global communication and kindle the fires of an information revolution [7, 8].

As the name implies, optical fibers are the core component of fiber optic technology. Their supremacy in the telecommunication industry is well justified: fibers exhibit extremely low propagation losses and transmission bandwidths orders of magnitude greater than traditional copper alternatives. Besides, by doping with rare-earths, these can be made into powerful in-line amplifiers of weak signals [9]. Consequently, fibers nowadays form a complete backbone of the long-haul data transmission infrastructure.

While it is nearly impossible to detach optical fibers from their achievements within the realm of telecommunications, we should not dismiss all the real and potential applications in other domains. Fibers are used to develop optical signal processing components and have been demonstrated in niche applications such as power-transfer to hazardous locations (with power-over-fiber technology)[10, 11], and, as we intend to show, fibers also naturally lend themselves as an excellent sensing platform.

This section introduces the technical fundamentals of the work developed over the course of the doctoral program by laying the foundations over which later chapters shall be built upon. We present an introduction to light propagation in optical fibers and a summary description of the principles that are at the heart of distributed sensing. We finish with an analysis of the relevant phenomena that affect light as it propagates through the fiber.

2.1 Propagation and detection of light

Classically, the propagation of light in free-space is described in full by the Maxwell's equations [12, 13]. In their differential form, these are

$$\nabla \cdot \mathbf{D} = \rho \tag{2.1a}$$

$$\nabla \cdot \mathbf{B} = 0 \tag{2.1b}$$

$$\nabla \times \mathbf{E} = -\frac{\delta \mathbf{B}}{\delta t} \tag{2.1c}$$

$$\nabla \times \mathbf{H} = \mathbf{J} + \frac{\delta \mathbf{D}}{\delta t}, \tag{2.1d}$$

where $\mathbf{E}$ and $\mathbf{H}$ are the electric and magnetic fields, and $\mathbf{D} = \varepsilon_0 \mathbf{E} + \mathbf{P}$ and $\mathbf{B} = \mu_0 \mathbf{H} + \mathbf{M}$ the electric and magnetic flux densities (which take into account the induced electric and magnetic polarizations of the material $\mathbf{P}$ and $\mathbf{M}$). Here, ε_0 and μ_0 are the electric permittivity and magnetic permeability in vaccum, while $\mathbf{J}$ and ρ relate to current and charge densities and can be set to zero for non-conducting media. Equations 2.1 clearly attest the co-dependency of electric and magnetic fields: Any time variation of the electric field generates a perpendicular magnetic field, and vice-versa. This property permits a self-sustaining cycle to perpetually repeat and physically propagate across space, perpendicularly to the oscillation of both fields. Electric and magnetic fields, therefore, are so fundamentally intertwined that we consider them two composing aspects of a single entity called an electromagnetic field.

The wave behavior of the electromagnetic field may be formally described through wave equations, achieved by manipulating equations 2.1. In the case of free-space propagation (i.e., setting the material polarization terms $\mathbf{P}$ and $\mathbf{M}$ to 0), the corresponding wave equations are

$$\nabla^2 \mathbf{E} = c_0^2 \frac{\delta^2 \mathbf{E}}{\delta t^2} \tag{2.2a}$$

$$\nabla^2 \mathbf{B} = c_0^2 \frac{\delta^2 \mathbf{B}}{\delta t^2}, \tag{2.2b}$$

for speed of light $c_0 = \sqrt{\mu_0 \varepsilon_0}$. Describing both components, however, is redundant, since propagation is based on the periodic transfer of energy between $\mathbf{E}$ and $\mathbf{B}$. For the sake of brevity, we shall henceforth adopt the electric component to describe the optical field, as it dominates most light-matter interactions.

The wave equations 2.2 are linear, so the superposition principle applies. An arbitrary wave can be decomposed into a sum of independent monochromatic components of the form

$$\mathbf{E}(\mathbf{r}, t) = \mathbf{E}_0 \cos(\mathbf{k} \cdot \mathbf{r} - \omega t + \varphi_0) = \mathrm{Re}\left\{ \mathbf{E}_0 \, e^{i(\mathbf{k} \cdot \mathbf{r} - \omega t + \varphi_0)} \right\} \tag{2.3}$$

with angular frequency ω and wavevector $\mathbf{k}$ ($||\mathbf{k}|| = 2\pi/\lambda$, pointed towards the wave's propagation), at position $\mathbf{r}$, and initial phase φ_0. Note that in the complex exponential representation, it is common to omit the $\mathrm{Re}\{\cdot\}$ operator, though only the real part of the wave has physical meaning [14].

2.1.1 Superposition of waves: Interference and beating

The superposition of several co-polarized same-frequency waves combines them into a single wave of equal frequency. The resulting wave has its phase and amplitude dependent on the phase-relationship of the component waves, in a phenomenon known as interference.

Observing these effects implies detecting light: converting the electric field amplitude at some position into some quantified value. It is not trivial, however, to directly measure the electric field amplitude. Instead, optical detection is achieved by means of a highly absorbing material, commonly a photodiode, which generates a current proportional to the incident light power over its sensitive area (the optical intensity). Furthermore, electronic devices cannot generate currents fast enough to keep up with the speed of individual oscillations of the applied field. As a consequence, the measured optical intensity is proportional to the squared magnitude of the electric field, averaged over a series of optical cycles [12, 14, 15].

$$I = \frac{c\varepsilon_0}{2}\langle |E_{PD}|^2 \rangle. \tag{2.4}$$

Where the expected value $\langle\cdot\rangle$ operator reflects the time-average of oscillating fields, which in this context entails setting all sinusoidal functions in the optical frequency range ($\sim$ THz) to their mean (0).

In order to describe the phenomenon of interference, then, consider two waves co-propagating in 1-dimensional space, having the same amplitude, frequency and wavenumber, but different initial phases φ_1 and φ_2. At an arbitrary position of detection z_{PD}, the net electrical field is given by

$$E_{PD} = E_0[\cos(k\,z_{PD} - \omega t + \varphi_1) + \cos(k\,z_{PD} - \omega t + \varphi_2)] \tag{2.5}$$

$$= 2E_0\cos(\frac{\varphi_1 - \varphi_2}{2})\cos(k\,z_{PD} - \omega t + \frac{\varphi_1 + \varphi_2}{2}), \tag{2.6}$$

where the two resulting cosine terms showcase the different effects of interference: the first is time-independent and demonstrates the amplitude effects of wave interference, with absolute value ranging from 0 (destructive interference) to 1 (constructive interference), while the second time-dependent cosine term evidences the effect of interference on the phase of the resultant wave (see Figure 2.1).

Consequently, at the point of detection (z_{PD}), the detected intensity of two interfering waves of the same amplitude is given as

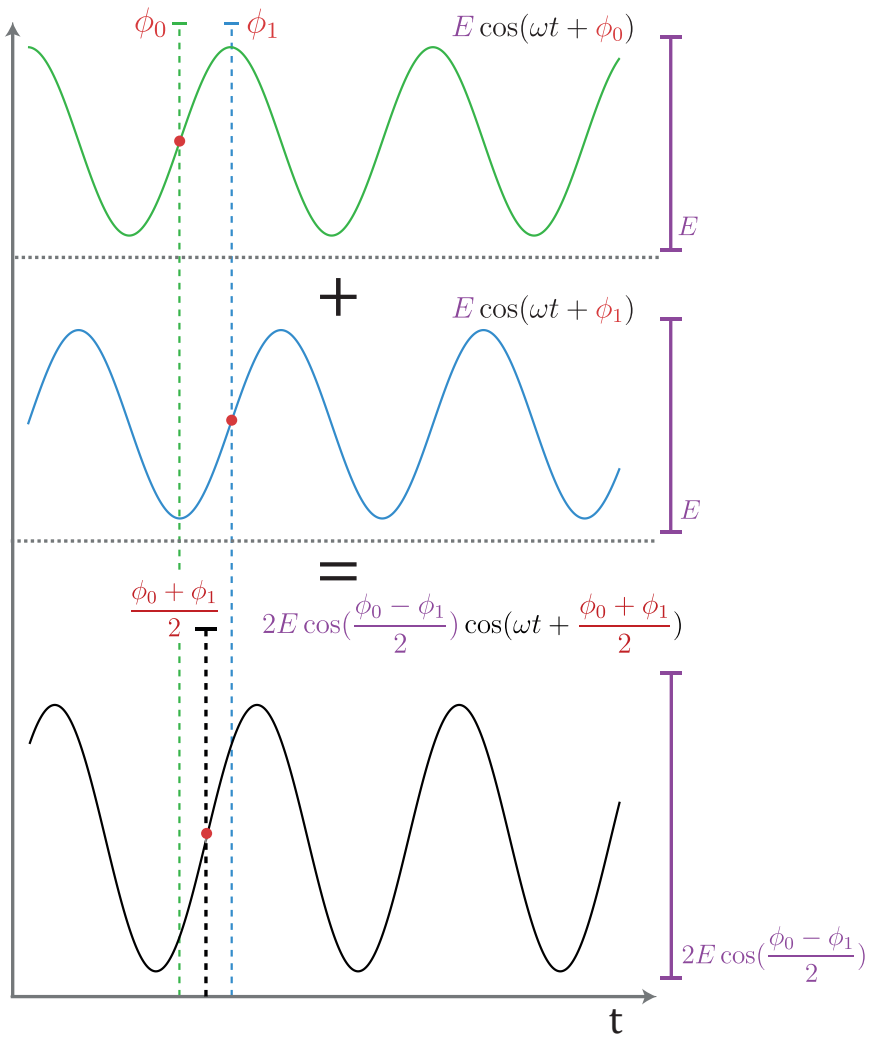

FIGURE 2.1: Visual depiction of two same-frequency waves (green and blue) and their superposition (black wave) as described in equation 2.6. The amplitude terms are marked purple and phase terms are marked red.

$$I = 2I_0\,(1+\cos(\varphi_1-\varphi_2)) \tag{2.7}$$

for $I_0 = \frac{c\varepsilon_0}{2}E_0^2$. Notice that the detected intensity may achieve any value within the range $[0, 4I_0]$, depending only on the phase relationship between both waves. Accounting for the possibility of different component wave intensities (I_1, I_2) we have

$$I = I_1 + I_2 + 2\sqrt{I_1 I_2}\cos(\varphi_1-\varphi_2), \tag{2.8}$$

which may be further generalized to any arbitrary number of N superposing waves, in which case there will be (C_2^N) interference terms, accounting for all possible pairs

of independent waves of the form $\sqrt{I_i I_j}\cos(\varphi_i - \varphi_j)$, as

$$I = \sum_{i}^{N} I_i + 2\sum_{j>i}^{N}\sum_{i}^{N-1}\sqrt{I_i I_j}\cos(\varphi_i - \varphi_j). \tag{2.9}$$

Generalizing the interference phenomenon to different-frequency waves results in a related, but different outcome known as *beating*. This phenomenon is particularly important, being at the root of frequency downconversion to detectable ranges and heterodyning (since, as we mentioned previously, electrical devices cannot react fast enough to the oscillations of light waves). Consider once again two co-polarized waves, co-propagating in 1-dimensional space of the same amplitude, but with frequencies (ω_1, ω_2) and the same amplitude. Following a similar analysis as the one in equation 2.7 while setting $z_{PD} = 0$ (for simplicity), we have

$$I(t) = 2I_0 + 2I_0\cos([\omega_2 - \omega_1]\,t + \varphi_1 - \varphi_2), \tag{2.10}$$

where the "beating" cosine term can typically reach frequencies much below the optical regime (THz), readily detectable by electronic equipment (operating within or below the GHz range).

2.1.2 Quasi-monochromatic sources and coherence

Ideal monochromatic waves with constant instantaneous frequency are not achievable in the physical realm. While some sources can be considered as such for specific applications (e.g. single-frequency lasers), the occupied bandwidth will necessarily be greater than 0. The emission spectrum of a quasi-monochromatic source theoretically presents a Lorentzian profile, owing to the typical dampened oscillation exhibited by a radiating charge [12]. The width of the (ideally) Lorentzian shape is named the source linewidth, and has direct implications in what is known as the coherence of a light source.

A non-zero bandwidth implies the continuous superposition of waves around a center angular frequency ω_c. We may, as such, model a simple non-monochromatic source as $\mathbf{E}_\Omega(t) = E_0\int_{-B/2}^{B/2}\cos(\omega_c t + \Omega t)d\Omega$ (for finite bandwidth B, where Ω is an auxiliary variable used to integrate over all non-zero frequency components). Coherence can then be thought of as a measure of how reliably we can expect light from such a source to behave as a monochromatic wave [15]. This notion of coherence can be easily verified by comparing the output at two time instants separated by a delay τ, in the quasi-monochromatic case ($B << \omega_c$)

$$\mathbf{E}_\Omega(t) = E_0\int_{-B/2}^{B/2}\cos((\omega_c + \Omega)t)d\Omega \tag{2.11a}$$

$$\mathbf{E}_\Omega(t+\tau) = E_0\int_{-B/2}^{B/2}\cos([\omega_c + \Omega]t + \omega_c\tau + \Omega\tau)d\Omega. \tag{2.11b}$$

Here, for small enough τ, the phase term $\Omega\tau$ is negligible and the wave behaviour is approximately monochromatic (i.e., the phase increases linearly with the delay τ and center frequency ω_c). As τ increases, however, the $\Omega\tau$ term becomes increasingly important, since each frequency component of the wave begins to co-exist at a different phase. After a long enough delay, the components within the narrow band $[\omega_c - B/2, \omega_c + B/2]$ will occupy the full range of potential phase states and light is said to be incoherent. The formal definition is given by the temporal degree of coherence, which is defined as the absolute normalized autocorrelation of the electric field over time,

$$|g(\tau)| = \left| \frac{\langle E^*(t)E(t+\tau)\rangle}{\langle E^*(t)E(t)\rangle} \right|. \tag{2.12}$$

The definition of coherence time τ_c follows directly from the shape of $|g(\tau)|$, with a generally accepted definition being its equivalent-power width [15]

$$\tau_c = \int_{-\infty}^{+\infty} |g(\tau)|^2 d\tau, \tag{2.13}$$

which, for the theoretical Lorentzian spectral shape of quasi-monochromatic sources that we alluded to, would be proportional to the full-width at half maximum of the power spectrum of the source as $\tau_c = \frac{1}{\pi\Delta\nu}$. Analogously, one may define a coherence length as $l_c = \tau_c c_0$.

One other useful, and perhaps more practical, way of quantifying the effects of coherence in the context of interferometry is the fringe visibility. Note that coherence measures the "effectiveness" of the interference between interacting waves: perfectly coherent waves can reach the full range of interference behaviour, from perfectly destructive interference to perfectly constructive interference. Perfectly incoherent waves, on the contrary, do not interfere at all, and always result in the same average power regardless of the delay between interacting waves. It is quite common to have an interference measurement which (over a long enough measurement time), yields the full range of possible values from the interference. In this case, visibility provides a good estimation of the effectiveness of the interference using direct intensity measurements only. Formally, assuming a time-series of intensity measurements of two interfering waves (with changing delay over time τ), we may define visibility as [14]

$$\mathcal{V}(\tau) = \frac{\max[I(\tau)] - \min[I(\tau)]}{\max[I(\tau)] + \min[I(\tau)]}. \tag{2.14}$$

In summary, when exploiting interference phenomena with quasi-monochromatic waves, the linewidth of the source is an important consideration, and must be selected according to the distance or time over which one requires interference to occur. In this work, we will make use of typical telecommunication lasers, featuring linewidths ranging from sub-kHz to some MHz.

2.1.3 Propagation of light in dielectric materials

While the speed of light is a fundamental constant of the universe, unchanged for all inertial reference frames, the apparent velocity of light can change depending on how "optically dense" the medium of propagation is. This "optical density" is quantified through the refractive index of a material as the denominator of the speed of light for a given medium ($n = c_0/v$, where v denotes the observed light velocity). Classically, the interpretation of refractive index in a dielectric material (such as fused silica) models the bound charges of the medium as damped oscillators, driven to forced ground-state vibrations upon the introduction of a transient electric field. The damped oscillating charges, consequently, radiate the stored energy with a phase shift.

What we perceive as the propagating wave, then, is in fact the superposition of incident light with all the medium-produced optical fields, manifesting as an apparent slow-down of light [16]. Hence, the refractive index arises from the response of a material to an applied transient electric or magnetic field, and can therefore be related to the electrical permittivity and magnetic permeability of the material

$$n = \sqrt{\frac{\varepsilon}{\varepsilon_0}\frac{\mu}{\mu_0}}. \tag{2.15}$$

Since dielectric materials boast almost no magnetic response ($\mu = \mu_0$), we concentrate only on the electric-field effects on the material. The result of a separation of positive and negative charges due to an external field, leading to a net dipole moment is known as the material's *polarization* (not be confused with polarization of light, discussed in a later section, which pertains to the direction of the oscillation of electric field). The constitutive relation that relates a material's polarization to the applied external field is

$$\mathbf{P}(\omega) = \varepsilon_0 \chi(\omega)\mathbf{E}(\omega), \tag{2.16}$$

for low enough electric fields under which the forced oscillation of the charged particles is linear with the applied field. Here, $\chi(\omega)$ is a frequency-dependent dimentionless quantity defined as the *susceptibility* of an isotropic dielectric medium to external electric fields, such that

$$n^2(\omega) = \frac{\varepsilon(\omega)}{\varepsilon_0} = 1 + \chi(\omega). \tag{2.17}$$

For the reasons stated above, our previous definition of the wave equation of light, as described by equation 2.2, must be corrected in order to account for the interplay between input electrical field and material response. Therefore, in order to properly describe propagation in dielectrics, we re-write equation 2.2 as [14]

$$\nabla^2\mathbf{E} - c_0^2\frac{\delta^2\mathbf{E}}{\delta t^2} = \mu_0\frac{\delta^2\mathbf{P}}{\delta t^2} \tag{2.18}$$

where the polarization and electric field terms share the same frequency (by equation 2.16), but are not necessarily in-phase. The frequency and phase response of each material arises from the atomic and molecular properties, and are expressed by letting the susceptibility χ be a frequency dependent complex-value: The real part of χ describes the effects of the material on the apparent velocity of light, while the imaginary part describes the transfer of energy to the material as heat (*i.e.*, absorption).

These material properties reflect upon the propagating wave's angular wavenumber k (the magnitude of the wavevector $\mathbf{k}$), which, for dielectric propagation is also a frequency-dependent, complex quantity. The real part of the wavenumber, associated to the wave's propagation velocity, is known as the propagation constant β. In the case of a quasi-monochromatic wave of central frequency ω_0 and propagation constant $\beta(\omega) = \omega\frac{n(\omega)}{c_0}$, $\beta(\omega)$ can be approximated around the central wavelength as

$$\beta(\omega) = \beta(\omega_0) + \beta'(\omega)|_{\omega=\omega_0}(\omega - \omega_0) + \mathcal{O}(\omega^2), \tag{2.19}$$

this frequency-dependence of the light's velocity has important implications, particularly in the case of pulsed light. The zero-th order term of $\beta(\omega)$ is related to the velocity at which each plane of constant phase travels (*i.e.*, the phase velocity)

$$v_p(\omega_0) = \frac{c_0}{n(\omega_0)} = \frac{\omega_0}{\beta(\omega_0)}, \tag{2.20}$$

which, in the case of a monochromatic, continuous lightwave, corresponds to the speed of light within the medium. For the case of quasi-monochromatic pulsed light, however, while each plane of constant phase will travel at the phase velocity, this is not necessarily true for the wave envelope (i.e., the pulse - see figure 2.2). The velocity of propagation of the pulse is known as the group velocity, and is determined by the first-order term in equation 2.19, as

$$v_g(\omega_0) = \frac{d\omega}{d\beta}\Big|_{\omega=\omega_0} = \frac{1}{\beta'(\omega)|_{\omega=\omega_0}} = \frac{c_0}{n(\omega_0) + \omega_0\frac{dn(\omega)}{d\omega}} = \frac{c_0}{n_g(\omega_0)}, \tag{2.21}$$

where $n_g(\omega)$ is the group index, describing the velocity of propagation of the pulse through the medium. The propagation constant dependency on wave frequency is generally non-linear, however, and higher order terms often need to be considered. The second order term characterizes the dispersion of the medium, which is seen as a broadening (or compression) of the pulse during propagation, combined with a re-ordering of spectral components, while higher order effects lead to distortions of the propagating pulse. For the purposes of the presented work, such higher-order effects can be considered negligible.

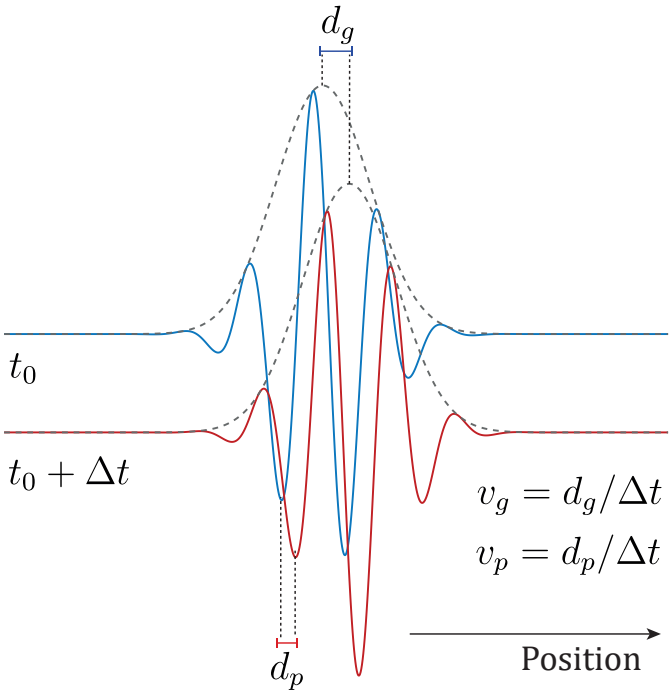

FIGURE 2.2: Visual representation of phase velocity (v_p) and group velocity (v_g).

2.2 Optical Fibers

Optical fibers are thin cylinders composed of a dielectric material, engineered to trap light within them so it propagates longitudinally with minimal losses. Fiber development is a fertile field of research, with application-specific fibers being manufactured in many shapes, sizes and materials, tailored to each specific need. It is not uncommon to employ fibers with special configurations (such as hollow fibers, or high-birefringence fibers) [17], different materials (such as exotic glasses or polymers) [18], or even with several cores [19]. Nevertheless, the great majority of fibers follows a standard of silica glass, step-index profile. In the work developed over this thesis, we shall mostly focus on the standard fibers that make up most of the telecommunication infrastructure, though some specialty fibers may be used sporadically in some components or for specific applications.

Typically, single-mode optical fibers are made of fused (amorphous) silica (SiO_2) glass with some added dopants (e.g. Germanium) to control the transversal refractive index profile. The most common configuration being the step-index profile, in which the fiber glass has a higher refractive index in the middle (core), and slightly lower in the periphery (cladding), with a well defined interface between both (see figure 2.3). The choice of silica as the preferred material results from its natural abundance (low cost), low propagation losses, and mechanical properties (surviving elongations above 1% in embedded conditions [20]). In most cases, the glass

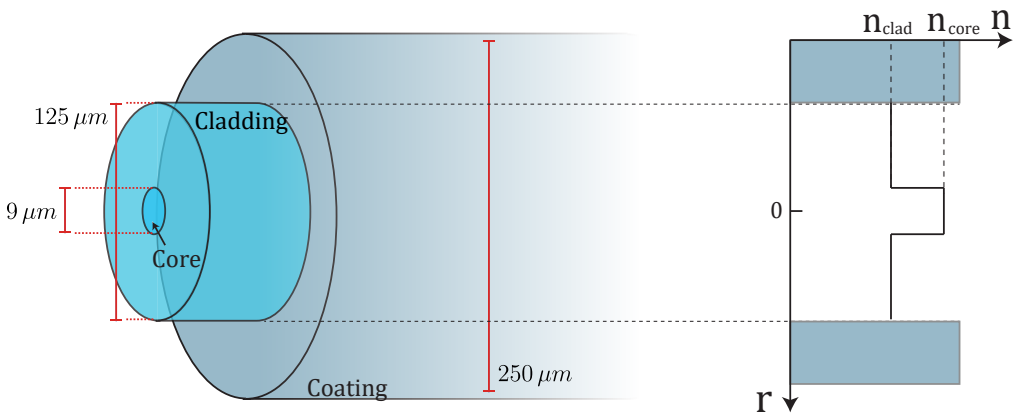

FIGURE 2.3: Diagram of a standard step-index single-mode optical fiber (right) and a visual representation of the refractive index profile (left)

is enclosed in a coating of acrylate or polyimide, which aids in protecting the brittle glass from environmental damage or atmospheric interactions [21]. An example schematic of such a fiber is depicted in figure 2.3.

2.2.1 Propagation of Light in Optical Fibers

The principle behind optical fiber communications is the confinement of light within the core, enabling low-loss transmission over vast distances, without radial leakage of power to the surrounding environment. Light propagation in optical fibers is often described using either a simplifying (albeit intuitive) model through ray optics, or a classically complete wave optics approach from the Maxwell's equations. The former is simple and offers a good approximation for fibers with a larger radius, but does not account for the wave behaviour of light (namely diffraction). For most telecommunication fibers (i.e. single-mode fibers), however, we need to rely on the wave model to accurately describe light propagation.

The simple geometrical model assumes that light behaves as a plane wave travelling in free-space, ignoring all diffraction effects. In this case, we can describe light as a set of rays pointing in the direction of propagation which represent a far-field wavefront of light. In this model, each wavefront can be considered as a plane orthogonal to the propagation, in which the optical field carries the same phase at every point.

Snell's law of refraction is easily visualized under this model: light travelling across the interface between two isotropic media with different refractive indices will generally see the incident ray partially reflected and deflected (refracted) upon transmission. The reflection emerges with the same angle θ_r as the incidence θ_i, while the refracted ray will be deflected according to the relationship

$$n_i \cos(\theta_i) = n_t \cos(\theta_t), \tag{2.22}$$

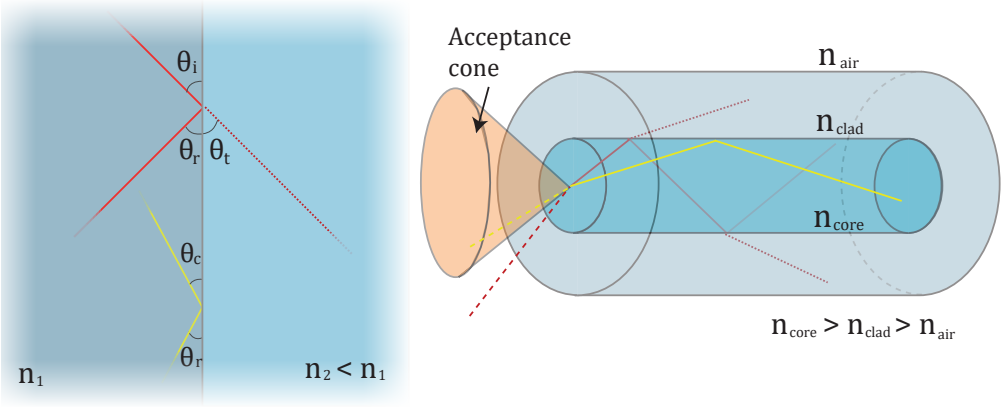

FIGURE 2.4: (Right) Visual representation of Snell's law between at a planar interface between two dielectric media. θ_i is the incident angle, θ_r is the reflected angle, θ_t is the transmitted angle, and θ_c is the critical angle. (Left) Visual depiction of the ray model for transmission in an optical fiber. The acceptance cone for an optical fiber is also represented, which encompasses all angles of input light which facilitate total internal reflection at the core-cladding interface.

for transmitted angle θ_t, and incident and transmitted refractive indices n_i and n_t. From this equation, it is clear that when going from a higher to a lower refractive index, there is a critical angle θ_c for which the refracted angle reaches 0^o [12]

$$\theta_c = \cos^{-1}(\frac{n_t}{n_i}). \tag{2.23}$$

Any light inciding at a narrower angle will not undergo any transmission to the second medium. Instead, all light is reflected in a phenomenon named *total internal reflection* [22].

Consider now a step-index fiber, such that the core-cladding interface is a cylindrical surface of radius p, and the refractive index of the core (n_{core}) and cladding (n_{clad}) are uniform and constant. According to equation 2.23, there is a range of input angles that will effectively trap light inside the core of the fiber (see figure 2.4), by ensuring that light always hits the core-cladding interface at a narrow enough angle $\theta_i < \theta_c$ [21]. Light entering the fiber within this cone ensures its (nearly) lossless propagation through a series of total internal reflections at the core-cladding interface.

Indeed, for cores much larger than the wavelength of the propagating lightwave (specifically, multimode or polymer optical fibers), this model provides a good approximation of light behavior within a fiber. For narrower cores, however, the effect of diffraction is no longer negligible: As a fiber core radius a approaches the wavelength λ, the diffraction angle $\theta_d = \lambda/(\pi n_{core} a)$ approaches θ_c. In this scenario, a purely geometrical optics approach fails to explain guidance in optical fibers, and we must rely on the Maxwell's equations. To do so, consider an ideal step-index fiber with an infinite cladding, with electric field **E** and magnetic field **H** having an

harmonic dependence in space and time as follows [23]

$$\mathbf{E}(r,\Theta,z,t) = \mathbf{E}(r,\Theta)\exp(j(\omega t - \beta(\omega)z)) \tag{2.24a}$$
$$\mathbf{H}(r,\Theta,z,t) = \mathbf{H}(r,\Theta)\exp(j(\omega t - \beta(\omega)z)) \tag{2.24b}$$

for angular optical frequency ω and propagation constant $\beta(\omega) = \frac{\omega n_{eff}}{c}$, depicted in cyllindrical coordinates (r,Θ,z). In this formalism, the Maxwell's equations for the angular $(\mathbf{E}_\Theta, \mathbf{H}_\Theta)$ and radial component $(\mathbf{E}_r, \mathbf{H}_r)$ can be written as functions of the longitudinal components $(\mathbf{E}_z, \mathbf{H}_z)$.

The guided solutions of the Maxwell equations for light propagating in this waveguide are those with fields asymptotically approaching zero at large r, implying no radial loss of power from the core to the cladding, and fulfilling the appropriate boundary conditions: in the core-cladding interface, the tangential components (z,Θ) of the electric and magnetic field have to be continuous [23].

$$\mathbf{E}_z^{(core)} = \mathbf{E}_z^{(clad)} \tag{2.25a}$$
$$\mathbf{E}_\Theta^{(core)} = \mathbf{E}_\Theta^{(clad)} \tag{2.25b}$$
$$\mathbf{H}_z^{(core)} = \mathbf{H}_z^{(clad)} \tag{2.25c}$$
$$\mathbf{H}_\Theta^{(core)} = \mathbf{H}_\Theta^{(clad)} \tag{2.25d}$$

Fulfilling these boundary conditions yields a discrete and finite number of solutions [24], each characterized by a distinct propagation constant β and spatial distribution of power $\mathbf{E}(r,\Theta)$ and $\mathbf{H}(r,\Theta)$ called *modes*. Mode theory reveals that there is, in fact, a substantial portion of light travelling inside the cladding as well: Each solution's planar distribution of power yields an harmonic shape in the confines of the core, and a radial exponential decay (evanescent) within the cladding.

For a fiber of a given radius a and indices n_{core}/n_{clad}, at a given wavelength, the discrete number of modes that can be carried by the fiber depends on the parameter V

$$V = \frac{2\pi a}{\lambda}\sqrt{n_{core}^2 - n_{clad}^2} \approx 2\frac{\theta_c}{\theta_d}, \tag{2.26}$$

in the weak guiding approximation (i.e. small difference between n_{core} and n_{clad}, characteristic of most common fibers), some of the modes "cluster" together in families of degenerate modes, sharing the same propagation constant β, dispersion curve and spatial distribution of power. These are called the linearly polarized (LP) modes.

A fiber can, therefore, be engineered towards carrying or cutting-off a given number of modes at given light frequencies, by adjusting the indices and radius. The two most common types of fiber, however, are those with large cores, carrying hundreds of modes (multimode), and those carrying a single mode (single-mode). Multimode fibers are typically very efficient at capturing light, but pose difficulties in long-haul data transmission due to pulse broadening from mode-dispersion and interference between modes, limiting the total possible transmitted bandwidth.

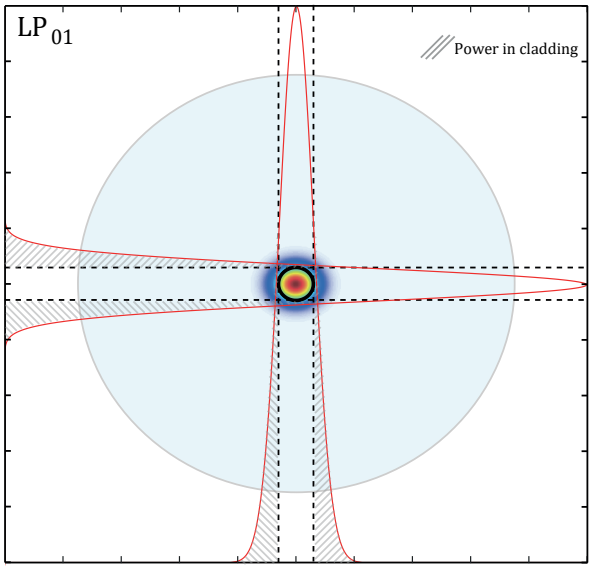

FIGURE 2.5: Diagram of the transverse section of a single mode optical fiber, and the intensity profile of the LP_{01} mode. Notice that a significant portion of the light may be carried within the cladding.

Conversely, single-mode fibers avert these complications, making up the most of long-haul data transmission infrastructure.

Single-mode operation generally requires a parameter $V < 2.405$ [12], allowing only the LP_{01} mode (degenerate in its two orthogonal eigenstates of polarizations), with an approximately 2-D Gaussian power distribution (often carrying 25% of its power in the cladding), as depicted in figure 2.5.

2.2.2 Loss mechanisms in optical fibers

Transmission loss (or attenuation) in optical fiber quantifies the reduction in the intensity of the propagating light beam as it traverses the fiber medium. The physical origin of attenuation derives from either intrinsic phenomena to the silica material, or sporadic extrinsic phenomena, such as damage or external stressors. Most commonly, the losses are quantified by an attenuation coefficient (in dB/km), which abstracts from the physical mechanisms leading to the loss, as

$$\alpha_{dB} = \frac{-10}{L} \log\left(\frac{P(L)}{P(0)}\right), \tag{2.27}$$

under the assumption of constant homogeneous losses along the whole fiber (or the fiber section used to estimate the loss). This assumption is generally valid when we refer only to the intrinsic loss mechanisms to the optical fiber.

The intrinsic mechanisms by which light is attenuated during propagation through fibers are absorption and scattering. Absorption is the phenomenon

by which selective wavelengths of light are prone to excite certain atomic and molecular resonances, thus converting the absorbed energy into some other form (typically heat). In silica fibers, there are electronic and vibrational resonances in the ultraviolet and far-infrared regions respectively. The background absorption resulting from the combination of the tails of these resonances, in silica, is minimized at low-absorption window for light in the $0.5\,\mu m - 2\,\mu m$ wavelength range. Nonetheless, if impurities are present within the fiber structure, they may lead to sporadic peaks of high absorption (one pervasive example is that of OH^-, leading to a narrow peak at 1380 nm). Current manufacturing techniques and standards, however, have evolved to the point that these peaks have been mostly mitigated through careful control of the fiber contamination during drawing.

The other intrinsic loss mechanism is scattering. More specifically, Rayleigh scattering is the predominant contribution to intrinsic losses in current standard fibers. The phenomenon occurs from the rapid polarization of the medium followed by re-emission in a random direction, scattering a portion of light either in reverse propagation to the transmitted wave (backscattering), or in a direction that facilitates its escape through the cladding. Due to its $1/\lambda^4$ dependency, this effect is particularly dominant at lower wavelengths.

The net attenuation, resulting from the combination of both effects (scattering and absorption) is minimized across a narrow wavelength band between 1.3 μm and 1.55 μm, as depicted in figure 2.6. Losses in this band can readily reach values as low as 0.2 dB/km, with most of the band being limited by scattering induced losses.

As we stated previously, however, we can often abstract from the physical origin of the (intrinsic) attenuation, and simply quantify the total losses at our wavelength of interest through the attenuation coefficient defined in equation 2.27.

Deviations from the losses predicted from the attenuation coefficient are typically linked to extrinsic phenomena and localized events. Commonly, these originate from damaged sections of fiber, spliced sections, connectors, or tight bending of the fiber (leading to a loss of mode confinement inside the core, allowing light to leave the fiber).

2.2.3 Scattering

Scattering is the process by which light, interacting with a material medium, is re-radiated in an arbitrary direction, often different than that of the original wave. Understanding scattering phenomena is fundamental to fiber optic technology, as it not only comprises one of the two driving forces for intrinsic attenuation, but also because the scattered light can be recovered for use in multiple applications (the main topic of study of this thesis, distributed optical fiber sensing, being one of them).

Common methods of distributed sensing work by recovering a portion of the scattered light, thus converting the fiber from an otherwise simple conduit of information into the measurement device itself, without inducing any prior change to physical medium. Broadly speaking, we can categorize scattering processes as

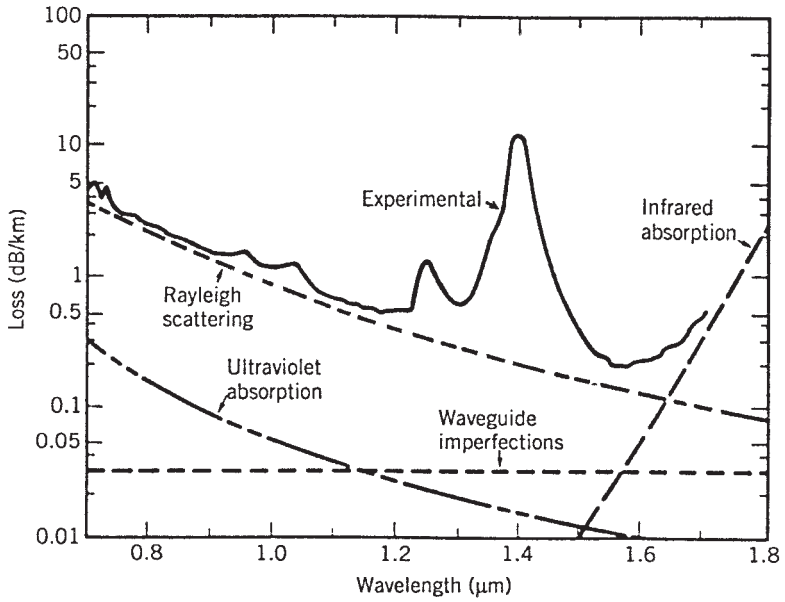

FIGURE 2.6: Attenuation spectrum of a typical optical fiber, highlighting each intrinsic loss mechanism as well (as presented in reference [7]). The sporadic OH^- absorption peak is also visible.

elastic (Rayleigh or Mie. The latter, originating from larger imperfections, has been mostly eliminated in modern fibers) or inelastic (Raman or Brillouin), depending on whether there is a net energy transfer between the material and the incident light after the interaction (perceived as either an increase or decrease in the scattered light frequency, see figure 2.7).

Elastic Scattering (Rayleigh)

Elastic scattering processes imply no net transfer of energy between the incident light and the material, after the interaction has occurred. This means that there is neither a change in the scattering wavelength, nor an electronic excitation or de-excitation in the material molecules. Instead, the transient electric field polarizes the material medium into a ground-state vibration and consequent re-emission as a secondary wave, with power directly proportional to that of the incident wave.

Elastic scattering processes can be divided into Mie and Rayleigh contributions, which are distinguished by the size of the inducing scatterer (a common quoted condition for Rayleigh is $d < \lambda/15$, d being the scatterer radius). Mie scattering is a wavelength-independent process, and occurs for larger defects, being usually a remnant from poor manufacturing and negligible in modern standard optical fibers. In contrast, Rayleigh scattering (the dominant scattering interaction in standard optical fibers) is highly wavelength dependent (follows a $\propto 1/\lambda^4$ dependency), and comprises the major driving force for attenuation in the telecom band.

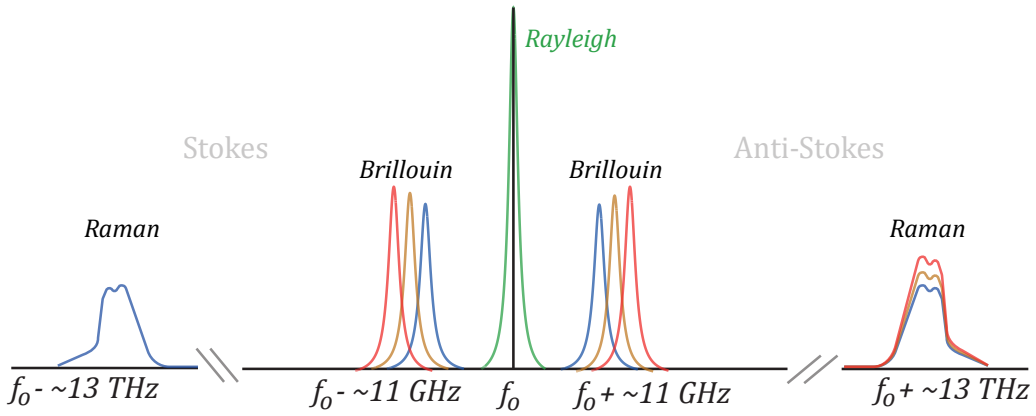

FIGURE 2.7: Visual representation of the spectrum produced by the scattering of light by different elastic and inelastic scattering phenomena

The previously mentioned scatterers consist in localized inhomogeneities in the material's refractive index. If the medium is perfectly homogeneous, the phase-relationship between the material-produced secondary waves cancels for all but the forward propagating contribution, and there is no observed scattering loss [21]. On the other hand, in the presence of non-homogeneities, such as the constant density fluctuations in the amorphous silica structure of glass fibers, the secondary waves may re-direct the incident light energy. These inhomogeneities originate from residual strains and stresses which remain "frozen-in" from the cooling of molten silica.

Each of these scattering centers may be modelled as an oscillating dipole, unable to radiate along the plane of oscillation. In an optical fiber, translating into a radially symmetric probability of radiation in the $1 + cos^2(\theta)$ direction, as shown in figure 2.8, relative to the longitudinal propagation of light ($\theta = 0$ corresponding to the forward propagation and $\theta = \pi$ corresponding to the backward propagation). Some of the scattered light is re-captured by the fiber core, either in forward or backwards propagation. The case of backwards propagating light is of particular importance, as it is the recovery of this residual light that enables distributed measurements from elastic scattering.

Unlike other (inelastic) scattering processes, Rayleigh scattering is itself insensitive to variations of strain and temperature. Instead, each backscattered wave is functionally equivalent to one coming from a very low reflectivity mirror at the longitudinal position of the scatterer. So in order to exploit this type of scattering for measurements, one has to either rely on the interference of multiple scattered waves, or on other properties of light.

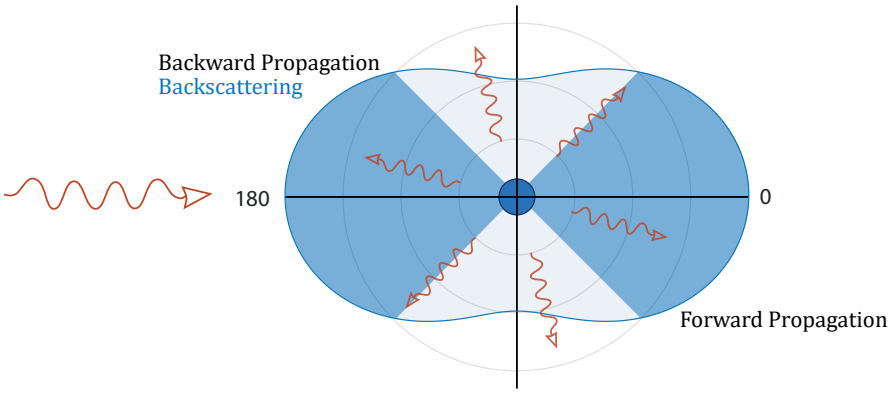

FIGURE 2.8: Spatial distribution of Rayleigh scattering in an optical fiber.

Raman and Brillouin Scattering

A scattering process is deemed inelastic whenever, after the interaction, there is an observable energy transfer between the lightwave and the surrounding material. The type of interaction is commonly categorized as *Stokes* or *anti-Stokes*.

In the *Stokes* case, some energy is transmitted from the incident light (which, as a consequence, undergoes a wavelength upshift) to the surrounding material in the form a phonon (acoustic wave) with a frequency corresponding to the difference between incident and emitted photon in the process. In the *anti-Stokes* case, the incident photon takes energy from a thermally-activated phonon (if the scattering is spontaneous), resulting in an increased frequency (wavelength downshift) of the scattered light, and annihilation of a corresponding phonon.

If the energy transfer results in the creation or annihilation of a molecular vibrational or rotational mode (i.e., an *optical* phonon), the interaction results in what is known as Raman scattering. The typical frequency for such phonons in silica, at telecom wavelengths, is around 13 THz. Conversely, whenever the energy transfer results in the creation or annihilation of a pressure wave in the material structure (i.e., an *acoustic* phonon), the interaction is known as Brillouin scattering, and the typical frequency for the generated phonon is in the order of $11GHz$ in silica. Physically, acoustic phonons consist of pressure waves, which may be created from electrostriction in the fiber. These interact with the optical wave through the consequent refractive index changes from photoelasticity. Optical phonons, instead, reflect the effect of local changes in the material polarization of the medium.

Both phenomena are intrinsically dependent on the current material state, making them obvious candidates for sensing applications: In the case of Brillouin scattering, the strict phase-matching requirement leads to a very narrow spectrum, at a frequency displacement given by $\nu_B = 2n\sqrt{K/\rho}/\lambda_0$ [21], for bulk modulus K and material density ρ. As such, the exact frequency shift experienced by the Brillouin light is both temperature and strain dependent, due to their direct impacts on n and

ρ. Raman phenomena, on the other hand, are directly sensitive to temperature, as the intensity of the anti-Stokes band will be proportional to the number of thermally activated optical-phonons.

Both of these processes occur spontaneously in a fiber medium. However, they can also be stimulated for increased efficiency. The stimulated regime is entered whenever the light power within the medium is enough to modify the local material properties, and influence the efficiency of these phenomena, moving into a non-linear interaction regime. Stimulated interactions are used extensively in fiber optic applications, from distributed amplification to sensing [25–28].

2.3 Polarization and Birefringence

Within the context of electromagnetic waves, polarization corresponds to the vectorial quality of a wave amplitude, or in other words, the direction of oscillation of the electric field. For light to be considered polarized, therefore, there has to be some predictability on the shape drawn by the tip of the electric field vector at a given position, over time. The predictable pattern drawn by this shape is what is known as the state of polarization (SOP) of light. If there is no identifiable pattern, light is said to be unpolarized.

The polarization of interacting waves impacts the outcome of the interaction. Co-polarized waves interfere as we described in section 2.1.1, while orthogonally polarized waves do not interfere, but instead add up to a new state of polarization. Polarization can also affect the propagation of light in materials, in case they exhibit a polarization-dependent refractive index (birefringence). This is the case for optical fibers, as they fail to fulfill the theoretical ideal of a circularly symmetric waveguide. Any deviations from the ideal cyllindrical geometry breaks the symmetry, yielding a non-isotropic response to polarization.

Birefringence can be desirable in some cases: some fibers are engineered with geometries that deliberately break the radial symmetry, enhancing birefringence. More commonly, however, birefringence is a pervasive and residual effect from installation and manufacturing, leading to polarization mode dispersion and other undesired phenomena of light during propagation.

In this section, we shall begin with a brief formal description of polarization of light followed by a simple model of birefringence in optical fibers.

2.3.1 Polarization

When polarized light traverses a fiber which fulfills the condition for the weakly guiding approximation (see section 2.2.1), such as most common single-mode fibers, the oscillating electromagnetic field will always be polarized in the transverse plane to the propagation.

Monochromatic sources intrinsically emit polarized light with an arbitrary SOP. It may be linear, circular, or more generally a combination of both. For a such a wave,

the SOP manifests as a 2-dimensional amplitude of the electric field, describing the polarized wave as a superposition of two orthogonal waves of the form depicted in 2.3

$$\mathbf{E}_0 = |E_x|e^{i\theta_x}\hat{x} + |E_y|e^{i\theta_y}\hat{y} \tag{2.28}$$

The shape drawn by such a wave follows a generally elliptical pattern, where the $\Delta\theta = \theta_x - \theta_y$ defines the ellipticity, such that integer multiples of π yield linear states, while odd multiples of $\pi/2$ yield circular states. Broadband light, on the other hand, may or may not be polarized, as each monochromatic component of the light may oscillate independently. Quasi-monochromatic light usually exists in a in-between state of partial polarization (i.e., the shape drawn by the electric field vector is noisy, but with a distinguishable periodic component).

There are two mathematical formalisms for describing states of polarization and their evolution: the Jones formalism, which comprises a simple 2-D representation of light through electrical field amplitudes (accounting only for fully polarized monochromatic light), and the Stokes formalism, which can account for partial polarization with a 4-D matrix formalism (though it is also common to work with 3-D normalized Stokes vectors as well).

Jones formalism follows directly from equation 2.28, by re-writing the equation as

$$\mathbf{E}(z,t) = E_{eff}(A\hat{x} + Be^{i\Delta\theta}\hat{y})e^{i(kz-\omega t)} = E_{eff}e^{i(kz-\omega t)}\begin{bmatrix} A \\ Be^{i\Delta\theta} \end{bmatrix}[\hat{x},\ \hat{y}], \tag{2.29}$$

with the column vector $[A, Be^{i\Delta\theta}]^T$ being the corresponding Jones vector, characteristic of the light's SOP. Any effect on the polarization state of the fiber due to propagation through a birefringent medium or device (i.e., rotation, polarization-dependent loss, etc.) may then be described by a 2x2 complex matrix operating on this vector. The main drawback of Jones model is in dealing with partially polarized light, and requiring knowledge of the complex electric field (i.e., the phase), which is not trivial to measure. To avoid these issues, one may opt to use Stokes formalism, which relies on optical intensities instead. In this case, a given SOP is defined by the following vector

$$\begin{bmatrix} S_0 \\ S_1 \\ S_2 \\ S_3 \end{bmatrix} = \begin{bmatrix} E_x^2 + E_y^2 \\ E_x^2 - E_y^2 \\ 2E_xE_y\cos(\Delta\theta) \\ 2E_xE_y\sin(\Delta\theta) \end{bmatrix}, \tag{2.30}$$

where S_0 depicts the total power of light. It is therefore common to represent a state in the compact 3-D version of normalized Stokes vectors $(s_1, s_2, s_3) = \frac{1}{S_0}[S_1, S_2, S_3]^T$. These three vectors, s_1, s_2 and s_3 measure the relative intensities of light at orthogonal

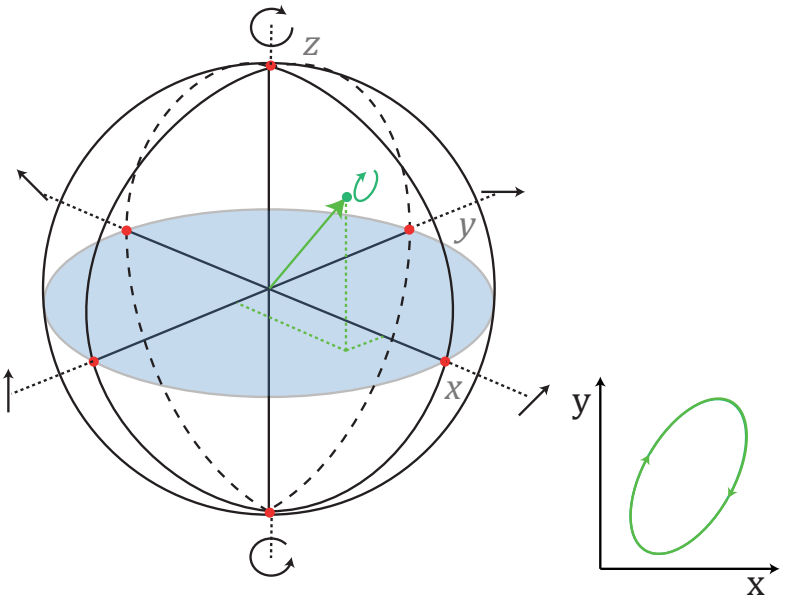

FIGURE 2.9: The Poincaré sphere. A sample representation of a given SOP is depicted in green. The blue plane maps all linear states of polarization.

SOP pairs: s_1 measures the relative amount of power that is horizontally polarized against the vertically polarized (1 corresponding to fully horizontal and -1 to fully vertical), s_2 between linear 45^o and 135^o polarized light and s_3 represents the relative power of light that is circularly polarized (1 for right and -1 for left circularly polarized light).

In this formalism, unpolarized light is quantified through the degree of polarization (DOP) as the percentage of light that is polarized

$$\text{DOP} = \frac{P_{polarized}}{P_{polarized} + P_{unpolarized}} = \sqrt{s_1^2 + s_2^2 + s_3^2}. \tag{2.31}$$

Analogously to the Jones matrices we alluded to earlier, any device or element acting on the polarization state of light can be modelled by a matrix under the Stokes formalism. In this case, however, these are 4-D real matrices called Mueller matrices, which may also account for depolarizing effects.

The 3-D normalized Stokes vectors lend themselves directly to a graphical representation. The graphical representation of the whole space of possible Stokes vectors is called the Poincaré sphere (Figure 2.9). In the Poincaré representation, the xy-plane maps all linearly polarized states, while the azimuth measures the ellipticity of the SOP, in either a clockwise ($z > 0$) or anti-clockwise ($z < 0$) direction. Any two diametrically opposed points in the sphere correspond to physically orthogonal states, and the length of the vector representing the polarization state corresponds to the degree of polarization.

TABLE 2.1: Stokes and Jones representation of basis states of polarization

State	Jones	Normalized Stokes
Linear (Horizontal)	$[1,0]^T$	$[1,0,0]^T$
Linear (Vertical)	$[0,1]^T$	$-[1,0,0]^T$
Linear (+45^o)	$1/\sqrt{2}\ [1,1]^T$	$[0,1,0]^T$
Linear (-45^o)	$1/\sqrt{2}[-1,1]^T$	$-[0,1,0]^T$
Right Circular	$1/\sqrt{2}\ [1,j]^T$	$[0,0,1]^T$
Left Circular	$1/\sqrt{2}[1,-j]^T$	$-[0,0,1]^T$

Birefringence

Non-homogeneous media may exhibit birefringence: a polarization-dependent response to the traversing light. While material birefringence may be desired, in some cases, it is very often a limiting aspect of the material. Practically, it is impossible to obtain a perfectly symmetric fiber, as birefringence stems from imperfect manufacturing [29], deviations from the ideal symmetry of the core, induced stresses, inhomogeneities in the doping concentrations, among other unavoidable imperfections. Indeed, even in the event of a theoretically perfect fiber, any bending/twisting [30] or the onset of electric/magnetic fields could all lead to birefringence phenomena.

As we described in section 2.2.1, the mode theory description for light propagating in a single-mode fiber permits only a single mode LP_{01}. While this is often a good enough approximation, in reality there are two modes, one for each orthogonal eigenstate of polarization (LP_{01x} and LP_{01y}). In an ideal fiber, these are *degenerate*, meaning that the propagation constant β, or the refractive index are the same for both modes, making them indistinguishable. Birefringence, however, breaks this degeneracy: Each eigenstate becomes characterized by a slightly different propagation constant. In practice, the effective refractive indices of LP_{01x} and LP_{01y} are very similar in standard fibers. In the current state-of-the-art, the total difference in effective index can be as low as 10^{-9}.

Formally, birefringence is often quantified as either the total difference between propagation constants, or equivalently, between the refractive indices of both eigenstates of the fiber

$$\Delta\beta = |\beta_s - \beta_f|; \tag{2.32}$$

$$B = |n^s_{eff} - n^f_{eff}|, \tag{2.33}$$

where $\beta_{s,f}$ are the propagation constants ($n^{s,f}_{eff}$ the effective indices) for the slow and fast axes, respectively. If light travelling along a birefringent medium is not aligned with one of the two eigenstates, the resulting projections of the wave in each eigenstate will accumulate a delay during propagation. The induced phase-shift for a travelled length L is given as

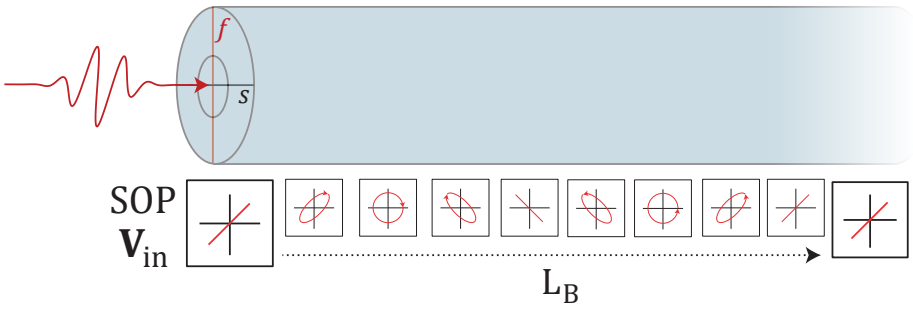

FIGURE 2.10: Beat length representation in an optical fiber, modeled as a homogeneous birefringent element. f - fast axis of birefringence, s - slow axis of birefringence. Note that light aligned with any of the axes retains its SOP during propagation.

$$\Delta\theta = |\beta_s - \beta_f|L = \Delta\beta L. \tag{2.34}$$

The change in phase between the two components manifests as a periodic evolution of the SOP into a new polarization state. The total length to complete one period (i.e., return to the original state) is given by $\Delta\beta L_B = 2\pi$ (see figure 2.10), and is called the beat length of the fiber.

In the case of pulsed light, there is more than just a change of the state-of-polarization, as a different propagation constant also leads to a differential group delay

$$DGD = \frac{d\Delta\beta}{d\omega}L, \tag{2.35}$$

which limits the rate of information transfer possible in the fiber.

Birefringence can be mathematically described as a vector, defined in normalized Stokes space, pointed towards the slow eigenstate of polarization [31]. This enables a description of the magnitude and type of birefringence (whether linear, circular or elliptical), as well as a geometrical understanding of its interaction with polarization states.

In standard step-index single-mode fibers, the birefringence vector changes directions and fluctuates in amplitude unpredictably throughout the whole medium, due to local inhomogeneities and imperfections [32]. One useful model to describe an optical fiber, as such, is by picturing a concatenation of small homogeneously birefringent elements (figure 2.11). At their interface, the output SOP is projected into the new fast and slow states of the input element. In Jones formalism, an optical fiber section of length z can be modelled as

$$\mathbf{J}_{fiber}(z) = \mathbf{J}_{n(z)}\mathbf{J}_{n-1}\cdots\mathbf{J}_1\mathbf{J}_0, \tag{2.36}$$

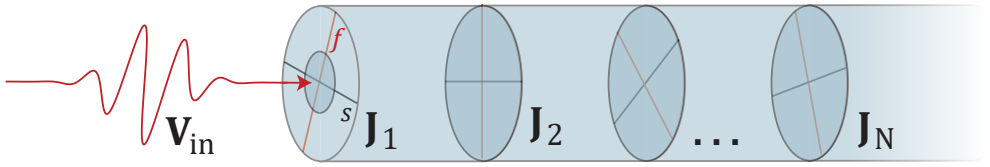

FIGURE 2.11: Polarization mode coupling model of a randomly birefringent optical fiber.

where $n(z)$ is the n-th element of fiber, at position z. The cumulative effect of all the delays induced by each small element in the fast and slow components of the electric field traversing them leads to a "smear" or broadening of the pulse, an effect known as polarization mode dispersion, which is a main limitation in long-haul communication links.

The final concern with birefringence lies on the effect of backscattering in the SOP of the scattered light. The polarization transformation can be modelled as a Jones or Mueller matrix, depending on the formalism of our choice. Expanding on the Jones formalism analysis of equation 2.36, the SOP recovered at the fiber input ($\mathbf{V}_B(z)$), after backscattering at position z, is given by

$$\mathbf{V}_B(z) = \mathbf{J}_{fiber'}(z)\mathbf{J}_{BS}\mathbf{J}_{fiber}(z)\mathbf{V}_{in}(z), \tag{2.37}$$

where $\mathbf{J}_{fiber'}(z)$ corresponds to the fiber model of 2.36, with the elements stacked in reverse order, $\mathbf{J}_{BS}$ refers to the direct effect of backscattering in the polarization state of light, and $\mathbf{V}_{in}$ is the input SOP. As backscattering merely changes the direction of propagation, there is no effect to linear states of polarization (i.e., the x and y components of the coordinate system for forward and backward propagation remain unaffected). There is, however, a difference in the phase relationship between the orthogonal states between incident ($\Delta\varphi$) and backscattered wave ($-\Delta\varphi$). This is consistent with setting $\mathbf{V}_B = \mathbf{V}_B^*$. In practice, as can be seen in table 2.1, this corresponds to maintaining the linear component of the state, and reversing the handedness (of the circular component of polarization) during backscattering.

Chapter 3

Distributed Acoustic Sensing

Since the early days of fiber optics technology, there has been a considerable research effort to develop techniques for the sensing and measurement of physical parameters [33]. These efforts were motivated by the attested benefits of using passive silica fibers instead of the traditional electronic infrastructure.

Indeed, besides the high performances and sensitivities promised by optical measurements [34], there are some application-specific advantages to using optical fibers. The most commonly mentioned are the immunity to electromagnetic interference and voltage spikes, low-power consumption, lack of Joule heating, small/lightweight dimensions for embedded applications, and the broad range of adverse environments where they can be installed.

Nonetheless, perhaps the greatest benefit of sensing with optical fibers is the ease of multiplexing sensor structures into large arrays on a single optical fiber, minimizing the cost/complexity of deployment and maintenance. This advantage is fully expressed in distributed sensing techniques, where every position in the fiber functions as both an information-carrying element and a sensing element [21, 35].

Nowadays, multiple designs and techniques for distributed sensing have been proposed and developed. For the measurement of fast perturbations, however, the most promising alternative consists of sensors based on the interference of multiple waves resulting from local Rayleigh scattering. The advantages provided by this type of sensors are critical whenever a large number of points have to be monitored at fast acquisition rates, and have been successfully demonstrated in fields such as seismology [36], defense (perimeter security) [37, 38], pest control [39] or pipeline integrity [40].

In the following chapter, we will introduce the concept of distributed optical fiber sensors, followed by a short state-of-the-art of the distributed acoustic sensing (DAS) techniques, used for the measurement of fast mechanical perturbations. We will conclude with an in-depth description of the Chirped-Pulse Phase-Sensitive Optical Time-Domain Reflectometry (CP-φOTDR) technique, which is the focus of this work.

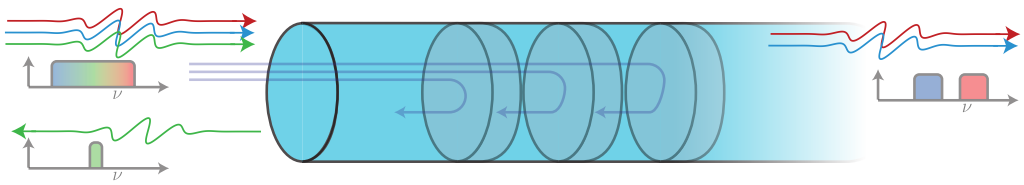

FIGURE 3.1: Illustration of the operation principle of a fiber Bragg grating, the most common intrinsic point sensor in optical fibers. The structure functions as a wavelength-selective mirror.

3.1 Point, quasi-distributed and distributed sensors

The most conventional conception of a sensor is the *point* or *punctual* sensor, being the traditional paradigm for an electronic sensor. In this case, the sensor structure is connected to the interrogator/acquisition device, with a dedicated cable for power/data transmission. In passive fiber optics, this entails that most of the fiber behaves solely as a data transmission element, apart from a singular engineered position which is sensitive to the surrounding environment.

The most commercially popular example of an optical fiber sensor, the fiber Bragg grating (FBG - figure 3.1) [41], falls under this description. An FBG consists of a periodic variation of the effective refractive index imprinted over a short length of the optical fiber. These variations behave as multiple reflectors, creating an interferometric structure with a fixed phase-relationship between the reflected waves. Only specific wavelengths, when reflected, fulfill the phase-matching condition and interfere constructively (yielding a phase difference that is an integer multiple of 2π), while all others mix incoherently.

One remarkable advantage of optical fiber sensors (and an important selling point for FBGs, for instance) is their ability to be easily multiplexed. Whenever multiple point sensors are concatenated within a single fiber cable it is common to refer to the sensor device as *quasi-distributed*. The most common multiplexing methods allocate either a specific wavelength band (wavelength division multiplexing), time-of-flight window (time-division multiplexing) to each sensor, or a combination of both, in order to distinguish between sensors within the same cable (see figure 3.2).

Quasi-distributed designs can retrieve a spatial profile of the measurand over the fiber length using a single interrogator channel. Nonetheless, these sensors rely on a pre-inscription of the sensitive structures in the fiber at discrete positions, while the remaining non-inscribed portions of the fiber work solely as a data transmission element.

The final method for fiber sensing, then, foregoes the inscription of sensitive structures completely. By measuring the effects of intrinsic light-matter interactions of the optical fiber it is possible to build a *distributed* sensor: every position of the

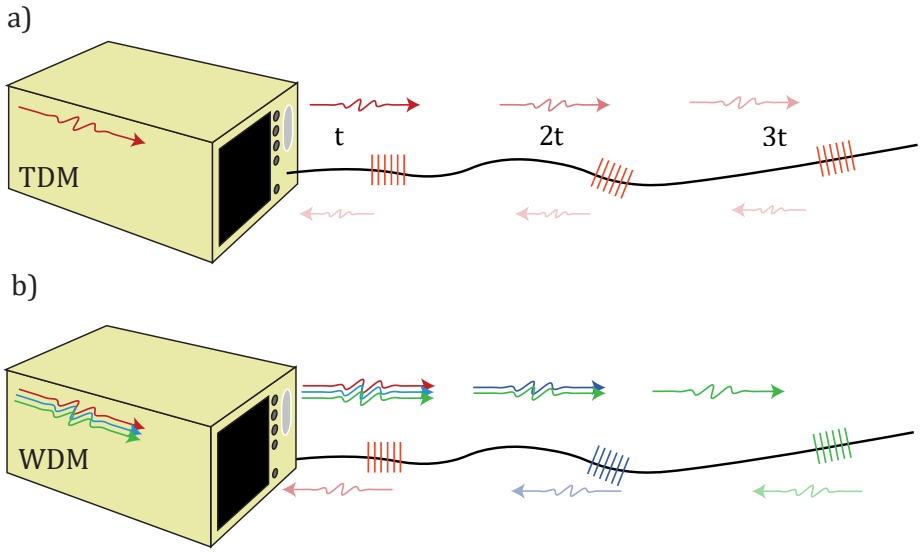

FIGURE 3.2: Illustration of the two most basic types of multiplexing of point sensors in optical fibers, through a) time-division multiplexing (each sensor is interrogated at a given time since the probe is sent) or b) wavelength-division multiplexing (each sensor is interrogated by a specific wavelength)

fiber functions as both a data-transmission and sensitive element, and the interrogator is able to randomly access any position along the fiber length for interrogation. The notion of sensor position is replaced by that of spatial resolution, which is defined by the user at the time of interrogation by altering properties of the probe signal.

The advantages of distributed methods are clear in applications where extended distances or high spatial density of measurements is required. Current systems allow several kilometers to be monitored at high sampling rates, with high sensitivity, reducing installation complexity and costs-per-sensor. Removing the need to imprint or alter a pre-existing fiber also enables any already installed fiber to be retrofitted into a dense sensor array, not limited to measuring at pre-determined fixed positions of interest (although fibers may still be enhanced for improved performances [42, 43]).

The possibility of fully distributed measurements is perhaps the greatest divergence of fiber-sensing technology from electronic sensing alternatives [44]. A visual comparison of point, quasi-distributed and distributed sensor systems is presented in figure 3.3.

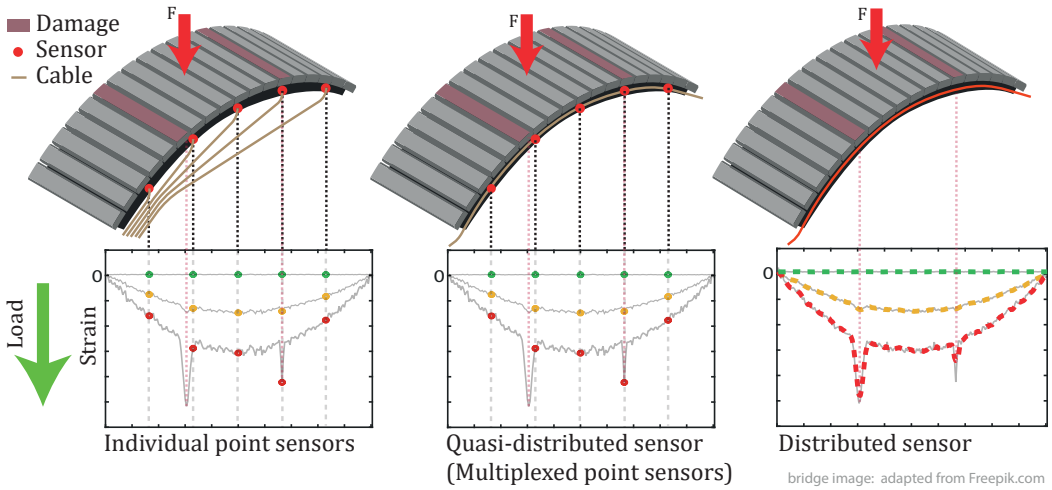

FIGURE 3.3: Illustrative depiction of the differences between point sensors (left), quasi-distributed (center) and distributed sensors (right). Both punctual sensor arrays or quasi-distributed sensor arrays produce a sequence of narrow snapshots of the local conditions experienced by a structure (e.g., strain), at the sensing positions. The quasi-distributed implementation, however, reduces costs and installation complexity. A distributed sensor, in contrast, yields a continuous estimation of the strain over a finite length given by its spatial resolution.

3.2 Distributed Fiber Sensors

A distributed sensor needs to accurately relay two independent pieces of information: the local amplitude of the perturbation and the location from where each measurement originates [45]. Consequently, these sensors are often classified according to the methods used to retrieve each of these parameters.

The measurand estimation is usually accomplished by observing local scattering processes (for a brief description of each, refer to section 2.2.3) [45–48]. Inelastic scatterings (Raman and Brillouin) lend themselves directly to sensing of specific parameters, being measurand-sensitive phenomena. Rayleigh systems, on the other hand, need to depend on other properties of the scattered light for the measurement (usually interference).

The two predominant ways of encoding the position information are time-domain reflectometry (TDR) or frequency-domain reflectometry (FDR), somewhat analogous to the multiplexing techniques alluded to earlier (TDM and WDM, respectively). Most sensors, particularly those for dynamic measurement purposes, are based on time-domain reflectometry.

In this section, we shall briefly overview the common options of distributed sensors for DAS measurements. For an in-depth state-of-the-art of current distributed sensing methods, we guide the reader towards some excellent reviews that have been published on the topic ([45–48]).

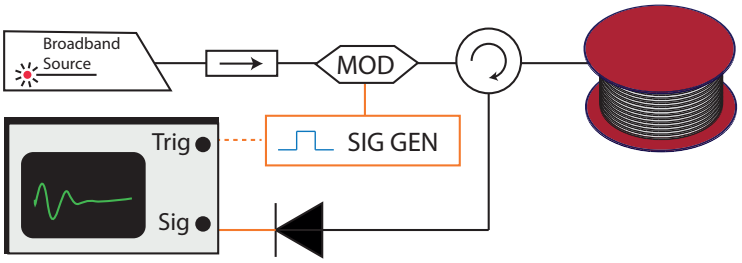

FIGURE 3.4: Typical basic implementation of an incoherent OTDR

3.2.1 Position Information

Time-Domain Reflectometry

The first and most straightforward method for encoding the measurement location consists in launching pulsed light into the fiber and timing the arrival of the counterpropagating echoes from local scattering. This technique is called Optical Time Domain Reflectometry (OTDR, see figure 3.4). Each longitudinal position z can then be mapped to a different time-of-flight, akin to time-division multiplexing. The total time it takes for light to travel to-and-from a position z in the fiber is

$$\tau(z) = \frac{2z}{v_g}, \tag{3.1}$$

where v_g is the group velocity of the light pulse. In these techniques, the spatial resolution is limited by the interaction region of the pulse as

$$\Delta z = \frac{c\tau_p}{2n_g}. \tag{3.2}$$

The measurand sampling rate of these methods is dictated by the repetition rate of the laser pulses, with an imposed limit of the total travel time of the pulse within the fiber: One pulse must only enter after the previous pulse and all of its echoes have completed their course. As such, the maximum sampling rate for a basic time-domain reflectometry system is given as

$$f_{sampling} = \frac{1}{2L_{fiber}} v_g, \tag{3.3}$$

for a fiber of length L_{fiber}.

Frequency-Domain Reflectometry

The other common option of encoding position information relies on a position-to-frequency mapping of the fiber, achieved through frequency-modulated continuous

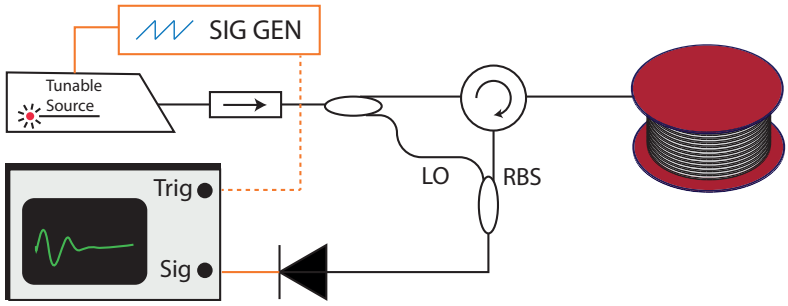

FIGURE 3.5: Typical basic implementation of an OFDR

wave interference. This technique is called Optical Frequency Domain Reflectometry (OFDR, see figure 3.5). In this case, the fiber is probed with continuous-wave light from a coherent tunable source, able to be linearly modulated without mode hops over a broad enough range, and a dual-path interferometer: The measurement path connects to the fiber-under-test (FUT), and the reference path is used to yield a stable local-oscillator (LO) signal.

Under the ideal conditions of linearity in the sweep and polarization alignment, each beat-frequency component resulting from mixing the LO with the backscattering light is tied to a single position z in the fiber. The longitudinal position can then be found according to the following relation

$$z = \frac{c}{2n\gamma} f_b, \tag{3.4}$$

for beat-frequency f_b, and rate of change of the source frequency γ, in Hz/s.

Accordingly, the spatial resolution is given by the total range of scanned frequency, Δf, as

$$\Delta z = \frac{c}{2n\Delta f}. \tag{3.5}$$

The sampling rate is ultimately limited by the total time taken to execute the sweep, which must be strictly lower than the total roundtrip time of light inside the fiber [49].

3.2.2 Raman-based methods

Raman-based sensors [27, 50, 51] adapt the longstanding technique of non-contact chemical thermometry to optical fibers, in which temperature estimates from the scattered power ratio between the spontaneous scattering at the Raman Stokes and anti-Stokes bands.

Sensors of this type are insensitive to strain and incapable of dynamic measurements, demanding long averaging times owing to the inefficiency of Raman scattering [47, 48]. As such, Raman-based systems are unsuitable for DAS.

3.2.3 Brillouin-based methods

Over the past 2 decades, Brillouin-based sensors have experienced substantial research and development among distributed sensors. The two predominant implementations consist on either measuring the frequency shift (or intensity) of the spontaneously scattered Brillouin light, called the Brillouin Optical Time-Domain Reflectometer (*BOTDR*)[52], or on evaluating the efficiency of a parametric process between two optical waves [26] (mediated by the Brillouin acoustic wave) at each position, known as the Brillouin Optical Time-Domain Analyzer (*BOTDA*) [53, 54].

Brillouin scattering is significantly stronger than Raman in optical fibers, leading to looser averaging requirements for measurement. Additionally, since Brillouin scattering is sensitive to the local refractive index and acoustic velocity of the medium [55], these sensors are able of strain and temperature measurements [46, 56, 57].

These properties imply the possibility of Brillouin-based measurements of dynamic strains at acoustic frequencies (DAS). In practice, however, each estimation still entails extensive averaging, or repeated acquisitions at different probe/pump frequencies (in the BOTDA case). As a consequence, most systems are geared only towards static measurements of temperature or quasi-static strains ($\sim$ 1 Hz).

Nonetheless, there have been some directed efforts towards the development of dynamic Brillouin systems. One variant method, Brillouin Optical Correlation-Domain Analysis (BOCDA), achieved kHz sampling rates in short fibers (tens to hundreds of meters), with centimeter spatial resolutions [58, 59]. The biggest drawback of this technique, however, is that it typically can only retrieve a single predetermined position, instead of the full measurand profile of the fiber. Later attempts at solving this issue by periodically sweeping the frequency position (Differential Frequency Modulation BOCDA) yielded similar performances to the single position technique, but limited the sampling rate to 20 Hz [60].

Other efforts at achieving dynamic interrogation have tried to improve the conventional BOTDA design, either by avoiding the need for interrogation at successive frequencies by using a frequency-comb as the CW probe [53], or by sending sequential pumps with controlled wavelengths [61]. Nonetheless, these methods have mostly been reported for short fiber lengths ($\sim$ 100 meters), with spatial resolutions of several meters. Another proposed method consisted in the Slope-Assisted variant (SA-BOTDA), in which instead of tracking the Brillouin gain peak, the CW probe is set to a variable frequency that matches the mid-point of the rise (or fall) of the gain curve at every position in the fiber [62, 63]. In this variant, the estimation is done by monitoring gain variations in the probe as the stimulated scattering process

increases or decreases in efficiency. This technique enabled kHz sampling rates, but remained limited to short fiber lengths, of a few hundred meters at most.

More recently, two methods have been proposed that enable very high sampling rates. The first mitigates the need for averaging and sweeping, yielding the potential for single-shot measurements [64] (in what is known as Frequency-Swept Pulsed BOTDA). The authors reported single-shot interrogation of a 10-km fiber, fundamentally capped by the total time of flight of the pulse at 10 kHz sampling rate, with 100 m spatial resolution. The second method, Optical Chain Chirp BOTDA (OCC-BOTDA), [65], mitigates the need for a frequency sweep, thus enabling the achievement of sampling rates as high as 6.25 MHz in a 50 m long fiber, with 2 m spatial resolution.

All of the aforementioned methods have reported strain uncertainties of the order of tens of μstrain, being reserved mostly for measurements relatively large strain perturbations. The best reported dynamic strain performances with Brillouin techniques achieved (to the best of our knowledge) were of $\sim 50 \times 10^{-9} \varepsilon / \sqrt{Hz}$, although only for very short (5 meter) polarization-maintaining fibers [66].

3.2.4 Rayleigh-based methods

Rayleigh methods fundamentally differ from inelastic scattering techniques, since the underlying phenomena is itself insensitive to the changes in the local fiber state, demanding the interrogation to focus on other properties of light. By probing an optical fiber with a broadband source and measuring the intensity of the Rayleigh echoes over time, one is able to estimate the intensity evolution of the pulse during propagation (assuming uniform scattering properties). This technique is called Optical Time-Domain Reflectometry (OTDR) 3.4, and is an industry standard for the characterization of fiber links [67]. A more in-depth explanation of the technique is presented in the next section.

The first proposed distributed sensor designs based on Rayleigh scattering attempted to circumvent the insensitivity issue by using doped or liquid core fibers [68], with temperature-dependent Rayleigh scattering coefficient. The highly specialized requirements, however, make such methods impractical. Other early attempts proposed probing the fiber with controlled polarization states and observing changes to the evolution of the SOP during propagation [69]. These methods, known as the polarization OTDR (P-OTDR), have been mostly reserved for measurements of local birefringence or characterization of local polarization-mode dispersion in fibers [47, 70, 71], or static measurements of bend and twist-induced birefringence [72, 73], due to the inherent stability of SOP-based measurements. Apart from a few preliminary results of perturbation detection [74, 75], there have been no reports in using these techniques for measurement of dynamic strains, to the best of our knowledge.

The more prevalent option of employing Rayleigh scattering for measurement consists in probing a traditional OTDR with a coherent source. In this case, the local

Rayleigh backscattering can be used for interferometry. Known as phase-sensitive OTDR (φOTDR), these setups exploit the time-invariance of the density fluctuations that induce Rayleigh scattering. Any fiber section, then, can be modelled as a multi-wave interferometer, composed of several very low reflectivity mirrors. Each returning OTDR echo relays the response of the effective interferometer at its position of origin, which remains unaltered until the respective fiber section is perturbed.

These methods have seen extensive development in the recent years [76], largely due to their potential in detecting and measuring dynamic strains and perturbations with extremely high sensitivities, over very long distances of fiber (up to 175 km when assisted with amplification techniques [28, 77–79]). The advantages arise from the relatively high amplitude of Rayleigh scattering which relaxes the averaging requirements.

The first implementations of the coherent OTDR relied solely on intensity measurements, boasting very non-linear/ non-monotonic responses to the measurand and variable sensitivity at each sensing position, owing to the complex and unknown response of each effective interferometer. Solving these issues has been a hot-topic of research in the distributed sensing community in the past decade, and numerous variants have been developed [76, 80–82]. Being the focus of this current work, this method and its variants will be reviewed in-depth in the following section.

The alternative option for coherent Rayleigh measurements consists in using optical frequency-domain reflectometry (OFDR) [83]. In this case, the method involves probing the fiber with a highly coherent continuous-wave light source, while it is being linearly modulated in frequency. Before being launched to the fiber, some power of the laser source is kept in order to form a local oscillator (LO) with the same frequency sweep as the probing light. At the time of detection, the backscattered light is mixed with the swept LO. The obtained time-domain signal may then be inspected in the frequency domain, where each position of measurement will be mapped to a specific beat frequency component. The recovered features will undergo a local shift when perturbed. OFDR methods have shown the ability to reach extremely high resolutions, at the cost of measurement speed and probing distance.

The advantages manifest as a departure from the typical trade-offs of OTDR, in which the SNR and measurement distance are inversely proportional to the spatial resolution. While generally beneficial for the potential spatial resolutions achievable with this method, these trade-offs are often not favorable for dynamic sensing applications. The high coherence requirements limit the total length of interrogated fibers, and the sampling rate is reduced due to the sweeping requirements [47]. Typical acquisition rates are of the order 10 Hz. Nonetheless, some specialized attempts at DAS-based OFDR (using a sinusoidal frequency scan) were able to interrogate a $\sim$ 1.5 km long fiber at 21 kHz, with sub-meter spatial resolutions [49]

For the remained of this work, we shall focus on OTDR based methods, due to their predisposition for long-range, high-performance DAS.

3.3 Optical Time-Domain Reflectometry

As we alluded to earlier, an incoherent OTDR [67] measures the evolution of pulse power as it propagates through an optical fiber. This is done by launching broadband optical pulses into the fiber under test (FUT) through an optical circulator with a photodiode and data acquisition setup connected to the return end (see figure 3.4).

As light propagates through the fiber, it encounters inhomogeneities in density and refractive index (hereby known as "scattering centers" or "scatterers"). These produce a faint echo of the incident light, which may be re-coupled in backward propagation, finally reaching the detection arm. The resulting measurement yields a scaled estimation of the pulse power at each position, under the reasonable assumption of constant scattering properties along the fiber.

By neglecting coherent effects, this can be formally understood from a simple macroscopical model: knowing the attenuation scattering coefficient $\alpha_S(\lambda)$ and the backscatter capture fraction $B_c(\lambda)$ (*i.e.*, the portion of scattered light that falls within the acceptance angle for counter-propagation), the light recovered from a narrow pulse of peak power P_{peak} and width W at each position z can be calculated as [21]

$$P_B(z) = P_{peak} B_c(\lambda) \alpha_S(\lambda) \frac{W}{2} e^{-2\int_0^z \alpha(u)du}, \tag{3.6}$$

where $\alpha(z)$ is the attenuation coefficient (see section 2.2.3), and the factor of 2 in the exponent of the attenuation term reflects the round-trip of the pulse and echo. Clearly, for homogeneous scattering properties, the time-series represents a scaled estimation of the intensity evolution of the pulse, as it is attenuated from the propagation. This is commonly known as the OTDR trace, and is typically used to measure the length of fiber links (by timing the Fresnel reflection at the end of a fiber) or obtain a spatially-resolved characterization of the losses and defects in the fiber: sporadic reflections or losses from splices, connectors or other local effects (as depicted in figure 3.6).

In an OTDR, each position of measurement is tied to a specific time-of-flight, under the reasonable assumption of an approximately constant group velocity within the medium. As such, light originating from each position z reaches the photodetector at time

$$t(z) = 2\int_0^z \frac{n_g(z)}{c} dz \approx \frac{2n_g}{c} z, \tag{3.7}$$

where t = 0 marks the time at which the center of the pulse enters the fiber.

In the case of a non-infinitesimal pulse, there is a finite region of interaction within the fiber from which all scattered light reaches the input end simultaneously. This area corresponds to half the total length of the pulse within the fiber. To understand this, consider the fact that the pulse is continuously propagating as it is being backscattered, with the same velocity of propagation in both directions. The leading components of the pulse are backscattered first, but have a longer travel distance to

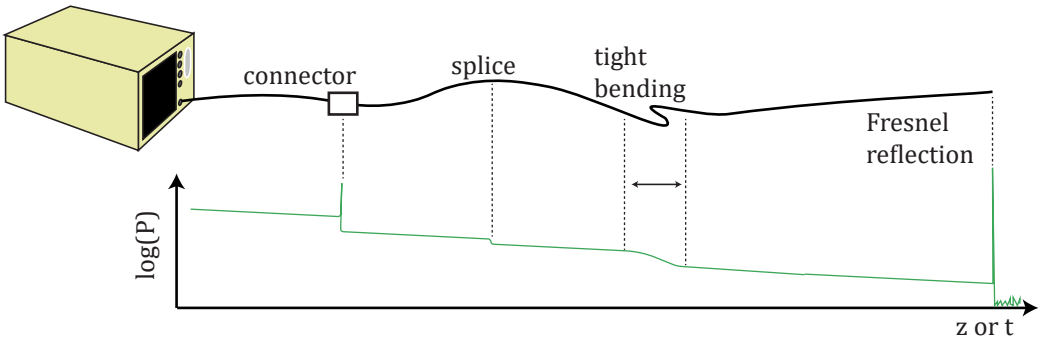

FIGURE 3.6: Example acquisition from an incoherent OTDR. The local slope is correlated with the fiber losses. Sporadic losses and reflections due to connectors, splices or bending are also visible, as well as the Fresnel reflection formed by the silica-air interface at the end of the fiber.

cover than the trailing components. Therefore, using a pulse of length $W = \frac{c}{ng}\tau_p$ (τ_p being the time-width of the pulse) for interrogation, the interaction region is of length

$$\Delta z = \frac{c\tau_p}{2n_g}, \tag{3.8}$$

where Δz also defines the spatial resolution of the system, limiting the minimum spacing between measured points that ensures independent readings.

In these types of measurements, since both the position and measurand information are taken over a time-span, it is common to distinguish between "slow" and "fast" axes: one for the optical acquisition (mapped to position, corresponding to the OTDR trace), and the other one for the measurement (see Figure 3.7) [46].

Specifically, the slow axis is tied to the repetition rate of the laser pulse: Each shot takes a snapshot of the fiber which, at the time of representing the measurand, is normally considered to happen simultaneously for all fiber. Thus, the laser repetition rate is limited, since it is necessary to wait for the last echo to leave the fiber before sending the new pulse. The maximum sampling rate for a basic time-domain reflectometry system is given as

$$f_{sampling} = \frac{c}{2n_g L_{fiber}} \tag{3.9}$$

for a fiber of length L_{fiber}.

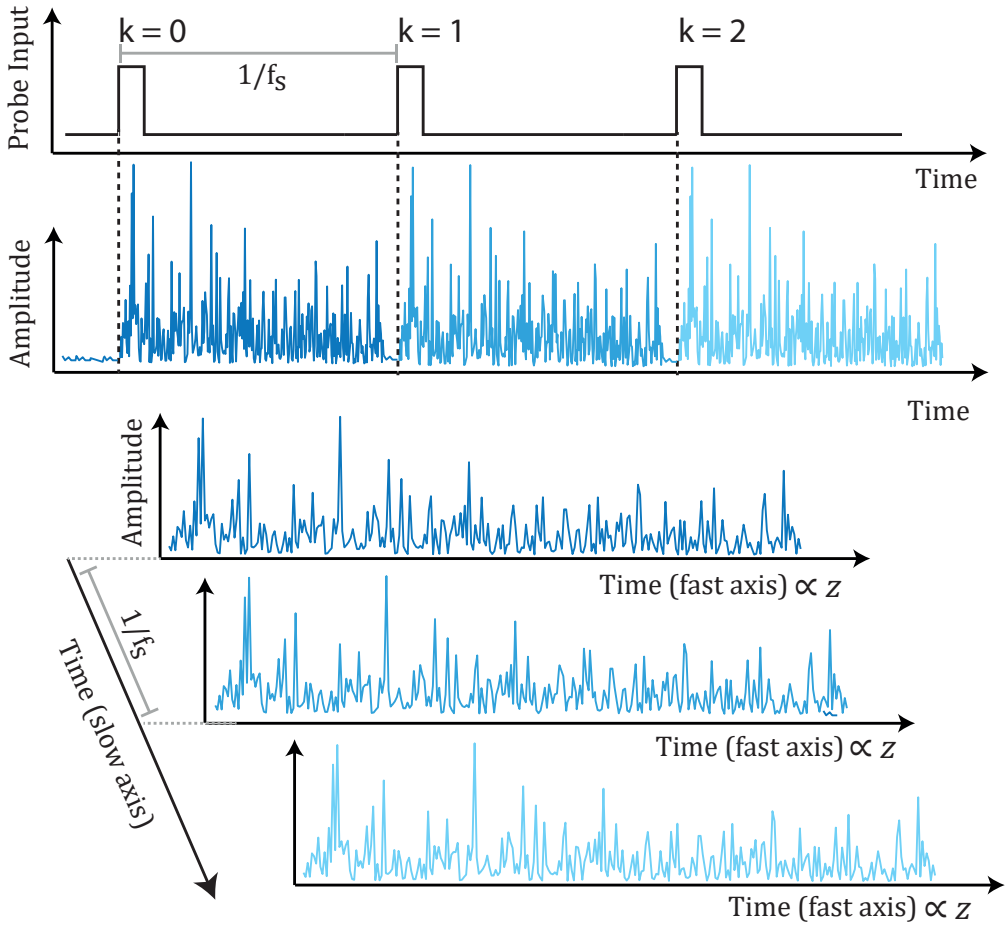

FIGURE 3.7: Slow and fast time axis of a φOTDR. A perturbation is measured as a time-series of measurand estimations at constant intervals, for each position of the fiber. The measurement discrete time axis is usually called the slow axis, and is sampled at the same rate as the probe repetition rate. The position information of an OTDR is mapped to time as well, and is usually denoted as the fast axis. This figure also highlights why there is a maximum sampling rate for a given length of fiber, since all the information from each pulse must be retrieved before sending another probe. Adapted from [46].

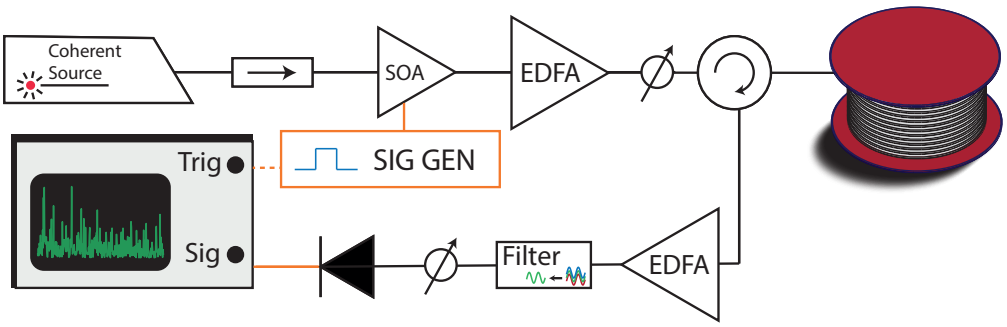

FIGURE 3.8: Basic design of a φOTDR setup. The SOA modulates the continuous wave into a pulse with high extinction ratio. The attenuators are used to prevent the onset of non-linear effects (in the emission stage), or damage to the photodetector (in the detection stage). In a traditional implementation, the filter mitigates ASE from the amplifiers.

3.3.1 Phase-sensitive Optical Time-Domain Reflectometry

By merely changing the light-source employed in an OTDR system to a coherent source (i.e., a source with a coherence length much longer than the pulse length), one fundamentally changes the potential information retrieved from a measurement. On the one hand, the local coherent effects enable interferometric measurements from the natural echoes of the fiber. On the other, the jagged appearance of the produced interferometric pattern masks the power evolution of the pulse.

Phase-sensitive OTDR (or φOTDR) fixates on the coherent noise contribution of the backscattered time-series for interferometric measurements, by probing the fiber with a quasi-monochromatic source. While coherent OTDR techniques share many traits with the incoherent technique (most of the analysis of the previous section still holds true), the purely macroscopical model introduced in equation 3.6 is now insufficient to describe the recovered signal.

For the coherent model, then, we shall consider a monochromatic pulse with a rectangular envelope to be launched into the fiber, ignoring polarization effects

$$E_{in}(t) = E_0 \exp\{-j2\pi\nu_0 t\} \operatorname{rect}\{\frac{t}{\tau_p}\}, \tag{3.10}$$

where E_0 is the peak amplitude, ν_0 the center frequency and τ_p is the pulse width. In the case of conventional single-mode fibers, we can reasonably consider 1-dimensional propagation. Then, a fiber can be modelled as a concatenation of N discrete reflectors with random interspacing and reflectivities [82]. We shall treat each reflector as an independent source of a secondary wave, counterpropagating to the input pulse with a randomly scaled amplitude. The wave reaching the input end of the fiber from a single reflector, then, is given by

$$E_{sc}(t, z_s) = E_{in}\left(2(t - \frac{nz_s}{c})\right) r(z_s) \exp\{-\alpha z_s\}, \tag{3.11}$$

where $r(z_s) << 1$ is a random variable representing the reflectivity of the equivalent reflector at position z_s. For simplicity, we assume an approximately constant group index (so $t(z_s) \approx \frac{n_g}{c} z_s$) and attenuation over the fiber.

The net backscattered signal at the input end of the fiber, over time, results from the superposition of all scattered secondary waves that reach the input end simultaneously

$$E_{out}(t) = \sum_{s \in M(\bar{z}(t))} E_{sc}(t, z_s) \tag{3.12}$$

where $M(z)$ is defined as the set of all reflectors within the interaction region $[z - W/4,\ z + W/4]$. We define $\bar{z}(t) = \frac{tc}{2n_g}$ as the pulse center position and $W = \frac{\tau_p c}{n_g}$, as the length occupied by the light pulse within the fiber: A single point in the retrieved optical trace carries information from a section of length $W/2$ around the pulse position, for the same reason specified for the incoherent OTDR case.

The described model is effectively equivalent to considering each section of fiber as a multiple-wave interferometer (such as the one described in equation 2.8) composed of $|M(z)| \leq N$ mirrors. Accordingly, the detected intensity at the output can be divided into phase dependent and independent contributions

$$I_{out}(t) = I_{\varphi ind.}(t) + I_{\varphi dep.}(t) \propto |E_{out}(t) E^*_{out}(t)|, \tag{3.13}$$

in which the phase-independent component comprises $|M(z)|$ contributions from the equivalent interferometer at z, and $C_2^{|M(z)|}$ phase-dependent ones.

$$I_{\varphi ind.}(t) = I_0 \sum_{i \in M(\bar{z}(t))} r(z_i)^2 \exp\{-2\alpha z\} \tag{3.14}$$

$$I_{\varphi dep.}(t) = I_0 \sum_{j \neq i} \sum_{i \in M(\bar{z}(t))} r(z_i) r(z_j) \exp\{-\alpha(z_i + z_j)\} \cos \varphi_{i,j}. \tag{3.15}$$

Here, $I_0 \propto E_0^2$ and $\varphi_{i,j}$ is the phase difference between the secondary-waves originating from the i-th and j-th scatterer,

$$\varphi_{i,j} = \varphi_i - \varphi_j = \frac{4\pi \nu_0}{c} n(z_j - z_i). \tag{3.16}$$

Notice that this model still holds for the incoherent OTDR case, as $\langle I_{\varphi dep.}(t) \rangle \approx 0$, leaving the phase-independent component which carries information only about the intensity evolution of the input wave during propagation.

3.3.2 Considerations of φOTDR traces

The obtained intensity trace from a φOTDR consists of a noise-like stochastic time-series with an exponential probability distribution [84, 85], analogous to a speckle

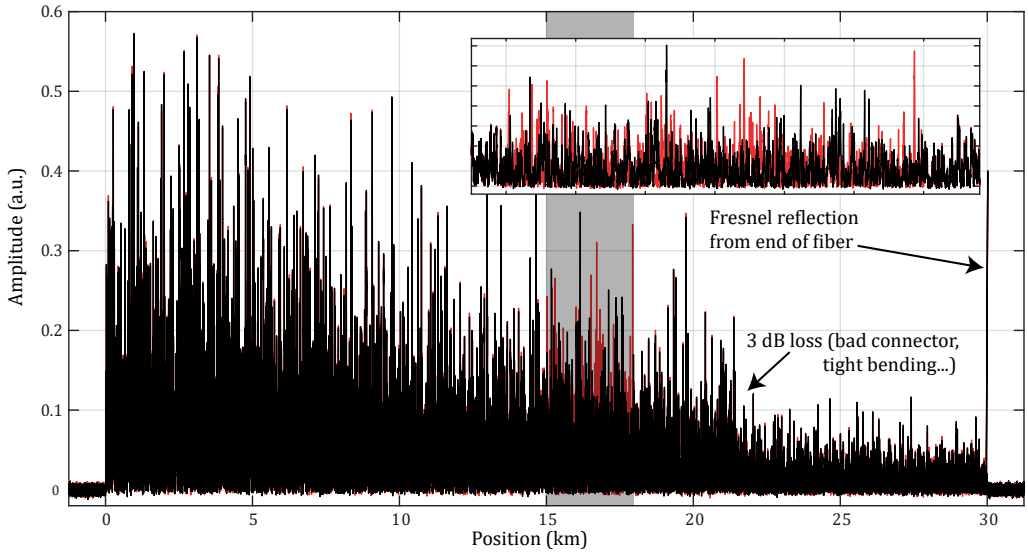

FIGURE 3.9: Simulated example acquisition for a φOTDR. Unperturbed (in black) and with a perturbation applied (in red) at the highlighted region (inset plot).

pattern in free-space optics with coherent sources. The quality of the acquired optical traces is then tied to the visibility of the fringes in the speckle pattern (equation 2.14). This, in turn, depends on the coherence of light, and the local signal-to-noise ratio (SNR). For this section, we shall assume the simplest interrogation method, consisting of tracking the changes in amplitude at every point with respect to a previously acquired reference (see figure 3.9).

In general, the measurement SNR deteriorates as the pulse propagates through the fiber, due to the loss-induced reduction in signal energy. In order to understand the signal performance it is instructive to consider the incoherent OTDR case. Looking at equation 3.6, one may infer that the average power of a given interferometer at position z, assuming homogeneous losses, is

$$\langle P(z) \rangle = P_{peak} \alpha_{bs} \frac{W}{2} e^{-2\alpha z} \tag{3.17}$$

Where α_{bs} is the backscattering coefficient, condensing the scattering coefficient of the fiber and the capture fraction for backscattering. In standard single-mode optical fibers, this is usually ≈ -72 dB/m [86]. Assuming constant noise, the SNR will decay with the same $\propto e^{-2\alpha z}$ dependency.

Improving SNR ensures better quality of measurements and longer potential ranges of measurement. Equation 3.17 suggests that the total return energy from any sensing position may be increased by either increasing the total pulse-width (thus having more reflectors per interferometer contributing to the total energy), or the peak power. Both solutions, however, have their caveats: Increasing the pulse-width, on the one hand, directly impacts the spatial resolution of the system. On

the other hand, the input peak power is fundamentally capped by the onset of non-linear effects if it overcomes a given threshold [13, 87, 88]. In practice, this value can usually be assumed to be maximized, so the typical implied trade-off is between measurement quality and sensing range versus spatial resolution.

The noise in a phase-sensitive OTDR trace can be broadly categorized by its origin, be it from an optical source or from an electrical source. Electrical noise originates mainly from the photodetection process, due to shot noise and thermal (Johnson-Nyquist) noise. In modern-day detectors, the noise contributions are already close to the fundamental minimums, leaving only the options of either reducing the detection bandwidth or the temperature of the photodetector for improvement. Conversely, optical noise has two main sources: Amplified Spontaneous Emission (ASE) from the amplifier stages, and noise originating from the imperfect extinction ratio (ER) of the pulses [89–91]. We shall briefly break down these two sources and comment on how to address them.

ASE originates from the emission and amplification of broadband light from the amplifier stages which is uncorrelated with the input signal. Mitigating ASE noise is a matter of optical filtering before the detection stage, since it has a very broadband spectrum. After detection, the ASE noise generates in-band beat components with itself (spontaneous-spontaneous) and with the signal (signal-spontaneous), which cannot be easily separated.

The second source, regarding the ER, has to do with the low-quality of the generated pulses: More specifically, when there is remnant continuous-wave light that manages to get into the fiber. Being continuous, this lightwave is scattered by the whole fiber at all times, leading to a intra-band component of noise due to an added interference term from all scatterers (not-localized). The ER is defined as the ratio between the pulse peak-power and the remnant continuous-wave power ($ER = P_{peak}/P'_{cw}$). However, its impact on the performance of the SNR is more nuanced, as the coherence of the laser also comes into play. Notably, in the case of non-perfect extinction ratio, a higher coherence laser may underperform a lower-coherence one, given that both fulfill the coherence requirements for measurement (coherence length of at least the pulse-width) [90].

Mitigating this noise source usually involves selecting the best equipment in order to carve the pulse from the CW source: electro-optic modulators (EOM), typically, have worse extinction ratios than acousto-optic modulators (AOM) or semiconductor optical amplifiers (SOA) [90].

Improving SNR

Several techniques have been developed to improve SNR without directly increasing the signal energy through either the pulse-width or peak-power, or reducing the noise. This way, greater resolutions, ranges and measurement performances can be achieved. Generally, these consist in distributed amplification methods, pulse compression, pulse coding techniques, or post-processing of the optical traces.

Distributed amplification makes use of non-linear behavior, specifically stimulated Brillouin or Raman scattering, to bolster the signal as it propagates inside the fiber under test [78, 92–97]. This way, the tradeoff between signal attenuation and amplification can be balanced in order to maintain the signal below the threshold for non-linearities. For φOTDR, Raman amplification has been extensively employed, both in first-order [92] and second-order configurations [78, 93]. Brillouin amplification has also been demonstrated [98, 99], although it is not as common since the Brillouin spectrum is narrow and the Brillouin frequency shifts with perturbations to the fiber, making this method unreliable in measurement environments. Nonetheless, using both second-order Raman and Brillouin amplification has led to record measurement lengths of 175 km of fiber [77].

Coding techniques aim to improve SNR (or spatial resolution) by probing the fiber with a train of pulses for each acquisition, allowing several probes to exist concurrently within the fiber at a given time, which may then be combined in order to provide greater sensing performance.

Generally, this requires linearity in the addition of the traces generated from each bit of code. While this is the case for incoherent OTDR, the superposition of coherent waves is highly non-linear in intensity. As such, in order to achieve pulse coding with a phase-sensitive system, one normally has to rely on coherent detection [100–102]. Nonetheless, the use of direct detection has also been proposed under the condition that the laser coherence length is carefully controlled in order to avoid each bit's trace to interfere [103, 104].

Pulse compression in φOTDR takes after the already developed pulse-compression radar techniques [105]. Fundamentally, the idea is to spread the energy of the probe pulse over a longer time while ordering its spectral contents as well (as a linear frequency modulation). After propagation through the fiber under test, the introduced quadratic phase term is compensated in order to return the pulse to its original time-width and spectrum, reproducing the original transform limited (short) version of the pulse.

In this fashion, one is able to break the link between pulse-width and spatial resolution, allowing more total energy to be sent into the system without provoking non-linear behavior. Compression can be achieved in the optical domain, through the use of a filter device (i.e., a chirped grating) [106], or in the digital domain through matched filtering (or even not fully matched filters, in some cases [107]). Working in the digital domain, however, requires a measurement of the full information contained in the electric field phasor (amplitude and phase), so one needs to employ a coherent detection scheme.

Post processing methods are another reported way of improving the optical trace quality. The most straightforward approach to post-processing the trace is simply to combine the information of several consecutive optical traces through averaging. The implied trade-off, in this case, is the reduction of acquisition bandwidth: Without averaging, the sampling rate is set by equation 3.9, limiting the maximum measurement bandwidth to the Nyquist rate of the system, as $f_\varepsilon < f_{sampling}/2$ (for perturbation frequency f_ε) [76]. Averaging N_{avg} consecutive traces, then, improves the SNR by a factor $\sqrt{N_{avg}}$, while yielding a new maximum strain frequency given by

$$f_\varepsilon < \frac{1}{N_{avg}} f_{sampling}/2 = \frac{1}{N_{avg}} \frac{c}{4L_{fiber}n_g}. \tag{3.18}$$

Similarly, the other basic method is through linear filtering of the traces (usually low-pass filtering) in order to remove any noise outside of the band of interest that may have remained from the detection. More advanced attempts at post-processing come at the cost of additional computational overhead: 2D- and 3D- image processing methods have been proposed, though these have not been demonstrated yet for φOTDR systems, being reserved for BOTDA [108]. Other 2D methods, such as bilateral filtering [109] and edge detection [110] has been proposed for alarm systems based on φOTDR, though not for improving the trace quality itself. Other groups have also proposed the use of time-frequency analysis, such as wavelet-domain thresholding for denoising the trace [111], and others have attempted to improve the quality of measurements through the use of moving average and moving differential algorithms [112], or empirical mode decomposition [113] methods.

Non-linear effects

When the input peak power overcomes a certain threshold, non-linear effects begin to have a meaningful impact in the recovered optical traces. The most notable (as it is the first to become noticeable) is modulation instability, originating from the interplay of Kerr effect and anomalous group velocity dispersion. This phenomenon manifests as the dissipation of the pulse energy from the center frequencies into two noise sidebands located symmetrically around the probe pulse frequency [114].

The use of rectangular pulses aggravates the problem, as it generally induces a power exchange between a pulse and the sidebands known as the Fermi-Pasta-Ulam recurrence [87, 115]. This leads to a periodic transfer of energy between the center frequency band of the pulse and its sidebands, resulting in a periodic loss of coherence which leads to measurement dead-zones of several kilometers (see figures 3.10 and 3.11)

The onset of these minimums of visibility may be delayed by appropriately selecting the pulse envelope shape [115]: *rect*-like pulse windows show the earliest

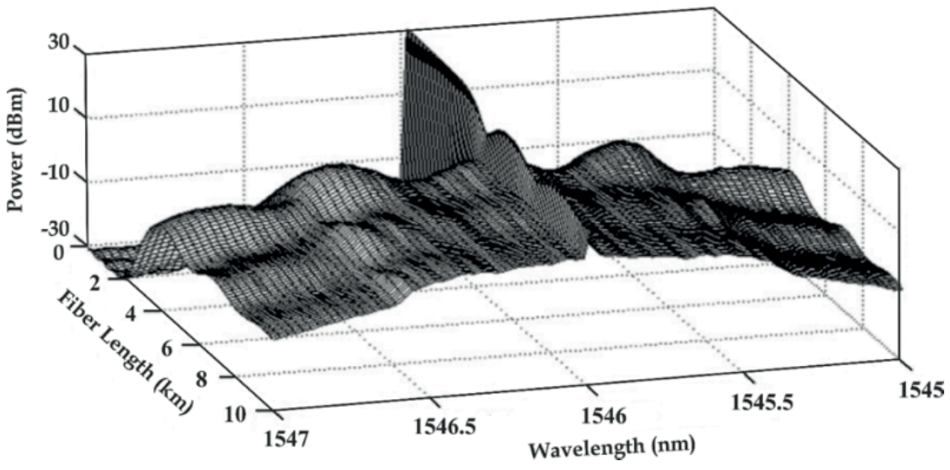

FIGURE 3.10: Simulation of pulse spectrum evolution due to modulation instability: Light from the center frequency of the wave is periodically transferred to between the center wavelength and two MI-generated sidebands. Figure taken from [87].

onset of modulation instability, while Gaussian envelopes allow longer probing distances before the onset of non-linear effects.

3.3.3 Interrogation methods

The final and crucial step in a phase-sensitive OTDR system is to convert the observed changes to the optical power trace into local measurements of perturbation. This comprises the problem of interrogation, and several methods have been proposed, based on either estimation of local intensity or amplitude changes, measurement of the local phase evolution of the electric field or measurement of a the equivalent frequency shift to the change in optical path at a perturbed section.

Intensity-based interrogation

The earliest implementations of φOTDR simply monitor the local changes in intensity of the acquired trace [37, 38, 80]. These setups hold the most modest requirements: The source coherence length must be of some meters (the width of the pulse) and the detection bandwidth is defined by the transform-limited bandwidth of the used pulse. Nonetheless, there have been attempts at improving the basic setup while retaining the same interrogation principle. One such example employs heterodyne detection and post-processing, in order to improve the SNR of measurement [112]. The use of a local oscillator, however, introduces polarization alignment requirements, which manifest as sections of polarization fading in the traces. Subsequent attempts by the same group used polarization-maintaining setups to

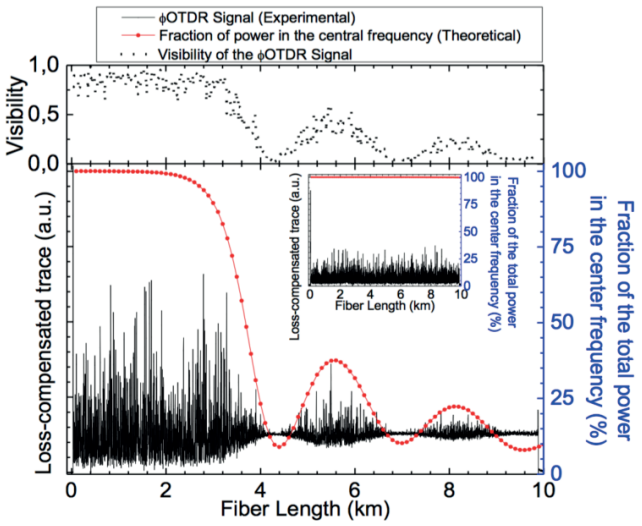

FIGURE 3.11: Effects of modulation instability and FPU recursion on the optical trace visibility. Figure taken from [87]

counteract these issues [116], at the expense of increased cost and complexity in the measurement scheme. While these implementations display the typical capability of long-range, single-shot measurements, they display two major shortcomings: non-linearity and fading (figure 3.12).

Non-linearity arises from the fact that each effective sensor boasts an unknown intensity response. The sum of cosine terms in equation 3.15 leads to a highly non-linear, non-monotonic response, with an unknown sensitivity to the applied perturbation. Thus, these methods are mostly suited as alarm systems where one is interested in detecting (but not necessarily in quantifying) an induced dynamic perturbation.

The other problem, fading, has to do with the random nature of the response of each interferometer, and the intensity of each measurement point [46]. Since the sensitivity of the system is non-homogeneous and random for each position, points of very low intensity or of very reduced sensitivity may be unable to measure. These positions are commonly called the "fading points" of the system. Despite these issues, these methods have provided successful implementations in some niche applications, such as intrusion detection [38], perimeter control [37] or pest control [39].

Recently, there have been reports on intensity-based estimation methods that achieve linear measurements by interrogating the fiber with a frequency-comb pulse [117], or using information from multiple modes in multimode fiber [118].

Phase-demodulation-based interrogation

One solution to address the linearity problem of traditional implementations is to measure the evolution of the phase of the backscattered electric field, since the phase evolution of the backscattered electric field should remain unaltered as long as the

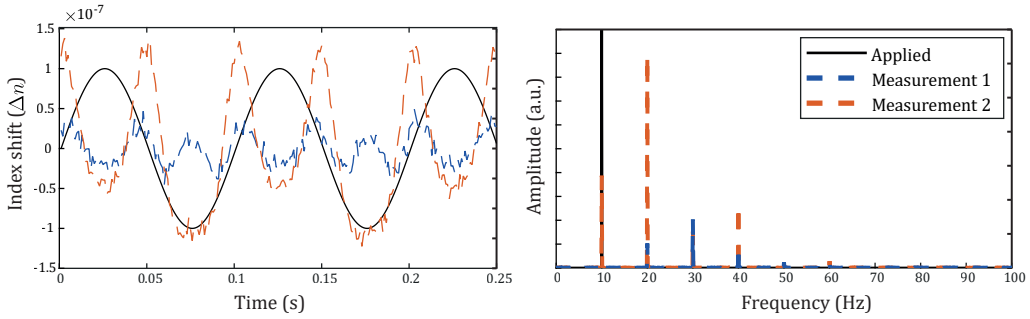

FIGURE 3.12: Simulated measurements on two neighboring positions from a traditional intensity-based interrogation system. Applied perturbation in solid black, measurements in dashed lines. Note the highly non-linear behavior of measurements, even with relatively small perturbation amplitudes.

optical path remains unchanged. Under an applied perturbation, however, the local phase evolution should change linearly with the applied perturbation [46]. The first proposal of using the phase for φ OTDR measurements was done by Posey et al. [119], however only for an individual section of fiber at a time. Since then, it has been one of the main avenues of research in order to achieve linearity in Rayleigh based systems. Several designs have been proposed with the intent of measuring phase, by relying on coherent detection by mixing with a local oscillator, and via incoherent measurements.

Coherent methods [120] attempt to recover the phase (φ) by mixing the backscattered light (E_{out}) with a local oscillator (E_{LO}) before detection. After photodetection, then, one is left with the following

$$I(t) \propto E_{LO}(t)^2 + E_{out}(t)^2 + 2E_{LO}(t)E_{out}(t)\cos(\theta_P(t))\cos(2\pi\Delta\nu + \varphi(t)), \tag{3.19}$$

where θ_P is the relative polarization angle between the LO and the backscattered field. The two DC components are typically removed via balanced detection. Since the power of the LO is typically much higher than the backscattered power, coherent methods incur a gain in the backscattered field, since the phase dependent term has an amplitude $\propto E_{LO}E_b >> E_b^2$, compared to the case of direct detection. These methods may be divided into either heterodyne methods, whenever the backscattered probe is mixed with local oscillator at a different frequency ($\Delta\nu \neq 0$),where the phase difference is measured at the intermediate frequency component [121], or homodyne methods, such as IQ detection [122]. Homodyne methods, in which the LO is kept at the same frequency as the probe, typically have slightly more complex implementations, but require a lower detection bandwidth.

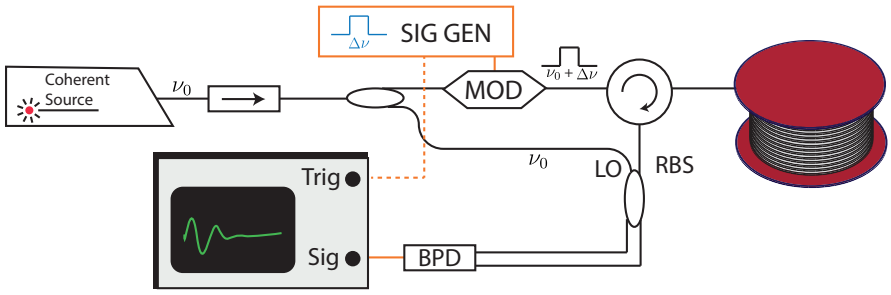

FIGURE 3.13: Example basic implementation of a phase-demodulation based φOTDR. In this case, with heterodyne detection.

The use of a local oscillator, however, is generally undesirable: Firstly, it demands much higher coherence of the laser (of the total length of the fiber). Secondly, it introduces strict polarization requirements, which, if not accounted for, induce polarization-fading, since it is impossible to maintain polarization alignment between the backscattered field and the LO (as one randomly changes and the other is fixed). Preventing fading demands either polarization-maintaining setups or polarization-diversity detection [123], ramping up the costs and unpracticality of the setup considerably.

There has also been some research in incoherent detection methods, such as 3x3 interferometer demodulation [124, 125], at the cost of tripling the detection scheme; Dual pulse methods [126, 127], which estimate the phase difference between two pulses travelling along the fiber with different phases or frequencies; or single pulse direct detection methods, by post-processing of the sum and difference of sections of the trace (for perturbations much smaller than the spatial resolution) [128].

Nevertheless, while phase-detection offers a solution for the linearity problem, it also bears a high price: the coherence requirements for the laser are typically much higher, and demodulating the phase implies a differentiation process which amplifies the noise in the measurement. Also, the issue of fading remains, as positions in which the Rayleigh backscattering adds up to low amplitudes cannot produce an adequate phase estimation. Therefore, the performance of these systems is highly uneven [129] (although there has been considerable research in mitigation of fading in phase-demodulation based systems, usually through non-linear post-processing methods). Additionally, phase measurements are intrinsically bounded within the $[-\pi, \pi]$ range between measured samples, demanding cost-intensive phase unwrapping [130] algorithms in post-processing. Phase unwrapping is a non-linear operation, and noise in the acquisition may produce instabilities in the algorithm, severely deteriorating the sensor performance.

Frequency-based interrogation

The last option for interrogation addresses both the linearity and fading issues. These methods essentially focus on estimating the equivalent frequency shift that compensates the change in measurand. Noting that on equation 3.16 a change in optical path ($OP = nL$, for length L) is equivalent to a change in frequency, one can easily infer the following relation

$$\frac{\Delta OP}{OP} = -\frac{\Delta \nu_0}{\nu_0}. \tag{3.20}$$

This method was first established for Rayleigh-based static measurements. In essence, the fiber is probed sequentially with pulsed light at different center frequencies, covering a broad spectral range. Thus, the frequency response of the equivalent sensor for each position is obtained. Under a perturbation, the local frequency response undergoes an apparent shift (detuning) in direct proportion to the change in optical path.

The method, then, consists in acquiring the frequency response of all sensors over some range, by probing the fiber over a broad range of frequencies, and then finding frequency detuning of each effective sensor with respect to a previously acquired reference [82, 131]. Interrogating in this way shows great linearity and robustness to fading-points (since the measurement intrinsically requires extensive frequency diversity), and there are no coherent detection requirements. Nevertheless, it is only suited for static measurements, given the time-demanding frequency sweep.

In order to adapt the frequency-based interrogation to dynamic measurements, some work has been done either by interrogating the fiber using alternating frequencies [132], or probing the fiber with chirped pulses [133]. The latter is the method in which this thesis is concentrated, and can be succintly explained as a direct extension of the frequency sweep method: A linear chirp with a sufficiently wide band maps frequency-detuning into equivalent time-delays. As such, measurement becomes an estimation of local time-delay within the trace. Chirping, then, is an effective method for the interrogation of dynamic perturbations, avoiding the issues of linearity and fading [134] that impair other techniques, at the cost of greater detection bandwidth.

While the standard implementation of chirped-pulse is the focus of this work, there is also the notable mention of other groups who have employed a similar technique combining the chirped-pulse interrogation method and coherent detection for partial pulse compression. The technique, known as time-gated digital optical frequency-domain reflectometry [107], relies on chirping a very wide probe and compressing it with a non-matched filter to retain some of the chirp. More recently, other pulse-compression chirped-pulse techniques, have also been developed using a novel extraction algorithm [135]. The coherent detection scheme, however, comes at the cost of its characteristic disadvantages, that we previously mentioned.

3.4 Chirped-Pulse φOTDR

The experimental developments of this thesis are mostly improvements of the chirped-pulse phase-sensitive OTDR (CP-φOTDR) technique. This technique was first proposed and formalized in 2016 by Pastor-Graells et al. [133], describing the idea of altering the probe of a standard φOTDR by adding a linear frequency modulation.

While the technique is still quite recent, it has already become a reference among distributed acoustic sensing methods, addressing most of the pervasive issues of the traditional implementations without the drawbacks of other solutions (*e.g.*, fading and polarization issues of coherent methods [136, 137], or the measurement time of frequency-sweep methods [133]), while retaining an extremely simple implementation with minimal alteration to the conventional setup. The maturity of the technique is evidenced by its implementation in already-available commercial equipments (*e.g.*, the HDAS by Aragon Photonics and the ODAS by Omnisens), and numerous industrial and academic projects.

Indeed, in the short years since its inception, the technique has already seen extensive characterization and development [138]. There have been improvements in range [106], measurement performance [139, 140], as well as measurand dynamic range [141, 142] and long-term stability [138]. Also, the impact of different error sources on the technique's performance has been extensively studied and formally described. This includes the effect of additive noise [140], phase-noise [136, 143], crosstalk [144, 145], and the statistical performance of the technique [136, 137]. Some variants to the basic setup have also been developed in attempts to improve the spatial resolution [146, 147]. Many of these developments were undertaken over the course of this doctoral program, and will be described in detail in the following sections.

The technique has also been applied to a wide range of applications. It has been demonstrated as a promising tool for seismology [148, 149], particularly for underwater measurements [36]. The high performances have also been successfully applied/proposed for applications such as fast birefringence measurements [150], anemometry [151], gas measurements [152], hydrogen diffusion [153], bolometry [154] and solar irradiance measurements [155].

This section shall introduce the fundamentals of the technique. The following chapters will cover the developments that were undertaken as a part of the doctoral program.

3.4.1 Description of the technique

Being a frequency-based deconvolution method, it is instructive to start describing CP-φOTDR by briefly introducing interrogation via frequency-detuning, typical of the frequency-sweep method.

To do so, we consider a reference trace (acquired at instant $k = 0$) from an arbitrary unperturbed optical fiber, when interrogated with a monochromatic pulse of frequency ν_0. Consider, now, that a section of length L at the center of the fiber undergoes a small refractive index change. Probing again (at instant $k = 1$), all pairs of scatterers within the perturbed section will experience the following change in their phase relationship

$$\Delta\varphi_{i,j} = \varphi_{ij}^{k=1} - \varphi_{ij}^{k=0} \tag{3.21}$$

$$= \frac{4\pi L_{ij}}{c}(n+\Delta n)\nu_0 - \frac{4\pi L_{ij}}{c}n\nu_0 = \frac{4\pi L_{ij}}{c}\Delta n\nu_0, \tag{3.22}$$

which incurs an alteration to the shape of the trace over that position. If, however, at instant $k = 2$, the probe is changed so that now its center frequency becomes $\nu = \frac{n\nu_0}{(n+\Delta n)}$, the change in phase relationship with respect to the reference is cancelled

$$\Delta\varphi_{i,j} = \varphi_{ij}^{k=2} - \varphi_{ij}^{k=0} \tag{3.23}$$

$$= \frac{4\pi(n+\Delta n)L}{c}\left(\frac{n\nu_0}{(n+\Delta n)}\right) - \frac{4\pi nL}{c}\nu_0 = 0, \tag{3.24}$$

i.e., the optical trace at the perturbed section recovers the original, unperturbed shape (while changing its shape at all unperturbed sections). The frequency detuning $\Delta\nu = \nu - \nu_0$ required to achieve this compensation, for small perturbations, can be approximated as

$$\frac{\Delta\nu}{\nu_0} \approx -\frac{\Delta n}{n}. \tag{3.25}$$

This is more commonly generalized for the case of different optical paths as

$$\frac{\Delta OP}{OP} \approx -\frac{\Delta\nu}{\nu_0}. \tag{3.26}$$

One simple interrogation method, then, consists in finding the frequency detuning $\Delta\nu$ that recovers the shape of a previously acquired and calibrated reference state, and then relating the frequency detuning to the change in measurand. This process is visually depicted in figure 3.14.

The chirped-pulse technique builds upon this concept by mapping each frequency detuning ($\Delta\nu$) to a unique time section of the pulse (*i.e.*, a time delay Δt), thus overcoming the need for the frequency sweep (see figure 3.15). This is done by adding a linear frequency modulation to the pulse. It is important to recall that as a finite quasi-monochromatic source, the pulse has an intrinsic non-zero transform-limited bandwidth. In order to achieve proper mapping of its frequency contents, the bandwidth added by chirping has to be wide enough to render the natural bandwidth effects of the pulse negligible. This can be understood by modelling a chirped probe pulse of frequency $\nu(t) = (\nu_0 - \delta\nu/2) + \frac{\delta\nu_p}{\tau_p}t$ ($\delta\nu$ being the chirp bandwidth and τ_p the pulse width) as the product of a rectangular monochromatic pulse with a

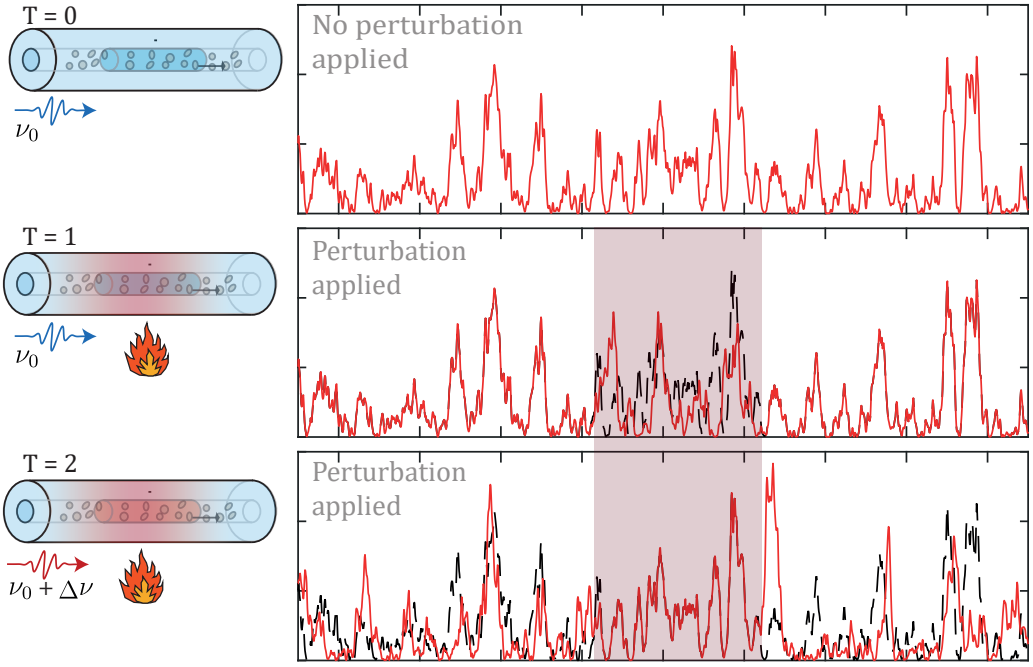

FIGURE 3.14: Schematic representation of frequency based interrogation, as exemplified in the text. Black line is the reference acquisition (same as the red line in T = 0).

quadratic phase modulation term

$$E_{in}(t) = A\,\mathrm{rect}\{\frac{t}{\tau_p}\}\exp\left\{-j2\pi((\nu_0 - \delta\nu/2)t + \frac{\delta\nu_p}{2\tau_p}t^2)\right\} \tag{3.27}$$

$$= E_0(t)\exp\left\{-j2\pi\frac{\delta\nu_p}{2\tau_p}t^2\right\}. \tag{3.28}$$

We now represent the above product as a convolution of both terms in the frequency domain

$$\widehat{E_{in}}(\omega) = \widehat{E_0}(\omega) * \mathcal{F}\left\{\exp\left\{-j2\pi\frac{\delta\nu_p}{2\tau_p}t^2\right\}\right\} \tag{3.29}$$

$$= \sqrt{\frac{\tau_p}{\delta\nu_p}}\int_{-\infty}^{\infty}\widehat{E_0}(\Omega)\exp\left\{j\frac{\tau_p}{4\pi\delta\nu_p}(\omega-\Omega)^2\right\}d\Omega. \tag{3.30}$$

$$= \sqrt{\frac{\tau_p}{\delta\nu_p}}\exp\left\{j\frac{\tau_p\omega^2}{4\pi\delta\nu_p}\right\}\int_{-\infty}^{\infty}\widehat{E_0}(\Omega)\exp\left\{-j\frac{\tau_p\omega\Omega}{2\pi\delta\nu_p}\right\}\exp\left\{j\frac{\tau_p\Omega^2}{4\pi\delta\nu_p}\right\}d\Omega, \tag{3.31}$$

where $\mathcal{F}\{\cdot\}$ is the Fourier transform operator, and Ω is an auxiliary variable with units of angular frequency used for the convolution operation.

If we now assume that the function $\widehat{E_0}(\Omega)$ is well-defined and contained within the transform-limited band $2\pi\Delta B_{TL} \propto \tau_p^{-1}$, and we ensure the following condition

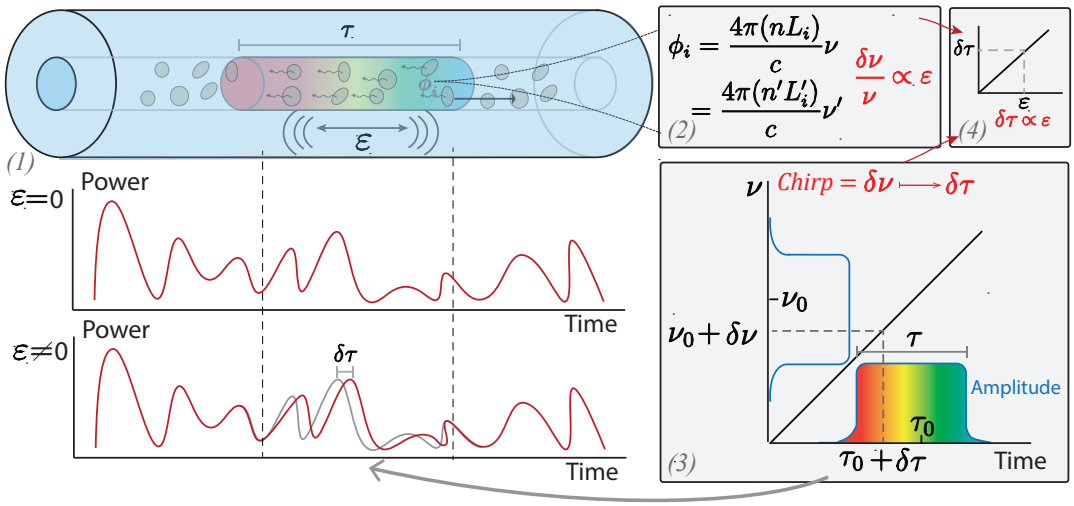

FIGURE 3.15: Schematic representation of the working principle of a CP-φOTDR. A (1) chirped-pulse replaces the traditional quasi-monchromatic probe. And the light is elastically scattered by existing scatterers. An applied perturbation ε introduces a change to the phase relationship between scatterers (2) which may be compensated through a frequency detuning. (3) A wide enough linear frequency modulations maps each time-instant across the pulse to a specific frequency component, so a time-to-frequency mapping is achieved, leading to an (4) apparent time-delay proportional to the applied perturbation.

$$\frac{\tau_p}{\delta\nu_p} \ll \frac{1}{\Delta B_{TL}^2} \Rightarrow \tau_p \delta\nu_p \gg 1, \tag{3.32}$$

the term $(\frac{\tau_p}{4\pi\delta\nu_p}\Omega)$ becomes negligible. We can then re-write equation 3.31 as

$$\widehat{E_{in}}(\omega) \propto \exp\left\{ j\frac{\tau_p\omega^2}{4\pi\delta\nu_p} \right\} \int_{-\infty}^{\infty} \widehat{E_0}(\Omega) \exp\left\{ -j\frac{\tau_p\omega\Omega}{2\pi\delta\nu_p} \right\} d\Omega \tag{3.33}$$

$$= \exp\left\{ j\frac{\tau_p\omega^2}{4\pi\delta\nu_p} \right\} \mathcal{F}^{-1}\{\widehat{E_0}(\Omega)\}. \tag{3.34}$$

This condition reflects the frequency-to-time mapping of the pulse [156]: the time and spectral envelopes coincide, with frequency and time mapped through the following linear relation

$$t = -\frac{\tau_p}{\delta\nu_p}\nu, \tag{3.35}$$

ν being the instantaneous frequency. This is what is commonly referred to as frequency-to-time mapping, as we can attribute a time instant to a specific instantaneous frequency, and within it underlies the principle of chirped-pulse based interrogation, where a small deviation in frequency is mapped to a small deviation in time:

$$\Delta t = -\frac{\tau_p}{\delta \nu_p}\Delta \nu. \tag{3.36}$$

In this case, equations 3.26 and 3.36 lead to the following relationship

$$\frac{\Delta OP}{OP} = -\frac{\Delta \nu}{\nu_0} = -\frac{1}{\nu_0}\frac{\delta \nu}{\tau_p}\Delta t. \tag{3.37}$$

This last equation implies that the trace shall undergo an apparent delay (along the fast-time axis/apparent position axis) at the measurement location, proportional to the measurand. Visually, this can be understood by realizing that launching a chirped-pulse of a different center frequency is extremely similar to launching a time-delayed version of the same probe pulse (see figure 3.15).

The estimation of measurand, then, comprises an estimation of time-delay using local windows of width $T \geq \tau_p$. Going above the pulse width, however, entails a deterioration of the spatial resolution.

Equation 3.32 condenses a necessary condition to fulfill. Otherwise, the optical trace deformations typical of a traditional φOTDR system are non-negligible, leading to non-even sensitivities or non-linearities in the measurand estimation.

The most notable drawback of the CP-φOTDR technique is the increased bandwidth requirements for detection. Apart from the increased costs in the detection stage, detecting a wider range of optical frequencies increases the amount of in-band noise that cannot be easily removed by linear filtering, so the achievable optical SNRs are lower when compared to similar powers and pulse widths in a traditional system. The outcome of increased bandwidth on measurement performance, however, is not so trivial. For the case of a time-delay estimation measurement, an increased bandwidth translates into greater accuracy in the measurements. The specific effects of bandwidth, SNR and spatial resolution on the performance of measurement will be discussed in detail in the next chapter (section 4.1).

3.4.2 Sensitivity to strain and temperature

Any interferometric sensor system is directly sensitive to changes in the optical path ($OP = nL$), or the "effective distance" that light travels assuming constant speed. A change in optical path, therefore, may be quantified in terms of refractive index and total length changes as

$$\Delta \mathrm{OP} = \Delta nL + n\Delta L + \Delta n \Delta L. \tag{3.38}$$

While a broad range of parameters can be sensed after some engineering, this means that there are two physical parameters to which intrinsic fiber interferometers are directly sensitive, and which are of common interest to physicists and engineers: the relative elongation (strain) and temperature.

At a glance, the influence of longitudinal strain on the optical path is straightforward, as an elongation of the material implies a longer distance for light to cover.

However, there is an added component of induced index-shift from the deformation of the mechanical medium. This strain-optic contribution accounts to approximately 20% of the change in optical path in an optical fiber, so that

$$\frac{\Delta OP}{OP} \approx [1 + \rho_\varepsilon]\varepsilon = K_\varepsilon \varepsilon, \tag{3.39}$$

where K_ε is the coefficient that summarizes the effects of strain in the optical path difference and ρ_ε is the strain-optic coefficient, indicating the change in effective index due to the longitudinal mechanical deformation.

In the case of temperature, the change in optical path length is mostly dominated by the thermo-optic effect (*i.e.*, the temperature dependence of refractive index). This dependence is approximately linear for changes within a few hundred Kelvin [35]. Nevertheless, there is another temperature-induced contribution (about 10 times smaller), occurring due to thermal expansion of the silica glass (and surrounding materials, such as the coating and bonding). As such, the thermal-induced change in optical path is given by

$$\frac{\Delta OP}{OP} \approx [K_\varepsilon \alpha_T + \zeta]\Delta T = K_T \Delta T \tag{3.40}$$

where K_T is a coefficient that encapsulates the thermal effects of the fiber, α_T is the effective thermal expansion coefficient of the fiber/coating/bonding, and ζ is the thermo-optic coefficient.

For standard fibers, such as the ones used over the course of this work, the following coefficients are typically considered

$$K_T = 6.678 \times 10^{-6}\, {}^{o}\mathrm{C}^{-1} \tag{3.41}$$

$$K_\varepsilon = 0.78\, m \cdot m^{-1}. \tag{3.42}$$

In the context of CP-φOTDR, then, these coefficients lead to the following sensitivities to strain and temperature [133]

$$\Delta T = -\frac{1}{K_T}\frac{1}{\nu_0}\frac{\delta\nu}{\tau_p}\Delta t \tag{3.43}$$

$$\Delta \varepsilon = -\frac{1}{K_\varepsilon}\frac{1}{\nu_0}\frac{\delta\nu}{\tau_p}\Delta t \tag{3.44}$$

3.4.3 Implementations of CP-φOTDR

The chirped pulse technique has been reported in two possible designs, differing in the method used to chirp the probe pulse. Although the principle of measurement is fundamentally the same for both techniques, since both are used over the course of this work it is relevant to briefly introduce both designs and describe the advantages and disadvantages of each. The two common emission arm schemes can

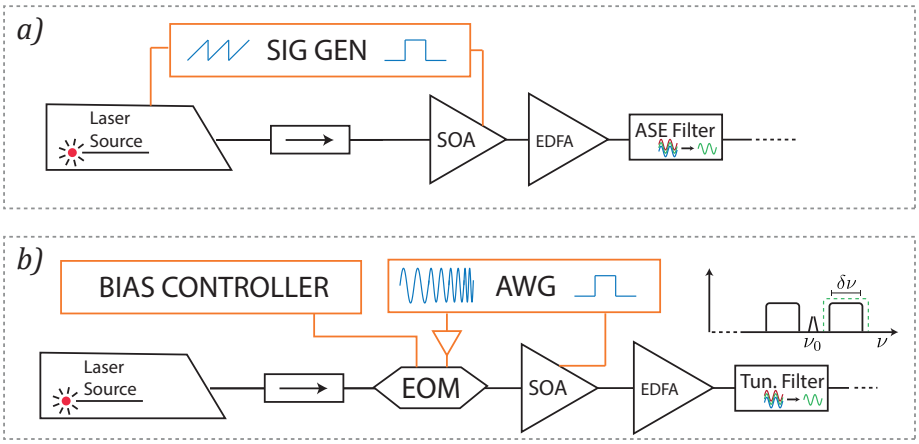

FIGURE 3.16: Typical emission arms for chirped-pulse phase sensitive OTDR measurements. a) Direct current modulation; b) External modulation

be described as the direct current modulation method and the external modulation method (Figure 3.16).

The direct current modulation method, as reported in the original paper by Pastor-Graells et al. [133], consists in directly modulating the laser current using a sawtooth wave in order to induce the chirp. The frequency modulated continuous-wave laser is then time-gated with a synchronized signal, using an external high extinction ratio element (*e.g.* SOA), with the same repetition rate as the sawtooth waveform. The advantages of this type of design for the emission arm are apparent from the very modest requirements for implementation, requiring only the laser and two channels of a (relatively slow) signal generator. However, there are a couple of considerations: first, it is important to verify the linearity of the laser frequency with the applied current, taking care to avoid jumps in the frequency. Also, more coherent lasers are typically not as tunable as other options. Therefore, the total chirp that can be added to the probe pulse may be limited by the tunability of the laser, and the amplitude may also be affected by the induced current changes.

External modulation, on the other hand, is much more costly. Typically, it requires a fast arbitrary waveform generator (AWG) and an amplitude modulator (such as an electrooptic modulator) to externally modulate the laser in amplitude with a chirp. This generates two sidebands of the carrier wave with the desired chirp. Then, by filtering one of the sidebands, one is able to generate the probe pulse. This can be understood by considering the following transfer function for a typical Mach-Zehnder electro-optic modulator

$$E_{out}(t) \propto E_{in} \exp\{i2\pi\nu_0 t\} \sin\left(\frac{\pi V_{in}(t)}{2V_\pi} + \phi_{bias}\right), \tag{3.45}$$

where $E_{in}\exp\{i2\pi\nu_0 t\}$ is the input field and $E_{out}(t)$ is the output field, V_π is the modulator sensitivity, $V_{in}(t)$ is the RF input and ϕ_{bias} is the bias phase, controlled in this case to set the modulator in suppressed carrier operation. In order to produce a chirp waveform of bandwidth $\delta\nu$, the following V_{in} is generated at the AWG output and fed to the RF input of the modulator [141]

$$V_{in}(t) = V_0\cos\left(2\pi\cdot\left(f_c+\frac{\delta\nu}{2\tau_p}t\right)t\right)\mathrm{rect}(t/\tau_p) \tag{3.46}$$

In this case, keeping V_0 small enough, we may apply a paraxial approximation to equation 3.45. In this case, two sidebands are generated around the carrier frequency, separated by f_c (which should be selected in order to accomodate the bandwidth of the equipments and allow adequate filtering), of the same form of $V_{in}(t)$. Filtering one of the sidebands, then, yields the waveform of interest

$$E_{chirp}(t)\propto E_{in}V_0\exp\left\{j(2\pi\cdot(\nu_0+f_c)t+2\pi\frac{\delta\nu}{2\tau_p}t^2\right\}. \tag{3.47}$$

There are several advantages to this type of implementation. Particularly, any laser can be used at any chirp, regardless of its ability to be tuned. As such, the chirp is typically limited only by the specifications of the modulator and detection equipment, and facilitates the use of very narrow linewidth lasers. However, this method has new requirements, in the form of a fast enough signal generator able to generate the chirped pulse, an electrooptic modulator (and RF signal driver), a bias controller and a tunable filter in order to retain only the sideband of interest. Also, it entails a loss on the optical power from the modulator and from the rejected sideband and remnant carrier (of at least 3 dB with fully suppressed carrier, and neglecting power losses from the modulator).

3.4.4 Time-delay estimation

The frequency-to-time mapping changes the estimation process into one of time delay. Time-delay estimation (TDE) is a well-known problem, extensively studied [157–160] in several fields, from radar/sonar to ultrasound medical measurements. Several algorithms have been developed for estimating delays between measurements. For simple cases of time-delay estimation (without effects such as multiple reflections or resonances), such as the case of CP-φOTDR, the most commonly employed estimator consists in finding the lag at which there is a maximum of the cross-correlation function, and some filtering. This is typically known as the generalized cross-correlation (GCC) algorithm.

The GCC method [157, 158, 161] is advantageous to other similarity-measuring algorithms for TDE (such as sum of absolute differences, or sum of square differences) since it can be efficiently computed in the frequency domain by exploiting the convolution theorem and fast Fourier transform algorithms. For the purpose

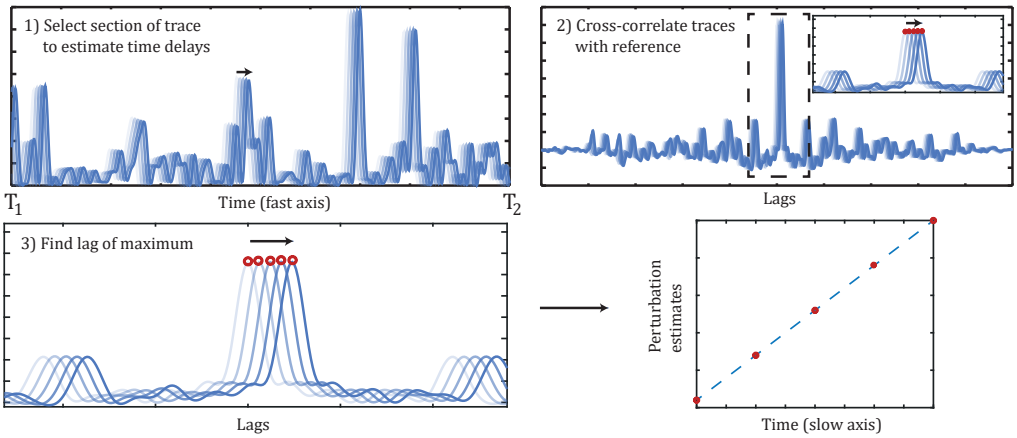

FIGURE 3.17: Visual representation of the generalized cross correlation algorithm for time-delay estimation in the context of CP-φOTDR. 1) The same section of fiber is measured in sequential acquisitions, which are then cross-correlated (or cross-covariance, if not zero mean) with a previously acquired reference trace (usually the first acquisition). 3) The lag at which there is the absolute maximum of the cross-correlation function is tracked. The lag can then be converted to a perturbation measurement.

of CP-φOTDR measurements, since the acquisitions are not zero-mean, the cross-correlation should be replaced with the cross-covariance in order to prevent biasing the result. For the sake of simplicity, however, we shall assume that the mean is removed from signals before processing, and henceforth refer to the cross-correlation.

Using this algorithm, the estimate of the time-delay D_{rm} ($\langle \hat{D}_{rm} \rangle = D_{rm}$) between the reference (r-th acquisition) and the m-th acquisition of the same trace section, is acquired by computing

$$\hat{D}_{rm} = \text{argmax}\,\{R_{rm}(\tau)\}, \tag{3.48}$$

where $R_{rm}(t)$ is the cross-correlation function between a trace-section acquired at a previous instant to be used as reference ($x_r(t)$) and the m-th acquired trace ($x_m(t)$), acquired at a later instant. The aforementioned process can be understood by considering that a time-delay between 2 noiseless signals can be represented as

$$x_m(t) = x_r(t - D(m)), \tag{3.49}$$

so $R_{rm}(t)$ is defined as (assuming the mean is removed from the signals $x_r(t)$ and $x_m(t)$, to avoid unnecessary complexity)

$$R_{rm}(\tau) = \int_{T1}^{T2} x_m(t)x_r(t+\tau)dt \tag{3.50}$$

$$= R_{rr} * \delta(t - D(m)). \tag{3.51}$$

Here $R_{rr}(t)$ is the autocorrelation function of the reference signal, and δ is the Dirac delta function. Note that this is a local estimation, focused on the time-window defined by $[T1, T2]$. A visual depiction of the basic algorithm for time-delay estimation is displayed in figure 3.17.

3.4.5 Spatial resolution and gauge length

In terms of the displayed optical trace, we can describe the spatial resolution as the length required between measured positions to ensure independent readings. This section is the same as the region of interaction for a regular OTDR, as we described previously, and is of half the total length of the pulse.

For purposes of measurement, however, we are interested in defining the spatial resolution as the distance between two measurement points which can be considered decorrelated. The time-delay estimation problem in CP-φOTDR also requires the definition of a section of trace, on which to evaluate the local time-delay. This is akin to the definition of gauge length in a "phase-demodulation" base system, where one estimates the phase evolution across a given length of fiber, defined between two points of measurement.

The optical trace time-section selected for time-delay estimation (of width T) is, in principle, completely independent from the pulse width τ_p and can be set to any value. This value is typically set to the same as the pulse width, for optimal spatial resolution for a given pulse-width. The result, measurement-wise, is a convolution of the time-delay estimation window (i.e., gauge length) and the spatial resolution due to the effects of the pulse. The resulting impulse response has a FWHM equal to the resolution imposed by the pulse-width. The measurand spatial resolution is often defined by this FWHM, so the spatial resolution of CP-φOTDR is given by [138]

$$W = c\tau_p/2n_g \tag{3.52}$$

3.4.6 Range considerations and distributed amplification

The same trade-off between sensing range and input pulse energy, typical of other implementations of phase sensitive OTDR is still present in the chirped pulse configuration. In summary, the total interrogated range is directly proportional to both the pulse peak power and the pulse width. However, there is a limit to the potential improvements by only increasing the pulse peak power before this strategy backfires due to the onset of non-linear effects (specifically modulation instability), leading

to periodic loss of coherence of the optical laser (resulting in periodic fading of the optical trace and rapidly limiting the total range of interrogated fiber). Thus, the remaining option is to increase the pulse width, yielding a trade-off between sensing range and spatial resolution. This trade-off has limited typical implementations of CP-φOTDR in standard SMF, to resolutions of some meters for a few tens of kilometers (30 - 50) [138].

One method to circumvent this trade-off consists in implementing distributed amplification strategies to compensate the power loss in the pulse over the fiber length, while retaining the peak power below the threshold for non-linearity. Distributed amplification strategies in φOTDR methods have been demonstrated using both Brillouin and Raman stimulated scatterings. However, the narrow bandwidth of Brillouin effect ($\sim$50MHz in SMF), being lower than the typical spectral content of the chirped pulses used for the CP technique, makes this effect generally unsuitable for implementation. On the other hand, distributed Raman amplification has successfully been demonstrated for traditional φOTDR measurements [28, 77, 96, 99], and the concept has also been applied to CP-φOTDR measurements [162].

The challenge of first-order Raman amplification in a φOTDR system lies on the optimization of probe peak power and Raman pump powers, with the aim of maximizing the probe power for the longest possible distance without overcoming any non-linearity thresholds. The first proof-of-concept work highlighted the additional considerations of CP-φOTDR, since any non-linear effects, chromatic dispersion, or pump depletion that may affect the pulse shape or instantaneous frequency profile may affect the frequency-to-time mapping and thus the measurement-ability of the system [162, 163]. In the work published by Pastor-Graells et al. [162], first-order Raman amplification was implemented using a dual-ended (bidirectional) configuration, demonstrating a total of 75 km of interrogated fiber. This was achieved using Raman pump powers well within the specifications of typical optical connectors (set at 230 mW and 350 mW for the co-propagating and counter-propagating pumps, respectively), proving the viability of the technique for field applications. The CP-φOTDR design used a direct current modulation to develop the chirp in the probe laser, and introduced a Raman pump laser (emitting in continuous wave at 1455 nm), which is divided by a 50/50 coupler and multiplexed into both ends of the fiber (see figure 3.18).

The non-linear effects on the probe were evaluated for different input peak powers, and they were found to be negligible at 25 mW (see figure 3.19 b)) with negligible effects to both the amplitude envelope and the instantaneous frequency profile. The effects of RIN (Relative Intensity Noise) and pump depletion were also analyzed: pump depletion was found to be only relevant for probe peak powers much higher than the MI threshold, and the RIN transfer was found to be equivalent to that of standard φOTDR.

More recent attempts using Raman amplification strategies have reached interrogated ranges of lengths of 80 to 100 km [138].

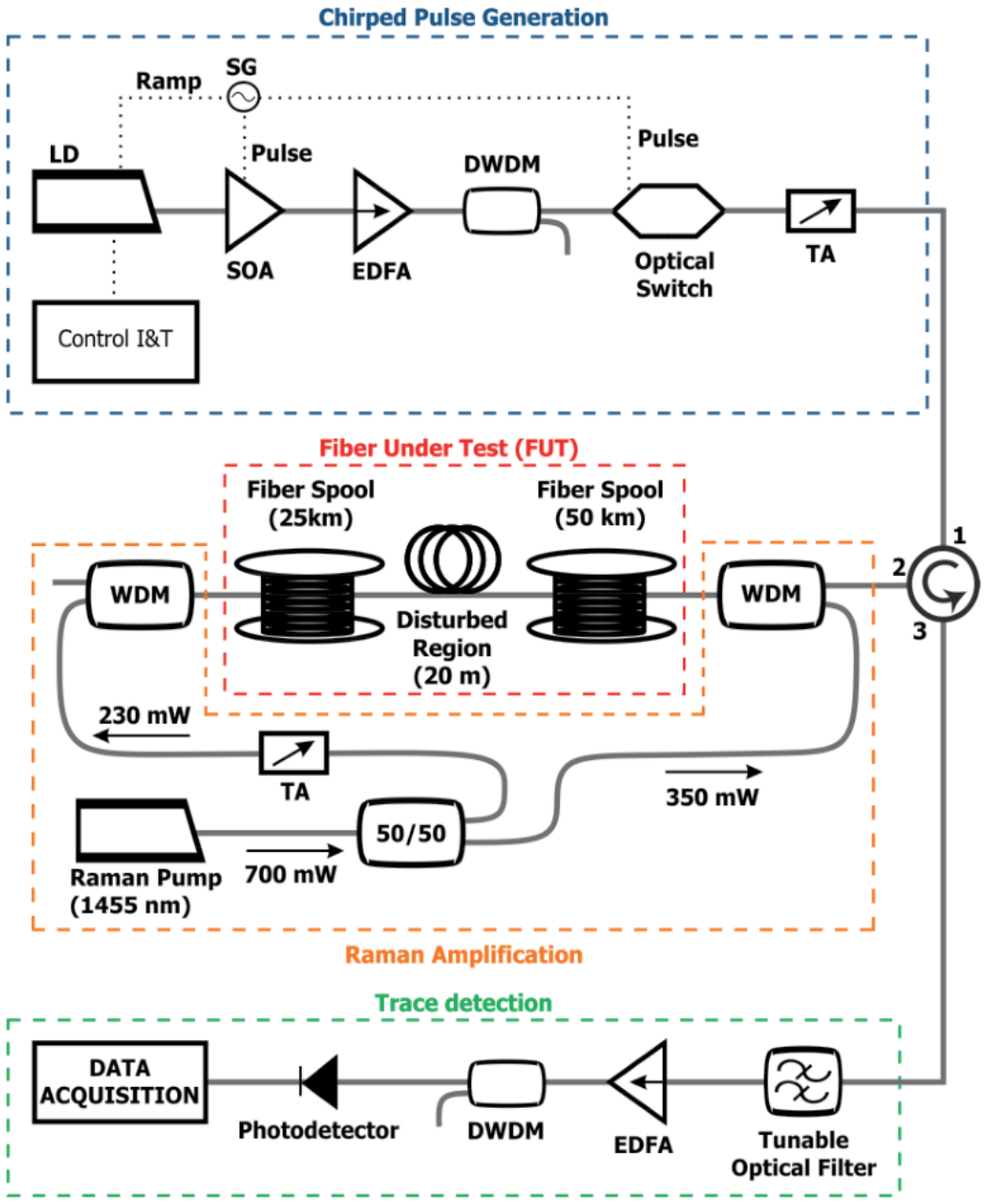

FIGURE 3.18: Setup used in [162] for the demonstration of Raman amplification in CP-φOTDR. Taken from [162]

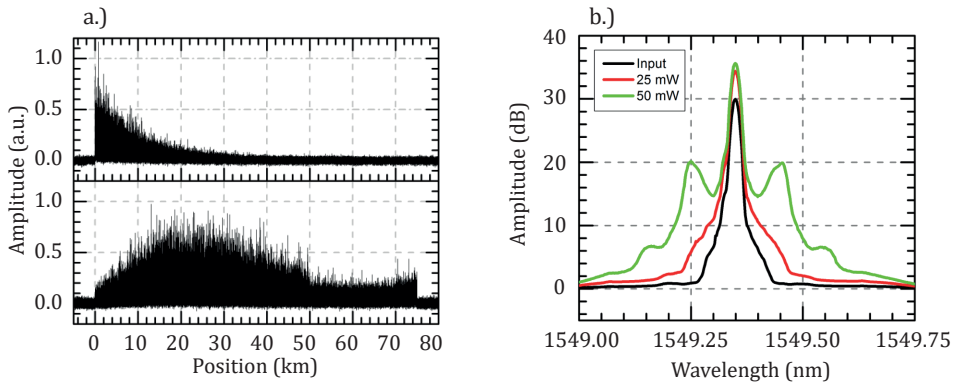

FIGURE 3.19: Results of Raman amplification in CP-φOTDR. a) Comparison of traces without amplification (top) and with amplification (bottom), b) Probe spectrum after propagation, for different input powers. Note the importance of optimizing input powers to prevent the onset of modulation instability. Taken from [162]

3.4.7 Effects of laser phase and frequency noise

One important source of noise in coherent-probe systems emerges from the random variations of the laser output phase or drifts in the laser center frequency. This can be easily understood by modelling the continuous-wave laser output as being continuously experiencing slow drifts in its phase. At the time of each laser shot, the effective phase drift can be modelled to the first order as a frequency shift which is imprinted into the pulsed light - *i.e.*, the whole pulse has a frequency drift with respect to the average center frequency of the laser. The effect of phase-noise on the instantaneous frequency of the laser can be described as

$$\nu_r(t_m) = \frac{1}{2\pi}\frac{\delta\varphi_r(t_m)}{\delta t} \tag{3.53}$$

where $\varphi_r(t_m)$ is the phase-noise drift function, and $t_m = \frac{m}{f_{acq}}, m \in \mathbb{N}$ represents the instants at which the probe is pulsed, and relates to the slow time-axis of measurement.

Consider now the description of a measurement through frequency demodulation as explained previously. A change in frequency is effectively the same as an applied strain (from a measurement perspective), with one crucial difference: while a strain change is a material-bound property (and thus, localized), a change in frequency is a light property and affects the whole fiber measurement. We can conclude, then, that phase-noise directly translates to measurement noise which is fully spatially correlated. Practically, this reflects as an apparent time-delay across the fiber trace which can be calculated as

$$\Delta t_r(t_m) = \frac{\tau_p}{\delta\nu}\nu_r(t_m). \tag{3.54}$$

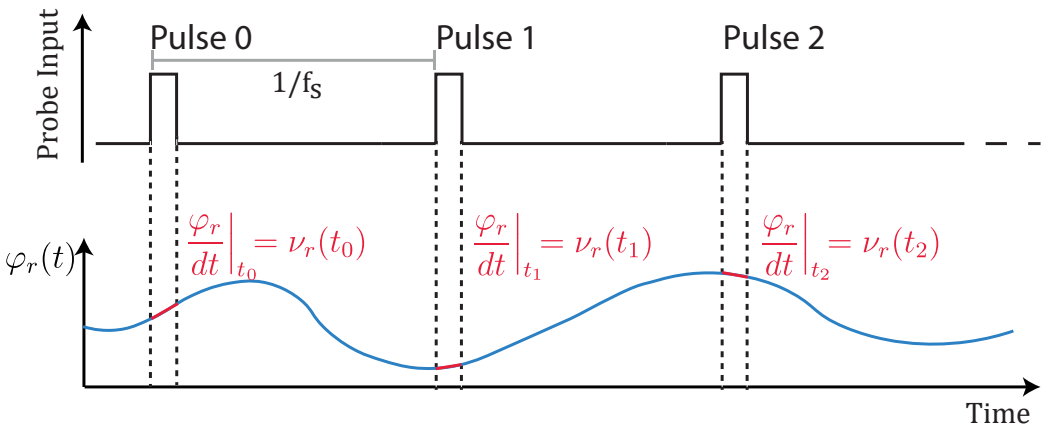

FIGURE 3.20: Effects of phase-noise on the laser. A slow phase drift, yields a fixed quasi-linear phase-modulation across each pulse (*i.e.*, a frequency shift). In the case of a phase-demodulation scheme relying on a LO, the LO phase-noise is not fixed, for all fiber positions.

Note that, in this case, the delay Δt_r refers to the fast axis (*i.e.*, the position axis), and the variable t_m refers to the slow axis (i.e., the measurement time series). It is evident that the estimation of measurand via time-delay is affected directly by the change in frequency of the probe. The induced noise power spectral density (PSD), then, will be proportional to the spectral density of the fluctuations of the laser frequency, which can be shown to be proportional to the static linewidth of the employed laser [164, 165], as,

$$S_{\nu_r} \propto \Delta f_{laser}, \tag{3.55}$$

for the noise PSD of the laser source S_{ν_r} and static laser linewidth Δf_{laser}.

In the case of strain measurements, then, the strain noise PSD S_ε can be computed as

$$S_\varepsilon = \frac{S_{\nu_r}}{(0.78\nu_0)^2}. \tag{3.56}$$

The inverse proportionality between the probe chirp and the time-delay evidenced in equation 3.54 is effectively cancelled by the fact that changing the chirp also affects the sensitivity to measurand by the same amount (equation 3.36), so the measurement noise due to the laser phase-noise is invariant with the added chirp. Mitigating phase noise, then, entails either a compensation strategy or employing a narrower linewidth source.

It is important to note that all coherent probe systems suffer from the phase drifts of the source, and this problem is not exclusive to CP-φOTDR. In the specific case of coherent detection schemes, the use of a local oscillator undergoing continuous drifts

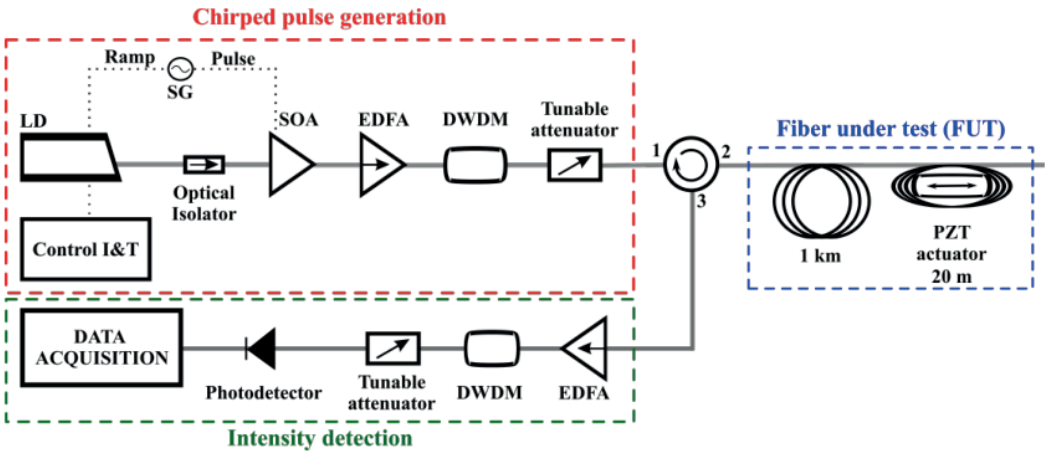

FIGURE 3.21: Setup for the demonstration of phase-noise effects with lasers of different linewidths. DWDM - Dense Wavelength Division Multiplexer. Figure from [136].

in phase entails that each fiber position experiences a different net effect of phase-noise. In the chirped-pulse case, however, each probe pulse has a "fixed" frequency deviation which is determined at the time of the pulse generation, fluctuating randomly from pulse to pulse. This is visually depicted in figure 3.20.

Linewidth and phase noise

The effect of laser linewidth on phase noise (and its effect on measurement performance in CP-φOTDR measurements) was demonstrated using a chirped-pulse system with direct current modulation [136].

The setup consisted in chirping the probe laser using a current control, which applied a sawtooth signal wave to the current modulation, yielding a linear chirped output. The continuous-wave output was time-gated through an high extinction-ratio semiconductor optical amplifier (SOA), ensuring linearity in the introduced frequency modulation. The chirp was controlled by varying the peak voltage of the sawtooth-wave signal. The linewidths of the employed lasers were estimated through a self-heterodyne method [166].

In this paper, three commercial lasers of different linewidths (5 MHz, 50 kHz and 25 kHz) were used to interrogate a 100 m fiber with a section with a controlled strain perturbation, with vastly different performance outcomes, depicted in figures 3.22 and 3.23 a). The researchers also noted the effects of changing the pulse chirp for the 25 kHz laser, which resulted in no improvement in the measurement performance, for the reasons specified earlier, as demonstrated in figure 3.23 b). The different laser performances were compared by quantifying the SNR of a 40 nε perturbation at 2 kHz, as the ratio between perturbation power and mean noise-floor power level of

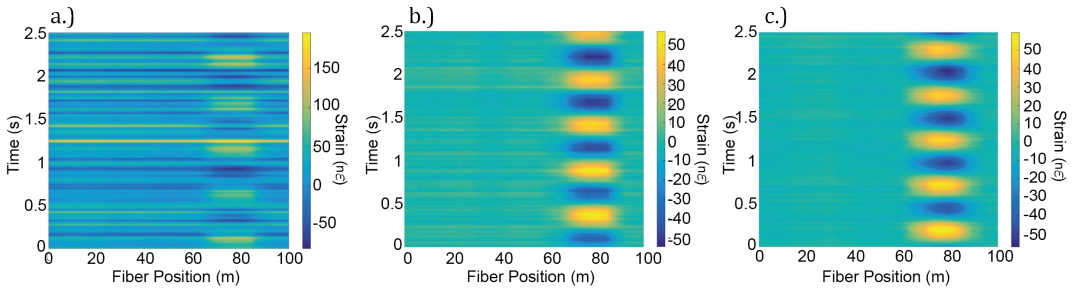

FIGURE 3.22: Position-time measurements of lasers with different phase-noises. a) 5 MHz linewidth laser; b) 50 kHz linewidth laser; c) 25 kHz linewidth laser. Figures from [136].

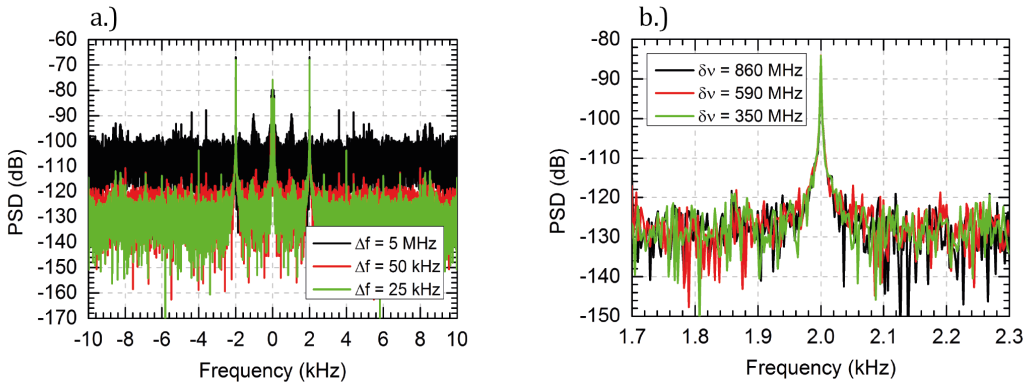

FIGURE 3.23: a) Comparison of the phase nose for the 3 lasers used, with different linewidths; b) Effects of the chirp on the strain PSD noise. Figures from [136].

the strain PSD. For a 0.4 s measurement, the researchers observed a 34.4 dB SNR for the 5 MHz linewidth laser, and 54.7 dB and 56.7 dB for the 50 kHz and 25 kHz lasers respectively, in accordance to theoretical predictions. Conclusively, the main limitation of noise floor in all of these cases is due to the laser phase noise.

Cancellation of phase noise

Under the assumption that any change to the frequency-sweep rate across the pulse can be neglected, then, the effects of phase noise on the measurement can be considered a first-order effect with constant error associated to each laser shot. A change of center frequency in the probe pulse will be experienced by all positions, so the resultant first-order phase noise is fully spatially correlated.

In this case, a simple yet effective cancellation strategy consists in allocating an unperturbed section of fiber to estimate the phase-noise function, which may then be subtracted from all positions in the fiber. Averaging a long enough length of fiber

ensures that any eventual local strain/temperature noise is reduced, leaving only the phase-noise induced perturbations.

Given a change of the center frequency of the laser ν_r, the induced temporal delay across the whole trace is given by equation 3.54. Cancellation, then, consists in estimating the spatially correlated noise component and subtracting it from all fiber positions.

This may be understood by considering the following strain signal model, where each strain acquisition $x_m(z)$, corresponding to the signal at position z of the fiber acquired at time t_m (slow time-axis, $t_m = m \times 1/f_{acq}$) is modelled as the sum of the measurand amplitude $s_m(z)$ (related to any environmental effects acting on the fiber), and an additive noise term $e_m(z)$.

$$x_m(z) = s_m(z) + e_m(z). \tag{3.57}$$

Notably, the noise term $e_m(z)$ may then be divided in two parts:

$$e_m(z) = e_{m,awgn}(z) + e_{m,laser}, \tag{3.58}$$

where $e_{m,laser}$ is the fully spatially correlated component (onset from the frequency drifts of the laser) which the algorithm intends to estimate and $e_{m,awgn}(z)$ is an additive white Gaussian noise component, intrinsic to the strain estimation process due to the additive noise of the trace (and can be considered fully decorrelated in z and m).

The previously described cancellation method consists in allocating a section of fiber, ideally with $s_m(z) = 0$, by isolating it from environmental perturbations. The estimation of $e_{m,laser}$, then, is done by

$$\langle e_{m,laser} \rangle = \frac{1}{N} \sum_{j=0}^{N} x_m(z_j), \tag{3.59}$$

with z_j representing discrete decorrelated positions of measurement, separated by at least the spatial resolution (thus ensuring uncorrelated measurements), and N is the number of independent windows (sensing points, spaced at least one spatial resolution) that constitutes the compensation section of fiber.

The algorithm then, consists in subtracting the estimated laser noise component from all fiber positions

$$x_{m,comp}(z) = x_m(z) - \langle e_{m,laser} \rangle \tag{3.60}$$

This method has been validated using the same measurement as those in figure 3.22, with the results displayed in figure 3.24.

When opting for such an algorithm to cancel phase noise, it is important to consider the minimum compensation length that should be employed in order to yield an improvement. A careful look at the previous equations reveals that when compensating the noise in this fashion we are also adding a method noise component to

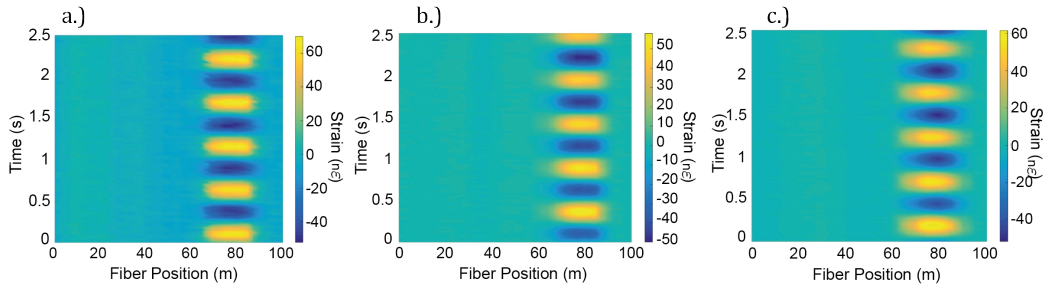

FIGURE 3.24: Position-time measurements after the algorithm. Same measurements as those in figure 3.22. a) 5 MHz linewidth laser; b) 50 kHz linewidth laser; c) 25 kHz linewidth laser. Figures from [136].

all positions (thus, spatially correlated), due to the averaged AWGN component of the channels in the compensating section

$$x_{m,comp}(z) = x_m(z) - e_{m,laser} - \sum_{j=0}^{N} e_{m,awgn}(z_j) \tag{3.61}$$

where $e_{m,comp} = \sum_{j=0}^{N} e_{m,awgn}(z_j)$ yields a new AWGN variable with amplitude $\sigma_{comp} = \frac{\sigma_{awgn}}{\sqrt{N}}$.

The criteria to fulfill in order to ensure improvement, then, is a function of the amplitude of each noise source, and the number of windows that we employ for estimation (*i.e.*, independent sensing positions). In order to guarantee an improvement, the following condition must be ensured

$$N \geq \left\lceil \frac{\sigma_{awgn}^2}{\sigma_{nocomp}^2 + \sigma_{awgn}^2} \right\rceil \tag{3.62}$$

where $\sigma_{nocomp}^2 = (\sigma_{laser}^2 + \sigma_{awgn}^2)$ corresponds to the noise power without any compensation, and σ_{awgn}^2 can be estimated analytically, or verified as the asymptotic value of noise floor floor for an infinite number of compensation windows. For $\sigma_{laser}^2 >> \sigma_{awgn}^2$, a single window ($N = 1$) is enough to ensure a performance improvement. However, for the case of higher quality lasers, this condition becomes increasingly important.

Demonstration of the compensation performance

The performance of the cancellation algorithm and previously mentioned conditions were experimentally verified using lasers with vastly different levels of phase-noise in the two common setups of CP-φOTDR described [143] (direct current modulation, and external modulation methods). For the comparison, both configurations used a 400 MHz chirp bandwidth, with 100 ns pulse width (10 m spatial resolution), at 1 kHz repetition rate, and measured for the total duration of 10 seconds.

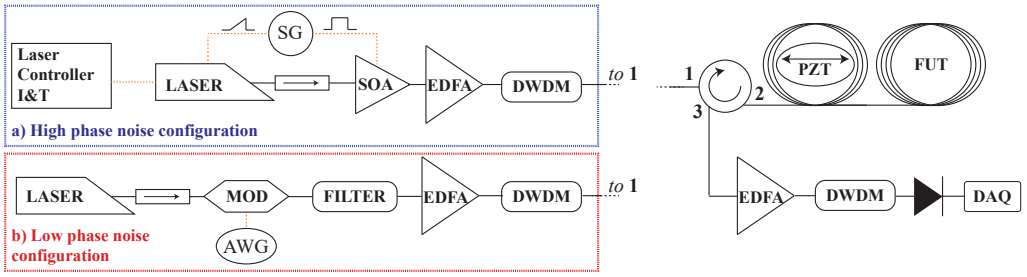

FIGURE 3.25: The two setups for the evaluation of the algorithm performance in lasers with different levels of phase-noise. a) High phase-noise configuration; b) Low phase-noise configuration. FILTER - Tunable filter, MOD - Electrooptical modulator, AWG - Arbitrary waveform generator, DAQ - Oscilloscope, DWDM - Dense Wavelength Division Multiplexer. Taken from [143].

The high phase-noise configuration (figure 3.25 a)) is a direct current modulation setup with an external cavity modulation. An high extinction ratio SOA is used to time-gate the pulse with a rect waveform. A DWDM was used as an ASE filter after the amplification stage. Before any compensation, this configuration yielded a noise floor of $3.442 \times 10^{-10} \varepsilon / \sqrt{Hz}$, which is mostly due to the laser phase noise.

The low phase-noise configuration (figure 3.25 b)) uses an external modulation setup. An ultra low-phase noise laser is used, which is sent through an electro-optic modulator, which was controlled by an arbitrary waveform generator and a bias controller working in suppressed carrier mode. A tunable filter was then used to extract only the upper sideband, rejecting the lower sideband and the remnant carrier. In this case, the noise floor prior to any compensation was of $4.282 \times 10^{-11} \varepsilon / \sqrt{Hz}$.

In both cases, the detection arm consists of an amplification stage (EDFA) followed by a DWDM to reduce ASE noise and a 1.5 GHz photodetector. In both previous cases, the noise floor was estimated as the average noise floor in the first 5 km of fiber (consisting of 500 independent measurement windows of 10 m). The compensation section chosen began at meter 500, with a length of $N \times 10$ m, N being the number of windows chosen for compensation.

The measurement section of fiber consisted of a fiber section coiled around a piezoelectric transducer, of length of 60 m, followed by a stable fiber spool of 26 km in a water bath, isolated from mechanical perturbations. A perturbation of 78.65 $n\varepsilon$ was applied to the PZT section for calibration of the system sensitivity. The long spool in the stable environment ensured a large enough number of windows for the compensation.

The resulting effects of compensation with an increasing number of windows for both setups are displayed in figure 3.26, for the high phase-noise case in a) and the low phase-noise case in b). Notably, the high phase-noise case benefits immediately,

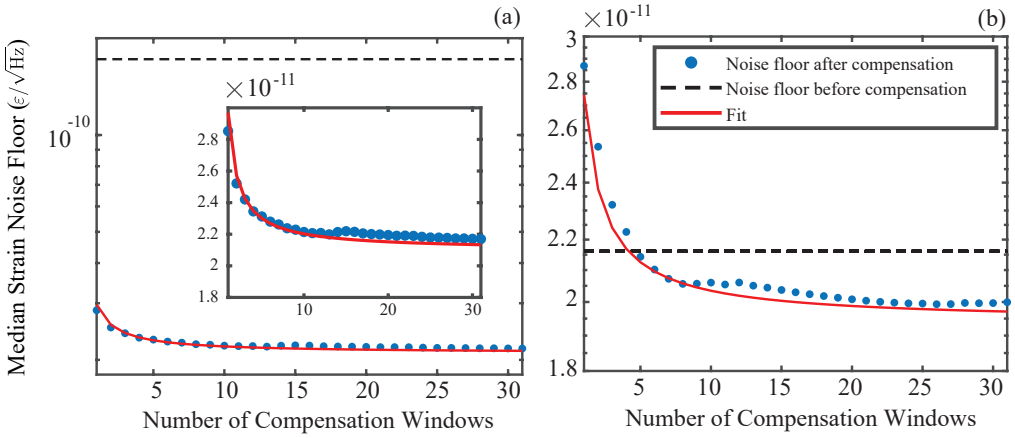

FIGURE 3.26: Comparison of the performance of the compensation algorithm in high phase-noise and low phase-noise lasers/setups. a) the high phase-noise setup and b) the low-phase noise setup. In the low-phase noise setup, compensation only yields an improvement after 5 windows. Nonetheless, the performances are extremely similar for both lasers after compensation, evidencing the potential of the compensation algorithm. Taken from [143].

even with compensation from a single window. In the case of the low-phase noise setup, 5 windows are required to ensure an improvement.

Even with an insufficient number of windows for compensation, the maximum increase in noise floor is of only a factor of $\sqrt{2}$ over the asymptotic noise floor. Both cases have reached similar asymptotic noise floors, of $3.86 \times 10^{-11}\varepsilon/\sqrt{Hz}$ in the low phase-noise case, and $4.15 \times 10^{-11}\varepsilon/\sqrt{Hz}$ for the high-phase noise. These small differences can be attributed mostly to differences to the laser power from each source. Most notably, the cancellation algorithm is effective enough to lead to similar performances from both high- and low-phase noise lasers, despite the vast differences in cost. Nonetheless, in scenarios where having stable section of fiber is not attainable, a low-phase noise laser may be well justified.

Chapter 4

Limits of Performance of CP-φOTDR

4.1 Noise-floor lower bound of CP-φOTDR

The CP-φOTDR technique converts the process of measurement into a local time-delay estimation (TDE). While this change is at the root of many of the technique's advantages, a new estimation process suggests new trade-offs and performance impacts instigated from signal or noise properties which must be studied and characterized. We previously presented an in-depth analysis of the effects of laser phase-noise in CP-φOTDR measurements, and reported on a strategy to fully compensate phase-noise effects to the first order (section 3.4.7). In the following pages, we shall continue the discussion of noise effects on CP-φOTDR measurements, by describing the effects of additive noise (and other trace signal properties) on the performance limits of a time-delay based estimation process.

The minimum possible error variance of a noisy, unbiased estimation is limited by the Cramér-Rao Lower Bound (CRLB) of the estimation process. The fundamental limits of time-delay estimation, in particular, have been widely studied in the context of radar and sonar [157, 158, 167, 168], and the CRLB for TDE has been established as a function of signal SNR, bandwidth and estimation time-window. The first goal of this section is to build upon this body of knowledge to determine a CRLB for the signals expected from a CP-φOTDR. Afterwards, we experimentally attempt to reach CRLB-limited levels of performance in the measurement of dynamic strains. In doing so, we demonstrate that after phase-noise/jitter is adequately corrected [136, 143], the main hurdle at reaching the performance lower bound is onset from sampling error, which may be easily addressed through Whittaker-Shannon (sinc) interpolation without the introduction of bias [169]. After mitigating sampling error and phase-noise sources we experimentally achieve CRLB-limited levels of performance for the system, demonstrating a measurement with robust performances over the whole interrogated length (10 km) with $\sim p\varepsilon/\sqrt{\text{Hz}}$ dynamic strain sensitivity in the acoustic range (> 100 Hz).

At the time of publication of the research presented in this section (see references [139, 140]), the best reported performances consisted of wavelength-scanning

methods [170] which reached dynamic strain noise floors of $\sim 100 \times 10^{-12}\varepsilon/\sqrt{\text{Hz}}$, in 500 meters of fiber at 2 kHz sampling rate acquisition (with 5 meter spatial resolution), or on quasi-distributed approaches relying on phase-detection setups and fibers inscribed with ultra-weak gratings [171], reaching $p\varepsilon/\sqrt{\text{Hz}}$. The results reported here achieved record strain sensitivities with conventional fibers and a simple direct detection setup, improving performances by roughly 2 orders of magnitude when compared to contemporary, fully distributed, standard fiber techniques. Since then, other methods have achieved similar, or slightly improved performances [117, 135].

4.1.1 Noise model of time-delay estimation measurements

The backscattering from each successive m-th φOTDR probe launched into the FUT produces an optical trace $x_m(t)$, which is a noise-like intensity time-series representative of the fiber physical state at the instant of the m-th probe launch.

To estimate the measurand amplitude at a specified position, local trace features of each measurement trace $x_m(t)$ are compared to a previously acquired reference trace $x_r(t)$. Conventionally, this reference is taken as the first launched probe, $m = 0$, such that

$$x_r(t) = x_0(t), \tag{4.1}$$

where t corresponds to the fast-axis of time and is related to an individual measurement point at position $z = ct/2n_g$, for speed of light c and refractive index n_g (see 3.3).

In the case of a CP-φOTDR measurement, when the interrogated fiber is stressed, local features of $x_m(t)$ undergo an apparent delay relative to $x_r(t)$, proportional to the amplitude of the applied perturbation. Therefore, the simple case of a perturbation (*e.g.*, strain) acting homogeneously across the whole fiber at the m-th instant may be modelled as

$$x_m(t) = s(t - D_m) + n_m(t);\ D_0 = 0, \tag{4.2}$$

$$x_r(t) = s(t) + n_0(t), \tag{4.3}$$

where $s(t)$ and $n_m(t)$ are the signal and noise components (considering an additive white gaussian noise model - AWGN) of the acquired optical trace, and D_m corresponds to the perturbation-induced delay to the signal features of x_m.

The strain information may then be obtained via an estimate of the delay D_m, $\widehat{D}_m$, which can computed using the GCC algorithm (section 3.4.4), *i.e,* by finding the lag at which there is a maximum of the cross-covariance between $x_m(t)$ and $x_r(t)$ (cross-correlation for zero-mean signals, which we shall assume for simplicity). The estimation of strain-induced time-delay at the trace section bounded between times $t = [T_1, T_2]$ may then be written as

$$\begin{aligned} R_{m,r}(\tau) &= \int_{T_1}^{T_2} x_m(t) x_r(t+\tau) dt \\ &= R_{s,s} * \delta(t - D_m) + R_{s,n_m} + R_{s,n_r} + R_{n_m,n_r}, \end{aligned} \tag{4.4}$$

$$\widehat{D}_m = \text{argmax}\{R_{m,r}(\tau)\}, \tag{4.5}$$

where $R_{m,r}(\tau)$ represents the cross-correlation between the measurement trace and reference, τ is the lag, $\delta(t)$ is the Dirac delta function, and the terms $R_{s,s}$ / R_{s,n_m} / R_{s,n_r} / R_{n_m,n_r} define the autocorrelation of the signal term, the signal-noise correlation terms and the noise-noise correlation term. The time width of the section defined for the cross-correlation ($T = T_2 - T_1$) defines the gauge length of the system, which in optimal operation is set as equal to the pulse width ($T = \tau_p$, see section 3.4.5).

To produce a valid estimate from the GCC algorithm, some conditions must be fulfilled: a minimum correlation length is required with respect to the signal bandwidth [160] (*i.e.*, the time-bandwidth product of the optical trace section has to be sufficiently high, $T >> 1/B$, B being the signal bandwidth), the SNR should not be very low and the reference and measurement signals should be highly correlated. These three conditions are generally fulfilled in conventional CP-φOTDR operation, since a large time-bandwidth product is a pre-requirement for frequency-to-time mapping (see section 3.4.1), Rayleigh-based methods can ensure good measurement SNR for tens of kilometers, and the reference-measurement trace pairs remain correlated over much longer periods than that of the perturbations of interest (in the acoustic regime), assuming no extrinsic sources of decorrelation.

Derivation of the lower bound

The TDE estimation error from cross-correlation is quantified by the mean square error between the estimate and the true value of delay as

$$\sigma^2_{MSE} = \langle (\widehat{D_m} - D_m)^2 \rangle, \tag{4.6}$$

where the $\langle \cdot \rangle$ operator, in this case, represents the expected value. Assuming a well-conditioned signal for cross-correlation based TDE (yielding a negligible probability of anomalous estimation [141, 160, 172]), the mean-square-error lower bound for each estimation is given by the CRLB, which quantifies the best achievable performance ($\sigma^2_{MSE} \geq \sigma^2_{CRLB}$) when employing a minimum variance unbiased estimator [157, 159, 168].

The TDE lower bound for a bandlimited active system (in conditions of low and high SNR) can be derived by following the procedures in [168], by identifying what is the equivalent case to a CP-φOTDR system. By assuming high SNR and negligible decorrelation, the correlation term of both noises in equation 4.4 (R_{n_m,n_r}) may be neglected. The resulting noise, then, originates from the two signal-noise correlation terms, one corresponding to a correlation between signal and reference noise

(R_{s,n_r}), and the other with signal and measurement noise (R_{s,n_m}). While both the reference and measurement acquisitions are noisy (similar to the passive radar case), one of the noise contributions remains unchanged for all acquisitions as the reference is kept constant. As such, the R_{s,n_r} term does not add to the noise variance over a strain time-series acquisition, manifesting instead as a systematic error in measurement (which is typically irrelevant when dealing with dynamic perturbations). Neglecting this systematic error, the CP-φOTDR behaves analogously to an active radar detection system, without reference noise.

In this case, according to [168], the minimum variance of a delay estimation at a selected measurement window (of time width T) can be determined as

$$\sigma^2_{CRLB} = \frac{1}{d^2 B^2_{RMS}}, \tag{4.7}$$

where $d^2 = 2E/N_0$, E being the signal energy, $N_0/2$ being the noise spectral density (assuming two-sided AWGN of constant power across the whole signal band) and B_{RMS} being the root-mean-square (RMS) signal bandwidth, determined as

$$B^2_{RMS} = \frac{\int_{-\infty}^{+\infty} \omega^2 S(\omega) d\omega}{\int_{-\infty}^{+\infty} S(\omega) d\omega}. \tag{4.8}$$

for a two-sided autospectrum with bandlimited signal spectral power $S(\omega)$. As we described in section 3.4.1, the frequency-to-time mapping matches the envelope of the time and frequency domain of the pulse representation. A square pulse, then, after square-law detection, yields a Rayleigh backscattered spectrum with an approximately triangle shape across the baseband. We can then approximate the two-sided signal spectral power envelope as $S(f) = \frac{S_0}{2}\left(1 - \frac{f}{B}\right)$ in the range $[-B, B]$, and 0 outside of the bandwidth B, such that

$$B^2_{RMS} = \frac{2(2\pi)^2 \int_0^B f^2 \left(1 - \frac{f}{B}\right) df}{2 \int_0^B f^2 \left(1 - \frac{f}{B}\right) df} = \frac{(2\pi)^2 B^2}{6}. \tag{4.9}$$

The lower bound condition specified in equation 4.7, then, becomes

$$\sigma^2_{CRLB} = \frac{6N_0}{2E(2\pi)^2 B^2}. \tag{4.10}$$

Notice now that the signal energy over a window of time T is given by $E = ST$, for signal power S, and that the total white noise power is given by $N = N_0 B$. With the appropriate substitutions we can re-write the previous equation as a function of SNR, bandwidth B and estimation time-window length T as

$$\sigma^2_{CRLB} = \frac{3}{4\pi^2} \frac{1}{T} \frac{1}{\text{SNR}} \frac{1}{B^3}, \tag{4.11}$$

where $\text{SNR} = S/N$.

Equation 4.11 describes a mean-square-error lower bound for TDE of any signal with the typical properties of a CP-φOTDR, independent of its physical origin. B corresponds to the bandwidth of the acquired trace and T is the time-window selected for the estimation of time-delay. To estimate the effects of this error on the performance of strain measurements, we need to account for the system sensitivity as well. The strain per perceived trace delay in a standard fiber is given by

$$d\varepsilon/dt = \frac{B_c}{(-0.78)\tau_p \nu_0}, \tag{4.12}$$

where ν_0 is the center frequency of the employed laser, τ_p is the pulse width, and B_c is the chirped probe pulse bandwidth. We may then describe a lower bound for strain measurement as

$$\sigma^2_{CRLB\varepsilon} = \sigma^2_{CRLB}(d\varepsilon/dt)^2 = \frac{3}{(2\times 0.78\pi)^2\nu_0^2}\frac{1}{\mathrm{SNR}}\frac{B_c^2}{B^3}\frac{1}{T\tau_p^2}. \tag{4.13}$$

Typical operation of CP-φOTDR has $B = B_c$, and a time-window for cross-correlation selected to optimize spatial resolution ($T = \tau_p$). In this case, the CRLB for the system simplifies to

$$\sigma^2_{CRLB\varepsilon} = \sigma^2_{CRLB}(d\varepsilon/dt)^2 = \frac{3}{(2\times 0.78\pi)^2\nu_0^2}\frac{1}{\mathrm{SNR}}\frac{1}{B_c}\frac{1}{\tau_p^3}. \tag{4.14}$$

This equation fully describes the lower bound for the variance of the strain estimation as a function of the probe properties B_c and τ_p, and the specified trace section's SNR, or alternatively, the total noise power introduced from the estimation process. This manifests as a perfectly white noise floor, being the result of uncorrelated errors on each successive delay estimation of the same variance. Being perfectly white, the noise power is spread over the whole acquired bandwidth, so for a given acoustic detection bandwidth $f_{acq}/2$ (determined by the probe laser repetition rate) the lower bond for TDE of dynamic strain measurements manifests as a noise floor at $\mathrm{NF}_\varepsilon = \sigma_{CRLB\varepsilon}/\sqrt{f_{acq}/2}\ \varepsilon/\sqrt{\mathrm{Hz}}$, where f_{acq} is the probe laser repetition rate.

Reaching the lower bound

The CRLB-imposed noise floor determines the best achievable dynamic sensitivity of a CP-φOTDR system when only additive noise sources are accounted for. To reach it, then, it is important to ensure that the effect from other sources of noise is comparatively negligible. Two notable sources of error that impede the achievement of CRLB-limited levels of performance are laser phase-noise and sampling error.

Phase-noise and jitter apply a time delay applied to the whole fiber. After measurand estimation, this reflects as a fully spatially correlated noise over the whole interrogated fiber length (section 3.4.7). The perfect spatial correlation of these noise sources enables their cancellation to the first order [136, 143], by allocating a fiber section to its estimation.

The other source, sampling error, results from the discrete-time acquisition of the optical traces. Even in infinite SNR conditions, an error of half the sampling period remains when estimating time-delay. Sub-sample accuracy may be readily achieved through interpolation of the signal, although some care must be taken to not introduce bias in order to produce a pertinent comparison to the theoretical lower bound (and avoid non-linearities in measurement). While the GCC algorithm itself is unbiased, conventional curve-fitting methods such as a parabolic fit of the three points surrounding the main correlation peak [159] introduce a heavy bias in estimation, despite their simplicity and ease of computation. Alternatively, assuming adequate sampling, bandlimited signals may be reconstructed at an arbitrarily higher sampling rate through Whittaker-Shannon (sinc) interpolation (resulting directly from the Nyquist sampling theorem). In practice, this may be easily achieved through zero-padding in the frequency domain [173, 174]. In the case of periodic or infinite signals, this method is regarded as perfect in reconstructing infinite or periodic discrete signals at higher sampling rates. Aperiodic or finite signals, however, may experience some artifacts in the form of time-domain "ringing" from the Gibbs phenomenon [175, 176], although these can easily be made negligible by reconstructing a sufficiently long acquisition.

4.1.2 Numerical assessment of the lower bound

In order to assert the validity of the previous analysis and the derived lower bound in equation 4.14, we performed a series of numerical simulations of CP-φOTDR traces while carefully controlling each relevant performance parameter. The fiber was simulated as an array of equally spaced (1 cm) elements, each characterized by a refractive index (homogeneous throughout the fiber), a random (Gaussian distributed) reflectivity and a uniformly distributed random phase. Each simulation represented a 400 m long section of fiber, sampled at 10 GS/s with an applied 1 kHz perturbation the refractive index (equivalent to a 1 nε amplitude perturbation in optical path [82]).

The virtual fiber was sampled at 10 kHz for a total integration time of 0.05 s (500 acquisitions). Each of the retrieved signals was then corrupted with additive spectrally flat Gaussian noise across the signal bandwidth, with variable power in order to yield the desired SNR of each experiment, and no phase-noise was considered for the simulation. The sampling error was mitigated by reconstructing each cross-correlation at 1000 times higher sampling via sinc interpolation.

The simulation was repeated for different pulse widths/correlation windows (50 ns, 100 ns, 200 ns, 400 ns), chirp bandwidths (0.5 GHz, 1 GHz, 2 GHz, 4 GHz) and trace SNR (10 dB, 15 dB, 20 dB, 25 dB). These parameters were chosen in order to represent realistic operation scenarios, while ensuring that the system remains well within the appropriate conditions for cross-correlation-based estimation to reach minimum variance, avoiding anomalous estimations [141, 160, 172].

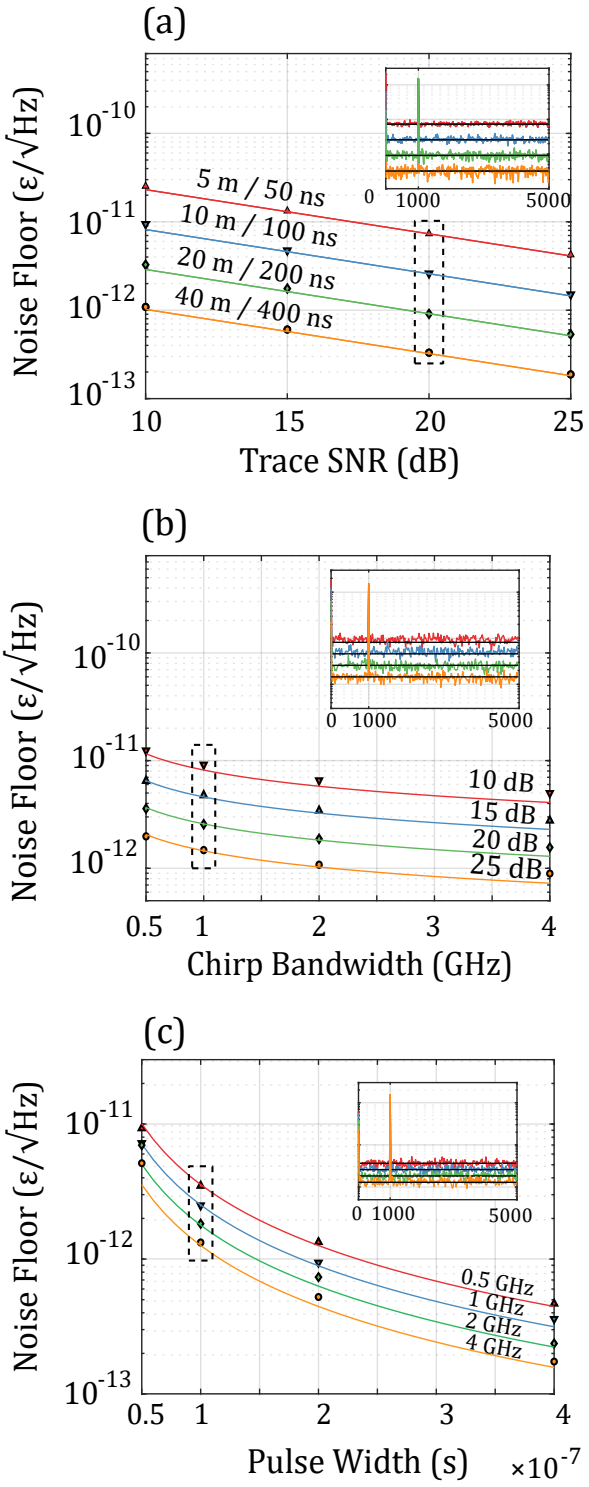

FIGURE 4.1: Noise floors of simulated data and the theoretical estimation of the CRLB for different probe parameters. The inset figures represent the one-sided strain amplitude spectral densities used to measure the noise floor, of the simulations corresponding to the boxed data points.
a.) Varying window sizes and trace SNR, for a fixed chirp bandwidth of 1 GHz; b.) Varying trace SNR and chirp bandwidth, for a fixed pulse width of 100 ns; c.) Varying chirp bandwidths and correlation window sizes, for a fixed SNR of 20 dB.

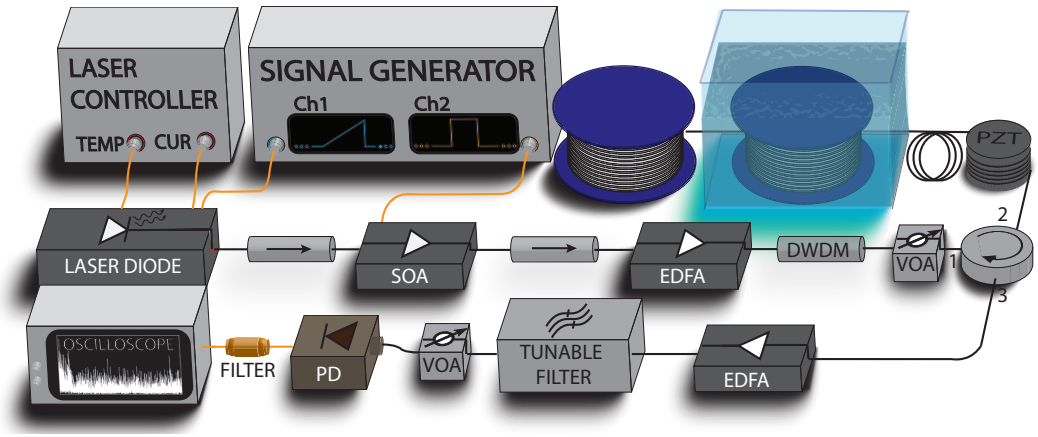

FIGURE 4.2: Experimental setup, as described in the main text. PD - Photodetector, VOA - Variable optical attenuator, FILTER - 1 GHz RF low pass filter. Other acronyms in the text.

Figures 4.1 a.), b.) and c.) depict the results of the simulation, comparing the numerically obtained noise floors to the calculated lower bound estimated from equation 4.14. All acquisitions show remarkable agreement with the expected lower bound. The effects of poor signal conditioning are slightly noticeable at the lower SNRs, when the measured values start to slightly underperform the predicted CRLB. While some tighter bounds have been proposed which have less strict requirements on the signal conditioning (such as the Barankin or Ziv-Zakai bounds [177]), we found the CRLB to be a sufficiently comprehensive lower bound without too much needless complexity, since the typical operation of chirped-pulse measurement itself uses well-conditioned signals.

As an important side-note, it is important to realize that the relevant parameters for the determination of the lower bound are generally not independent in practice. A longer probe pulse entails more signal energy and better SNR, while an increased bandwidth allows more noise components in the system, implying a worse SNR. In the simulations, however, all parameters were controlled independently.

4.1.3 Experimental demonstration of lower bound

The ability to experimentally reach the proposed lower bound was tested using a CP-φOTDR design like the one described by Pastor-Graells et al. [133], with a direct current modulation emission arm (see section 3.4.3). The employed setup is depicted in figure 4.2.

An external cavity semiconductor laser (RIO) emits with center wavelength 1550.2, controlled in temperature and current by an ILX Lightwave LDC-3724 laser diode controller. The laser output frequency is swept by directly modulating the laser current, through an Agilent 81150A signal generator channel outputting a sawtooth wave, which is then time-gated as 100 ns pulses via a SOA controlled by

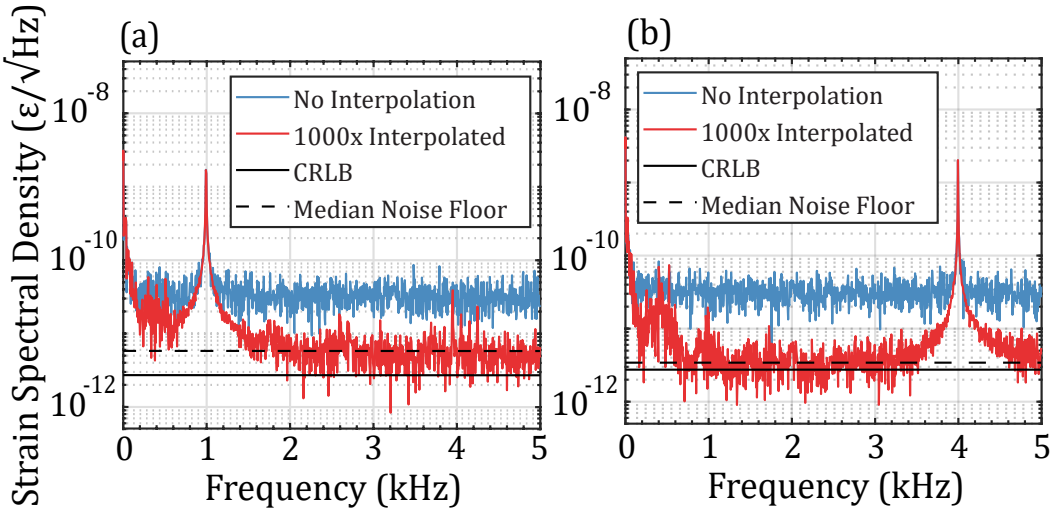

FIGURE 4.3: One-sided strain amplitude spectral densities of a 0.2 second acquisition in the PZT region.
a.) 1 kHz applied perturbation, estimated trace SNR = 19.47 dB, CRLB calculated at $2.715 \times 10^{-12}\varepsilon/\sqrt{\text{Hz}}$ and median noise floor estimated at $5.178 \times 10^{-12}\varepsilon/\sqrt{\text{Hz}}$;
b.) 4 kHz applied perturbation, estimated trace SNR = 19.38 dB, CRLB calculated at $2.744 \times 10^{-12}\varepsilon/\sqrt{\text{Hz}}$ and median noise floor estimated at $3.421 \times 10^{-12}\varepsilon/\sqrt{\text{Hz}}$;

another channel of the same signal generator, at the same frequency of the sawtooth wave. The work point (current/temperature) driving the laser was carefully selected in order to produce a linear chirp from the external current modulation, without jumps or non-linearities, with 1 GHz total chirp bandwidth. The resulting pulse is amplified through an EDFA and filtered with a DWDM to mitigate some of the introduced ASE noise, and controlled in peak power in order to prevent the onset of modulation instability.

The fiber under test (FUT) consisted of a first 200 meter-long section, with 20 m tightly wrapped around a cylindrical piezoelectric actuator, followed by a 1 km spool for phase-noise compensation, kept in a stable water bath in order to mitigate temperature drifts or residual strains. This spool is connected to a $\sim$ 8.7 km spool for a total interrogation length of $\sim$ 10 km.

The recovered backscattered light is guided to the detection arm, where it is once again amplified by an EDFA and filtered to mitigate the ASE. The detection is done using a 9.5 GHz PDA8GS Thorlabs photodetector, and electrically filtered with an analog 900 MHz low-pass filter, before digitizing. Each measurement consisted of a 0.2 second acquisition at 10 kHz repetition rate, with an applied 300 mV amplitude amplitude to the piezoelectric at frequencies between 1 and 4 kHz, corresponding to approximately 10 nε perturbation amplitude.

The TDE for measurand estimation was achieved through the GCC algorithm

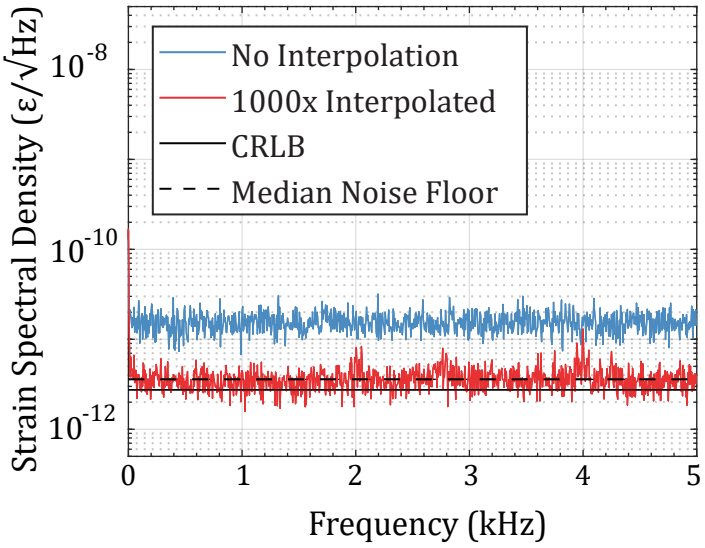

FIGURE 4.4: One-sided strain amplitude spectral densities of a 0.2 second acquisition in the thermally stable section of fiber. Estimated optical SNR = 19.62, CRLB calculated at $2.668 \times 10^{-12}\varepsilon/\sqrt{\text{Hz}}$ and median noise floor estimated at $3.590 \times 10^{-12}\varepsilon/\sqrt{\text{Hz}}$. The PSDs were taken over 25 m and averaged in order to narrow the spectral variations and improve visibility of the noise floor.

which we introduced earlier. In order to remove sampling error without the introduction of bias, each cross-correlation was reconstructed at 1000 times higher sampling. The laser phase-noise and instrument jitter were then cancelled using the same method specified in section 3.4.7, using a section of the stabilized 1 km spool for compensation.

The results are presented in figures 4.3, for applied perturbations of 1 kHz and 4 kHz. Notably, there is no effect on the amplitude of the interpolated and non-interpolated frequency components, attesting to the negligible bias introduced from the proposed method. The estimated lower bound is presented as a solid black line, calculated with an estimated SNR obtained at the section of measurement (with no applied perturbation), and compared to the actual verified median noise floor (represented as a dashed black line). The obtained results fall very close the established CRLB, within less than a factor of 2. The observed differences may appear due to environmental noise, spectral leakage or error in the estimation of SNR. When measuring the noise-floor in the stabilized section of fiber a noise floor of $3.590 \times 10^{-12}\varepsilon/\sqrt{\text{Hz}}$ was observed for a calculated lower bound of $2.668 \times 10^{-12}\varepsilon/\sqrt{\text{Hz}}$, for an estimated SNR of 19.62 dB. The small discrepancies might also originate from error in the estimation of the signal parameters (bandwidth and optical SNR), and statistical variations of the correlation window quality over time, owing to the stochastic nature of the signal [134].

4.1.4 Discussion of results

Here, we have formally described the impact of additive noise sources on estimation in CP-φOTDR, and derived the lower bound for dynamic sensitivity of such a system, imposed from the effect of signal properties on the time-delay estimation process. The validity of the signal model used to derive the lower bound was then demonstrated by comparison to measurements using simulated CP-φOTDR signals, showing very good agreement to the estimated lower bound.

We then proposed a method to experimentally reach CRLB-limited levels of dynamic sensitivity. In summary, we postulated that by selecting probe parameters that ensure good signal conditions for cross-correlation, reducing the sampling error from the time-delay estimation without the introduction of bias, and cancelling the phase-noise to the first order, the main limitation of performance should be given by the fundamental limits of noisy TDE. This performance limit was shown to be readily achievable in the acoustic frequency range (> 100 Hz), highlighting the high performances achievable with the CP-φOTDR technique. Experimentally, $p\varepsilon/\sqrt{\text{Hz}}$ dynamic strain sensitivities in the acoustic frequency range were demonstrated over 10 km of interrogated length.

The obtained performance values may now be compared to other known limits of optical fiber sensing. The ultimate lower-bound of dynamic sensitivity arises from local thermodynamic fluctuations which randomly affect the optical path of light. While some highly specialized point-sensors claim to have reached this "thermodynamic limit" [178, 179], such performances remain elusive to distributed techniques. Specifically, an interferometer with cavity length equal to the employed spatial resolution for the measurements presented in this section (10 m) would theoretically reach approximately three orders of magnitude better performances, if limited only by thermodynamic noise [179].

Having a formally defined CRLB explicitly defines how each probe parameter may affect measurement performance, and confirms that current CP-φOTDR measurements are fundamentally limited by the additive noise sources in the trace, motivating research in new ways to improve the trace SNR, such as special fibers [42] or pulse compression methods [106]. A close look at the dependency of the derived lower bound also highlight the major impact that pulse length and spatial resolution have on performance, due to its effect on sensitivity, TDE performance and SNR. While most leading applications of the technology (*e.g.*, seismology [36]), can afford worsening the resolution at the expense of major gains in performance, this notion heightens the perception of the trade-offs between spatial resolution and measurement accuracy, characteristic of φOTDR methods.

4.2 Upper-limit of measurable strain

One of the hallmarks of φOTDR techniques is the relative nature of the produced measurements, requiring each estimation of measurand to be obtained from a comparison of the "measurement" fiber state to a previously acquired "reference" state. However, there are limits to the maximum measurable difference between two states which vary in origin depending on the chosen interrogation method.

Coherent detection methods, for instance, are unable to overcome π phase shifts without phase unwrapping [130], and standard frequency sweep measurements are limited to the total range of frequencies covered by the sweep. Similarly, as we demonstrate in this section, each CP-φOTDR estimation is fundamentally limited to perturbations that can be compensated by a frequency shift much smaller than the total chirp bandwidth.

The measurement upper bound of CP-φOTDR exists due to the non-negligible decorrelation between traces occurring from large perturbations, which greatly amplifies the probability of anomalous estimations of local time-delay, and consequently outliers in measurement [139, 141, 160, 172]. In the following pages, we observe the effect of these limitations and propose some simple alterations to the post-processing which enable these limits to be exceeded.

The proposed method consists in updating the reference trace after every laser shot, thus executing a measurement of differential strain as opposed to a direct strain measurement relative to a fixed reference. We show that, in this way, it is possible to exploit the oversampling in the acoustic signal to greatly mitigate the appearance of outliers on the acquisition, by reducing the maximum shot-to-shot strain. Moreover, the statistical nature of outliers allows this oversampling to be further employed through an additional post-processing median filtering method, completely removing the sporadic anomalies in estimation.

The proposed method is demonstrated experimentally by measuring a 50 Hz perturbation with an amplitude greater than 1000 $\mu\varepsilon$, with high harmonic rejection [141, 142] and high SNR. We conclude this section with a discussion on the implications of a differential strain measurement in terms trade-offs and performance limits, when compared to the conventional fixed-reference approach.

4.2.1 Overcoming the upper bound

The previous descriptions of CP-φOTDR presented in this thesis were concentrated on low amplitude perturbations over short measurement times. In these conditions, trace decorrelation can be considered negligible and the first trace of each acquisition serves as a high quality reference for all future measurements. This is no longer the case when working with large perturbations, as the induced delay over a section of fiber induces non-negligible trace decorrelation with respect to the initial reference.

When referring to decorrelation in the context of CP-φOTDR technique, we refer to the change in correlation coefficient between reference and a delayed version

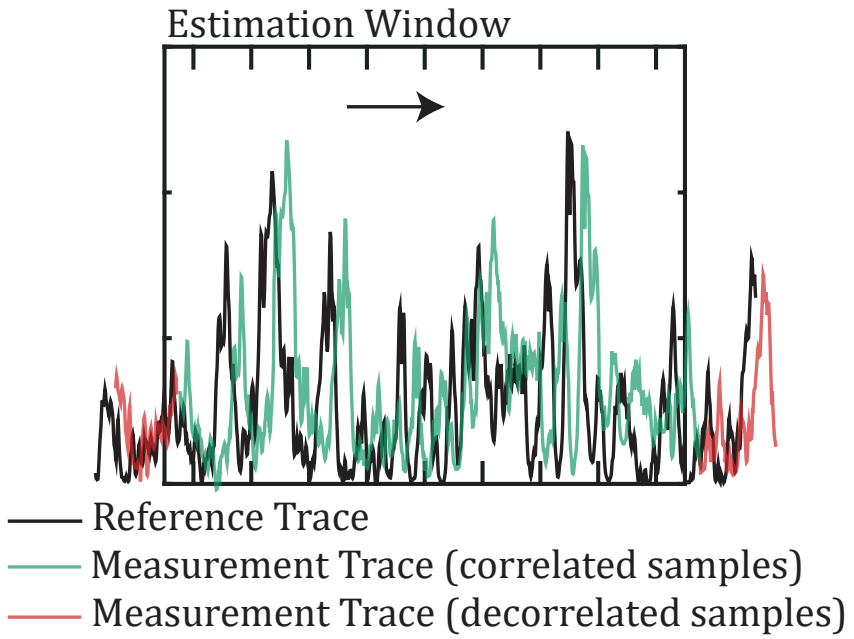

FIGURE 4.5: Depiction of the mechanisms of trace decorrelation from large measurements. Notice that the delayed version of the trace has some of its features slightly deformed (on top of the actual delay). Similarly, after the delay, some correlated (green) samples fall outside of the estimation window, while some decorrelated (red) samples move inside.

of the measurement trace. This decorrelation results from the combination of two different effects. The first one consists of the change in shape of the delayed trace following a perturbation. Notice that each chirped-pulse measurement technique is ultimately limited by the total interrogated frequency range covered by chirp (of a few hundred MHz to a few GHz, corresponding to an equivalent strain of a few $\mu\varepsilon$ at 1550 nm, as defined in equation 3.44). Additionally, in order to exploit the frequency-to-time mapping and retrieve a delayed trace, a time-shifted probe pulse must be highly correlated to itself after a frequency shift (equivalent to the induced perturbation). For this to occur, the frequency shift must be much smaller than the total chirp bandwidth. As the time-shift grows, the trace also experiences slight deformations in shape. The second contribution to the total decorrelation has to do with having an apparent delay at a fixed estimation position. Essentially, the perturbation-induced apparent delay moves some correlated samples out of the estimation window, and introduces new uncorrelated signal samples into the estimation window (by shifting samples from outside the measurement window to the inside). Both of these effects are evidenced in figure 4.5.

Decorrelation has a direct effect in the quality of estimates obtained via the GCC algorithm (or any other similarity-based TDE method). When attempting to estimate a time-delay between poorly conditioned or partially decorrelated traces, the

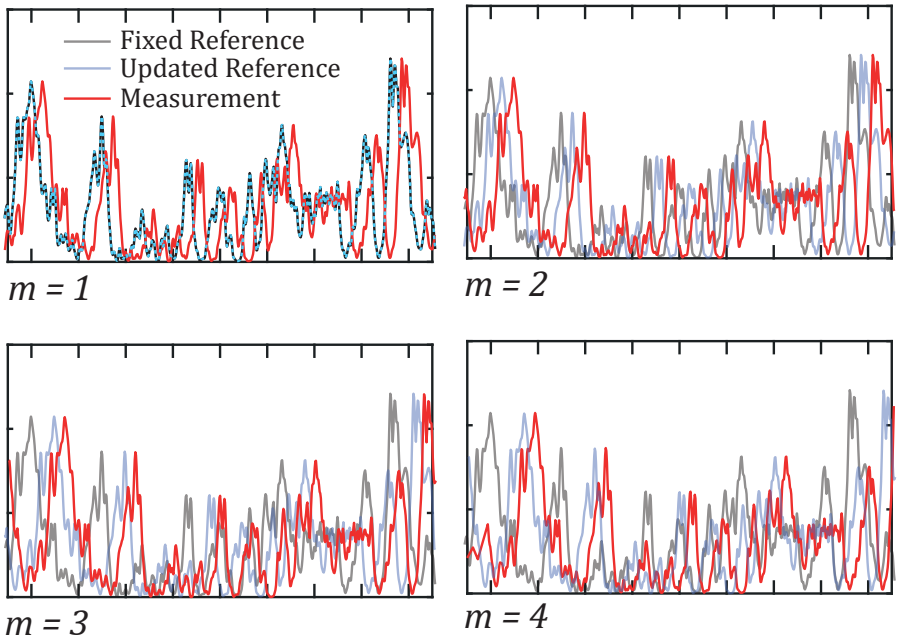

FIGURE 4.6: Comparison of a fixed reference approach and an updated reference approach. Fixed reference is depicted in grey, updated reference is depicted in blue and measurement trace in red. By changing the last measured trace to the new reference, the similarity between measurement and reference traces is kept high.

increased signal decorrelation attenuates the main peak of cross-correlation. If any secondary peak ends up prevailing over the main correlation peak, the result is an anomalous estimation which produces an *outlier* in the acquisition. In practice, the probability of outliers is also a function of the applied perturbation relative to the initial state of the fiber, and the trace signal properties (bandwidth, time and SNR), comprising a soft upper bound on the maximum measurable strain.

Since this limitation is tied to the decorrelation between measurement and reference trace, it may be addressed by updating the reference at every shot, thus minimizing the total difference in state between the reference and measurement acquisitions. In this case, the problem explained in section 4.1.1 (equation 4.3) may be re-defined as

$$x_m(t) = s(t - D_m) + n_m(t); \tag{4.15}$$

$$x_r(t) = x_{(m-1)}(t), \tag{4.16}$$

where the index m relates to the current measurement trace, corresponding to the m-th sample of the strain acquisition (of the slow time axis, such that $t_m = m/f_{acq}$, $m \in \mathbb{N}$). The reference (r-th) trace is updated at every measurement, instead of comprising a fixed reference. A comparison between both methods is depicted in figure 4.6 .

Each delay estimate, $\widehat{D_m}$, will then be proportional to the strain increment $\Delta\varepsilon_m$

$$\Delta\varepsilon_m \propto \widehat{D_m} = \arg\max\{R_{m,(m-1)}(\tau)\}, \tag{4.17}$$

which may then be converted to strain as

$$\varepsilon_m = \sum_{j=1}^{m} \Delta\varepsilon_j. \tag{4.18}$$

Clearly, with this alteration to the processing, the upper bound of measurable strain applies to the incremental strain instead. As such, there is no intrinsic limit to the absolute amount of strain measured, so long as the shot-to-shot strain falls within acceptable bounds. Nonetheless, the onset of anomalies in estimation is still statistically driven, given the noisy and stochastic nature of the trace signal. Empirically, it was estimated that the shot-to-shot strain should be kept below 3% - 5% of the total chirp bandwidth (equivalent frequency shift), for a well-conditioned signal, in order to produce an acceptably low probability of outliers [133]

$$|\Delta\varepsilon_m| \leq \alpha \cdot \frac{\delta\nu}{0.78\nu}; \;\; \alpha \sim 0.03 \tag{4.19}$$

for a chirp bandwidth $\delta\nu$ and laser center frequency ν.

Notably, by changing the limitation to a shot-to-shot limit, higher strain rates may be measured by oversampling the perturbation (above the Nyquist criterion). This implies a trade-off between maximum measurable perturbation slew rate and maximum length of interrogated fiber when using this process, since the maximum acquisition frequency is $f_{acq,max} = \frac{2c}{Ln_g}$.

An example of an outlier in cross-correlation is depicted in figure 4.7. The figure represents the result of cross-correlating a perturbed section of successive traces using the aforementioned method (50 Hz strain perturbation of 750 $\mu\varepsilon$). The correlation between traces $r = 1$ and $m = 2$ (top) and the one between traces $r = 3$ and $m = 4$ (bottom) show a clear unambiguous peak for the estimation of time delay. Conversely, the cross correlation between traces $r = 2$ and $m = 3$ (middle) has a noise-like appearance with no discernible main peak, producing an outlier in estimation [160, 172].

The aforementioned process focuses on reducing the likelihood of such anomalous estimations in the cross-correlation, by reducing the maximum differences in state between measurement and reference. However, due to their statistical nature, it is impossible to completely prevent the sporadic appearance of outliers when approaching the measurement limits, as it can be seen in the figure. Indeed, the probability of outliers is proportional to the slew-rate of the signal at each time, leading to a non-uniform distribution throughout the acquisition.

As we previously remarked, the overall probability of outliers may be reduced further by increasing the acquisition rate (reducing the shot-to-shot strain for a given

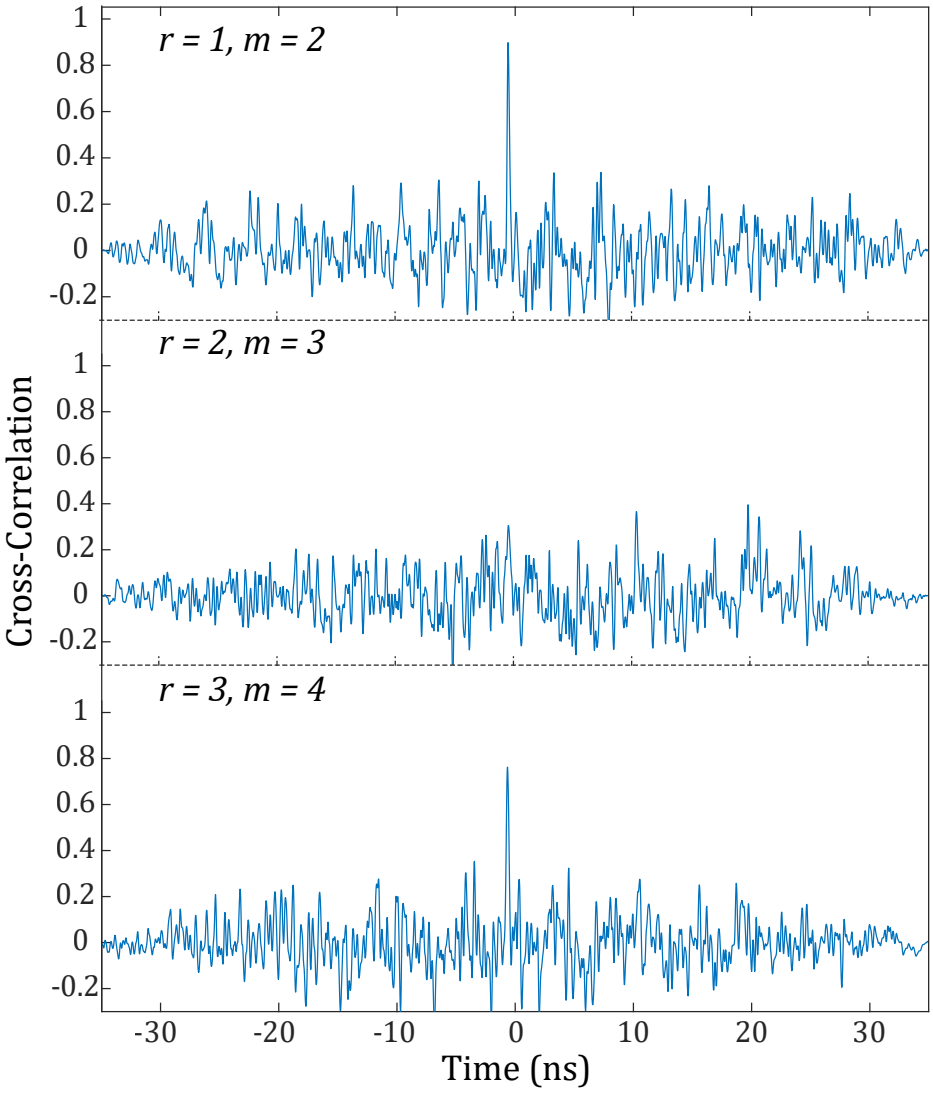

FIGURE 4.7: Cross-correlation between 3 pairs of 4 consecutive traces, representing a section of fiber undergoing a 50 Hz,750 $\mu\varepsilon$ perturbation. The top and bottom correlations lead to unambiguous correlation peaks. The middle trace yields a noise-like appearance, in which the GCC algorithm yields a sudden strain jump of 18.64 $\mu\varepsilon$, clearly an outlier. Adapted from [141].

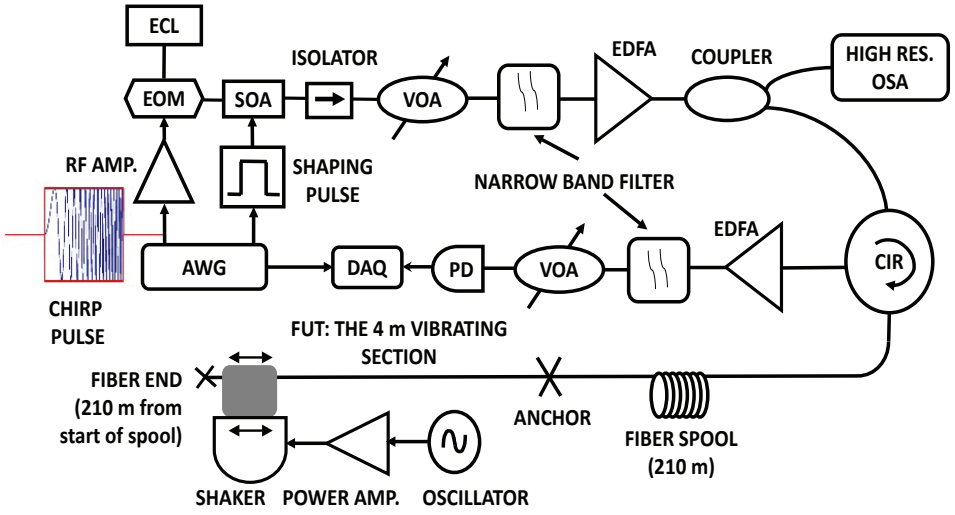

FIGURE 4.8: Experimental setup used for the demonstration. ECL: External Cavity Laser; SOA: Semiconductor Optical Amplifier; VOA: Variable Attenuator; EOM: Electrooptical Modulator; EDFA: Erbium doped fiber amplifier; CIR: Circulator; FUT: Fiber under test; PD: Photodetector; DAQ: Data acquisition; AWG: Arbitrary Waveform Generator. Taken from [141].

slew rate). In case we have an oversampled acoustic signal, we may exploit the redundant information obtained from oversampling through suitable post-processing in order to correct any sporadic anomalies. Outliers manifest as impulse noise in the differential strain time-series. Impulse noise may then be easily corrected by applying a N-tap median filter (or other robust statistic based filter) to the differential strain signal, defined as

$$\Delta\varepsilon'_m = \text{median}\{\Delta\varepsilon_{m-N/2} \ldots \varepsilon_{m+N/2}\}. \tag{4.20}$$

In doing so, the effective acoustic bandwidth is reduced to $f_{acq}/(2N)$. By selecting N to be lower than the acoustic oversampling factor, this incurs minimal undesirable effects on the acquired signal as the cost of correcting the outlier errors.

4.2.2 Experimental demonstration

Description of the setup

In order to demonstrate the potential for measurement of large strains, a CP-φOTDR setup was assembled with an external modulation configuration for the emission arm (see section 3.4.3), as depicted in figure 4.8.

The setup consisted of an external cavity laser diode (ECL), externally modulated using an amplitude electro-optical modulator (EOM) driven by an arbitrary

waveform generator (AWG), producing a 35 ns long rect-envelope chirped pulse waveform with 5 GHz chirp bandwidth centered at 6.5 GHz. The EOM output was time-gated through a SOA in order to improve the pulse extinction ratio, and sent through a tunable spectral filter to remove the the lower sideband and any remnant carrier. This pulse was then amplified using an EDFA and launched into the FUT, while controlling the power in order to prevent the onset of non-linear phenomena.

The return light from Rayleigh backscatter was once again amplified in detection and filtered in order to mitigate amplifier ASE, being then detected by a 9.5 GHz photodetector and digitized at 40 GS/s. The FUT consisted of a $\sim$ 210 m fiber spool with a 4 m long segment stretched and secured at both ends. One of the ends was fixed while the other was attached to a mechanical shaker (while pre-straining the fiber), which was placed at a different optical table in order to prevent the introduction of mechanical noise to the optical setup. The shaker was driven by an amplified signal generator to produce large sinusoidal motions.

Each measurement consisted of a 160 ms acquisition of successive traces, at a rate of $f_{acq} = 200$ kHz (laser repetition rate). The processing was done according to the method described in section 4.2.1, cross-correlating successive traces instead of using one common reference. The correlation time-window was optimally set as the same as the pulse width (35 ns), yielding a spatial resolution of $\sim$3.5 m.

Experimental measurements

For the demonstration of a measurement of large strains, a 50 Hz perturbation with 1190 $\mu\varepsilon$ peak-to-peak amplitude was applied to the fiber. The value of amplitude and frequency were chosen so that the maximum shot-to-shot strain differences obtained for such a perturbation yields $\sim (1\mu\varepsilon)$ at the acquisition rate of 200 kHz, near the limit imposed by equation 4.19. The differential strain and computed strain measurements are represented in figure 4.9. The raw differential strain acquisition is depicted on the top, and after correction with a 5-point median filter in the middle. The reconstructed absolute strain, using the median filtered differential strain data, is represented in the bottom figure.

In the raw acquisition, we can observe that the signal is heavily corrupted by impulse noise due to outliers, with higher density at the points where the perturbation absolute slew rate is highest. The resulting impulse noise is fully compensated after median filtering, implying that even in the regions of highest outlier density, 3 out of every 5 consecutive points comprise good estimates. A 5-tap median filter reduces the original acoustic bandwidth ($f_{acq}/2 = 100$ kHz) to 20 kHz, which is still well above the frequency of the perturbation of interest. The effect of employing a non-linear filtering process was also evaluated by repeating the correction with a 7-point median filter (yielding an effective acoutic bandwidth of $\sim$ 14 kHz). This produced a negligible normalized rms difference of less than 10^{-3} between both strain signals, indicating that even when correcting such a large amount of outliers,

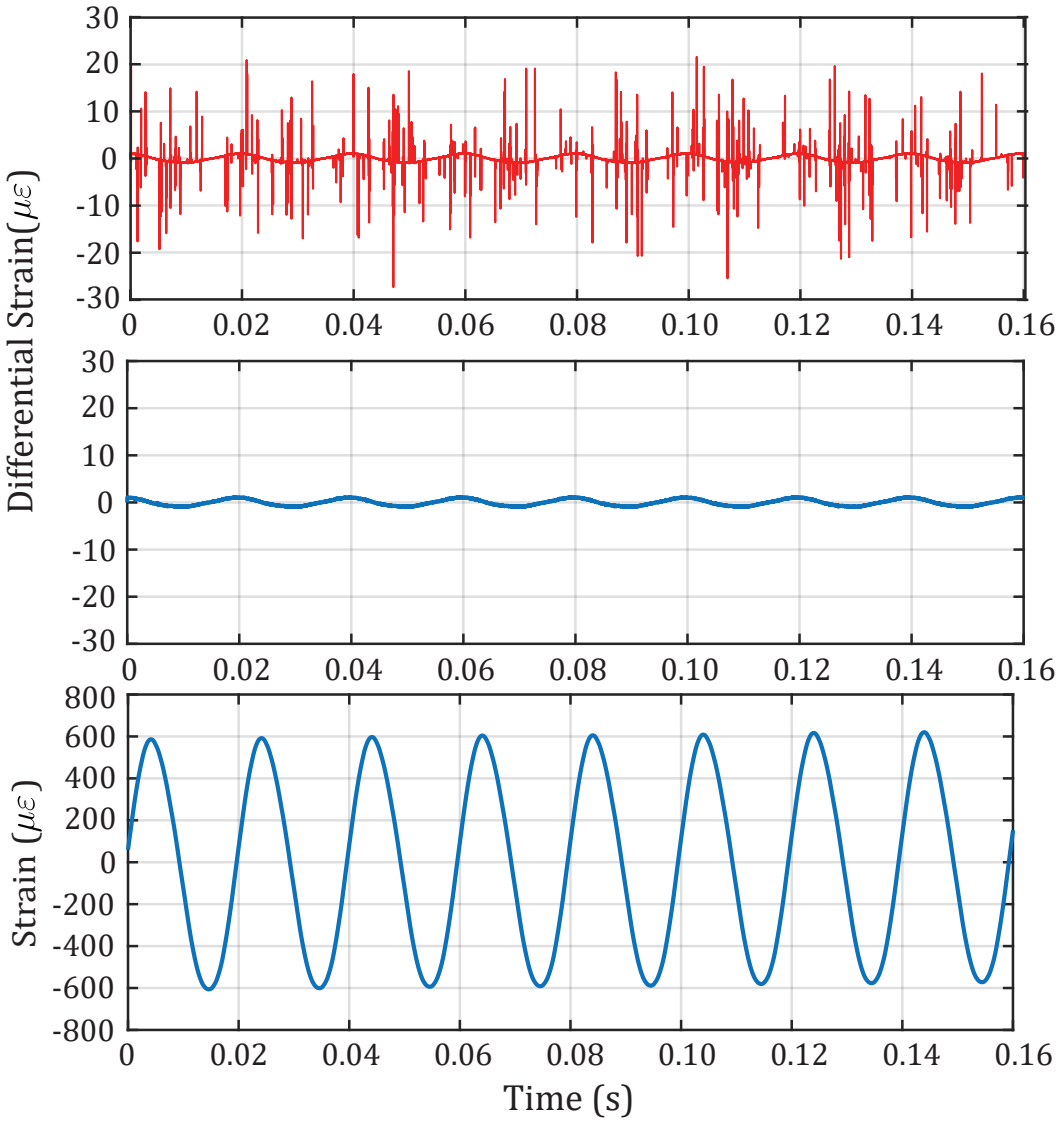

FIGURE 4.9: Strain measurement of a 50 Hz, 1190 $\mu\varepsilon$ (peak-to-peak) perturbation. The raw signal (top) is clearly heavily corrupted with outliers, with greater density at the times of maximum and minimum slew rate. In the middle, the same result after 5-point median filtering. The reconstructed strain from the strain increments is represented in the bottom figure. Adapted from [141].

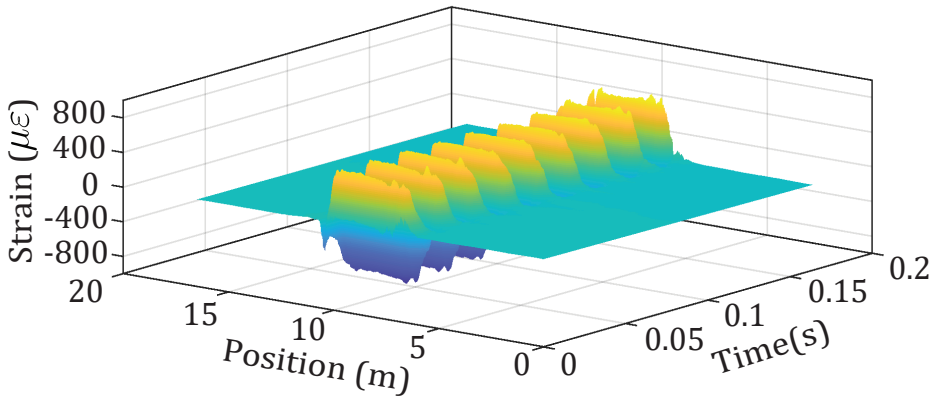

FIGURE 4.10: Time and position resolved measurements of the 50 Hz, 1190 $\mu\varepsilon$ (peak-to-peak) perturbation, demonstrating the distributed capabilities of the technique. Note thaat there are some non-uniformities in the applied strain, which may contribute to the appearance of outliers. Adapted from [141].

the non-linearity introduced from the application of a non-linear filter in the signal is negligible.

In figure 4.10, we show the strain map of the whole interrogated fiber, where some position dependent non-uniformities in strain can be observed. The existence of these strain gradients within the spatial resolution may be at the origin of the high number of outliers (despite keeping the perturbation within the limit imposed by equation 4.19). Non-uniform strain across a single spatial resolution may lead to further decorrelation of traces, as well as a inaccurate time-delay estimation.

Attempts at significantly higher strain amplitudes (maintaining the frequency of 50 Hz) proved impossible due to high outlier concentration at the times of greatest perturbation slew-rate. Fixing the slew rate in accordance to the condition specified in equation 4.19, we demonstrated faster perturbations of overall lower amplitude (200 Hz/250 $\mu\varepsilon$ and 400 Hz / 150 $\mu\varepsilon$), using the same 5-point median filtering post-processing. The results are displayed in figure 4.11

4.2.3 Noise performance of large strain measurements

The proposed strategy for incremental measurements changes the estimation process in a way that affects the noise statistics and dynamic noise floor. This may be easily understood by comparing the fixed reference measurement process (see 4.1) and the incremental measurements. In the typical, fixed reference case, the m-th estimate of strain can be modelled as

$$\widehat{\varepsilon}_m = \varepsilon_m + e_m, \tag{4.21}$$

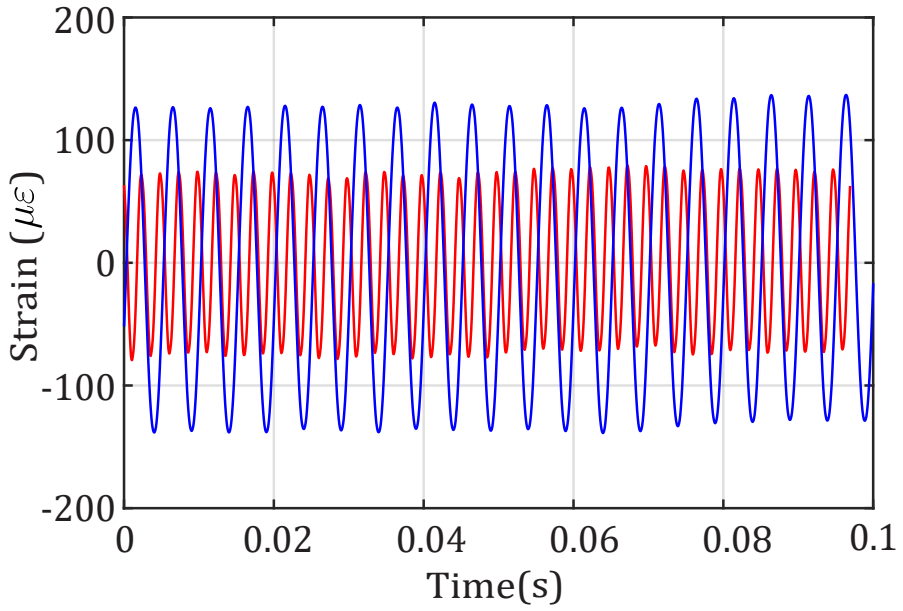

FIGURE 4.11: Other measurements, one 200 Hz perturbation with 250 $\mu\varepsilon$ amplitude (blue line) and another 400 Hz with 150 $\mu\varepsilon$ amplitude (red line). Adapted from [141].

where e_m is the error in estimation associated with the m-th measurement, ε_m is the true strain of the system and $\widehat{\varepsilon}_m$ is the produced estimate. Under good trace conditions for estimation, the variable e_m comprises a white Gaussian process with variance equal to the Cramér-Rao Lower Bound (equation 4.14), for the reasons explained in the previous section. This is changed for the incremental case, since the m-th estimation produces

$$\widehat{\Delta\varepsilon}_m = \Delta\varepsilon_m + e_m, \tag{4.22}$$

which may then be converted to strain as

$$\widehat{\varepsilon}_m^{incr} = \sum_{j=0}^{m} \Delta\varepsilon_m + e_m = \varepsilon_i + \sum_{j=0}^{m} e_m. \tag{4.23}$$

Notably, the error component is increased: The result from accumulating a white Gaussian process spectrally manifests as $1/f$ (Brownian) noise ($1/f^2$ in power), since each individual noise sample is replaced by a step-function of the same amplitude. As such, introducing this method impacts the performance of the sensor at lower frequencies. This effect is noticeable in figure 4.12, where 3 power spectral densities (PSD) of the strain measurement are compared (computed using Hanning-weighted periodograms [180]): In the perturbed section of fiber (blue line), in an unperturbed section with the incremental measurement strategy (red line), and in the same unperturbed section with the regular fixed-reference strategy (black line). Notably, the white noise is replaced by a $1/f$ component when doing incremental

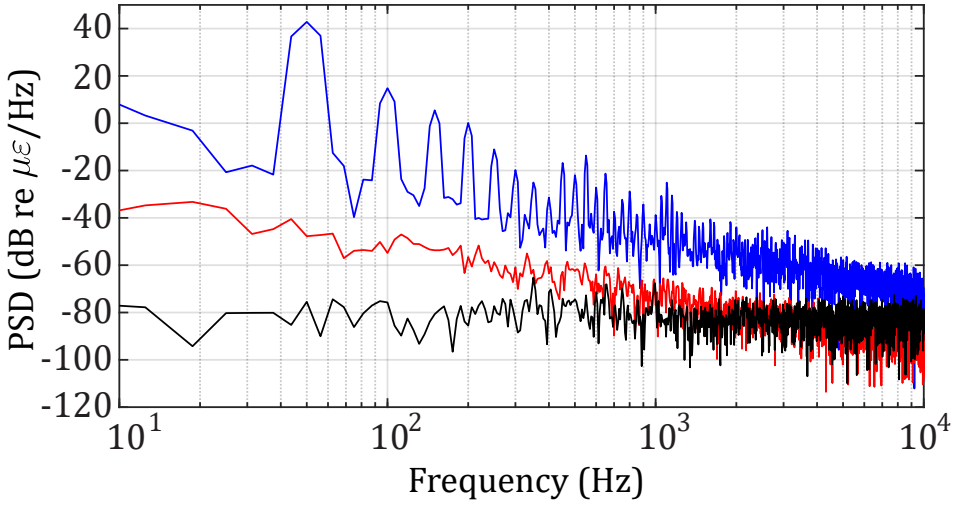

FIGURE 4.12: Estimated power spectral densities of the large strain measurement point (blue line), as well as two unperturbed sections using the conventional method and the incremental method (red and black lines). Adapted from [141].

measurements.

In addition, the perturbed region shows a slightly higher noise floor than expected from only reference updating. There are two probable origins for this noise. First, it is possible that the median filtering process also introduces some amount of method noise, which should increase depending on the number of outliers that need to be corrected. Secondly, even when condition 4.19 is fulfilled, large strains imply successive correlations between two partially (non-negligibly) decorrelated signals, which may hinder the performance of time-delay estimation.

In figure 4.12, the noise level at 50 Hz (in the perturbation section) is estimated to be $0.1\mu\varepsilon/\sqrt{\text{Hz}}$ for the blue line (although the noise level seems to increase with the applied perturbation). The SNR of the acquired strain waveform is estimated at over 40 dB, with harmonic rejection greater than 28 dB (indicating high linearity).

4.2.4 Discussion of results

The presented findings, published in [141, 142], successfully demonstrated measurements of large strains using the chirped-pulse technique, introducing and demonstrating a mitigating strategy for the effect of measurement outliers which occur at high strain amplitudes. The proposed mitigation strategy consists in changing the absolute strain measurements to differential strain measurements by incrementally updating the cross-correlation reference. In turn, this alters the typical limit of maximum strain amplitude to a limit of maximum shot-to-shot strain. As this strategy is conducive to exploiting the acoustic oversampling of strain signals in order to boost the maximum measurable strains, it is further consolidated by correcting any sparse outliers through median filtering of the differential strain signal.

This method was tested for its impact in the signal integrity, which was found to be negligible so long as the signal is sufficiently oversampled. We experimentally presented measurements of several perturbations of 1190 $\mu\varepsilon$ @ 50 Hz, 250 $\mu\varepsilon$ @ 200 Hz and 150 $\mu\varepsilon$ @ 400 Hz, all with approximately equal maximal slew rates, for fiber lengths of 210 m.

The oversampling benefit also implies a trade-off between the measurable perturbations using this method and the total length of fiber (which limits the maximum probe repetition rate). In this case, a sampling rate of 200 kHz was used for a 210 m-long fiber, in order to measure sub-kHz acoustic perturbations.

The proposed method also leads to different dynamic noise properties. The estimation error is accumulated at every estimation, leading to a $1/f$ noise-floor, which appears to be also signal dependent (higher perturbation slew-rates lead to higher noise increments).

The demonstrable possibility of measuring very large perturbations paves the way to new applications in fields such as structural health monitoring. Further study should be done on other robust statistics to mitigate outliers and reduction of the accumulated error.

4.3 Statistical evaluation of the performance of CP-φOTDR

We have previously described the common methods through which linearity is achieved in φOTDR measurements. One common option relies on retrieving the full electric field information, and infer the perturbation from changes to the phase evolution of the propagating probe [82, 122]. These methods demand the use of coherent detection schemes, which introduce additional requirements when compared to direct detection alternatives. Specifically, the source must ensure coherence between the local oscillator (LO) and probe light throughout the whole fiber length, and the effects of differences in polarization between probe and LO must be accounted for.

Even if these requirements are fulfilled, typical phase-demodulation systems do not address the fading problem of φOTDR, since at positions where the result of local backscattering yields very low amplitudes it is impossible to obtain a relevant phase estimate. Indeed, the performance of each measured position is directly tied to the ability to accurately retrieve the phase. The φOTDR backscattered electric field from the random inhomogeneities results in a Rayleigh distribution of field amplitudes, entailing a high variability of measurement performance, and a significant number of fading points [37, 129]. While some developments have been reported on potential mitigation strategies, these usually further increase complexity and sacrifice sensor performance [181].

A statistical assessment of the variations in acoustic sensitivity was presented in [129], revealing a long-tail statistical distribution of the sensitivity for DAS systems based on phase demodulation and coherent detection. More importantly, this study highlighted that in phase-demodulation based DAS, a significant portion of positions exhibit unacceptable levels of performance (directly related to fading).

The different estimation process used by the chirped-pulse technique tracks time displacements of trace sections. This method is generally regarded as robust to fading, since the estimation occurs over a time section and is independent of the amplitude of one individual sample of the retrieved optical trace. In the following section, we experimentally justify this claim by presenting a statistical evaluation of the performance of chirped-pulse DAS in SNR and sensitivity, as well as a direct comparison with coherent detection alternatives. We show that the statistical distribution of performance is significantly different to phase-demodulation techniques, when operating under similar conditions of resolution and acoustic bandwidth. The performance has a much narrower distribution to that of phase-demodulation DAS, attesting to the robustness of the technique.

Afterwards, considering similar conditions and the upper bounds for measurement of each technique (without any additional strategies such as those presented in 4.2), the performance dynamic ranges of both techniques are also compared.

This section reflects the results of the work published in [134].

4.3.1 Origin of statistical variations of performance

The information used to estimate the measurand from any φOTDR system results from the interference of scattered electric fields at frozen-in fiber inhomogoneities. At the fiber input, the resulting backscatter from the m-th launched probe yields

$$e_m(t) = A_m(t) \cdot \exp\{j\phi_m(t)\}, \tag{4.24}$$

where t is the time (corresponding to the fast axis), $A_m(t)$ is the backscattered amplitude field, and $\phi_m(t)$ is the phase of the backscattered wave detected at time t. The subscript m can alternatively be understood as the m-th sample of the discrete time slow axis. The recovered $e_m(t)$ is seemingly random and noise-like, with the distribution of amplitudes $A_m(t)$ following a Rayleigh distribution and the phases ($\phi_m(t) \in [-\pi, \pi]$) following a uniform distribution. Nonetheless, the retrieved electric field is deterministic and characteristic of the probed fiber current state.

Phase-demodulation methods infer local perturbations by measuring changes to the evolution of $\phi_m(t)$ over t. To do this, these methods typically employ a coherent detection scheme, which carries increased coherence and polarization requirements to the setup. However, the ability to estimate phase at any given position is directly tied to the retrieved amplitude at that position. In a noisy detection process, some positions will fall below a minimum threshold for measurement, thus impeding the estimation of phase (yielding a fading point). Even more points may fall in a region where phase estimation is possible, but with comparatively low performance (given the broad Rayleigh distribution of amplitudes) [129].

Alternatively, direct detection methods, such as CP-φOTDR, are unable to retrieve electric field information. Instead, the measurand estimation is given by a noisy optical intensity signal, modelled as

$$p_m \propto A_m^2(t) + n_{m,PD} = s_m(t) + n_m(t) \tag{4.25}$$

where $n_{m,PD}$ summarizes the additive noise components that arise from the photodetection process (both electrical noise and amplitude optical noise) and $s_m(t) = A_m^2(t)$ is the signal component, which has an exponential distribution resulting from squaring a Rayleigh-distributed random variable [182]. In this case, we have neglected non-additive sources of noise (such as laser phase noise), since it may be aptly corrected in the technique of CP-φOTDR, as explained in section 3.4.7.

In the case of the CP-φOTDR technique, quantitative measurements with direct detection are enabled through a combination of frequency demodulation and frequency-to-time mapping, achieved by chirping the probe with enough bandwidth to fulfill the temporal far-field condition [183] (see section 3.4.1). As a result, a perturbation will incur a directly proportional local time delay, as specified by the relationship in equation 3.37 [133].

A local time-delay measurement is intuitively advantageous in terms of the system's robustness to fading points: when estimating a pattern shift across a time

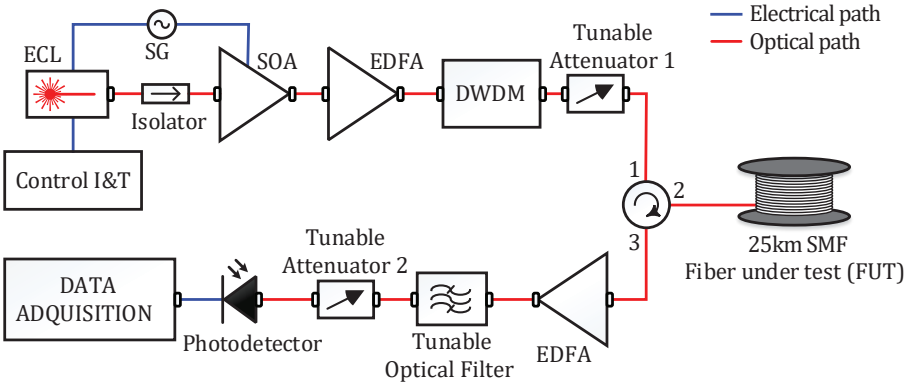

FIGURE 4.13: Setup used to evaluate the statistical performance. ECL: External Cavity Laser; SOA: Semiconductor Optical Amplifier; EDFA: Erbium doped fiber amplifier; FUT: Fiber under test. Taken from [134].

window, isolated low SNR points have a reduced influence in the final measurement performance. This intuition is supported by the results provided in section 4.1, where we demonstrated that under conditions of no phase noise, adequate interpolation and acceptably low decorrelation between compared traces, each sensing position performance is ultimately limited by the spatial resolution, chirp bandwidth, and the interrogated section SNR (equation 4.14).

Given that the spatial resolution and bandwidth are fixed for all measured points, any variation in performance must originate from local variations in SNR. When estimated along a sizeable time-delay estimation window, the SNR should remain relatively stable, with only slight variations accounting for the specific shape of the trace at a given instant. Consequently, the sensor performance should not vary extensively at a given position of fiber with changes in the trace shape.

4.3.2 Experimental assessment of statistical performance in CP-φOTDR

In this section, we experimentally evaluate the sensitivity statistics of CP-φOTDR measurements. The assembled setup (depicted in figure 4.13) consisted of a typical CP-φOTDR with a direct current modulation emission arm (see section 3.4.3). An external cavity laser (ECL) was employed as the laser source, being controlled externally in current and temperature in order to fix the center wavelength. In order to produce the chirp, a secondary current control was introduced with a sawtooth electrical output to modulate the laser frequency. The pulse was then time-gated using a high extinction ratio SOA (driven with a *rect* window), at a time-section yielding good linearity in the resulting frequency modulation.

The generated pulses were then amplified by an EDFA and filtered through a dense wavelength-division multiplexer (DWDM), working as a bandpass filter to

remove undesired ASE. Before being launched into the fiber under test (FUT), the resulting probe peak power was controlled and kept below the threshold for non-linearity. The resulting probe had a peak power of 200 mW, 100 ns of pulse width (yielding a spatial resolution of 10 m in optimal conditions), and 1 GHz of chirp bandwidth.

The recovered light at the fiber input from the backscattering was once again amplified by an EDFA in the detection arm and filtered using a tunable bandpass filter. The detection was accomplished using a 1 GHz bandwidth photodetector (digitized at 4 GS/s).

The laser phase and frequency noise was cancelled using the method described in section 3.4.7, and sampling-noise was reduced by centroid interpolation of the cross-correlation's main peak [184]. The centroid function was chosen due to its simplicity, low computational cost and low absolute levels of bias.

In order to produce a statistically relevant, position-resolved determination of the noise power distribution over a 25 km-long fiber analysis with a single fiber, we took advantage of the random decorrelation observed in the φOTDR trace over time from exposure to uncontrolled environmental conditions. Drifts in the laser frequency and an accumulation of temperature/strain gradients over lengths smaller than a spatial resolution ensure that the trace is randomized every few minutes. By replacing the reference at this time (see section 4.2), one is able to use the same section of fiber, which behaves as a fundamentally new independent sensor, with the same incident probe power. Empirically, we found that if the fiber left uncontrolled in the laboratory, the trace naturally decorrelates every few minutes. The data was acquired over the course of 10 hours of measurement.

The statistical distribution of the measured acoustic noise power is depicted in figure 4.14. Clearly, the mean acoustic noise power for each position follows the tendency given by the evolution of the SNR (see equation 4.14), decaying naturally from the effect of fiber losses in trace SNR. This indicates that the limiting factor in performance is indeed additive noise in the trace. Exceptionally, the first 5 km display a constant mean noise power, since these were used for phase-noise compensation. This can be understood by recalling that phase-noise compensation introduces a method noise component which is ultimately limited by the sections of highest noise used for compensation (as explained in section 3.4.7). Notably, the noise variance presents an approximately Gaussian distribution for all fiber positions along the fiber length.

4.3.3 Comparison with coherent detection methods

The measured performance statistics were then compared against a phase-demodulation, coherent detection based system. The statistics and performance of phase-demodulation DAS were analyzed in ref. [129], under the assumption of a system limited by additive noise sources. While the effects of phase-noise

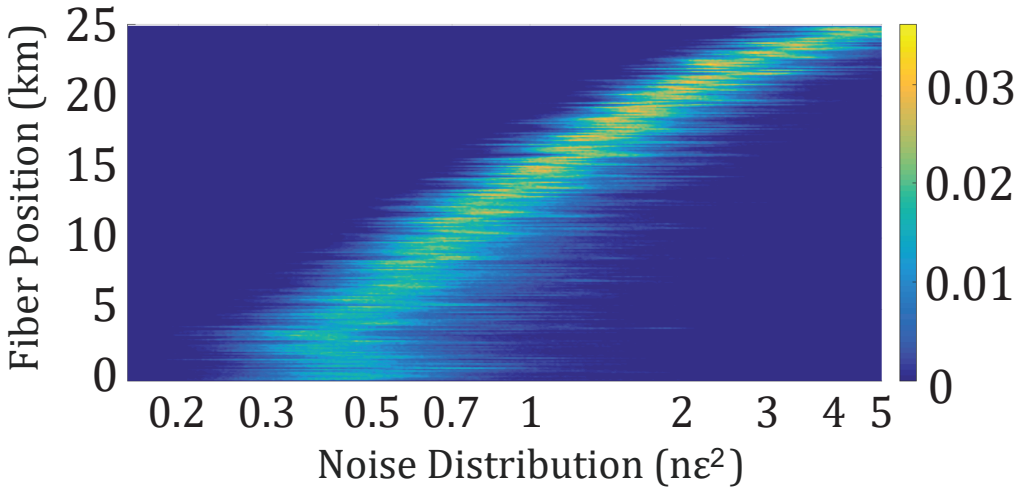

FIGURE 4.14: Distribution of strain noise power and fiber position, along a 25 km-long fiber. The first 5 km were used for phase noise compensation (see section 3.4.7). Taken from [134].

in chirped-pulse and phase-demodulation DAS techniques are different, the comparison applies whenever phase-noise is either negligible or compensated.

In the study cited in ref. [129], a 2 km long fiber (with a perturbation applied to the mid point, at $z = 1$ km) was used to obtain the statistical noise properties of the system. Different effective sensors were selected, choosing one resolution cell before and one after the perturbation, in order to create an array of independent effective sensors. Their analytical description for the noise resulted in the following noise performance [129]

$$n_{m,CD}(i,i') = \frac{\sigma_n^2}{2}\left[\frac{1}{A^2(i)} + \frac{1}{A^2(i')}\right], \tag{4.26}$$

where σ_n^2 is the variance of the detected trace, obtained from a fiber of 2 km, and i, i' are the positions of the resolution cells before and after the perturbation, respectively. $A^2(i)$ and $A^2(i')$ are the corresponding signal powers at each resolution cell, where $A^2(t)$ is a noise-like time series with an exponential distribution.

For the sake of comparison, this noise model distribution was compared to the noise distribution acquired for the CP-φOTDR system after 2 km of fiber, with traces generated from probes of similar power, pulse width and noise spectral density. As a result, in the coherent detection method case, the trace SNR was estimated to be 37 dB while the trace SNR for the CP-φOTDR technique obtained after 2 km was estimated SNR at 28 dB. The differences in SNR arise from the higher detection bandwidth required for the chirped-pulse operation, allowing more unfiltered noise into the detected band.

The comparison of statistical performance of both methods is presented in figure 4.15. Note that while the mean noise powers of both techniques are similar, the shape

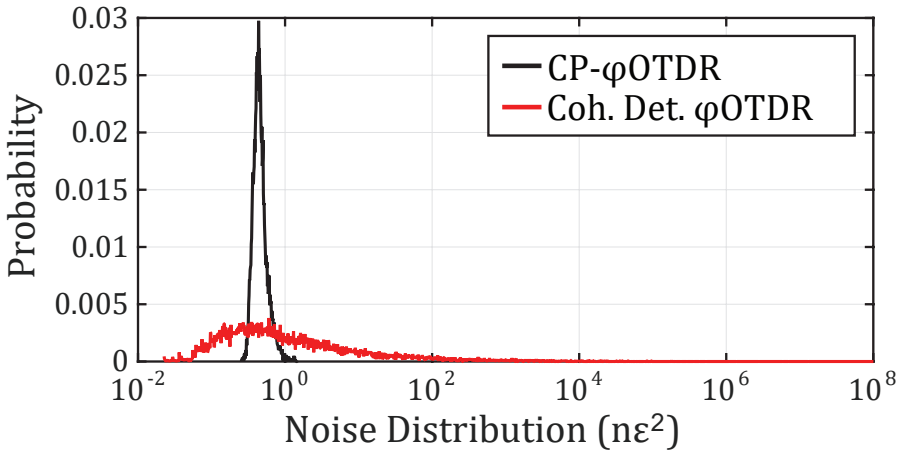

FIGURE 4.15: Comparison of noise statistics of different φOTDR methods. Black line represents CP-φOTDR, and red line represents phase-demodulation φOTDR through coherent detection. Both statistics consider similar pulse peak power, pulse width (spatial resolution) and noise power spectral density. Taken from [134].

and width of the distributions are strikingly different. In the phase-demodulation case, despite the overall healthy levels of trace SNR, about 6% of all points can be regarded as fading points, with an SNR of less than 1 (versus 0% in the CP-φOTDR case). Moreover, the full-width at 10% of the chirped-pulse measured noise power distribution is of $0.39\,n\varepsilon^2$, while in the coherent detection scheme, the same variation of noise power is $79.38\,n\varepsilon^2$.

These results may be extended to determine a dynamic range for each of these systems. Previously, we showed that, in regular operation, the maximum measurable perturbation is limited for CP-φOTDR systems, as the perturbation-equivalent frequency shift must be kept much smaller (<5%) than the total chirp bandwidth (see section 4.2). Similarly, phase-demodulation systems are limited by a shot-to-shot maximum variation of π rad. As such, the previous results may also be used to estimate an effective dynamic range of incremental strain for both techniques, under the defined conditions.

In this case, we define the dynamic range as the ratio between the expected maximum measurable shot-to-shot perturbation, and minimum measurable perturbation. The maximum measurable value assumed for CP-φOTDR is of 5% of the total frequency, and π rad for the phase-demodulation method. As for the minimum measurable value, we define it statistically, allowing only a given portion of measurements below a performance threshold (SNR $\leq$ 1) .

The results are shown in figure 4.16, for the cases of allowing 50% (yellow-shaded region and purple-shaded region) or 1% (green-shaded region and pink-shaded region) of sensors to yield an acoustic SNR $\leq$ 1. Allowing 50% of the points to have an

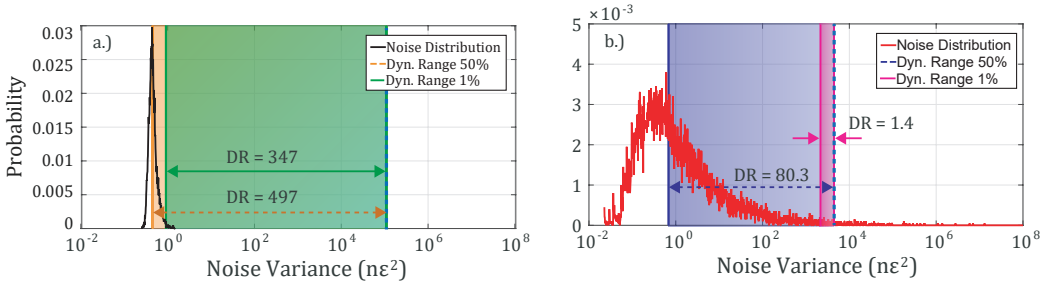

FIGURE 4.16: Noise distribution and dynamic range comparison for each sensor. Vertical dashed lines point out the maximum measurable perturbation (shot-to-shot). Green and pink rectangles determine the dynamic range limits assuming 1% sensors allow acoustic SNR ≤ 1; yellow and purple rectangles determine the dynamic range limits assuming 50% sensors allow acoustic SNR ≤ 1. a.) Chirped-pulse φOTDR; b.) Phase-demodulation φOTDR with coherent detection. Taken from [134].

acoustic SNR ≤ 1, the dynamic range for a chirped-pulse DAS would be of 497, versus 80.3 for a coherent detection system. In the stricter condition of only allowing 1% of sensors to have an SNR ≤ 1, the contrast is much sharper, yielding a 347 dynamic range for the chirped-pulse method, versus a 1.4 dynamic range for the coherent-detection case. Notably, this entails only a $\sim$ 30% decrease in the dynamic range of the chirped-pulse technique, despite the much stricter requirements, attesting to the high robustness of CP-φOTDR.

To complete the comparison with the study in [129], we also present a statistical analysis of the SNR, signal and noise distributions as a function of the sensor resolution. We interrogated a 1 km fiber, with a 20 m section strapped around a piezoelectric transducer, with an applied sinusoidal strain perturbation at a frequency of 100 Hz and 127 nε peak-to-peak amplitude. The spatial resolution was controlled by varying the probe pulse and (using $\tau_p = 50$ ns, 75 ns and 100 ns probes, corresponding to 5 m, 7.5 m and 10 m). To this effect, Given the direct current modulation nature of the chirp, the instantaneous frequency slope is fixed to 0.01 GHz/ns, so the pulse bandwidths were $\delta\nu = 500$ MHz, 750 MHz and 1 GHz, respectively. The laser repetition rate was set at 5 kHz. The results are represented in figure 4.17.

Evidently, the signal distribution of power remains approximately constant, independent of the selected probe parameters, with a variation of 1.4 dB (full width at $1/e$ height), likely due to poor mechanical coupling between the fiber and PZT transducer. The distribution of SNR is then governed by the variation of noise power, which presents a full width at $1/e$ of $\sim$ 4.4 dB, independent of probe parameters. As expected for the reasons described in section 4.1, in this case, the higher bandwidth, longer correlation time-window and improved trace signal-to-noise ratio of the longer probe yields greater acoustic SNR.

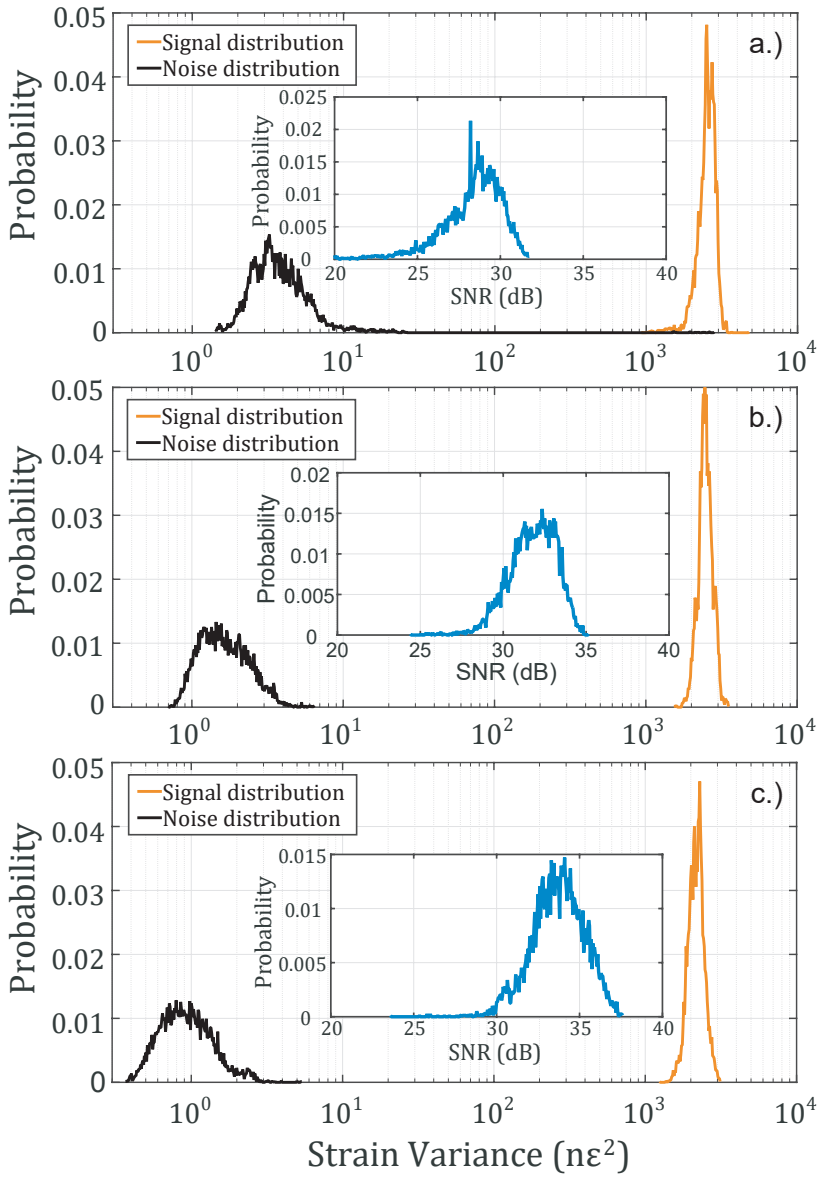

FIGURE 4.17: Comparison of acoustic signal, noise and SNR distributions obtained from a CP-φOTDR system with different spatial resolutions and bandwidths. Signal power distribution is represented with an orange line and noise power distribution with a black line. The SNR distribution is depicted in the inset plots. Probe pulses are a.) 50 ns/0.5 Ghz; b.) 75 ns/0.75 GHz; c.) 100 ns/1 GHz. Taken from [134].

4.3.4 Discussion

In this section we have demonstrated the robustness of CP-φOTDR. There was no verifiable occurrence of fading points in any of the chirped pulse measurements. This is in sharp contrast to coherent detection methods, which have previously been described in [129], which show a non-negligible probability of fading points and high variability in performance, even in good measurement conditions.

Still, the SNR performance was shown to stochastically vary $\sim$ 4dB, closely following the distribution of acoustic noise power obtained (with a 1/e of width $\sim$ 4.4dB). The fluctuation is likely due to the changes to the specific shape of the trace section used for cross-correlation. Nonetheless, the overall performance distribution is much narrower than phase-demodulation techniques.

In our comparison, we have also established a definition for dynamic range in which it is possible to attest the broad dynamic range of chirped-pulse-based DAS, even in standard operation. In this analysis, we defined the dynamic range on the shot-to-shot limits for both techniques (chirped-pulse and phase-demodulation), accounting already for the possibility of strategies such as the one described in section 4.2 (or phase unwrapping, in the phase-demodulation case [130]). We have demonstrated that the CP-φOTDR technique can consistently provide a broad shot-to-shot dynamic range (> 300) across all measurable fiber positions.

The high reliability demonstrated by the CP-φOTDR technique, due to its characteristic time-delay estimation based measurement, highlights its potential for application in critical systems and infrastructures.

4.4 Cross-talk in CP-φOTDR

Previously, we described the benefits of a local TDE-based measurand estimation. These advantages come in the form of measurand linearity [133] (section 3.4.1), high dynamic strain sensitivities [139] (section 4.1), potential for high dynamic range [141, 142] (section 4.2), and robust performance [134] (section 4.3). However, a local TDE approach implies that the time-axis used for measurand estimation is the same as the one used for position determination.

Up to now, in our description of OTDR, we have considered an approximation of an homogeneous group index for the whole fiber, and no fiber elongations (*i.e.*, the fiber retains the same length across measurements). In truth, changes to the local surroundings of a fiber locally modify the optical path, thus affecting the time it takes for light to reach all subsequent positions. While this is an underlying principle of fiber-based sensing, the magnitude of this effect on positional uncertainty in OTDR is typically considered negligible.

In the case of CP-φOTDR, however, the minute time-delays are also used to compute the local measurand information. It follows that the effects of a perturbation may induce an apparent measurement at all subsequent positions, analogous to having cross-talk between effective sensors. The aim of the following pages (reflecting the work reported on [145]) is to evaluate the existence of cross-talk in chirped-pulse systems, and quantify its effects. We begin by describing the effect of a refractive index change over a length of fiber on subsequent positions. We then present an experimental demonstration of this effect compared with the theoretical prediction.

4.4.1 Description of the problem

OTDR systems map each longitudinal position in the interrogated fiber to the specific time it takes for a pulse of light to complete the round trip to-and-from that point. The total round-trip time ($t_{RT}(z)$) of a pulse travelling to-and-from a longitudinal position z of fiber is given by

$$t_{RT}(z) = 2\int_0^z \frac{n(\zeta)}{c} d\zeta \tag{4.27}$$

where $n(z)$ is the fiber's group index at position z. Clearly, this equation shows that a change in local index delays or anticipates the arrival of the pulse at all subsequent positions. The net effect of such a perturbation in the positional accuracy, however, is generally negligible, given the range of index and elongations that a fiber may be exposed to and the spatial resolutions of OTDR systems systems. Therefore, OTDR methods typically assume an invariant group index along z, and no elongation at any position of the fiber. Note, however, that this effect is cumulative, and not local. A perturbation at position z_i introduces an error for at all further positions $z > z_i$. This may be visualized in figure 4.18.

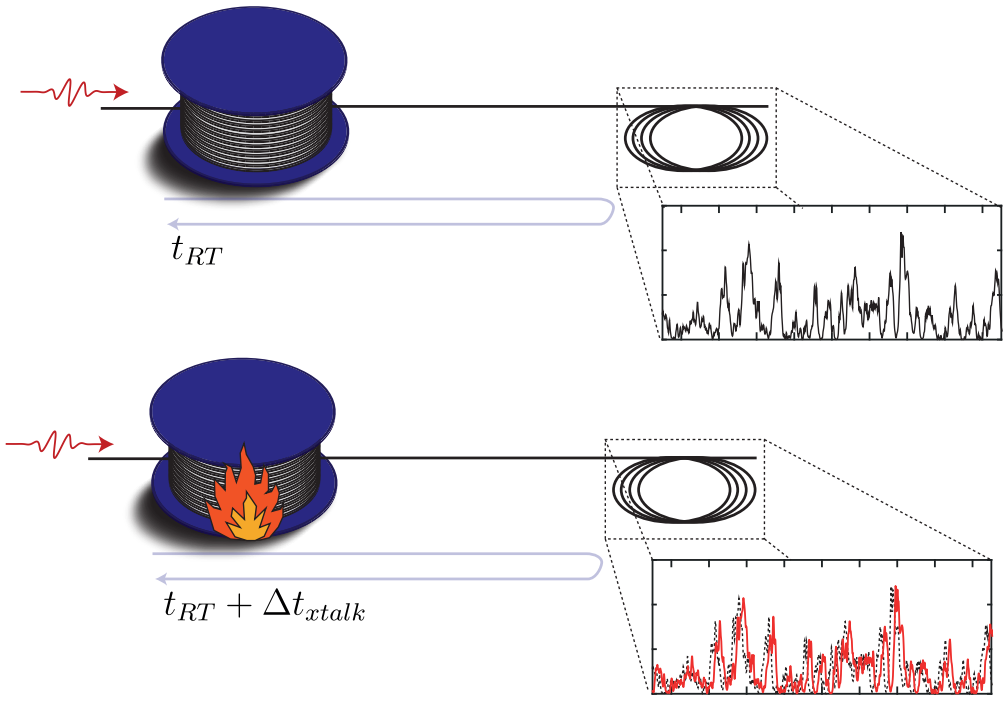

FIGURE 4.18: Visualization of the cross-talk effect. A perturbation over a section of fiber affects the optical path, and as such, the time for light to reach subsequent positions. This appears as a time-delay, which is indistinguishable from a perturbation in CP-φOTDR

CP-φOTDR relies on minute shifts in the position of features along the fast time-axis for measurand estimation. Essentially, the effect of a change of index $\Delta n(z)$ manifests as an apparent local time-delay of the trace, $\Delta t(z)$, as

$$\Delta t(z) = -\nu_0 \frac{\Delta n(z)}{n} \frac{\tau_p}{\delta \nu}, \tag{4.28}$$

where ν_0 is the laser central frequency, $\delta\nu$ is the chirp bandwidth, and τ_p is the pulse width. It is important to realize that the apparent delay imparted by this effect is local. In other words, only the features at the position of perturbation are shifted, but previous and subsequent positions are unaffected by the perturbation.

The estimation of measurand in the chirped pulse technique, however, is a simple TDE at the estimated location of the effective sensors. As such, both the measurand induced local shift, and the cumulative error in effective sensor position are indistinguishable in estimation, so the cumulative effect due to a change in optical path will be erroneously interpreted as localized perturbation in all subsequent positions.

This can be formally understood by considering a fiber of length L_{TOT}, in which a section of length L undergoes an optical path perturbation due to an elongation ΔL and a change in index Δn such that $\tilde{L} = L + \Delta L$ and $\tilde{n} = n + \Delta n$ (*e.g.*, due to induced temperature). In this case, the total time it takes for light to travel this section of fiber

will change. Compared to the unperturbed case, all interrogated positions following the perturbed section ($z > L$) will reach the detector with an additional delay given by

$$\begin{aligned}\Delta t_{xtalk}(\tilde{L}) &= 2\left[\int_0^{\tilde{L}} \frac{\tilde{n}}{c} d\zeta - \int_0^{L} \frac{n}{c} d\zeta\right] = 2\left[\frac{\tilde{n}\tilde{L}}{c} - \frac{nL}{c}\right] = \\ &= 2\left[\frac{(n+\Delta n)(L+\Delta L)}{c} - \frac{nL}{c}\right] \approx 2\left[\frac{n\Delta L}{c} + \frac{L\Delta n}{c}\right],\end{aligned} \tag{4.29}$$

where the $\Delta L \Delta n$ term was considered negligible.

As we stated, this delay Δt_{xtalk} is generally neglected in terms of the positional uncertainty it introduces. However, a TDE-based measurand estimation targets the minute differences in the time location of trace features. The accumulated delay will thus be translated into a virtual local perturbation of amplitude (in equivalent index shift)

$$\Delta n_{xtalk} = -\frac{n}{\nu_0}\frac{\delta\nu}{\tau_p}\Delta t_{xtalk}. \tag{4.30}$$

Combining equations 4.29 and 4.30, we quantify the cumulative effect in as

$$\Delta n_{xtalk} = -2\frac{n}{\nu_0}\frac{\delta\nu}{\tau_p}\left[\frac{n\Delta L}{c} + \frac{L\Delta n}{c}\right], \tag{4.31}$$

where clearly, the cross-talk amplitude varies as a function of the system's sensitivity. Nonetheless, it is instructive to estimate the order of magnitude of cross-talk induced from this effect: Considering typical probe parameters ($\nu_0 \sim 10^{14}$, $\delta\nu \sim 10^9$, $\tau_p \sim 10^{-7}$), the cross-talk induced perturbation is of $\Delta n_{xtalk} \approx 10^{-6}(L\Delta n + n\Delta L)$, where L is the length over which the perturbation is applied. In the context of temperature/strain, a $1\text{K}/1\mu\varepsilon$ perturbation over 1 km of fiber would induce an apparent shift of $\sim 1\text{mK}/1\text{n}\varepsilon$ to all subsequent positions.

4.4.2 Experimental demonstration

The experimental measurement of the induced cross-talk was conducted by applying a large thermal variation to a long section of fiber in a spool, while another section of fiber (at a later position) was kept thermally and mechanically isolated from any perturbations, and kept far apart from the perturbed spool. The FUT layout is depicted in figure 4.19.

When affected by temperature, the fiber is refractive index (due to thermo-optic effect) and total length (due to thermal expansion) are altered as $n(T) = \bar{n} + \xi_T \Delta T n$ and $L(T) = \bar{L} + \alpha \Delta T L$, respectively. In amorphous silica, these coefficients can be approximated as $\alpha \approx 0.55 \times 10^{-6}$ [185] and $\xi_T \approx 6.92 \times 10^{-6}$ [82].

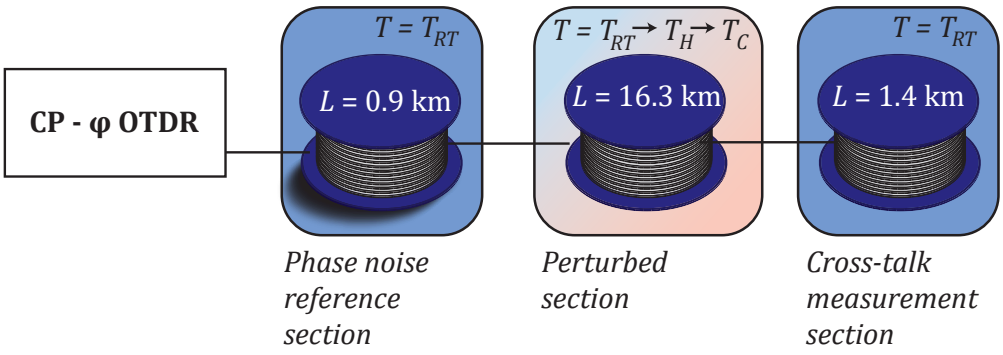

FIGURE 4.19: Experimental setup. The fibers are all in thermal baths, isolated from mechanical measurements. The phase-noise reference spool and the cross-talk measurement spool are in room temperature baths, while the perturbed spool is changed from a hot bath to a cold bath. The CP-φOTDR layout is the same as in figure 4.13

Equation 4.31 may now be rewritten in terms of an apparent induced temperature $\Delta T_{xtalk}(t)$, and a temperature perturbation $\Delta T(t)$ over a section of fiber of length L as

$$\begin{aligned}\Delta T_{xtalk}(t) &= -2\frac{1}{K_T}\frac{1}{\nu_0}\frac{\delta\nu}{\tau_p}\left[\frac{n\Delta L(t)}{c}+\frac{L\Delta n(t)}{c}\right] \\ &= -2\frac{1}{K_T}\frac{1}{\nu_0}\frac{\delta\nu}{\tau_p}\frac{nL}{c}\left[\alpha+\xi_T\right]\Delta T(t) = \frac{1}{\nu_0}\frac{\delta\nu}{\tau_p}\frac{nL}{c}\Delta T(t),\end{aligned} \tag{4.32}$$

where K_T is a coefficient that summarizes both thermal effects (thermo-optic and thermal expansion) in silica fibers.

The experiment was performed using a current-modulation based CP-φOTDR equal to the one used in section 4.3. The probe was pulsed at 1 kHz repetition rate, generating $\tau_p = 100\,\text{ns}$ long pulses of total chirp bandwidth $\delta\nu = 1\text{GHz}$. Considering these probe parameters, the induced cross-talk is of $\Delta T_{xtalk}(t) \approx 5\times10^{-7}L\Delta T(t)$, assuming a refractive index of $n = 1.46$, and length of perturbation L. The FUT layout (figure 4.19) consists of three spools of fiber: One first section in a stable environment, isolated from thermal and mechanical perturbations, for phase-noise compensation [136, 143] (with a length of $\sim$ 900 m), followed by a large spool of 16.3 km to which the large temperature perturbation was applied. Finally, the cross-talk effects of this large perturbation were verified on a third ($\sim$ 1400 m-long) spool, isolated from the other two and in a thermally and mechanically stable environment (kept in a room-temperature water bath).

In order to correctly evaluate the large perturbation induced in the stressed section of fiber, a reference update strategy similar to the one proposed in section 4.2

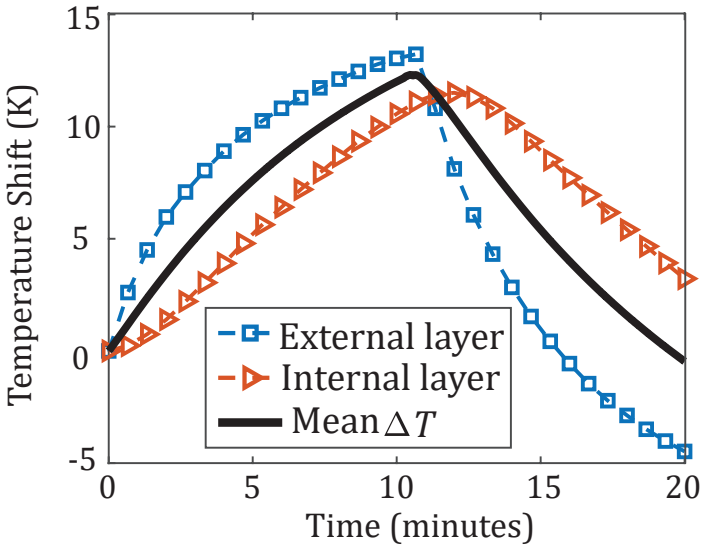

FIGURE 4.20: Thermalization of inner and outer layers of the perturbed section's spool. The inner layers thermalize slower, while the outer layers thermalize faster. For the modelling, the mean temperature of the whole section was considered.

was used: the reference was updated at regular intervals in order to improve the total range of measurement with minimal addition of low frequency noise in the system.

The temperature stress was applied by immersing the perturbed spool in hot ($T_H \approx T_R + 15\text{K}$, T_R being the room temperature) and cold ($T_C \approx T_R - 8\text{K}$) water baths, with large enough volumes of water so that water thermalization from the introduction of the fiber spool may be considered negligible. The high thermal capacity of the water allows fast thermalization of the fiber, which mitigates the effect of other environmental low frequency noise-sources on measurement. The fiber was kept in each bucket for 10 minutes in order to approach the intended temperature.

It should be noted that the coiled disposition of the fiber in each spool, added with the low thermal conductivity of the fiber, introduces a non-homogeneous time to thermalization for each section of the immersed fiber, as inner coils take longer to thermalize than the outer coils. This is clearly verifiable in figure 4.20, where we compare the thermalization of inner and outer layers of the spool, as well as the mean temperature evolution of the whole fiber section.

The effect of this induced perturbation was then observed in the third spool (while it was kept at rest in a room-temperature thermal bath). The results of 1 km of fiber were averaged and represented in figure 4.21, and compared with the theoretical model. The theoretical model considered the mean temperature evolution of the stressed fiber section and $L = 16300$. A corrective coefficient $K = 0.78$ was multiplied to the model in order to improve fitting, implying a $\sim$20% deviation between experiment and theory. The reasons for this deviation are not fully

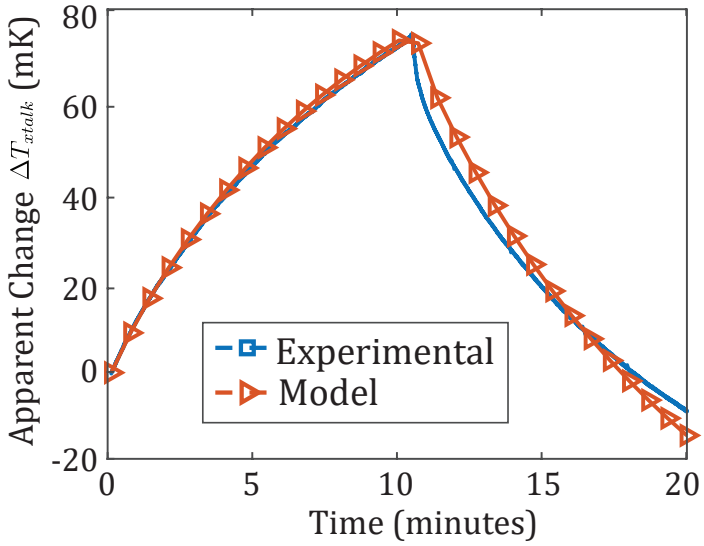

FIGURE 4.21: Experimental results and theoretical model, scaled by a factor $K = 0.78$ for better fitting. The inclusion of this factor is discussed in the main text.

understood, but we believe this may occur due to slightly different values of the thermo-optic coefficient and thermal expansion of the fiber (due to the addition of coating and the plastic spool structure), and accumulation of errors from the reference updating (i.e., inaccuracies in the temperature measurement of the perturbed coil). Despite the ∼20% deviation, the curves show remarkable agreement in behavior, with a slight mismatch during cooling which may be caused by strains induced in the fiber when moving it from the hot thermal bath to the cold bath, and further accumulation of reference update errors (see section 4.2).

The effect of noise accumulation due to reference updating has been documented in section 4.2. In this experiment, the accumulation is evident when plotting not only the average value of all independent time-windows over time, but also the standard deviation of all time-windows within the fiber section, which is depicted in figure 4.22.

4.4.3 Discussion of results

In this section, which represented the results published in [145], we have proposed and tested a model to evaluate the cross-talk induced in CP-φOTDR systems, due to the changes imposed to the travel time of light to each probed position after a perturbation.

While the presented results were formally described for a temperature-induced perturbation or an index shift, it is straightforward to convert this into a strain induced error from a strain measurement (or even generalize to other measurands). In

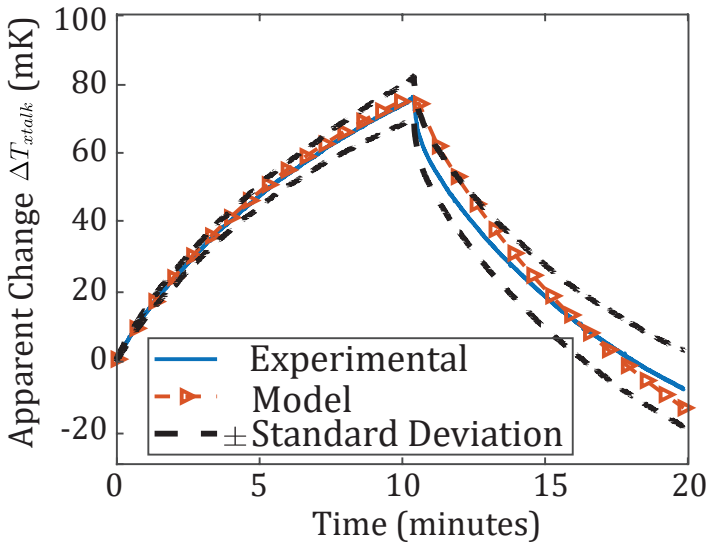

FIGURE 4.22: Evolution of the standard deviation of measurements across the 1 km section over the measurement time.

doing so, equations 4.31 and 4.32 can be re-written as

$$\Delta\varepsilon_{xtalk}(t) = \frac{1}{\nu_0}\frac{\delta\nu}{\tau_p}\frac{nL}{c}\Delta\varepsilon(t), \tag{4.33}$$

.

The proposed theoretical model was compared to an experimental demonstration of cross-talk induced from exposure of a long section of fiber to a large temperature gradient, showing good agreement in behavior, despite some mismatch in total amplitude which requires further study.

This cross-talk, under typical probe parameters, is shown to be relatively small, and likely negligible for most applications. Nonetheless, the proposed model in this study hints at the possibility of compensating such effects via a cumulative estimation of the noise effects in all subsequent positions. Further study is required in order to determine the performance impacts of such a correction.

Chapter 5

New applications of CP-φOTDR

5.1 Fast characterization of the linear birefringence profile

Birefringence is a pervasive characteristic of optical fibers. While it is intentionally induced in some special fiber designs (*e.g.*, polarization maintaining fibers), it is most commonly an unavoidable consequence of remnant anisotropies and imperfections in the fiber geometry from the manufacturing process, or induced during installation from uneven stresses applied to the glass due to bending or twisting [30].

A core limitation of long-haul, high bit-rate communications in modern fiber optic links is polarization mode dispersion (PMD), which happens from the existence of undesired birefringence [186]. Its mitigation relies on the improvement of manufacturing techniques (thus, reducing the strength of the birefringence vector at any given fiber position), or on other strategies, such as spin processing [187], aiming to circumvent the undesired effects of PMD by manipulating the birefringence vector without directly reducing its strength.

The ongoing race to mitigate these effects has led to standard commercial fibers with remarkably low levels of birefringence, posing a difficult characterization challenge for existing distributed techniques. Several methods have been proposed and attempted, in order to retrieve spatially resolved measurements of a fiber's birefringence, which fall under the categories of direct and indirect measurements.

Indirect methods study the evolution of the state of polarization of orthogonally polarized waves in order to estimate the polarization beat length at any position (see section 2.3) through mathematical models. Some examples of these techniques can be seen in BOTDR-based birefringence estimation [188] or the polarization OTDR (P-OTDR) [189–191].

Direct methods, on the other hand, estimate birefringence by measuring differences in index for orthogonally polarized probes. There have been reports on direct estimation methods on shorter fibers based on OFDR [192, 193], or on high birefringence fibers using dynamic Brillouin gratings (DBG) [194, 195], although these have typically high requirements in polarization alignment of 3 interacting waves, and require dual ended access to the fiber. Similarly, frequency-demodulation φOTDR has been used to measure the linear birefringence in standard single-mode fibers [196]. Nevertheless, these reports were time-consuming (due to averaging and frequency-sweeping) and were limited to fibers with a comparatively high birefringence, compared to the current state-of-the-art.

In this section, we shall report the findings published in [150]. Here, we leverage the recent developments and achievable performances in CP-φOTDR techniques (described in previous sections), proposing a modified design with an added polarization control to enable direct distributed measurements of birefringence. We report a relatively fast, direct estimation of the linear birefringence profile in modern single-mode fibers with high sensitivity.

5.1.1 Theoretical principle

In a reflectometry-based estimation process, only linear birefringence produces a measurable effect. This may be understood by reviewing the effects of backscattering in polarization, as described in section 2.3. In fact, it has been shown that circular birefringence is indistinguishable from a rotation of the linear birefringence vector, in reflection [197].

Summarily, this may be understood by noticing that the effect of birefringence in the total travelled optical path length is reinforced for light travelling across the axes of birefringence in the linear case, and cancelled in the circular birefringence case. To understand this, consider two discrete reflectors i, j separated by a distance $L_{i,j}$ in an optical fiber, within a given resolution cell. In a linear birefringent medium, for light polarized along the fast (f) and slow (s) axes of birefringence, the phase difference of returning light from these scatterers is given by

$$\Delta\phi_{ij}^{s,f} = \frac{4\pi L_{ij}}{\lambda}(\overline{n} \pm B/2), \tag{5.1}$$

where the slow case corresponds to the "$+$" and the fast case to the "$-$", B is the linear phase birefringence of the medium and $\overline{n}$ is the mean refractive index for unpolarized light. Conversely, in the case of a purely circular birefringent medium, with circularly polarized light across both axes of polarization, we expect the following

$$\Delta\phi_{ij}^{s,f} = \frac{2\pi L_{ij}}{\lambda}(\overline{n} \pm B/2) + \frac{2\pi L_{ij}}{\lambda}(\overline{n} \mp B/2) = \frac{4\pi L_{ij}}{\lambda}\overline{n}, \tag{5.2}$$

for circular birefringence B. Here we clearly see that the round trip cancels the differences in optical path, yielding the mean refractive index. Generalizing for the case of an elliptically birefringent medium, only the linear birefringence component shall induce any measurable effect, owing to the reversal of the handedness of the SOP in the round trip (as explained at the end of section 2.3).

We will now describe the principle of birefringence estimation through the CP-φOTDR technique. Consider a homogeneous section of the optical fiber with two orthogonal eigenstates of polarization ($\hat{v}_1$ and $\hat{v}_2$, such that $\hat{v}_1^* \cdot \hat{v}_2 = 0$). The polarization of an incident polarized light pulse $\hat{s}$ can be decomposed into a superposition of waves along each of those eigenstates as

$$\hat{s} = (\hat{v}_1^* \cdot \hat{s})\hat{v}_1 + (\hat{v}_2^* \cdot \hat{s})\hat{v}_2. \tag{5.3}$$

The electric field backscattered at any given fiber section may thus be described as

$$e(t) = (\hat{v}_1^* \cdot \hat{s})e_1(t)\hat{v}_1 + (\hat{v}_2^* \cdot \hat{s})e_2(t)\hat{v}_2. \tag{5.4}$$

As we previously described, however, an optical fiber does not behave as a homogeneous linear birefringent medium (see section 2.3). Instead, the state of polarization of light, $\hat{s}$, changes continuously during propagation within a single-mode

fiber (due to fluctuations of the local birefringence vector).

When photodetected after probing with a chirped-pulse, equation 5.4 leads to the superposition of the time-delayed traces as a function of the effective local index. As such, the retrieved photodetected intensity trace can be described as

$$q(t) = |\hat{v}_1 \cdot \hat{s}|^2 p(t-\tau) + |\hat{v}_2 \cdot \hat{s}|^2 p(t+\tau), \tag{5.5}$$

for a noiseless CP-φOTDR signal $p(t)$, obtained for a reference refractive index $\overline{n}$. Here τ is the observed delay for a $\Delta n = B/2$, as dictated by the system's sensitivity [133]

$$\tau = -\frac{\nu_0}{\delta\nu}\frac{t_p}{\overline{n}}\Delta n; \quad \Delta n = \frac{B}{2}, \tag{5.6}$$

where ν_0 is the probe laser center frequency, $\delta\nu$ the chirp bandwidth and t_p the pulse width.

It is now useful to move to a 3D Stokes formalism of polarization and birefringence (see section 2.3). Consider $\hat{V}$ as the Stokes vector associated with $\hat{v}_1$, such that $-\hat{V}$ is the one associated to $\hat{v}_2$, and $\hat{S}$ as the Stokes vector of $\hat{s}$. We can now write

$$|\hat{v}_i \cdot \hat{s}|^2 = \frac{1}{2}(1 \pm \hat{V} \cdot \hat{S}) = \frac{1}{2}(1 \pm \gamma), \tag{5.7}$$

where $\gamma = \hat{V} \cdot \hat{S}$ and $i = 1, 2$, corresponding to the choice of the "+" and "-" case, respectively (so the resulting $\pm\gamma$ term equals 1 if $\hat{S}$ and $\hat{V}$ are aligned, and -1 if they are orthogonal).

Consider now two acquisitions from a CP-φOTDR, obtained by sending two orthogonal states of polarization $\hat{S}$ (subscript "+") and $-\hat{S}$ (subscript "-"). The return trace signals will exhibit the following form

$$\begin{aligned} q_+(t) &= \frac{1}{2}[(1+\gamma)p(t-\tau) + (1-\gamma)p(t+\tau)], \\ q_-(t) &= \frac{1}{2}[(1-\gamma)p(t-\tau) + (1+\gamma)p(t+\tau)]. \end{aligned} \tag{5.8}$$

Consider, now, the cross-correlation of both of these acquired traces (i.e., assume that the reference is taken with probe polarization aligned along one eigenstate of polarization, and measurement is taken with probe polarization aligned along the other eigenstate). The cross correlation yields

$$R_{+-}(t) = \frac{1}{4}[2(1-\gamma^2)c(t) + (1+\gamma)^2 c(t-2\tau) + (1-\gamma)^2 c(t+2\tau)], \tag{5.9}$$

in which $c(t)$ is the autocorrelation of the trace $p(t)$. One may verify that for light aligned with the eigenstates of polarization of the fiber ($\gamma = 1$), Eq. 5.8 simplifies to $q_+(t) = p(t-\tau)$ and $q_-(t) = p(t+\tau)$, and Eq. 5.9 simplifies to $R_{+-}(t) = c(t-2\tau)$. This is what's expected from equation 5.6, as an index change of B should result in a 2τ delay in the optical trace.

Using the GCC algorithm 3.4.4, the estimation of delay is given by

$$\delta = \text{argmax}\{R_{12}(t)\}. \tag{5.10}$$

Considering a Gaussian peak as a simple model for the main peak of the cross correlation function, we may replace $c(t)$ in equation 5.9 by $c(t) = \exp[-t^2/(2w^2)]$. The maximum of the cross-correlation function may then be determined by letting $dR_{+-}/dt = 0$. The induced delay from birefringence, when no external perturbation is applied to the the fiber, is limited by $|\delta| \leq 2\tau$, corresponding to the case in which the reference trace and measurement traces are obtained with probe polarization aligned to the two orthogonal eigenstates of polarization. Assuming small enough potential delays with respect to the main correlation peak width ($w^2 >> \tau^2$), the peak position can be shown to be approximated by

$$\delta \approx 2\gamma\tau. \tag{5.11}$$

The condition that equation 5.11 is valid for small enough delays compared to the width of the correlation peak implies that the limits of measurement of this system are given by the chosen probe properties. Since peak width is inversely proportional to the chirp bandwidth ($w \approx 1/\delta\nu$), by equation 5.6 we see that the condition $\tau < w$ is equivalent to $B < 2\overline{n}/(\nu_0 t_p)$. Therefore, the maximum measurable birefringence for a typical probe pulse of a few meters corresponds, is in the order of 10^{-6}, confirming the method is well suited to measuring standard telecommunication fibers, using typical CP-φOTDR parameters.

Determining birefringence

The method by which one obtains a local estimation of birefringence consists in measuring the projection of the linear birefringence vector in an orthogonal basis in Stokes space, formed by probing the fiber with the following polarization state pairs : $0^o/90^o$, +45^o/-45^o and left/right circular (i.e., with Stokes vectors $\hat{S} \pm(1,0,0)$, $\pm(0,1,0)$ and $\pm(0,0,1)$). While these evolve unpredictably as they propagate, their relative orientation is maintained assuming static conditions for the fiber (i.e., the fiber remains unaffected between sent pulses).

Measuring δ for each of the 3 orthogonal pairs yields 3 delays, each corresponding to the projection of the linear birefringence vector $\hat{V}$ on the basis vector aligned with the chosen pair (in Stokes space). While this offers no information on the orientation of the birefringence vector (since the actual disposition of the basis is unknown for each fiber position), we can use measure the linear birefringence strength at each position. Consider, then δ_i, for $i = 1,2,3$, the delay measured for each of the three orthogonal pairs of polarization. The total birefringence delay may be calculated as

$$\sqrt{\delta_1^2 + \delta_2^2 + \delta_3^2} = 2\tau. \tag{5.12}$$

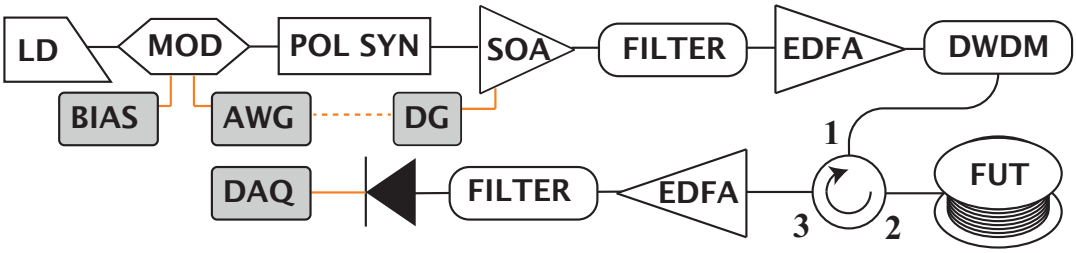

FIGURE 5.1: Schematics of the optical setup employed. LD - Laser Driver, MOD - Amplitude Modulator, POL SYN - Polarization Synthesizer, FILTER - Tunable filter, BIAS - Bias controller, AWG - Arbitrary Waveform Generator, DG - Delay Generator, EDFA - Erbium-doped fiber amplifier, DWDM - Dense wavelength division multiplexer, FUT - Fiber under test, DAQ - Oscilloscope

$$B = -\frac{\bar{n}}{\tau_p}\frac{\delta\nu}{\nu_0}\sqrt{\delta_1^2 + \delta_2^2 + \delta_3^2} \tag{5.13}$$

In the case of circular or elliptical local birefringence, we must consider the decomposition of the state into linear and circular components, where only the former gives a non zero contribution to the measured delay, as stated in equation 5.2.

5.1.2 Experimental demonstration

The assembled CP-ϕOTDR variant (depicted in figure 5.1) is composed of a very low phase-noise (<100 Hz linewidth) external cavity laser in continuous emission, externally modulated with a 50 ns long, 4 GHz chirped pulse waveform input. The electro-optic modulator (EOM) has its bias point selected in order to operate in maximally suppressed carrier.

The resulting modulated signal is sent through a polarization synthesizer, where the six states (3 orthogonal pairs in Stokes space) of polarization are cycled, before time-gating each pulse using a high extinction ratio semiconductor optical amplifier (SOA). A tunable filter is then used to isolate the upper sideband, removing the lower sideband and any remnant carrier. The resultant probe is amplified by an EDFA, followed by a 100 GHz DWDM to mitigate some of the ASE, and sent into the fiber under test through an optical circulator.

The recovered backscattered light is once again amplified, filtered and detected via a 20 GHz photodetector. The probe was pulsed at a rate of 1 kHz, and the digital acquisition was done at 10 GS/s. During post-processing, each cross-correlation was re-sampled to 10 times higher sampling through sinc interpolation, followed by a parabolic fit of the main peak, in order to mitigate sampling error in a computationally effective manner, with negligible addition of bias to the estimation (see section 4.1).

Each experiment consisted of a 1.8 s or 0.9 s long acquisition (depending on the interrogated fiber length, due to memory limitation of the acquisition device. During each acquisition, the polarization synthesizer was programmed to cycle through the

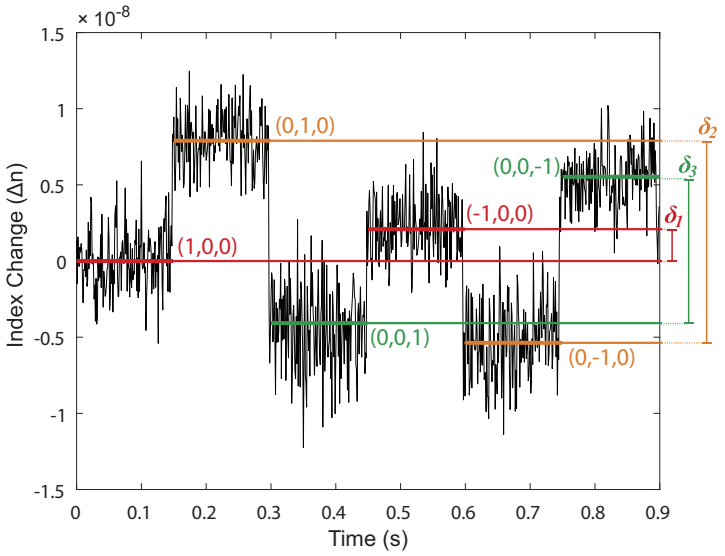

FIGURE 5.2: Visual description of a measurement at a given position. The values of δ required in Eq. 5.12 are obtained as from the perceived index difference between each orthogonal pair $(\hat{S}, -\hat{S})$. The numbers in the figure represent the $\hat{S}$ vector of light at the input for that given time section.

3 polarization state pairs $((1,0,0);\ (0,1,0);\ (0,0,1);\ (-1,0,0);\ (0,-1,0);\ (0,0,-1))$, holding each state for 300 ms in the two shorter fibers (1.8 s measurement) or 150 ms in the longer one (0.9 s measurement).

After processing, the measurand acquisition consists of a noisy, piecewise-constant function. The difference between the mean of each pair of piecewise constant sections (produced by probing with orthogonal states of polarization) is used to estimate the respective δ for that pair. An example depiction of the measurement procedure used to estimate the values of δ_i is depicted in figure 5.2.

After acquisition of all three deltas for a given position, the strength of the birefringence vector is estimated using equations 5.12 and 5.6.

This method for estimation of local birefringence was demonstrated in three different single-mode G.652D fiber spools from different manufacturers, each of a different length (1 km, 4 km and 10 km), and verified for self-consistency by comparing the acquired spatial linear birefringence profile measured from both ends of the fiber. In order to better visualize the results and remove noise, the measured birefringence was smoothed with a moving mean filter over 25 m.

Figure 5.3 shows the obtained results for the 10 km spool, and figure 5.4 shows the same experiment in three independent cases: The concatenation of the 4 km and 1 km fibers, the 4 km fiber and the 1 km fiber. In all figures, the black and green lines represent the acquired spatial profile when measured from each end of the fiber.

The results and an evaluation of the correlation between each pair of spatial profiles acquired (from each end) are summarized in Table 5.1. Column "Corr. Coeff." describes the correlation coefficient of both acquisitions, column $mean(B)$ describes

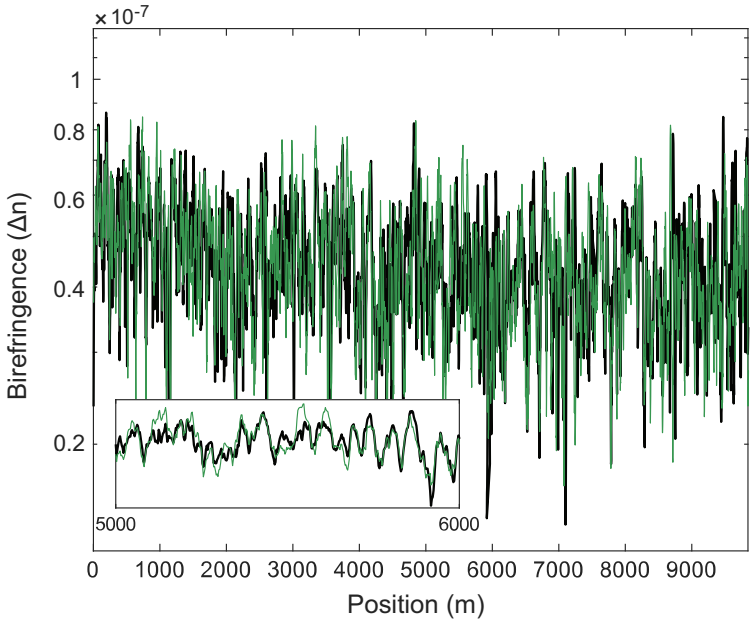

FIGURE 5.3: Birefringence profile obtained from both ends for the 10 km fiber. Spatial resolution of 25m (5 m pulse with a 25 m long moving average window applied).

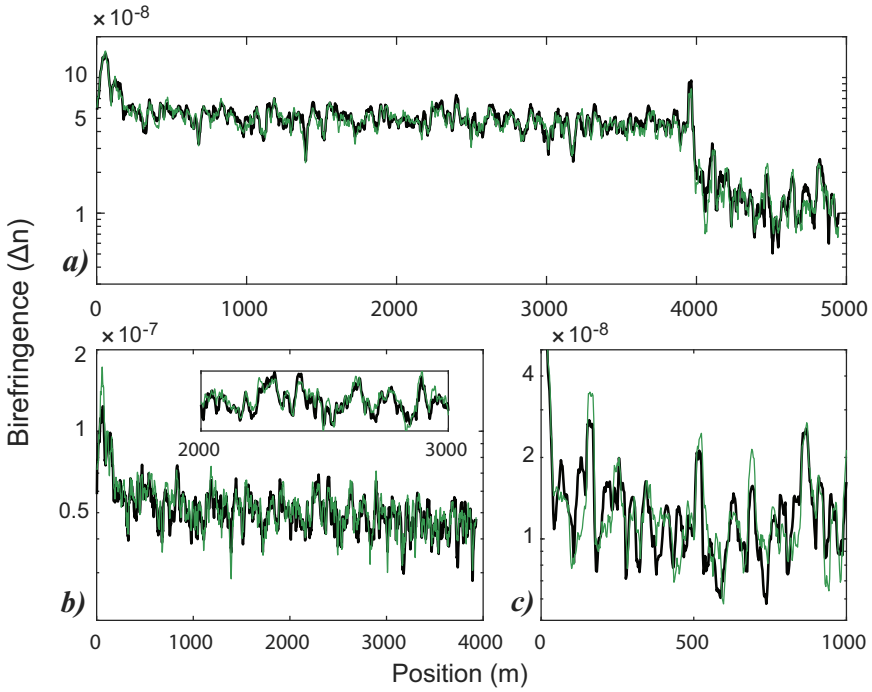

FIGURE 5.4: Birefringence profile obtained from both ends of a) 4 km + 1 km fiber concatenated; b) 4 km fiber; c) 1 km fiber. Spatial resolution of 25m (5 m pulse with a 25 m long moving average window applied).

TABLE 5.1: **Summary of characterization of each spool. Descriptions of each parameter in the main text.**

FUT	$mean(B)$	σ_{12}	Corr. Coeff.
1 km	1.4e−8	3.1e−9	0.91
4 km	5.3e−8	4.1e−9	0.92
10 km	4.5e−8	7.2e−9	0.81

the mean birefringence of each fiber, and column σ_{12} describes the standard deviation of the difference between measurements from both ends of the fiber, as an approximate estimation of the measurement error of the technique in each case. Notably, the noticeable decrease in average birefringence strength over the length of the longer fibers agrees with the bending induced birefringence expected from spooling ($\approx$ 20% in the 10 km fiber and $\approx$ 10% in the 4 km fiber): lower values of z in figs. 5.3 and 5.4 correspond to the inner layers of the spool, where the bending radius is smaller (thus, higher birefringence [30]). The verified change is consistent with a radius variation of some millimiters.

The small decorrelation verified in each acquired profile pair occurs from measurement noise, as well as temperature fluctuations, or other extrinsic environmental perturbations experienced by the fiber over the course of a single measurement. Note that while for the purposes of this research only a single cycle was used to perform the measurement, in principle several cycles may be used in order to obtain better performances (at the cost of measurement time).

5.1.3 Discussion

In this section we described the results published in reference [150]. We proposed and demonstrated a method to estimate the linear birefringence distribution along a spool of fiber, with high sensitivity and in a relatively quick time, with single ended access. While we limited ourselves to 10 km long fibers in length, the limit was imposed by the data acquisition device memory, and is not a hard limit of the technique. Indeed, as long as a relevant CP-φOTDR measurement can be produced, we expect the reported method to work.

In terms of spatial resolution, the limit may be tuned for each specific application. However, the pulse length should be comparatively small, with respect to the beat length of the fiber used (in order to avoid large gradients of birefringence along a single resolution cell). Whenever the birefringence vector undergoes fast spatial changes (much shorter than the spatial resolution, e.g. with spun fibers), we expect to measure the magnitude of the effective linear birefringence over the measured spatial resolution [198].

Additionally, the maximum measurable birefringence is inversely proportional to the pulse width used (as detailed in section 5.1.1). In our experiments, while we used a 25 m long spatial resolution (after averaging) for improved performances, we were fundamentally limited by the CP-φOTDR spatial resolution of 5 m, imposed

by the pulse width. Since the underlying model assumes small time-delays of the optical power trace, further work and analysis is required to assess the suitability of this method for highly birefringent fibers.

All the presented results consisted of a fast acquisition of a single cycle of the 6 polarization states (totalling 1 to 2 seconds). The fast measurement times raise the possibility to either average several consecutive cycles (in applications where speed is not a concern) for much improved performances, or to quickly determine the birefringence strength, which may be of interest for fast polarization-based distributed sensing in standard single-mode fibers [199].

5.2 Seismic measurements through *f-k* processing of DAS data

Distributed acoustic sensing methods facilitate dense measurements of strain, with high sensitivities, over very long distances. This advantage is decisive in applications such as pipeline protection [200], borehole monitoring [201], train tracking [202], and, as we aim to demonstrate in the following pages, for seismological measurements [36, 203]. The advantage in measurements of seismic activity is clear when considering that a DAS interrogated fiber comprises thousands of independent channels which may be measured in real-time, for long duration, providing dense spatially sampled measurements of seismic waves [36].

An ideal optical fiber seismic measurement array, however, should rely on dedicated fiber installations, with cabling specifically tailored for high and homogeneous mechanical coupling, and mitigating the influence of irrelevant sources of strain. Such a setup, however, would comprise prohibitive costs and installation complexity that might render it undesirable when compared to the alternative of installing an array of broadband seismometers, discouraging the adoption of the technique. Instead, the great potential of optical fiber seismology is evidenced in the possibility to retrofit pre-existing telecommunication fibers into sensing arrays by probing with typical DAS technology. This allows for a fast and cheap method to produce measurements of high spatial density and long coverage (tens of kilometers), by accepting the non-ideal sensing conditions of pre-installed telecommunication links.

This possibility fosters a clear purpose and drive for the employment of DAS technology in seismological measurements, as a supplement to other already established methods, with a relatively low entry barrier in cost. Nonetheless, there are challenges to be overcome if we are to retrieve relevant data from small amplitude seismic waves in conditions where the ambient noise may be overwhelming, and strain coupling may not be ideal. In this context, there are clear advantages in employing the CP-φOTDR technique for DAS measurements, given the performance reliability and immunity to fading points (see section 4.3), thus preventing spatial blind-spots and uneven density of measured positions in a probed array.

In this section, we report on the use of pre-installed telecommunication fiber in a metropolitan area to monitor seismic activity, in an environment where ambient noise sources are dominant over the contribution from seismic signals of interest. Specifically, we demonstrate a measurement of the 2018 Fiji earthquake (Magnitude M8.2) by using a telecommunication fiber in the city of Pasadena (California, United States of America). We show that the ambient noise can be filtered using 2D processing of the time-position signal obtained from the distributed strain signal. To do so, we exploit known properties of the seismic waves of interest (specifically, frequency range and wavenumber), and the high spatial density of high sensitivity measurements provided from a DAS acquisition. The recovered data allows post-processing in the reciprocal domain of time-position (frequency-wavenumber, shorthand *f-k*),

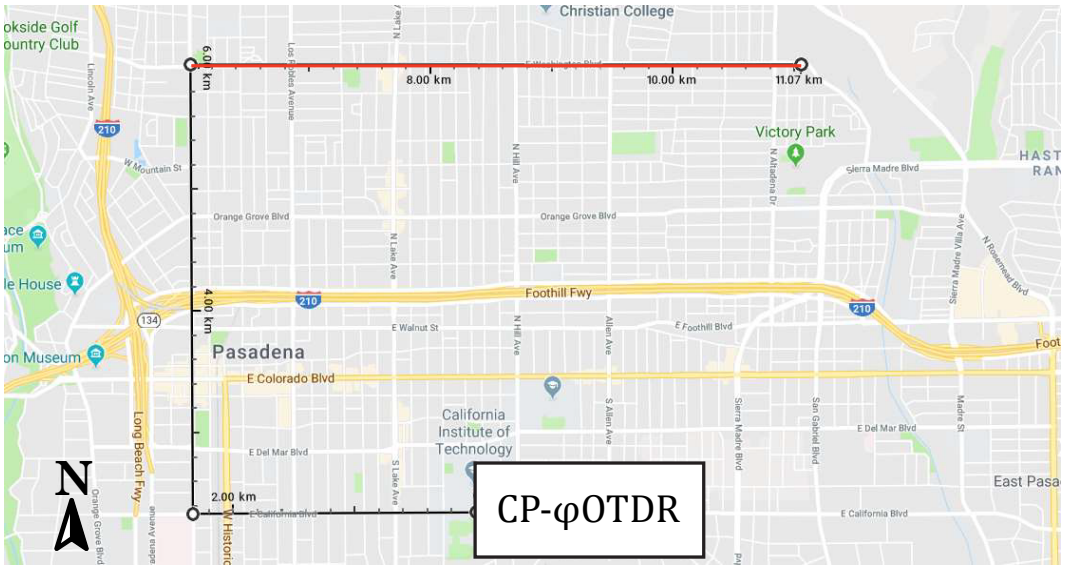

FIGURE 5.5: Rough depiction of the fiber array layout in Pasadena. Note that the total length of fiber is greater than the one depicted, due to fiber loops, and slight deviations in path. The red region depicts the section selected for analysis.

in order to successfully remove in-band noise from the seismic signal of interest.

5.2.1 Experimental description

The data was obtained from a fiber installation in the city of Pasadena (California, United States of America), which was being monitored continuously at the time of occurrence of the Fiji earthquake (Magnitude M8.2, August 19th 2018, 00:13 - 01:03 UTC). This fiber consists of standard G.652 cable and was installed for purposes of functioning as telecommunication link. A rough estimation of the spatial disposition of the interrogated fiber is depicted in figure 5.5. The sensing array is roughly divided in 3 main sections of measurement interest: the fiber exits the South Mudd building in the California Institute of Technology (where the interrogator is placed), going in the East-West direction for approximately 2 km. Then, there is a second section of straight fiber oriented South-North for about 6 km, followed by a final West-East segment for 5 km.

While these are the segments of interest for measurement, it is important to reiterate that the fiber disposition was not intended for measurement of strain data: the interrogated cable totals 25 km in length, due to the existence of fiber loops and deviations from the straight sections of cable shown in the figure. These include regions exposed to air which are heavily corrupted by noise signals (and fairly immune to the perturbations of interest).

The interrogation setup comprised a typical CP-φOTDR implementation with direct modulation emission arm, such as the one used in section 4.3. An external cavity laser is driven is controlled in current and temperature to fix its work point at a position which offers good linearity in the center frequency shift to current changes.

The laser diode current is then modulated with a sawtooth wave, and time-gated using a high extinction ratio SOA in order to produce the chirped pulse probe. The probe is then amplified via an EDFA, filtered through a dense wavelenght division multiplexer (DWDM), and launched into the fiber under test. Then, the backscattered light is recovered, amplified and filtered once again through a DWDM, and photodetected through a 9.5 GHz detector (with a 1 GHz electrical filter before acquisition at 1 GS/s). The generated probe pulses were 100 ns long (yielding 10 m spatial resolution) and covered a chirp bandwidth of 500 MHz. The traces were acquired at a rate of 2 kHz, and averaged in batches of 40 (in order to improve the trace SNR), resulting in an effective sampling rate of 50 Hz. Sampling error was mitigated via parabolic interpolation of the main peak of the correlation, due to the low computational cost.

As there was no dedicated section for the compensation of phase noise, the whole fiber was used for phase-noise compensation. This method is non-ideal as it introduces additional method noise in the fiber (due to strain noise present in all other positions). Additionally, such a method may slightly bias the amplitude measurements, since the perturbed section is used for compensation as well. As we aim to show, even in such conditions, it is possible to retrieve relevant seismic measurements. Recall that the strain coupling varies for all positions of measurement, which alone may affect the estimated strain amplitude at each position, and the varying disposition of the fiber in space leads to non-uniform strain perturbations across major lengths of fiber, so signals of interest are not fully spatially correlated and are averaged out during phase-noise compensation (see section 3.4.7).

5.2.2 *f-k* processing of strain data

The idea behind processing in the frequency-wavenumber domain consists in exploiting the information of the wave frequency and phase-velocity (wavenumber) simultaneously. Typical frequency domain processing enables the isolation of frequency bands of interest through, for example, the application of a window function in the frequency domain. The same principle is applicable when there is sufficient spatial sampling, so that a window function may be applied in the wavenumber domain as well. Combining both approaches, it is possible to generate a representation in the frequency-wavenumber domain, and derive the passband condition from prior knowledge of the dispersion relation (frequency/wavenumber) of the seismic waves of interest.

Essentially, *f-k* processing forces two conditions to be fulfilled for the signal to be considered within the passband. Therefore, noise components of the same band but of different wavenumber, or vice-versa, are easily rejected using this kind of processing. This type of processing is aided by the fact that, in this array, we have access to straight sections of fiber.

The *f-k* representation of data is obtained through 2D Fourier transform (through the 2D FFT algorithm) of the strain time-position map produced by the CP-φOTDR.

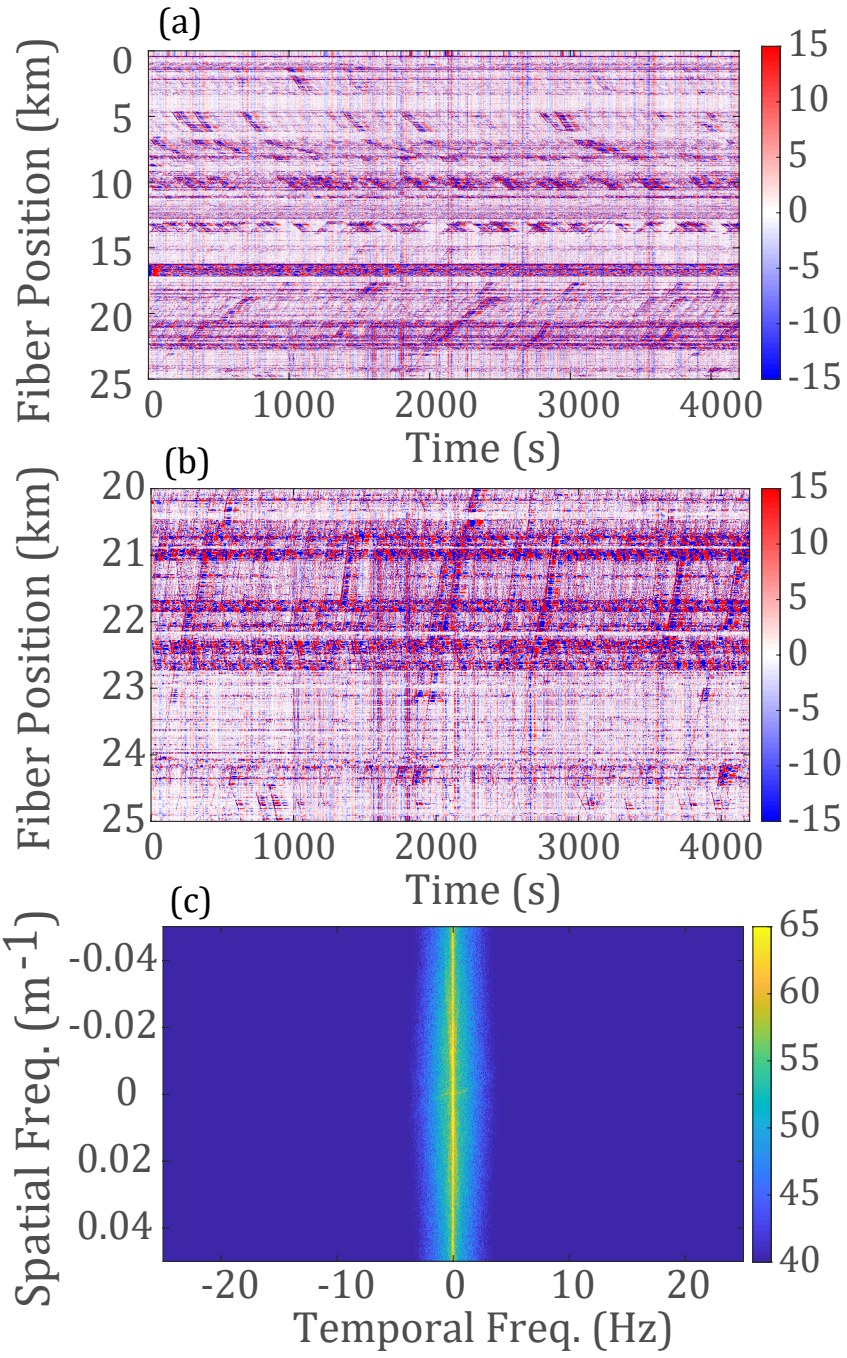

FIGURE 5.6: (a) Raw measurements of the whole interrogated Pasadena fiber array. Notice the vastly uneven noise levels and strain coupling. (b) Time-position strain map of the analysed section. Diagonal sections of increased noise comprise moving vehicles across the street. The faint near-vertical lines are the seismic activity that we pretend to isolate. (c) *f-k* map of the data. There is a dominant low frequency noise component. However, the seismic components can be observed as a faint low temporal and spatial frequency signals in the first and third quadrants (top right and bottom left), corresponding to fast travelling, long period waves, moving from west to east.

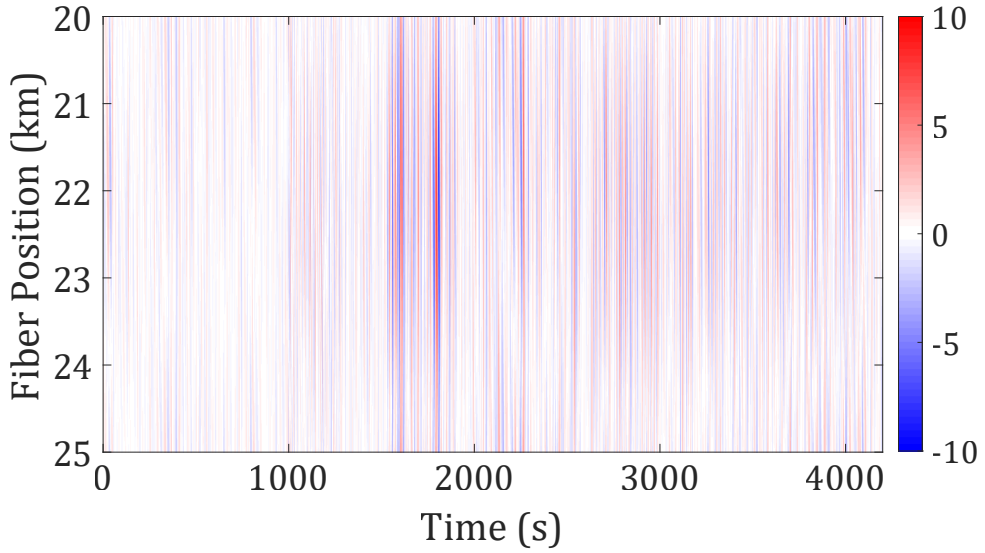

FIGURE 5.7: Time-position map after *f-k* filtering in the $[0.02, 1]$ Hz and $[0, 2 \times 10^{-4}]\text{m}^{-1}$ band, isolating the seismic signals of interest.

Since the fiber is installed in a metropolitan area, the dominant strain components in the strain time-position map will be due to strain noise sources such as ground vibrations induced from moving vehicles, and temperature drifts along the fiber cable. This is clearly observable by observing the raw strain data obtained in the last 5 km (West-East) section of the fiber, depicted in figure 5.6 a) and b). In the strain map, moving perturbations generate a linear trail of increased noise power with a slope proportional to the velocity of the perturbation. We may clearly distinguish diagonal regions of increased noise corresponding to moving vehicles along the section of fiber. Similarly, the variations of strain coupling are clearly distinguished as large variations in measurement noise power across different interrogated positions.

A closer look reveals some quasi-vertical (*i.e.,* long wavelength, low frequency perturbations) lines which originate from the seismic signal of interest. These waves reach velocities of several km/s, resulting in their vertical appearance in the strain map. Applying the 2D FFT to the strain data in figure 5.6 b) yields the *f-k* results in figure 5.6 c), where once again we clearly see a dominant component of low frequency noise from local strain and temperature gradients.

The dispersion curves for the seismic waves of interest are concentrated in the frequency band below 1 Hz and wavenumber below $2 \times 10^{-4}\text{m}^{-1}$. Applying a linear filtering process in the *f-k* domain, as a rectangular bandpass to the first and third quadrants of the Cartesian representation isolates the components of interest propagating in the West-East direction, with the wave properties of interest. The selected band was $[0.02, 1]$ Hz in frequency and $[0, 2 \times 10^{-4}]\text{m}^{-1}$ in wavenumber. The result of filtering is depicted in figure 5.7, preserving only the quasi-vertical lines of the original signal, while removing most of the metropolitan noise present in figure 5.6.

The filtered strain measurements of figure 5.7 were then stacked and averaged

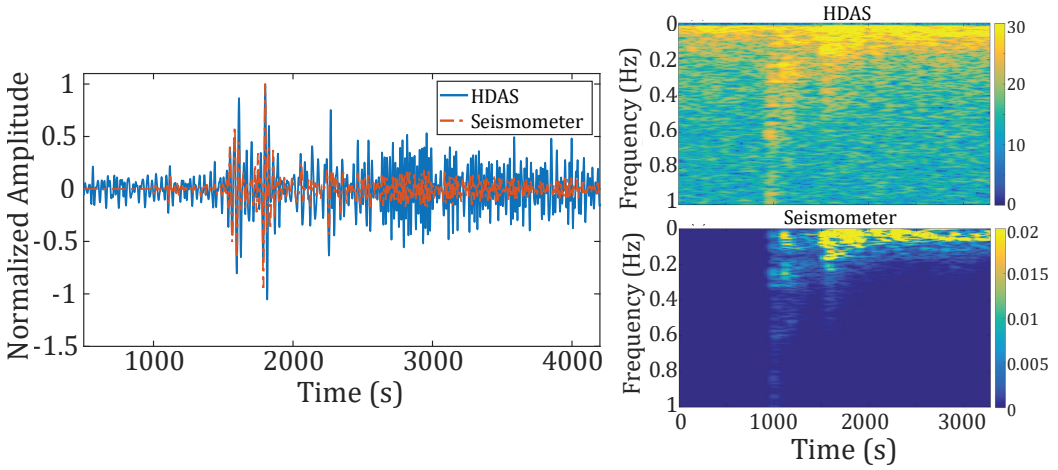

FIGURE 5.8: Right: Comparison between the stacked traces acquired by the HDAS and a reference W-E seismometer. Despite the much greater noise of the HDAS signal, the signal features are clearly identifiable in both sensors. Left: Comparison of spectrograms obtained by HDAS and seismometer measurements.

for comparison with a local seismometer. Figure 5.8 depicts the comparison of the obtained strain signal from the DAS measurement and a reference West-East seismometer signal located nearby, as well as a comparison of the spectrogram representations of the strain signals. While it is clear that the DAS signal is much noisier than the seismometer data, there is clear correlation between both measurements, validating the possibility of DAS for measurements of seismic activity.

5.2.3 Conclusions

The results described in this section, which were presented at the OFC 2019 conference [148], show a proof-of-concept demonstration of the use of retrofitted metropolitan area fibers for seismic measurements, even when considering the non-ideal conditions of installation. We demonstrate that the high spatial sampling provided by DAS measurements is conducive to isolation of seismic signals of interest in post processing, and removal of most of the metropolitan noise sources from measurement. The obtained signals were compared to those obtained by a traditional seismometer with high correlation. Particularly, the most notable times-of-arrival of different wave features are clearly distinguishible in both the HDAS and seismometer measurements, proving the potential use of CP-φOTDR in instrumenting telecommunication links for high sensitivity geophysical measurements.

The processing methods used in this section were fairly simple and comprise only a proof of concept, motivating new research in new and more sophisticated methodologies to extract seismic data from high spatial density measurements of strain, enabled by DAS technology.

5.3 Distributed measurement of sound pressure using a sensitivity enhancing cable structure

While optical fiber sensors are directly suited for measurements of longitudinal strain and temperature, a wide range of other parameters can be probed by additional engineering of either the waveguide (i.e. through the use of special fibers) or specialized cables or coatings. In the latter case, these parameters are usually transduced into measurable longitudinal deformations/thermal variations by the cable, enabling a wide range of parameters to be probed using standard silica glass fibers.

One particularly challenging parameter of interest for optical fiber measurements is pressure, since the effects of an applied pressure on the fiber imposed by Poisson effect (*i.e.*, inducing a measurable deformation) are extremely small. Measuring sound waves, for instance, fundamentally consists in a pressure measurement, given the lack of direct longitudinal deformation imposed by changes in air pressure on the optical fiber. As a result, direct measurements of sound using optical fibers are severely lacking in performance, or downright impossible.

Nonetheless, there is reason to strive for fiber-based sound measurement alternatives, as some applications demanding acoustic monitoring over long distances would benefit from the advantages of fiber-sensing over electronic alternatives. Namely, the vast multiplexing potential (reducing cost and installation complexity) and the passive nature of optical fiber sensors, enabling their installation in hazardous sites which may be threatened by explosion hazards (such as quarries or industrial plants).

Early demonstrations of fiber microphones/hydrophones appeared in the form of simple dual path interferometers (e.g., a Mach Zehnder design [204]). These proofs-of-concept consisted of punctual demonstrations of measurement, which failed to capitalize on the distributed potential of fiber measurements. The recent developments in fiber-based sensing, specifically in the field of DAS, have brought a resurgence of interest in the capture of sound using optical fibers, in a distributed fashion over long lengths of interrogated fiber cable. Current attempts rely, for the most part, of φOTDR-based implementations. Nonetheless, the innate insensitivity to pressure of the optical fiber remains a challenge that needs to be addressed, often requiring the use of diaphragm-like structures to amplify the acoustic response to sound waves.

One such demonstration used a phase-demodulation φOTDR [205], with coherent detection, to retrieve the strain experienced by a fiber section attached to a Polystyrene membrane. While the addition of a membrane addresses the lack of sensitivity, it comes at the heavy cost of rendering the measurement punctual, instead of distributed. At most, a quasi-distributed approach can be considered, if a series of independent membranes are attached to sections of fiber, each producing an effective sensor. Also, in this work, the focus was on relatively loud sound pressure

waves, above 90 dB (re 20 μPa) sound pressure level (SPL). More recent attempts [206] achieved better performances (measuring signals as low as 73 dB SPL) relying on a similar principle, but with a sheet metal membrane to detect a sound wave emitted at 5 cm distance. Once again, since each sensing point requires an independent membrane, this demonstration amounts to a quasi-distributed measurement. One other attempt traded the flat membrane by cylindrical coils, with fiber spooled around the cylinder [207]. This is advantageous for two reasons: the increased uniformity in the spatial response of the structure to the perturbation, and the ability to improve performance by using a longer fiber section per effective sensor. Essentially, each sensing position consists of a cylindrical structure, and second, the length of the cylindrical structure defines the gauge length of each sensor. Therefore, the fiber coiled around each sensor can be made as long (or as short) as needed in order to accommodate for the performance and number of sensing positions requirements. Still, this does not comprise a fully distributed approach.

In the following pages, we propose and assess the potential of using a flat cable structure that converts applied transverse pressure into longitudinal strains, with potential for fully distributed sound pressure measurements. We characterize the cable sensitivity and frequency response, interrogating with a chirped-pulse φOTDR, and discuss the potential limits of the method.

5.3.1 Plane cable structure design and principle

Sound measurements using optical fibers typically require the use of a diaphragm or membrane structure in order to convert air movements into longitudinal strain along the fiber. In order to avoid the need to install individual membranes, thus mitigating the distributed potential of a fiber sensor, we used a flat cable design in which sections of fiber are interleaved in an oscillatory fashion along the flat cable.

In our proof-of-concept sample, the fiber meanders back and forth in the cable three times with the oscillations displaced by a third of the length of a full oscillation (the fiber disposition within the cable is seen in figure 5.9).

This cable consisted of a 1.1 meter long strip, 8 cm in width and 2 mm in thickness. It was made by containing the fiber within two 1mm-thick rubber strips, which were then joined by a layer of liquid rubber and pressed with an uniform weight for a few days for curing. The fiber within the strip had a total length of 7 meters.

The spatial resolution of the sound measurement system, in this case, is determined by the length of interrogated section of the structure, not of fiber. The oscillatory disposition of fiber entails that 1 meter of structure encompasses $F \approx 2.1$ meters of fiber, F being the conversion factor. The spatial resolution of the measurement should be considered

$$SR_{structure} = \frac{SR_{\varphi OTDR}}{F}, \tag{5.14}$$

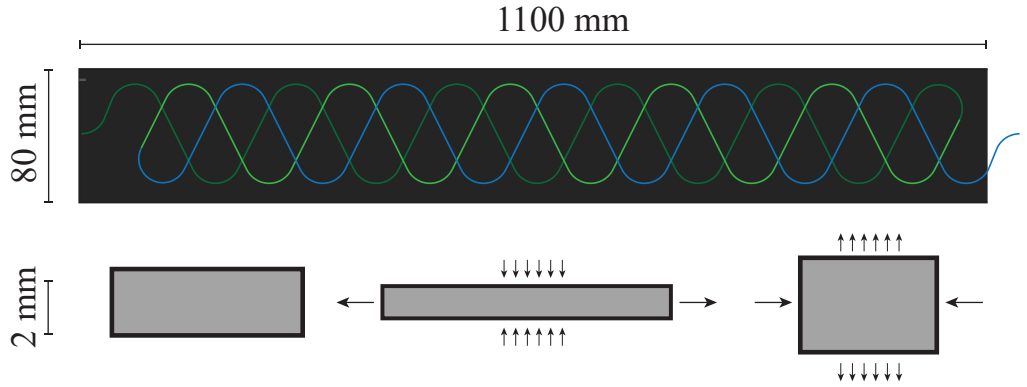

FIGURE 5.9: Schematic of pressure sensitivity enhancing structure (top) and visual description of working principle (bottom)

where $SR_{\varphi OTDR}$, typically, consists of the half the length of pulse used for interrogation (see section 3.3).

The working principle of this structure is depicted in the bottom part of figure 5.9. Through Poisson effect, any normally applied pressure to the surface of the strip induces an strain extension in all directions orthogonal directions. The strain component induced along the width of the structure translates into a longitudinal strain of the straight sections of fiber within the cable, thus resulting in a net longitudinal strain across the fiber length.

5.3.2 Sound measurements

Interrogation Setup

The fiber was interrogated using a typical external modulation CP-φOTDR (section 3.4.3). Light from a narrow linewidth external cavity laser diode (LD) is sent through an electro-optic modulator (EOM), which modulates the light in amplitude with a chirped pulse waveform, the modulator being set for suppressed carrier operation. The chirped waveform is generated by an arbitrary waveform generator (AWG), outputting a 35 ns long chirped pulse, covering 4 GHz with a center frequency of 10 GHz.

The resulting light, consisting of both generated sidebands and the residual carrier wave is time-gated through a semiconductor optical amplifier (SOA) driven by a delay generator (DG). The generated pulse is then amplified by an EDFA, filtered using a 100 GHz dense wavelength division multiplexer (DWDM) and launched into the fiber.

The backscattered portion of light is then recovered, amplified, and filtered using a narrow tunable filter, configured to allow only the upper sideband in the passband. The resulting light is detected using a 9.5 GHz low noise photodetector.

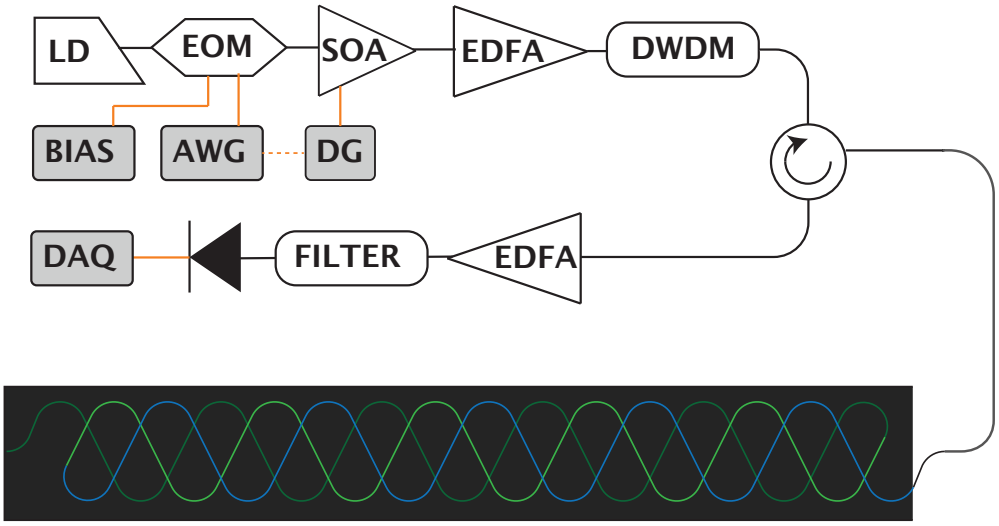

FIGURE 5.10: Setup used for the measurement of sound pressure. LD: Laser Diode; EOM: Electro-optic Modulator; SOA: Semiconductor optical amplifier; DWDM: Dense Wavelength Division Multiplexer; BIAS: Bias controller; AWG: Arbitrary Waveform Generator; DG: Delay generator; EDFA: Erbium-doped Fiber Amplifier; FILTER: Tunable Filter; DAQ: Oscilloscope.

Each measurement consisted of the acquisition of 65536 consecutive traces, each sampled at 10 GS/s, obtained at a rate of 50 kHz. The resulting maximum measurable time was $\sim$ 1.3 s (limited by the oscilloscope's memory depth).

The employed laser mitigates the need for phase-noise compensation (see 3.4.7), and sampling error was removed by signal reconstruction at 10 times higher sampling through sinc interpolation, followed by a parabolic fit, yielding negligible introduction of bias in the estimation. Note that the spatial resolution of the system (limited by the pulse width) is 3.5 meters. Accounting for the structure (equation 5.14), this yields a spatial resolution of the measurement system of $\sim 1.67m$.

Experimental results

In order to assess the performance of the cable strip in measuring sound pressure waves, we attempted to isolate it from mechanical vibrations by placing it in an optical table. As a reference, we used a calibrated soundmeter (TENMA 72-942), with the sensor placed at the center of the structure. A portable loudspeaker was used to generate the sound, placed at $\sim$ 1 m above the cable. This soundmeter was set to "A" frequency weighting in order to mitigate the influence of low frequency environmental noise from the laboratory in the readings of sound pressure level (*e.g.*, due to the fans of surrounding instruments), while keeping the full frequency response at 1 kHz. With this setup, the background noise of the laboratory was measured at around 55 dB ("A" frequency weighing).

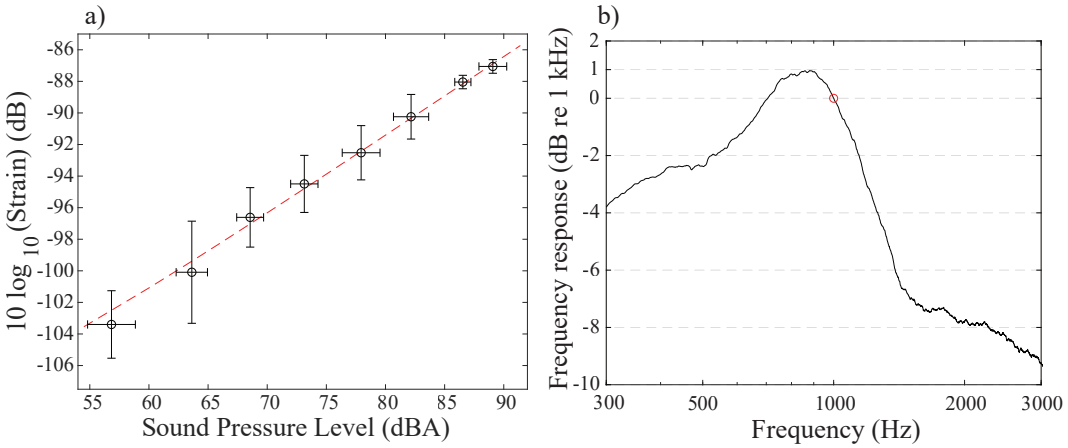

FIGURE 5.11: Characterization of the structure. (a) Sensitivity @ 1 kHz and (b) frequency response.

The sensitivity of the structure was determined through a series of 1 second long acquisitions, with the loudspeaker emitting a 1 kHz sine wave at varying intensities. The root-mean-square power of the 1 kHz strain component measured by the strip was then compared to the sound pressure level reported by the portable soundmeter. The selected position of measurement corresponds to the mid-point of fiber, which maximizes the response of the structure to the effects of the soundwave. The sensitivity at this position, at 1 kHz, was measured to be 3.6 nε/Pa (rms). The characterization can be seen in figure 5.11 (a).

We then measured the frequency response of the cable structure by sending a 0.6 s long chirped waveform from 300 Hz to 3 kHz. This measurement was repeated 10 times and averaged in order to improve the SNR of the acquisition. The normalized frequency response (relative to the sensitivity at 1 kHz) is represented in figure 5.11 (b), after a smoothing moving mean filter with width of 300 Hz.

It seems that the structure is most sensitive in the 530 to 1150 Hz range, in which the frequency response is contained within 3 dB of its sensitivity at resonance, following a sharp decline for higher frequencies, and a slow decline at lower frequencies. This band shall hereafter be denoted as the sensitive band of the structure. The reason for the narrowness of the band requires further research, in order to improve the responsive band on future prototypes.

With this characterization, we may determine the performance limits of the structure. Following the reasoning explained in section 4.1, the additive-noise limited lower bound of performance is given by the Cramér-Rao Lower Bound, and can be estimated knowing the trace SNR, chirp bandwidth and pulse width [139]. The SNR of the optical trace was estimated at 13 dB. In terms of strain, this yields a $\sigma_{CRLB} \approx 9.8 \times 10^{-10}\varepsilon$, corresponding to a noise floor at $\sigma_{CRLB} \approx 6.2 \times 10^{-12}\varepsilon/\sqrt{\text{Hz}}$, for the employed parameters, considering 50 kHz trace acquisition rate. A rough estimation of the noise floor in SPL (considering the sensitivity at 1 kHz, although a more rigorous derivation should keep in mind that the frequency response of the

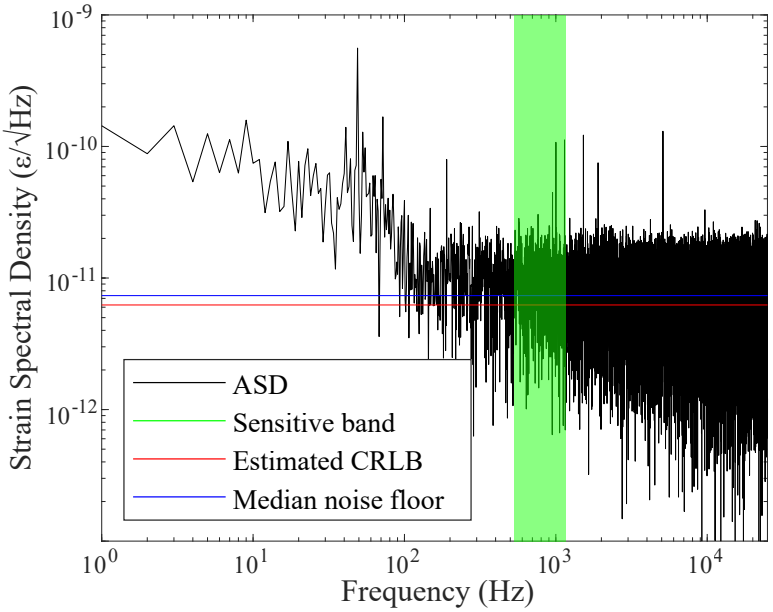

FIGURE 5.12: Amplitude spectral density of strain measurements. Green region denotes the defined sensitive band for the structure, where performance is within 3 dB of maximum sensitivity.

structure) yields a noise floor of 39 dBA/Hz SPL, and overall noise power at 67 dBA SPL, considering only the noise components within the sensitive band. The strain spectrum obtained is depicted in figure 5.12 for one example acquisition, as well as the sensitive band and the calculated CRLB.

5.3.3 Conclusions

In this section, we have proposed and characterized a new specialized cable able to convert pressure into longitudinal strains due to the geometrical disposition of the fiber within it, enabling distributed sound measurements. While the results presented in this section are preliminary and demand further investigation, we provide a proof-of-concept for fully distributed sound sensing, without relying on individual membrane or fiber structures. Additionally, we have reported (to the best of our knowledge) on the lowest noise floor in a distributed fiber microphone, as we were able to clearly identify sound waves with $\sim$ 55 dB SPL with 1 second integration time.

Further research is needed to understand the narrow frequency response, in order to potentially improve it in future prototypes, and in characterizing the spatial response and directivity of the cable to sound pressure. Additionally, the presence of several periodic strain gradients over the measurement resolution (due to oscillatory disposition of the fiber within the structure) may contribute to decorrelation of the trace, which should be assessed for potential performance impacts.

Chapter 6

Conclusions

Throughout this work we have presented several studies which build towards a more complete understanding of DAS technology, specifically through developments of the CP-φOTDR technique. In addition, we have identified and validated new potential areas of application. Both of these achievements were in direct accordance with the proposed objectives to be developed for the doctoral project.

We began this work by presenting the theoretical background required for the complete understanding of the fiber optic sensing technologies studied during the doctoral thesis. We also evaluated the current state of the art of distributed sensing technologies aimed at dynamic strain measurements, with a focus on φOTDR methods. We then presented an in-depth theoretical explanation of the principle of CP-φOTDR, compounding the preexisting body of knowledge with insights achieved from our research work.

Chapters 4 and 5 report the research work performed during the doctoral program. The main focus of research was presented in Chapter 4, where we improved the current understanding of CP-φOTDR and leveraged our findings towards designing general improvement strategies. In the first work we presented, we considered the effects of the characteristic estimation process of CP-φOTDR on the accuracy of its measurements. We derived the minimum variance achievable from this type of estimation, as a function of the retrieved signal properties. This analysis seemed to indicate that, if limited by additive noise sources, and using typical probe parameters, dynamic strain sensitivities of $\sim p\varepsilon/\sqrt{\text{Hz}}$ should be achievable at high acoustic frequencies. We then proposed a simple method to reach these levels of performance at higher acoustic frequencies, by adequately interpolating the cross-correlation function before time-delay estimation and then cancelling the first-order effects of laser phase noise.

The second work we presented aimed to analyze and address the current limits of maximum measurable perturbations using the CP-φOTDR technique. We showed that there is a soft upper bound of measurable strain, after which the probability of obtaining an estimation outlier is non-negligible. As an improvement, we proposed a slight variation of the interrogation algorithm which measures the strain incrementally, thus maximizing the similarity between cross-correlated traces. The limitations, then, are imposed on the shot-to-shot measured strain, instead of the

absolute measured strain. We also show that it is possible to further exploit the acoustic oversampling to increase the robustness to outliers when working close to the shot-to-shot strain limits. With this strategy, we demonstrated the measurement of a sinusoidal strain wave at 50 Hz with 1190 $\mu\varepsilon$ peak-to-peak amplitude, with 3.5-meter spatial resolution.

We then presented an experiment to evaluate the statistical distribution of noise in CP-φOTDR, as a way to validate and quantify the claims of increased robustness. We experimentally verified the measurement noise distribution as a function of position, over a long measurement time, showing that the noise power varies is contained within a $\sim$ 4 dB range. In contrast, phase-demodulation based systems show much greater variability of performance, with several fading positions of impossible measurement. Finally, in this chapter, we delved further into the implications of the TDE-based processing characteristic of the chirped-pulse technique. Specifically, we show how this may lead to cross-talk between independent events affecting the fiber, due to the effect of changing the optical path on the time-of-arrival of the pulse at different fiber positions. These differences in time-of-arrival may be misinterpreted as perturbations in the CP-φOTDR technique. We quantified these effect for typical probe parameters, observing an error of $\sim 10^{-6} K \cdot m^{-1} K^{-1}$ (in temperature), which, while small, may not be negligible in some application environments.

In chapter 5, we focused on developing proofs-of-concept for applications other than simple strain or temperature measurements. This involved specific alterations to the technique, either by changing the sensing fiber, the optical setup, or by developing application-specific post-processing.

We demonstrated the potential for fast, distributed characterization of linear birefringence in standard single-mode optical fibers by adding a polarization synthesizer to the traditional setup and probing the fiber with a sequence of controlled polarization states. We were able to measure the very low levels of birefringence in standard single-mode fibers (up to 10^{-8}) with only 1 to 2 seconds of measurement.

We also demonstrated the potential of CP-φOTDR for geophysical measurements in seismology, by employing retrofitted telecommunication fibers installed in metropolitan areas. Relying on the high spatial density of measurements, we are able to isolate the frequency-wavenumber characteristics of the seismic waves of interest and the direction of arrival. In doing so, we were able to mitigate most metropolitan noise and measure the 2018 Fiji Earthquake with an array in Pasadena, CA, at roughly 9000 km of distance. The results were confirmed by comparison with a nearby seismometer.

Finally, we demonstrate measurements of sound waves by using a fiber embedded in a flat cable structure, which amplified the response of the fiber to sound pressure waves. The structure uses the Poisson effect on the cable to longitudinally stretch sections of fiber. With this, sound waves as low as 55 dB SPL were detected.

Overall, the research work presented in this thesis constituted a stride in the development of the CP-φOTDR technology.

6.1 Open lines of research

The work presented in this dissertation leaves clear paths for exploration and investigation. Specifically, with respect to improving the current performance of the technique, we identify the following open lines of research:

- As we demonstrated, the current dynamic strain sensitivity is limited at higher acoustic frequencies from the estimation process. The limits are a function of signal parameters, specifically bandwidth, SNR and the pulse width. While pulse width is directly tied to the spatial resolution, there is an implication that increased signal bandwidth or trace denoising methods may work in favor of further improving the noise-floor. Additionally, while this limit is achieved at higher acoustic frequencies, there is vast room for improvement at lower acoustic frequencies ($<$ 100 Hz), where CRLB-limited levels of performance are still unreachable, motivating research on the sources of noise and mitigation strategies in that frequency band.

- The improvements of strain range proposed in this work heavily impact the noise performance of the sensor. As such, there is an implicit trade-off between noise floor and sensing dynamic range. The study of intelligent algorithms for updating the reference, and correcting the accumulation of noise error due to the reference update, as such, is desirable.

- We described the cross-talk induced from perturbations at supposedly uncorrelated measurement positions. It would be interesting to identify potential ways of compensating the cross-talk, for applications where large perturbations may affect very long sections of fiber coherently. Additionally, it is likely that such a compensation would entail a spatially cumulative measurement, which might have implications on correlated noise levels.

On the other hand, the work developed in chapter 5 opens the possibility to new research lines in new applications. For example, we identify the following open lines of research:

- The possibility to retrieve birefringence fast from standard telecommunication fibers may open the possibility to birefringence-based distributed sensing using such fibers. As such, we see potential in trying to measure changes in birefringence in SMF as a result of external stressors: e.g., induced magnetic fields, mechanical torsion, bending, or pressure.

- Seismological measurements using distributed acoustic sensing may benefit from additional phased-array processing techniques, given the high spatial density of sensing positions. Seismic measurements using DAS is currently seeing a lot of attention from the geophysical community.

- The presented results for sound measurement are still preliminary and open the possibility to develop similar structures with improved sensitivities and frequency response, by appropriate selection of materials and geometry. Additionally, the presented solution should be characterized in its spatial response.

6.2 Publications by the author

6.2.1 Publications in scientific journals

2020 High-resolution chirped-pulse φ-OTDR by means of sub-bands processing
L. Marcon et al., Journal of Lightwave Technology 38 (15) 4142-4149

2020 Long-Range Distributed Solar Irradiance Sensing Using Optical Fibers
R. Magalhães et al., Sensors 20 (3), 908

2020 Fast and direct measurement of the linear birefringence profile in standard single-mode optical fibers
L. Costa et al., Optics Letters 45 (3), 623-626

2019 Analysis of Disturbance-Induced Virtual Perturbations in Chirped Pulse φ-OTDR
L. Marcon et al., IEEE Photonics Technology Letters 32 (3), 158-161

2019 Distributed Acoustic Sensing Using Chirped-Pulse Phase-Sensitive OTDR Technology
M. R. Fernández-Ruiz et al., Sensors 19 (20), 4368

2019 Distributed detection of hydrogen and deuterium diffusion into a single-mode optical fiber with chirped-pulse phase-sensitive optical time-domain reflectometry
A. Garcia-Ruiz et al., Optics letters 44 (21), 5286-5289

2019 Fully Distributed Optical Fiber Strain Sensor With $10^{12}\varepsilon/\sqrt{Hz}$ Sensitivity
L. Costa et al., Journal of Lightwave Technology 37 (18), 4487 - 4495

2019 Analysis and Reduction of Large Errors in Rayleigh-Based Distributed Sensor
L. Zhang et al., Journal of Lightwave Technology 37 (18), 4710-4719

2019 Dynamic Measurements of 1000 Microstrains Using Chirped-Pulse Phase-Sensitive Optical Time-Domain Reflectometry
H.D. Bhatta et al., Journal of Lightwave Technology 37 (18), 4888-4895

2018 Steady-sensitivity distributed acoustic sensors
M.R. Fernández-Ruiz et al., Journal of Lightwave Technology 36 (23), 5690-5696

6.2.2 International Conference Proceedings

2020 Fast and direct measurement of longitudinal birefringence distribution in conventional single-mode optical fibers
L. Costa et al., Optical Fiber Sensors *(accepted for oral presentation)*

2020 Pressure transducing plane cable structure for fully distributed sound measurements
L. Costa et al., Optical Fiber Sensors, *(accepted for oral presentation)*

2019 Teleseisms monitoring using chirped-pulse OTDR
M.R. Fernández-Ruiz et al., Seventh European Workshop on Optical Fibre Sensors 11199, 1119921

2019 Characterization and modelling of induced virtual perturbations in chirped pulse - OTDR
M. Soriano-Amat et al., Seventh European Workshop on Optical Fibre Sensors 11199, 111992A

2019 Boosting the spatial resolution in chirped pulse -OTDR using sub-band processing
L. Marcon et al., Seventh European Workshop on Optical Fibre Sensors 11199, 111991W

2019 Optimization of first-order phase noise cancellation in CP-OTDR
L. Costa et al., Seventh European Workshop on Optical Fibre Sensors 11199, 111992D

2019 The measurement of large and fast strains using Rayleigh backscattering in optical fibers
H.D. Bhatta et al., OASIS 7

2019 Monitoring of remote seismic events in metropolitan area fibers using distributed acoustic sensing (DAS) and spatio-temporal signal processing
H.F. Martins et al., 2019 Optical Fiber Communications Conference and Exhibition (OFC), 1-3

2018 Reaching $p\varepsilon/\sqrt{Hz}$ sensitivity in a distributed optical fiber strain sensor
L. Costa et al., Optical Fiber Sensors, TuD3 **Awarded best student paper**

2018 Extending the measurement of true dynamic strain via chirped-pulse phase-sensitive optical time domain reflectometry to 100s of microstrains
H.D. Bhatta et al., Optical Fiber Sensors, WF14

2018 Statistical Analysis of SNR in Chirped-pulse OTDR
M.R. Fernández-Ruiz et al., Optical Fiber Sensors, WF16

2018 Transforming the Fiber-Optic Network into a Dense and Ultrasensitive Seismic Sensor Array
A Garcia-Ruiz et al., 2018 20th International Conference on Transparent Optical Networks (ICTON), 1-4

6.2.3 National Conference Proceedings

2019 Sensor acústico distribuido en fibra óptica con una sensibilidad de $p\varepsilon/\sqrt{Hz}$
L. Costa et al., OPTOEL 2019 - Zaragoza, **Awarded best student paper**

2019 Caracterización de errores sistemáticos inducidos en sistemas -OTDR de pulso chirpado
M. Soriano-Amat et al., OPTOEL 2019 - Zaragoza

2019 Monitorización de actividad sísmica usando sensores distribuidos en fibra basados en OTDR y pulsos con chirp
M.R. Fernandez-Ruiz et al., OPTOEL 2019 - Zaragoza

2017 Non-destructive guided wave damage detection using FBG sensors
L. Costa et al., OPTOEL 2017 - Santiago de Compostela

Bibliography

[1] J Hecht. *City of Light: The Story of Fiber Optics*. Oxford University Press paperback. Oxford University Press, 2004. ISBN: 9780195162554.

[2] Jacques Babinet. "Note on the transmission of light by sinuous canals". In: *Comptes Rendus* 15 (1842), p. 802.

[3] D. Colladon. "On the reflections of a ray of light inside a parabolic liquid stream". In: *Comptes Rendus* 15 (1842), p. 800.

[4] J Tyndall. "On some phenomena connected with the motion of liquids". In: *Proc R Inst Great Britain* 35.901 (1854), pp. 325–326. ISSN: 00280836. DOI: 10.1038/035325a0.

[5] William K. Johnston. "The birth of fiberoptics from "light guiding"." In: *Journal of endourology / Endourological Society* 18.5 (2004), pp. 425–426. ISSN: 08927790. DOI: 10.1089/0892779041271445.

[6] K. C. Kao and G. A. Hockham. "Dielectric-Fibre Surface Waveguides for Optical Frequencies." In: *IEE proceedings. Part J, Optoelectronics* 133.3 (1986), pp. 191–198. ISSN: 02673932. DOI: 10.1049/ip-j.1986.0030.

[7] Govind P. Agrawal. *Fiber-Optic Communication Systems*. 2002. DOI: 10.1002/0471221147.

[8] Gerd Keiser. "Optical Fiber Communications". In: *Wiley Encyclopedia of Telecommunications*. 2003. DOI: 10.1002/0471219282.eot158.

[9] E. Desurvire. "Erbium-doped fiber amplifiers for new generations of optical communication systems". In: *Optics and Photonics News* 2.1 (1991), p. 6. ISSN: 1047-6938. DOI: 10.1364/opn.2.1.000006.

[10] Glenn N. Merberg. "Current status of infrared fiber optics for medical laser power delivery". In: *Lasers in Surgery and Medicine* 13.5 (1993), pp. 572–576. ISSN: 10969101. DOI: 10.1002/lsm.1900130513.

[11] J.-G. Werthen et al. "Power over fiber: a review of replacing copper by fiber in critical applications". In: *Optical Technologies for Arming, Safing, Fuzing, and Firing*. Ed. by William J Thomes Jr. and Fred M Dickey. Vol. 5871. International Society for Optics and Photonics. SPIE, 2005, p. 58710C. DOI: 10.1117/12.619753.

[12] Eugene Hecht. *Optics*. 5th ed. Pearson, 2016. ISBN: 9781292096933.

[13] Govind P Agrawal. *Nonlinear Fiber Optics*. 5th. Academic Press, 2013. ISBN: 9780123970237. DOI: 10.1016/b978-0-12-397023-7.00018-8.

[14] Justin Peatross and Michael Ware. *Physics of light and optics: A free online textbook*. 2010. ISBN: 9781312929272. DOI: 10.1364/fio.2010.jwa64.

[15] B E A Saleh and M C Teich. *Fundamentals of Photonics*. 2nd ed. Wiley Series in Pure and Applied Optics. Wiley, 2013. ISBN: 9781118585818.

[16] Richard P. Feynman et al. *The Feynman Lectures on Physics; Vol. I*. Vol. 33. 9. 1965, pp. 750–752. DOI: 10.1119/1.1972241.

[17] David N. Payne, Arthur J. Barlow, and Jens J.Ramskov Hansen. "Development of Low- and High-Birefringence Optical Fibers". In: *IEEE Transactions on Microwave Theory and Techniques* 30.4 (1982), pp. 323–334. ISSN: 15579670. DOI: 10.1109/TMTT.1982.1131072.

[18] Mark G. Kuzyk. *Polymer fiber optics: Materials, physics, and applications*. CRC press, 2006, pp. 1–405. ISBN: 9781420017809.

[19] Kunimasa Saitoh and Shoichiro Matsuo. "Multicore fiber technology". In: *Journal of Lightwave Technology* 34.1 (2016), pp. 55–66. ISSN: 07338724. DOI: 10.1109/JLT.2015.2466444.

[20] Jae Min Kim et al. "Enhanced strain measurement range of an FBG sensor embedded in seven-wire steel strands". In: *Sensors* 17.7 (2017). ISSN: 14248220. DOI: 10.3390/s17071654.

[21] Luc Thévenaz. *Advanced Fiber Optics*. 2011, pp. 1–388. ISBN: 9781482247039. DOI: 10.1201/b16404.

[22] J. Arnaud. "Optical waveguide theory". In: *Optical and Quantum Electronics* 12.3 (1980), pp. 187–191. ISSN: 03068919. DOI: 10.1007/BF00620035.

[23] Katsunari Okamoto. *Fundamentals of Optical Waveguides*. 2006. ISBN: 9780125250962. DOI: 10.1016/B978-0-12-525096-2.X5000-4.

[24] John A. Buck and Ira Jacobs. "Fundamentals of Optical Fibers". In: *Physics Today* 49.2 (1996), pp. 58–62. ISSN: 0031-9228. DOI: 10.1063/1.2807510.

[25] T. R. Parker et al. "Temperature and strain dependence of the power level and frequency of spontaneous Brillouin scattering in optical fibers". In: *Optics Letters* 22.11 (1997), p. 787. ISSN: 0146-9592. DOI: 10.1364/ol.22.000787.

[26] E. P. Ippen and R. H. Stolen. "Stimulated Brillouin scattering in optical fibers". In: *Applied Physics Letters* 21.11 (1972), pp. 539–541. ISSN: 00036951. DOI: 10.1063/1.1654249.

[27] A. H. Hartog, A. P. Leach, and M. P. Gold. "Distributed Temperature Sensing In Solid-Core Fibres". In: *Electronics Letters* 21.23 (1985), pp. 1061–1062. ISSN: 00135194. DOI: 10.1049/el:19850752.

[28] Hugo F. Martins et al. "Phase-sensitive optical time domain reflectometer assisted by first-order raman amplification for distributed vibration sensing over >100 km". In: *Journal of Lightwave Technology* 32.8 (2014), pp. 1510–1518. ISSN: 07338724. DOI: 10.1109/JLT.2014.2308354.

[29] Scott C. Rashleigh. "Origins and Control of Polarization Effects in Single-Mode Fibers". In: *Journal of Lightwave Technology* 1.2 (1983), pp. 312–331. ISSN: 15582213. DOI: 10.1109/JLT.1983.1072121.

[30] Luca Palmieri, Andrea Galtarossa, and Tommy Geisler. "Distributed characterization of bending effects on the birefringence of single-mode optical fibers". In: *Optics Letters* 35.14 (2010), p. 2481. ISSN: 0146-9592. DOI: 10.1364/ol.35.002481.

[31] S. C. Rashleigh. "Wavelength dependence of birefringence in highly birefringent fibers". In: *Optics Letters* 7.6 (1982), p. 294. ISSN: 0146-9592. DOI: 10.1364/ol.7.000294.

[32] Andrea Galtarossa et al. "Statistical characterization of fiber random birefringence". In: *Optics Letters* 25.18 (2000), p. 1322. ISSN: 0146-9592. DOI: 10.1364/ol.25.001322.

[33] Eric Udd and William B. Spillman. *Fiber Optic Sensors: An Introduction for Engineers and Scientists: Second Edition*. Wiley, 2011. ISBN: 9780470126844. DOI: 10.1002/9781118014103.

[34] Trevor Rice. "Fiber Optic Temperature SensorsA New Temperature Measurement Toolbox". In: *AIP Conference Proceedings* 684.1 (2003), pp. 1015–1020. ISSN: 0094-243X. DOI: 10.1063/1.1627262.

[35] Eric Udd. *Overview of fiber optic sensors*. 2017, pp. 1–34. ISBN: 9781420053661. DOI: 10.1201/9781420053661.

[36] Ethan F. Williams et al. "Distributed sensing of microseisms and teleseisms with submarine dark fibers". In: *Nature Communications* 10.1 (2019), p. 5778. ISSN: 20411723. DOI: 10.1038/s41467-019-13262-7.

[37] Juan C. Juarez and Henry F. Taylor. "Distributed fiber optic intrusion sensor system for monitoring long perimeters". In: *Sensors, and Command, Control, Communications, and Intelligence (C3I) Technologies for Homeland Security and Homeland Defense IV*. Vol. 5778. 2005, p. 692. DOI: 10.1117/12.602638.

[38] Henry F Taylor and Chung E Lee. *Apparatus and Method for Fiber Optic Intrusion Sensing*. 1993. DOI: 10.1145/634067.634234..

[39] Islam Ashry et al. "Early detection of red palm weevil using distributed optical sensor". In: *Scientific reports* 10.1 (2020), p. 3155. ISSN: 20452322. DOI: 10.1038/s41598-020-60171-7.

[40] H. F. Martins et al. "Early detection of pipeline integrity threats using a smart fiber optic surveillance system: the PIT-STOP project". In: *24th International Conference on Optical Fibre Sensors*. Ed. by Hypolito José Kalinowski, José Luís Fabris, and Wojtek J Bock. Vol. 9634. International Society for Optics and Photonics. SPIE, 2015, p. 96347X. ISBN: 9781628418392. DOI: 10.1117/12.2192075.

[41] C. R. Giles. "Lightwave applications of fiber bragg gratings". In: *Journal of Lightwave Technology* 15.8 (1997), pp. 1391–1404. ISSN: 07338724. DOI: 10.1109/50.618357.

[42] Paul S. Westbrook et al. "Kilometer length low loss enhanced back scattering fiber for distributed sensing". In: *25th International Conference on Optical Fiber Sensors* 10323 (2017), 103239Q. DOI: 10.1117/12.2276357.

[43] Luc Thévenaz et al. "Novel technique for distributed fibre sensing based on faint long gratings (FLOGs)". In: *23rd International Conference on Optical Fibre Sensors*. Ed. by José M López-Higuera et al. Vol. 9157. International Society for Optics and Photonics. SPIE, 2014, 91576W. ISBN: 9781628411751. DOI: 10.1117/12.2059668.

[44] Brian Culshaw and Alan Kersey. "Fiber-optic sensing: A historical perspective". In: *Journal of Lightwave Technology* 26.9 (2008), pp. 1064–1078. ISSN: 07338724. DOI: 10.1109/JLT.0082.921915.

[45] Luc Thévenaz. "Review and Progress on Distributed Fibre Sensing". In: *Optical Fiber Sensors 2006*. January 2006. 2006, ThC1. DOI: 10.1364/ofs.2006.thc1.

[46] Arthur H. Hartog. *An introduction to distributed optical fibre sensors*. Series in Fiber Optic Sensors. CRC Press, 2017, pp. 1–440. ISBN: 9781482259582. DOI: 10.1201/9781315119014.

[47] Xiaoyi Bao and Liang Chen. "Recent Progress in Distributed Fiber Optic Sensors". In: *Sensors* 12.7 (2012), pp. 8601–8639. ISSN: 14248220. DOI: 10.3390/s120708601.

[48] Luca Schenato. *A review of distributed fibre optic sensors for geo-hydrological applications*. Vol. 7. 9. 2017. ISBN: 3904982958. DOI: 10.3390/app7090896.

[49] Eyal Leviatan and Avishay Eyal. "High resolution DAS via sinusoidal frequency scan OFDR (SFS-OFDR)". In: *Optics Express* 23.26 (2015), p. 33318. ISSN: 1094-4087. DOI: 10.1364/oe.23.033318.

[50] J. P. Dakin et al. "Distributed optical fibre Raman temperature sensor using a semiconductor light source and detector". In: *Electronics Letters* 21.13 (1985), pp. 569–570. ISSN: 00135194. DOI: 10.1049/el:19850402.

[51] Abhisek Ukil, Hubert Braendle, and Peter Krippner. "Distributed temperature sensing: Review of technology and applications". In: *IEEE Sensors Journal* 12.5 (2012), pp. 885–892. ISSN: 1530437X. DOI: 10.1109/JSEN.2011.2162060.

[52] Kaoru Shimizu et al. "Coherent Self-Heterodyne Brillouin OTDR for Measurement of Brillouin Frequency Shift Distribution in Optical Fibers". In: *Journal of Lightwave Technology* 12.5 (1994), pp. 730–736. ISSN: 15582213. DOI: 10.1109/50.293961.

[53] Prabodh Chaube et al. "Distributed fiber-optic sensor for dynamic strain measurement". In: *IEEE Sensors Journal* 8.7 (2008), pp. 1067–1072. ISSN: 1530437X. DOI: 10.1109/JSEN.2008.926107.

[54] Alejandro Dominguez-Lopez et al. "Novel scanning method for distortion-free BOTDA measurements". In: *Optics Express* 24.10 (2016), p. 10188. ISSN: 1094-4087. DOI: 10.1364/oe.24.010188.

[55] Marc Niklès, Luc Thévenaz, and Philippe A. Robert. "Brillouin gain spectrum characterization in single-mode optical fibers". In: *Journal of Lightwave Technology* 15.10 (1997), pp. 1842–1851. ISSN: 07338724. DOI: 10.1109/50.633570.

[56] S. M. Maughan, H. H. Kee, and T. P. Newson. "Simultaneous distributed fibre temperature and strain sensor using microwave coherent detection of spontaneous brillouin backscatter". In: *Measurement Science and Technology* 12.7 (2001), pp. 834–842. ISSN: 09570233. DOI: 10.1088/0957-0233/12/7/315.

[57] T. R. Parker et al. "A fully distributed simultaneous strain and temperature sensor using spontaneous Brillouin backscatter". In: *IEEE Photonics Technology Letters* 9.7 (1997), pp. 979–981. ISSN: 10411135. DOI: 10.1109/68.593372.

[58] Kwang-Yong Song, Zuyuan He, and Kazuo Hotate. "Distributed Strain Measurement with Millimeter-order Spatial Resolution based on Brillouin Optical Correlation Domain Analysis and Beat Lock-in Detection Scheme". In: *Optical Fiber Sensors*. Optical Society of America, 2006, ThC2. DOI: 10.1364/OFS.2006.ThC2.

[59] Kwang Yong Song and Kazuo Hotate. "Distributed fiber strain sensor with 1-kHz sampling rate based on Brillouin optical correlation domain analysis". In: *IEEE Photonics Technology Letters* 19.23 (2007), pp. 1928–1930. ISSN: 10411135. DOI: 10.1109/LPT.2007.908772.

[60] Kwang Yong Song et al. "High-repetition-rate distributed Brillouin sensor based on optical correlation-domain analysis with differential frequency modulation". In: *Optics Letters* 36.11 (2011), p. 2062. ISSN: 0146-9592. DOI: 10.1364/ol.36.002062.

[61] Asher Voskoboinik et al. "Sweep-free distributed Brillouin time-domain analyzer (SF-BOTDA)". In: *Opt. Express* 19.26 (2011), B842–B847. DOI: 10.1364/OE.19.00B842.

[62] Yair Peled et al. "Monitoring the propagation of mechanical waves using an optical fiber distributed and dynamic strain sensor based on BOTDA". In: *Optics Express* 21.9 (2013), p. 10697. ISSN: 1094-4087. DOI: 10.1364/oe.21.010697.

[63] Dexin Ba et al. "Distributed measurement of dynamic strain based on multi-slope assisted fast BOTDA". In: *Optics Express* 24.9 (2016), p. 9781. ISSN: 1094-4087. DOI: 10.1364/oe.24.009781.

[64] Chihiro Kito et al. "Dynamic Strain Measurement of 10-km Fiber With Frequency-Swept Pulsed BOTDA". In: *Journal of Lightwave Technology* 35.9 (2017), pp. 1738–1743. ISSN: 07338724. DOI: 10.1109/JLT.2017.2680458.

[65] Dengwang Zhou et al. "Single-shot BOTDA based on an optical chirp chain probe wave for distributed ultrafast measurement". In: *Light: Science and Applications* 7.1 (2018), p. 32. ISSN: 20477538. DOI: 10.1038/s41377-018-0030-0.

[66] A Bergman, T Langer, and M Tur. "Slope-assisted complementary-correlation optical time-domain analysis of Brillouin dynamic gratings for high sensitivity, high spatial resolution, fast and distributed fiber strain sensing". In: *Fifth Asia-Pacific Optical Sensors Conference*. Vol. 9655. International Society for Optics and Photonics, 2015, p. 96550V.

[67] E.-G. Neumann. "Optical time domain reflectometer: comment". In: *Applied Optics* 17.11 (1978), p. 1675. ISSN: 0003-6935. DOI: 10.1364/ao.17.001675.

[68] M. C. Farries et al. "Distributed Temperature Sensor using Nd3+ -Doped Optical Fibre". In: *Electronics Letters* 22.8 (1986), pp. 418–419. ISSN: 00135194. DOI: 10.1049/el:19860285.

[69] J. N. Ross. "Polarisation Optical Time Domain Reflectometry." In: *IEE Colloquium (Digest)* 16.1982 /60 (1982), pp. 489–490. ISSN: 09633308.

[70] J. G. Ellison and A. S. Siddiqui. "A fully polarimetric optical time-domain reflectometer". In: *IEEE Photonics Technology Letters* 10.2 (1998), pp. 246–248. ISSN: 10411135. DOI: 10.1109/68.655373.

[71] Marc Wuilpart et al. "Measurement of the spatial distribution of birefringence in optical fibers". In: *IEEE Photonics Technology Letters* 13.8 (2001), pp. 836–838. ISSN: 10411135. DOI: 10.1109/68.935820.

[72] Byoung Yoon Kim and Sang Sam Choi. "Backscattering measurement of bending-induced birefringence in single mode fibres". In: *Electronics Letters* 17.5 (1981), pp. 193–194. ISSN: 00135194. DOI: 10.1049/el:19810136.

[73] R. E. Schuh et al. "Theoretical analysis and measurement of effects of fibre twist on polarisation mode dispersion of optical fibres". In: *Electronics Letters* 31.20 (1995), pp. 1772–1773. ISSN: 00135194. DOI: 10.1049/el:19951208.

[74] Y. J. Rao et al. "Distributed intrusion detection based on combination of ϕ-OTDR and POTDR". In: *19th International Conference on Optical Fibre Sensors*. Ed. by David Sampson et al. Vol. 7004. International Society for Optics and Photonics. SPIE, 2008, p. 700461. ISBN: 9780819472045. DOI: 10.1117/12.786921.

[75] Fei Peng et al. "106km fully-distributed fiber-optic fence based on P-OTDR with 2nd-order Raman amplification". In: *Optical Fiber Communication Conference, OFC 2013*. Optical Society of America, 2013, JW2A.22. ISBN: 9781557529626. DOI: 10.1364/nfoec.2013.jw2a.22.

[76] Yonas Muanenda. "Recent Advances in Distributed Acoustic Sensing based on Phase-Sensitive Optical Time Domain Reflectometry". In: *Journal of Sensors* 2018.3897873 (2018), pp. 1–16. ISSN: 1687-725X. DOI: 10.1155/2018/3897873.

[77] Z. N. Wang et al. "Ultra-long phase-sensitive OTDR with hybrid distributed amplification". In: *Optics Letters* 39.20 (2014), p. 5866. ISSN: 0146-9592. DOI: 10.1364/ol.39.005866.

[78] Hugo F. Martins et al. "Distributed vibration sensing over 125 km with enhanced SNR using Phi-OTDR over a URFL cavity". In: *Journal of Lightwave Technology* 33.12 (2015), pp. 2628–2632. ISSN: 07338724. DOI: 10.1109/JLT.2015.2396359.

[79] Jingdong Zhang et al. "80 km Fading Free Phase-Sensitive Reflectometry Based on Multi-Carrier NLFM Pulse Without Distributed Amplification". In: *Journal of Lightwave Technology* 37.18 (2019), pp. 4748–4754. ISSN: 15582213. DOI: 10.1109/JLT.2019.2919671.

[80] R. Juškaitis et al. "Interferometry with Rayleigh backscattering in a single-mode optical fiber". In: *Optics Letters* 19.3 (1994), p. 225. ISSN: 0146-9592. DOI: 10.1364/ol.19.000225.

[81] Sergey V. Shatalin, Vladimir N. Treschikov, and Alan J. Rogers. "Interferometric optical time-domain reflectometry for distributed optical-fiber sensing". In: *Applied Optics* 37.24 (1998), p. 5600. ISSN: 0003-6935. DOI: 10.1364/ao.37.005600.

[82] Yahei Koyamada et al. "Fiber-optic distributed strain and temperature sensing with very high measurand resolution over long range using coherent OTDR". In: *Journal of Lightwave Technology* 27.9 (2009), pp. 1142–1146. ISSN: 07338724. DOI: 10.1109/JLT.2008.928957.

[83] B. J. Soller et al. "Measurement of localized heating in fiber optic components with millimeter spatial resolution". In: *2006 Optical Fiber Communication Conference, and the 2006 National Fiber Optic Engineers Conference*. Vol. 2006. Optical Society of America, 2006, OFN3. ISBN: 1557528039. DOI: 10.1109/ofc.2006.216020.

[84] P. Healey. "Correction to statistics of rayleigh backscatter from a single-mode fiber". In: *IEEE Transactions on Communications* 35.10 (1987), p. 1112. ISSN: 00906778. DOI: 10.1109/TCOM.1987.1096677.

[85] R. M. Howard. "Statistics of coherently detected backscatter and range performance of coherent OTDRs". In: *Optical and Quantum Electronics* 19.3 (1987), pp. 145–168. ISSN: 03068919. DOI: 10.1007/BF02030651.

[86] Rongqing Hui and Maurice O'Sullivan. *Fiber Optic Measurement Techniques*. 2009. ISBN: 9780123738653. DOI: 10.1016/B978-0-12-373865-3.X0001-8.

[87] Hugo F. Martins et al. "Modulation instability-induced fading in phase-sensitive optical time-domain reflectometry". In: *Optics Letters* 38.6 (2013), p. 872. ISSN: 0146-9592. DOI: 10.1364/ol.38.000872.

[88] Hisashi Izumita et al. "The Performance Limit of Coherent OTDR Enhanced with Optical Fiber Amplifiers Due to Optical Nonlinear Phenomena". In: *Journal of Lightwave Technology* 12.7 (1994), pp. 1230–1238. ISSN: 15582213. DOI: 10.1109/50.301816.

[89] Alireza Morsali et al. "Significance of high extinction ratio laser pulse generation in coherent optical time domain reflectometry". In: *Optical Sensing and Detection VI*. Ed. by Francis Berghmans and Anna G Mignani. Vol. 11354. International Society for Optics and Photonics. SPIE, 2020, p. 30. DOI: 10.1117/12.2553998.

[90] Hugo F. Martins et al. "Coherent noise reduction in high visibility phase-sensitive optical time domain reflectometer for distributed sensing of ultrasonic waves". In: *Journal of Lightwave Technology* 31.23 (2013), pp. 3631–3637. ISSN: 07338724. DOI: 10.1109/JLT.2013.2286223.

[91] Chams Baker et al. "Enhancement of optical pulse extinction-ratio using the nonlinear Kerr effect for phase-OTDR". In: *Optics Express* 24.17 (2016), p. 19424. ISSN: 1094-4087. DOI: 10.1364/oe.24.019424.

[92] Yun-Jiang Rao et al. "Long-distance fiber-optic Φ-OTDR intrusion sensing system". In: *20th International Conference on Optical Fibre Sensors*. Ed. by Julian D C Jones. Vol. 7503. International Society for Optics and Photonics. SPIE, 2009, 75031O. ISBN: 9780819478146. DOI: 10.1117/12.835324.

[93] H. F. Martins et al. "Comparison of the use of first and second-order Raman amplification to assist a phase-sensitive optical time domain reflectometer in distributed vibration sensing over 125 km". In: *23rd International Conference on Optical Fibre Sensors*. Ed. by José M López-Higuera et al. Vol. 9157. International Society for Optics and Photonics. SPIE, 2014, 91576K. ISBN: 9781628411751. DOI: 10.1117/12.2059483.

[94] Fei Peng et al. "Ultra-long high-sensitivity Φ-OTDR for high spatial resolution intrusion detection of pipelines". In: *Optics Express* 22.11 (2014), p. 13804. ISSN: 1094-4087. DOI: 10.1364/oe.22.013804.

[95] Félix Rodríguez-Barrios et al. "Distributed brillouin fiber sensor assisted by first-order raman amplification". In: *Journal of Lightwave Technology* 28.15 (2010), pp. 2162–2172. ISSN: 07338724. DOI: 10.1109/JLT.2010.2051141.

[96] Mohamed N. Alahbabi, Yuh T. Cho, and Trevor P. Newson. "150-km-range distributed temperature sensor based on coherent detection of spontaneous Brillouin backscatter and in-line Raman amplification". In: *Journal of the Optical Society of America B* 22.6 (2005), p. 1321. ISSN: 0740-3224. DOI: 10.1364/josab.22.001321.

[97] Sonia Martin-Lopez et al. "Brillouin optical time-domain analysis assisted by second-order Raman amplification". In: *Optics Express* 18.18 (2010), p. 18769. ISSN: 1094-4087. DOI: 10.1364/oe.18.018769.

[98] Jin Li et al. "124km phase-sensitive OTDR with Brillouin amplification". In: *23rd International Conference on Optical Fibre Sensors*. Ed. by José M López-Higuera et al. Vol. 9157. International Society for Optics and Photonics. SPIE, 2014, 91575Z. ISBN: 9781628411751. DOI: 10.1117/12.2059187.

[99] Z. N. Wang et al. "Phase-sensitive optical time-domain reflectometry with Brillouin amplification". In: *Optics Letters* 39.15 (2014), p. 4313. ISSN: 0146-9592. DOI: 10.1364/ol.39.004313. arXiv: sureshgovindarajan.

[100] H. F. Martins et al. "Real time dynamic strain monitoring of optical links using the backreflection of live PSK data". In: *Optics Express* 24.19 (2016), p. 22303. ISSN: 1094-4087. DOI: 10.1364/oe.24.022303.

[101] Zinan Wang et al. "Distributed Acoustic Sensing Based on Pulse-Coding Phase-Sensitive OTDR". In: *IEEE Internet of Things Journal* 6.4 (2019), pp. 6117–6124. ISSN: 23274662. DOI: 10.1109/JIOT.2018.2869474.

[102] Christian Dorize and Elie Awwad. "Enhancing the performance of coherent OTDR systems with polarization diversity complementary codes". In: *Optics Express* 26.10 (2018), p. 12878. ISSN: 1094-4087. DOI: 10.1364/oe.26.012878.

[103] Yonas Muanenda et al. "Hybrid distributed acoustic and temperature sensor using a commercial off-the-shelf DFB laser and direct detection". In: *Optics Letters* 41.3 (2016), p. 587. ISSN: 0146-9592. DOI: 10.1364/ol.41.000587.

[104] Yonas Muanenda et al. "A Cost-Effective Distributed Acoustic Sensor Using a Commercial Off-the-Shelf DFB Laser and Direct Detection Phase-OTDR". In: *IEEE Photonics Journal* 8.1 (2016), pp. 1–10. ISSN: 19430655. DOI: 10.1109/JPHOT.2015.2508427.

[105] Mark Richards. *Fundamentals of Radar Signal Processing*. 2nd Editio. McGraw-Hill, 2005. ISBN: 978-0071798327.

[106] Juan Pastor-Graells et al. "SNR enhancement in high-resolution phase-sensitive OTDR systems using chirped pulse amplification concepts". In: *Optics Letters* 42.9 (2017), p. 1728. ISSN: 0146-9592. DOI: 10.1364/ol.42.001728.

[107] Dian Chen et al. "Fiber-optic distributed acoustic sensor based on a chirped pulse and a non-matched filter". In: *Optics Express* 27.20 (2019), p. 29415. ISSN: 1094-4087. DOI: 10.1364/oe.27.029415.

[108] Marcelo A. Soto, Jaime A. Ramírez, and Luc Thévenaz. "Intensifying the response of distributed optical fibre sensors using 2D and 3D image restoration". In: *Nature Communications* 7 (2016). ISSN: 20411723. DOI: 10.1038/ncomms10870.

[109] Michael Elad. "On the origin of the bilateral filter and ways to improve it". In: *IEEE Transactions on Image Processing* 11.10 (2002), pp. 1141–1151. ISSN: 10577149. DOI: 10.1109/TIP.2002.801126.

[110] D. Marr and E. Hildreth. "Theory of edge detection". In: *Proceedings of the Royal Society of London - Biological Sciences* 207.1167 (1980), pp. 187–217. ISSN: 09628452. DOI: 10.1098/rspb.1980.0020.

[111] Zengguang Qin, Liang Chen, and Xiaoyi Bao. "Wavelet denoising method for improving detection performance of distributed vibration sensor". In: *IEEE Photonics Technology Letters* 24.7 (2012), pp. 542–544. ISSN: 10411135. DOI: 10.1109/LPT.2011.2182643.

[112] Yuelan Lu et al. "Distributed vibration sensor based on coherent detection of phase-OTDR". In: *Journal of Lightwave Technology* 28.22 (2010), pp. 3243–3249. ISSN: 07338724. DOI: 10.1109/JLT.2010.2078798.

[113] Zengguang Qin, Hui Chen, and Jun Chang. "Signal-to-noise ratio enhancement based on empirical mode decomposition in phase-sensitive optical time domain reflectometry systems". eng. In: *Sensors* 17.8 (2017), p. 1870. ISSN: 14248220. DOI: 10.3390/s17081870.

[114] Alem Karladani and Mohammad Mehdi. "Impact of modulation instability on distributed optical fiber sensors". PhD thesis. 2016. DOI: 10.5075/epfl-thesis-7007.

[115] Maria R. Fernández-Ruiz et al. "Phase-sensitive OTDR probe pulse shapes robust against modulation-instability fading". In: *Optics Letters* 41.24 (2016), p. 5756. ISSN: 0146-9592. DOI: 10.1364/ol.41.005756.

[116] Zengguang Qin et al. "High sensitivity distributed vibration sensor based on polarization- maintaining configurations of phase-OTDR". In: *IEEE Photonics Technology Letters* 23.15 (2011), pp. 1091–1093. ISSN: 10411135. DOI: 10.1109/LPT.2011.2157337.

[117] Brandon Redding et al. "Quantitative amplitude measuring ϕ-OTDR using multiple uncorrelated Rayleigh backscattering realizations". In: *Optics Express* 27.24 (2019), p. 34952. ISSN: 1094-4087. DOI: 10.1364/oe.27.034952.

[118] Matthew J. Murray et al. "Speckle-based strain sensing in multimode fiber". In: *Optics Express* 27.20 (2019), p. 28494. ISSN: 1094-4087. DOI: 10.1364/oe.27.028494.

[119] R. Posey, G. A. Johnson, and S. T. Vohra. "Strain sensing based on coherent Rayleigh scattering in an optical fibre". In: *Electronics Letters* 36.20 (2000), pp. 1688–1689. ISSN: 00135194. DOI: 10.1049/el:20001200.

[120] Ezra Ip et al. "Coherent detection in optical fiber systems". In: *Optics Express* 16.2 (2008), p. 753. ISSN: 1094-4087. DOI: 10.1364/oe.16.000753.

[121] Zhengqing Pan et al. "Phase-sensitive OTDR system based on digital coherent detection". In: *Asia Communications and Photonics Conference and Exhibition, ACP 2011* 8311.8 (2011), 83110S. ISSN: 0277786X. DOI: 10.1117/12.905657.

[122] Zinan Wang et al. "Coherent Φ-OTDR based on I/Q demodulation and homodyne detection". In: *Optics Express* 24.2 (2016), p. 853. ISSN: 1094-4087. DOI: 10.1364/oe.24.000853.

[123] Meiqi Ren et al. "Theoretical and Experimental Analysis of Φ-OTDR Based on Polarization Diversity Detection". In: *IEEE Photonics Technology Letters* 28.6 (2016), pp. 697–700. ISSN: 10411135. DOI: 10.1109/LPT.2015.2504968.

[124] A. Masoudi, M. Belal, and T. P. Newson. "A distributed optical fibre dynamic strain sensor based on phase-OTDR". In: *Measurement Science and Technology* 24.8 (2013), pp. 1–7. ISSN: 13616501. DOI: 10.1088/0957-0233/24/8/085204.

[125] Ali Masoudi and Trevor P. Newson. "High spatial resolution distributed optical fiber dynamic strain sensor with enhanced frequency and strain resolution". In: *Optics Letters* 42.2 (2017), p. 290. ISSN: 0146-9592. DOI: 10.1364/ol.42.000290.

[126] A E Alekseev et al. "Phase-sensitive optical coherence reflectometer with differential phase-shift keying of probe pulses". In: *Quantum Electronics* 44.10 (2014), pp. 965–969. ISSN: 1063-7818. DOI: 10.1070/qe2014v044n10abeh015470.

[127] A E Alekseev et al. "A phase-sensitive optical time-domain reflectometer with dual-pulse phase modulated probe signal". In: *Laser Physics* 24.11 (2014). ISSN: 10441549. DOI: 10.1165/ajrcmb.18.6.2918.

[128] Zhou Sha, Hao Feng, and Zhoumo Zeng. "Phase demodulation method in phase-sensitive OTDR without coherent detection". In: *Optics Express* 25.5 (2017), p. 4831. ISSN: 1094-4087. DOI: 10.1364/oe.25.004831.

[129] Haniel Gabai and Avishay Eyal. "On the sensitivity of distributed acoustic sensing". In: *Optics Letters* 41.24 (2016), p. 5648. ISSN: 0146-9592. DOI: 10.1364/ol.41.005648.

[130] Kazuyoshi Itoh. "Analysis of the phase unwrapping algorithm". In: *Applied Optics* 21.14 (1982), p. 2470. ISSN: 0003-6935. DOI: 10.1364/ao.21.002470.

[131] Xin Lu, Marcelo A. Soto, and Luc Thévenaz. "Temperature-strain discrimination in distributed optical fiber sensing using phase-sensitive optical time-domain reflectometry". In: *Optics Express* 25.14 (2017), p. 16059. ISSN: 1094-4087. DOI: 10.1364/oe.25.016059.

[132] Sascha Liehr et al. "Relative change measurement of physical quantities using dual-wavelength coherent OTDR". In: *Optics Express* 25.2 (2017), p. 720. ISSN: 1094-4087. DOI: 10.1364/oe.25.000720.

[133] J. Pastor-Graells et al. "Single-shot distributed temperature and strain tracking using direct detection phase-sensitive OTDR with chirped pulses". In: *Optics Express* 24.12 (2016), p. 13121. ISSN: 1094-4087. DOI: 10.1364/oe.24.013121.

[134] Maria Rosario Fernandez-Ruiz et al. "Steady-sensitivity distributed acoustic sensors". In: *Journal of Lightwave Technology* 36.23 (2018), pp. 5690–5696. ISSN: 07338724. DOI: 10.1109/JLT.2018.2877849.

[135] Ji Xiong et al. "Single-Shot COTDR Using Sub-Chirped-Pulse Extraction Algorithm for Distributed Strain Sensing". In: *Journal of Lightwave Technology* 38.7 (2020), pp. 2028–2036. ISSN: 15582213. DOI: 10.1109/JLT.2020.2968632.

[136] María R. Fernańdez-Ruiz et al. "Laser Phase-Noise Cancellation in Chirped-Pulse Distributed Acoustic Sensors". In: *Journal of Lightwave Technology* 36.4 (2018), pp. 979–985. ISSN: 15582213. DOI: 10.1109/JLT.2017.2766688.

[137] María R. Fernández-Ruiz et al. "Statistical analysis of SNR in chirped-pulse ΦOTDR". In: *Optics InfoBase Conference Papers*. Vol. Part F124-OFS 2018. Optical Society of America, 2018, WF16. ISBN: 9781943580507. DOI: 10.1364/ofs.2018.wf16.

[138] María R. Fernández-Ruiz, Luis Costa, and Hugo F. Martins. "Distributed acoustic sensing using chirped-pulse phase-sensitive OTDR technology". In: *Sensors* 19.20 (2019), p. 4368. ISSN: 14248220. DOI: 10.3390/s19204368.

[139] Luis Costa et al. "Fully Distributed Optical Fiber Strain Sensor with 10^{-12} $\varepsilon/\sqrt{Hz}$ Sensitivity". In: *Journal of Lightwave Technology* 37.18 (2019), pp. 4487–4495. ISSN: 15582213. DOI: 10.1109/JLT.2019.2904560.

[140] Luis Costa et al. "Reaching pε/Hz sensitivity in a distributed optical fiber strain sensor". In: *Optics InfoBase Conference Papers*. Vol. Part F124-OFS 2018. Optical Society of America, 2018, TuD3. ISBN: 9781943580507. DOI: 10.1364/ofs.2018.tud3.

[141] Hari Datta Bhatta et al. "Dynamic Measurements of 1000 Microstrains Using Chirped-Pulse Phase-Sensitive Optical Time-Domain Reflectometry". In: *Journal of Lightwave Technology* 37.18 (2019), pp. 4888–4895. ISSN: 15582213. DOI: 10.1109/JLT.2019.2928621.

[142] Hari Datta Bhatta et al. "Extending the measurement of true dynamic strain via chirped-pulse phase-sensitive optical time domain reflectometry to 100's of microstrains". In: *Optics InfoBase Conference Papers*. Vol. Part F124-OFS 2018. Optical Society of America, 2018, WF14. ISBN: 9781943580507. DOI: 10.1364/ofs.2018.wf14.

[143] Luis Costa et al. "Optimization of first-order phase noise cancellation in CP-ϕOTDR". In: *European Workshop on Optical Fibre Sensors (EWOFS)*. 2019, p. 103. ISBN: 9781510631236. DOI: 10.1117/12.2541033.

[144] Miguel Soriano-Amat et al. "Characterization and modelling of induced virtual perturbations in chirped pulse ϕ-OTDR". In: *European Workshop on Optical Fibre Sensors (EWOFS)*. 2019, p. 93. ISBN: 9781510631236. DOI: 10.1117/12.2540760.

[145] Leonardo Marcon et al. "Analysis of Disturbance-Induced 'Virtual' Perturbations in Chirped Pulse ϕ -OTDR". In: *IEEE Photonics Technology Letters* 32.3 (2020), pp. 158–161. ISSN: 19410174. DOI: 10.1109/LPT.2019.2963219.

[146] Leonardo Marcon et al. "Boosting the spatial resolution in chirped pulse -OTDR using sub-band processing". In: *European Workshop on Optical Fibre Sensors (EWOFS)*. Vol. 1. 1. 2019, p. 37. ISBN: 9781510631236. DOI: 10.1117/12.2539794.

[147] Leonardo Marcon et al. "High-resolution chirped-pulse ϕ-OTDR by means of sub-bands processing". In: *Journal of Lightwave Technology* 38.15 (2020), pp. 4142–4149. ISSN: 15582213. DOI: 10.1109/JLT.2020.2981741.

[148] Hugo F. Martins et al. "Monitoring of Remote Seismic Events in Metropolitan Area Fibers using Distributed Acoustic Sensing (DAS) and Spatio-Temporal Signal Processing". In: *2019 Optical Fiber Communications Conference and Exhibition, OFC 2019 - Proceedings*. 2019, pp. 1–3. ISBN: 9781943580538. DOI: 10.1364/ofc.2019.m2j.1.

[149] María R. R. Fernández-Ruiz et al. "Teleseisms monitoring using chirped-pulse ϕOTDR". In: *Seventh European Workshop on Optical Fibre Sensors*. Ed. by Kyriacos Kalli, Sinead O O'Keeffe, and Gilberto Brambilla. Vol. 11199. International Society for Optics and Photonics. SPIE, 2019, p. 54. ISBN: 9781510631236. DOI: 10.1117/12.2539966.

[150] Luis Costa et al. "Fast and direct measurement of the linear birefringence profile in standard single-mode optical fibers". In: *Optics Letters* 45.3 (2020), p. 623. ISSN: 0146-9592. DOI: 10.1364/ol.382559.

[151] Andres Garcia-Ruiz et al. "Long-range distributed optical fiber hot-wire anemometer based on chirped-pulse ΦOTDR". In: *Optics Express* 26.1 (2018), p. 463. ISSN: 1094-4087. DOI: 10.1364/oe.26.000463.

[152] Andres Garcia-Ruiz et al. "Distributed photothermal spectroscopy in microstructured optical fibers: towards high-resolution mapping of gas presence over long distances". In: *Optics Express* 25.3 (2017), p. 1789. ISSN: 1094-4087. DOI: 10.1364/oe.25.001789.

[153] A. Garcia-Ruiz et al. "Distributed detection of hydrogen and deuterium diffusion into a single-mode optical fiber with chirped-pulse phase-sensitive optical time-domain reflectometry". In: *Optics Letters* 44.21 (2019), p. 5286. ISSN: 0146-9592. DOI: 10.1364/ol.44.005286.

[154] Regina Magalhães et al. "Fiber-based distributed bolometry". In: *Optics Express* 27.4 (2019), p. 4317. ISSN: 1094-4087. DOI: 10.1364/oe.27.004317.

[155] Regina Magalhães et al. "Long-range distributed solar irradiance sensing using optical fibers". In: *Sensors* 20.3 (2020), p. 908. ISSN: 14248220. DOI: 10.3390/s20030908.

[156] Victor Torres-Company, Daniel E. Leaird, and Andrew M. Weiner. "Dispersion requirements in coherent frequency-to-time mapping". In: *Optics Express* 19.24 (2011), p. 24718. ISSN: 1094-4087. DOI: 10.1364/oe.19.024718.

[157] G. Clifford Carter. "Coherence and time delay estimation". In: *Proceedings of the IEEE* 75.2 (1987), pp. 236–255. ISSN: 15582256. DOI: 10.1109/PROC.1987.13723.

[158] G. Clifford Carter. "Time Delay Estimation for Passive Sonar Signal Processing". In: *IEEE Transactions on Acoustics, Speech, and Signal Processing* 29.3 (1981), pp. 463–470. ISSN: 00963518. DOI: 10.1109/TASSP.1981.1163560.

[159] Giovanni Jacovitti and Gaetano Scarano. "Discrete Time Techniques for Time Delay Estimation". In: *IEEE Transactions on Signal Processing* 41.2 (1993), pp. 525–533. ISSN: 19410476. DOI: 10.1109/78.193195.

[160] John P. Ianniello. "Time Delay Estimation Via Cross-Correlation in the Presence of Large Estimation Errors". In: *IEEE Transactions on Acoustics, Speech, and Signal Processing* 30.6 (1982), pp. 998–1003. ISSN: 00963518. DOI: 10.1109/TASSP.1982.1163992.

[161] Charles H. Knapp and G. Clifford Carter. "The Generalized Correlation Method for Estimation of Time Delay". In: *IEEE Transactions on Acoustics, Speech, and Signal Processing* 24.4 (1976), pp. 320–327. ISSN: 00963518. DOI: 10.1109/TASSP.1976.1162830.

[162] Juan Pastor-Graells et al. "Chirped-Pulse Phase-Sensitive Reflectometer Assisted by First-Order Raman Amplification". In: *Journal of Lightwave Technology* 35.21 (2017), pp. 4677–4683. ISSN: 07338724. DOI: 10.1109/JLT.2017.2756558.

[163] Juan Pastor-Graells. "Chirped-pulse Phase-sensitive Optical Time Domain Reflectometry". In: 2018.

[164] Stefano Camatel and Valter Ferrero. "Narrow linewidth CW laser phase noise characterization methods for coherent transmission system applications". In: *Journal of Lightwave Technology* 26.17 (2008), pp. 3048–3055. ISSN: 07338724. DOI: 10.1109/JLT.2008.925046.

[165] Juan Pastor-Graells et al. "Impact of the laser phase noise on chirped-pulse phase-sensitive OTDR". In: *25th International Conference on Optical Fiber Sensors*. Vol. 10323. 2017, 103238T. ISBN: 9781510610910. DOI: 10.1117/12.2266870.

[166] T. Okoshi, K. Kikuchi, and A. Nakayama. "Novel method for high resolution measurement of laser output spectrum". In: *Electronics Letters* 16.16 (1980), pp. 630–631. ISSN: 00135194. DOI: 10.1049/el:19800437.

[167] I. Cespedes et al. "Methods for Estimation of Subsample Time Delays of Digitized Echo Signals". In: *Ultrasonic Imaging* 17.2 (1995), pp. 142–171. ISSN: 01617346. DOI: 10.1006/uimg.1995.1007.

[168] Azizul H. Quazi. "An Overview on the Time Delay Estimate in Active and Passive Systems for Target Localization". In: *IEEE Transactions on Acoustics, Speech, and Signal Processing* 29.3 (1981), pp. 527–533. ISSN: 00963518. DOI: 10.1109/TASSP.1981.1163618.

[169] Thomas Schanze. "Sinc Interpolation of Discrete Periodic Signals". In: *IEEE Transactions on Signal Processing* 43.6 (1995), pp. 1502–1503. ISSN: 19410476. DOI: 10.1109/78.388863.

[170] Sascha Liehr, Sven Münzenberger, and Katerina Krebber. "Wavelength-scanning coherent OTDR for dynamic high strain resolution sensing". In: *Optics Express* 26.8 (2018), p. 10573. ISSN: 1094-4087. DOI: 10.1364/oe.26.010573.

[171] Mengshi Wu et al. "Highly sensitive quasi-distributed fiber-optic acoustic sensing system by interrogating a weak reflector array". In: *Optics Letters* 43.15 (2018), p. 3594. ISSN: 0146-9592. DOI: 10.1364/ol.43.003594.

[172] Li Zhang et al. "Analysis and Reduction of Large Errors in Rayleigh-Based Distributed Sensor". In: *Journal of Lightwave Technology* 37.18 (2019), pp. 4710–4719. ISSN: 15582213. DOI: 10.1109/JLT.2019.2917746.

[173] Saeed V Vaseghi. *Advanced Digital Signal Processing and Noise Reducion*. 4th Editio. 2008, pp. 257 –270. ISBN: 9780470754061. DOI: 10.1002/9780470740156.

[174] Julius O Smith Iii. *Mathematics of the Discrete Fourier Transform (DFT)*. Second Edi. W3K Publishing, 2002. ISBN: ISBN 978-0-9745607-4-8.

[175] Yih Chyun Jenq. "Sinc interpolation errors in finite data record length". In: *Conference Proceedings - 10th Anniv., IMTC 1994: Advanced Technologies in I and M. 1994 IEEE Instrumentation and Measurement Technology Conference* (1994), pp. 704–707. DOI: 10.1109/IMTC.1994.352003.

[176] Jesus Selva. "Convolution-based trigonometric interpolation of band-limited signals". In: *IEEE Transactions on Signal Processing* 56.11 (2008), pp. 5465–5477. ISSN: 1053587X. DOI: 10.1109/TSP.2008.929659.

[177] Steven Reece and David Nicholson. "Tighter alternatives to the cramér-rao lower bound for discretetime filtering". In: *Bayesian Bounds for Parameter Estimation and Nonlinear Filtering/Tracking*. Vol. 1. IEEE, 2007, pp. 717–722. ISBN: 9780470544198. DOI: 10.1109/9780470544198.ch72.

[178] G Gagliardi; et al. "Probing the Ultimate Limit of Fiber-Optic Strain Sensing". In: *Science* 330.6007 (2010), pp. 1081–1084.

[179] George Skolianos et al. "Photonics sensing at the thermodynamic limit". In: *Optics Letters* 42.10 (2017), p. 2018. ISSN: 0146-9592. DOI: 10.1364/ol.42.002018.

[180] A V Oppenheim. *Discrete-Time Signal Processing*. Pearson education signal processing series. Pearson Education, 1999. ISBN: 9788131704929.

[181] Dian Chen, Qingwen Liu, and Zuyuan He. "Phase-detection distributed fiber-optic vibration sensor without fading-noise based on time-gated digital OFDR". In: *Optics Express* 25.7 (2017), p. 8315. ISSN: 1094-4087. DOI: 10.1364/oe.25.008315.

[182] J W Goodman. *Statistical Optics*. Ed. by Wiley. 2nd Editio. Wiley Series in Pure and Applied Optics. Wiley, 2015. ISBN: 9781119009467.

[183] J W Goodman. *Introduction to Fourier Optics*. Ed. by Wiley. McGraw-Hill physical and quantum electronics series. Roberts and Company Publishers, 2005, 2005. ISBN: 9780974707723.

[184] Jun Wang et al. "Weighted centroid localization algorithm: Theoretical analysis and distributed implementation". In: *IEEE Transactions on Wireless Communications* 10.10 (2011), pp. 3403–3413. ISSN: 15361276. DOI: 10.1109/TWC.2011.081611.102209.

[185] G. K. White. "Thermal expansion of reference materials: Copper, silica and silicon". In: *Journal of Physics D: Applied Physics* 6.17 (1973), pp. 2070–2078. ISSN: 13616463. DOI: 10.1088/0022-3727/6/17/313.

[186] Ivan P. Kaminow. "Polarization in Optical Fibers". In: *IEEE Journal of Quantum Electronics* 17.1 (1981), pp. 15–22. ISSN: 15581713. DOI: 10.1109/JQE.1981.1070626.

[187] Luca Palmieri, Tommy Geisler, and Andrea Galtarossa. "Effects of spin process on birefringence strength of single-mode fibers". In: *Optics Express* 20.1 (2012), p. 1. ISSN: 1094-4087. DOI: 10.1364/oe.20.000001.

[188] Yuangang Lu et al. "Distributed birefringence measurement with beat period detection of homodyne Brillouin optical time-domain reflectometry". In: *Optics Letters* 37.19 (2012), p. 3936. ISSN: 0146-9592. DOI: 10.1364/ol.37.003936.

[189] A. J. Rogers. "Polarization-optical time domain reflectometry: a technique for the measurement of field distributions". In: *Applied Optics* 20.6 (1981), p. 1060. ISSN: 0003-6935. DOI: 10.1364/ao.20.001060.

[190] J. Neil Ross. "Birefringence measurement in optical fibers by polarization-optical time-domain reflectometry". In: *Applied Optics* 21.19 (1982), p. 3489. ISSN: 0003-6935. DOI: 10.1364/ao.21.003489.

[191] Andrea Galtarossa and Luca Palmieri. "Spatially resolved PMD measurements". In: *Journal of Lightwave Technology* 22.4 (2004), pp. 1103–1115. ISSN: 07338724. DOI: 10.1109/JLT.2004.825243.

[192] M. Wegmuller, M. Legré, and N. Gisin. "Distributed beatlength measurement in single-mode fibers with optical frequency-domain reflectometry". In: *Journal of Lightwave Technology* 20.5 (2002), pp. 828–835. ISSN: 07338724. DOI: 10.1109/JLT.2002.1007936.

[193] Mark E. Froggatt et al. "Characterization of polarization-maintaining fiber using high-sensitivity optical-frequency-domain reflectometry". In: *Journal of Lightwave Technology* 24.11 (2006), pp. 4149–4154. ISSN: 07338724. DOI: 10.1109/JLT.2006.883607.

[194] Marcelo A. Soto et al. "Highly sensitive distributed birefringence measurements based on a two-pulse interrogation of a dynamic Brillouin grating". In: *25th International Conference on Optical Fiber Sensors*. Ed. by Youngjoo Chung et al. Vol. 10323. International Society for Optics and Photonics. SPIE, 2017, 103238Z. ISBN: 9781510610910. DOI: 10.1117/12.2267471.

[195] Yongkang Dong et al. "Characterization of Distributed Birefringence in Optical Fibers". In: *Handbook of Optical Fibers*. Ed. by Gang-Ding Peng. Singapore: Springer Singapore, 2018, pp. 1–31. ISBN: 978-981-10-1477-2. DOI: 10.1007/978-981-10-1477-2_60-1.

[196] Marcelo A. Soto et al. "Distributed phase birefringence measurements based on polarization correlation in phase-sensitive optical time-domain reflectometers". In: *Optics Express* 23.19 (2015), p. 24923. ISSN: 1094-4087. DOI: 10.1364/oe.23.024923.

[197] Andrea Galtarossa et al. "Reflectometric measurement of birefringence rotation in single-mode optical fibers". In: *Optics Letters* 33.20 (2008), p. 2284. ISSN: 0146-9592. DOI: 10.1364/ol.33.002284.

[198] Luca Palmieri. "Polarization properties of spun single-mode fibers". In: *Journal of Lightwave Technology* 24.11 (2006), pp. 4075–4088. ISSN: 07338724. DOI: 10.1109/JLT.2006.883132.

[199] Andrea Galtarossa and Luca Palmieri. "Distributed polarization sensing". In: *25th International Conference on Optical Fiber Sensors*. Ed. by Youngjoo Chung et al. Vol. 10323. International Society for Optics and Photonics. SPIE, 2017, p. 1032318. ISBN: 9781510610910. DOI: 10.1117/12.2272460.

[200] Javier Tejedor et al. "Real Field Deployment of a Smart Fiber-Optic Surveillance System for Pipeline Integrity Threat Detection: Architectural Issues and Blind Field Test Results". In: *Journal of Lightwave Technology* 36.4 (2018), pp. 1052–1062. ISSN: 15582213. DOI: 10.1109/JLT.2017.2780126.

[201] T. M. Daley et al. "Field testing of modular borehole monitoring with simultaneous distributed acoustic sensing and geophone vertical seismic profiles at Citronelle, Alabama". In: *Geophysical Prospecting* 64.5 (2016), pp. 1318–1334. ISSN: 13652478. DOI: 10.1111/1365-2478.12324.

[202] Fei Peng et al. “Real-time position and speed monitoring of trains using phase-sensitive OTDR”. In: *IEEE Photonics Technology Letters* 26.20 (2014), pp. 2055–2057. ISSN: 10411135. DOI: 10.1109/LPT.2014.2346760.

[203] Philippe Jousset et al. “Dynamic strain determination using fibre-optic cables allows imaging of seismological and structural features”. In: *Nature Communications* 9.1 (2018). ISSN: 20411723. DOI: 10.1038/s41467-018-04860-y.

[204] J. H. Cole, R. L. Johnson, and P. G. Bhuta. “Fiber-optic detection of sound”. In: *Journal of the Acoustical Society of America* 62.5 (1977), pp. 1136–1138. ISSN: NA. DOI: 10.1121/1.381647.

[205] Ali Masoudi, Mohammad Belal, and Trevor P Newson. “Distributed optical fibre audible frequency sensor ”. In: *23rd International Conference on Optical Fibre Sensors*. Ed. by José M López-Higuera et al. Vol. 9157. International Society for Optics and Photonics. SPIE, 2014, pp. 537–540. DOI: 10.1117/12.2058484.

[206] Yuqing Wu et al. “Distributed Fiber Voice Sensor Based on Phase-Sensitive Optical Time-Domain Reflectometry”. In: *IEEE Photonics Journal* 7.6 (2015). ISSN: 19430655. DOI: 10.1109/JPHOT.2015.2499539.

[207] Liang Jiajing et al. “Distributed acoustic sensing for 2D and 3D acoustic source localization”. In: *Optics Letters* 44.7 (2019), p. 1690. ISSN: 0146-9592. DOI: 10.1364/ol.44.001690.